UNIVERSITY OF BELGRADE

Faculty of Physics

Suzana Miladić

QUANTUM MONTE CARLO STUDY OF POLARON MOBILITY

Doctoral Dissertation

Belgrade, 2026

UNIVERZITET U BEOGRADU

Fizički fakultet

Suzana Miladić

PROUČAVANJE POKRETLJIVOSTI POLARONA KORISTEĆI KVANTNE MONTE KARLO METODE

Doktorska disertacija

Beograd, 2026

Thesis Defense Committee

Thesis Advisor:

Dr. Nenad Vukmirović
Research Professor
Institute of Physics Belgrade
University of Belgrade

Committee Members:

Dr. Veljko Janković
Associate Research Professor
Institute of Physics Belgrade
University of Belgrade

Dr. Božidar Nikolić
Associate Professor
Faculty of Physics
University of Belgrade

Dr. Đorđe Spasojević
Full Professor
Faculty of Physics
University of Belgrade

Dissertation Data

Title: QUANTUM MONTE CARLO STUDY OF POLARON MOBILITY

Abstract

In this thesis, a numerically exact methodology is developed for calculating current–current correlation functions in electron–phonon coupled systems within the path-integral quantum Monte Carlo framework, with emphasis on mitigating the dynamical sign problem. This approach is used to determine the temperature dependence of the dc mobility of the Holstein polaron over a broad range of parameters. The resulting numerically exact data provide a basis for analyzing transport regimes and assessing the validity of approximate transport theories for the Holstein model.

The Holstein model, as the simplest microscopic model of a polaron with local electron–phonon interaction, is used to investigate mobility as a function of temperature and coupling strength. The path-integral Monte Carlo formalism enables a consistent treatment of real- and imaginary-time dynamics, but is limited by the sign problem and the instability of analytic continuation. These challenges are addressed by employing position and momentum representations of the electronic degrees of freedom, improving the accessible real-time range and statistical reliability. In addition, imaginary- and real-time data are combined to enhance the stability of the analytic continuation procedure.

The obtained numerically exact results are used to identify band, hopping, and polaron band transport regimes and to construct a transport regime diagram. Almost the entire explored parameter space is consistently described within these three transport mechanisms.

It is concluded that the proposed path-integral QMC framework provides a consistent description of charge transport within the Holstein model across different regimes and offers a reliable benchmark for assessing approximate theoretical approaches.

Keywords: Holstein model, polaron transport, electron-phonon interaction, quantum Monte Carlo, path-integral methods, current-current correlation function, mobility, transport regimes, dynamical sign problem, analytic continuation

Scientific field: Physics

Scientific subfield: Condensed matter physics

UDC number: 538.9

Podaci o doktorskoj disertaciji

Naslov: PROUČAVANJE POKRETLJIVOSTI POLARONA KORISTEĆI KVANTNE MONTE KARLO METODE

Sažetak:
U ovoj tezi, razvijena je numerički egzaktna metodologija za računanje struja-struja korelacionih funkcija u sistemima sa elektron-fonon interakcijom primenom kvantnog Monte Karlo metoda u okviru formalizma integrala po putanjama, sa fokusom na ublažavanju problema dinamičkog znaka. Ovaj pristup korišćen je za određivanje temperaturske zavisnosti pokretljivosti Holštajnovog polarona u širokom opsegu parametara. Dobijeni numerički egzaktni podaci predstavljaju osnovu za proučavanje transportnih režima i procenu validnosti približnih teorija transporta u Holštajnovom modelu.

Holštajnov model, kao najjednostavniji model polarona sa lokalnom elektron-fonon interakcijom, korišćen je za proučavanje pokretljivosti u zavisnosti od temperature i jačine interakcije. Kvantni Monte Karlo metod u kombinaciji sa formalizmom integrala po putanjama omogućava dosledan opis dinamike sistema u realnom i imaginarnom vremenu, ali je limitiran problemom dinamičkog znaka i poteškoćama analitičkog produženja. Ovi problemi se umanjuju korišćenjem bazisa položaja i impulsa elektrona. Na ovaj način povećan je domet simulacije u realnom vremenu kao i statistička tačnost rezultata. Dodatno, kombinacijom podataka u realnom i imaginarnom vremenu poboljšan je ishod analitičkog produženja.

Numerički egzaktni podaci korišćeni su za identifikaciju zonskog transporta, transporta preskakanjem i polaronskog zonskog transporta, te za konstruisanje dijagrama transportnih režima. Ispitani opseg parametara je velikim delom adekvatno opisan sa ova tri transportna mehanizma.

Zaključak je da kvantni Monte Karlo metod u kombinaciji sa formalizmom integrala po putanjama pruža adekvatan opis transporta Holštajnovog modela u različitim režimima i služi kao dobra referenca za procenu tačnosti približnih metoda.

Ključne reči: Holštajnov model, polaronski transport, elektron-fonon interakcija, kvantni Monte Karlo; metodi integrala po putanjama, struja-struja korelaciona funkcija, pokretljivost, transportni režimi, problem dinamičkog znaka, analitičko produženje

Naučna oblast: Fizika

Uža naučna oblast: Fizika kondenzovane materije

UDK broj: 538.9

Acknowledgments

The work presented in this thesis was carried out under the supervision of Dr. Nenad Vukmirović. I am deeply grateful for his guidance and support throughout this research. His physical insight and his approach to guiding a new PhD student through the concepts of computational physics made the learning process both accessible and enjoyable. He showed great patience, always adapting to my pace when progress was slower, and encouraged constructive discussions that significantly improved my understanding of polaron physics. Beyond research, he also provided valuable guidance on various aspects of academic and professional development.

The research presented in this thesis, as well as my entire PhD work, was carried out at the Scientific Computing Laboratory, Institute of Physics Belgrade. I am especially grateful to the late Dr. Antun Balaž, who first introduced me to the laboratory and to my mentor, Nenad. I will remember him as someone who had a profound impact on my life, as he provided me with the opportunity to pursue my ambition of becoming a scientist, while also offering guidance and help whenever it was needed. I would also like to thank the current head of the laboratory, Dr. Marija Mitrović Dankulov, for continuing in the same spirit and for providing ongoing understanding and support to PhD students.

During my PhD, I spent a significant amount of time in the SCL laboratory, surrounded by dear colleagues. Many of our discussions were both engaging and constructive, and I learned a great deal from them. I am grateful for the insights and knowledge they shared, which contributed greatly to different aspects of my work.

The greatest support, and a constant presence throughout this work, has been my mother, Svetlana. She recognized my interest in science from an early age and encouraged me to pursue what I love. During my PhD, she showed genuine interest in my work, even though her own background is not in science. Her encouragement and understanding carried me through to the end, even at times when the path felt difficult.

I am also grateful to my extended family and friends for their interest in my work and for their continuous encouragement and motivation. I would like to thank Stefan for his support and for his understanding and patience during the final months of writing this thesis.

The work on this thesis was supported by the Science Fund of the Republic of Serbia, Grant No. 5468, Polaron Mobility in Model Systems and real Materials - PolMoReMa. I also acknowledge the funding provided by the Institute of Physics Belgrade through a grant from the Ministry of Science, Technological Development, and Innovation of the Republic of Serbia and the support by the Serbia Accelerating Innovation and Growth Entrepreneurship (SAIGE) project within the SEED grant for young researchers.

Numerical computations were performed on the PARADOX-IV supercomputing facility at the Scientific Computing Laboratory, National Center of Excellence for the Study of Complex Systems, Institute of Physics Belgrade.

List of Figures

List of Tables

Contents

Chapter 1

Introduction

The development of modern technology is deeply intertwined with the ability to understand and control the motion of charge carriers in solids. From the first semiconductor devices in the early twentieth century to today's highly integrated microprocessors, progress in electronics has been driven by advances in both fundamental physics and materials science. The emergence of quantum mechanics and solid-state physics provided the theoretical framework for describing the electronic properties of materials, thereby enabling the design of semiconductor devices that form the backbone of modern computing.

The invention of the transistor in the mid-twentieth century marked a decisive turning point, making it possible to miniaturize and mass-produce electronic components. This progress accelerated rapidly with the development of integrated circuits, ultimately leading to modern computers and digital technologies. Over the past several decades, the number of components that can be integrated onto a single chip has increased exponentially, a trend commonly referred to as Moore's law. This continuous scaling has enabled extraordinary growth in computational power and has profoundly shaped modern society, influencing communication, industry, science, and everyday life.

At the same time, advances in computational capabilities have transformed the way physical systems are studied. The increasing availability of powerful computing resources has enabled the development of sophisticated numerical methods for investigating complex materials and transport phenomena, complementing analytical approaches and experimental techniques. As a result, theoretical and computational physics have become indispensable tools for understanding existing materials and guiding the design of new ones with tailored properties [1].

However, as conventional semiconductor technology approaches its physical and technological limits, new challenges emerge. Further miniaturization becomes increasingly difficult, while there is a growing demand for electronic devices that are not only smaller but also flexible, lightweight, and compatible with large-area fabrication. Applications such as wearable electronics, flexible displays, bio-integrated sensors, and low-cost energy devices require materials with properties that differ fundamentally from those of traditional inorganic semiconductors [2].

In this context, organic semiconductors have emerged as a promising class of materials offering new possibilities. These materials are composed of molecular building blocks with rich and tunable electronic structure, whose properties can be engineered through chemical design. Their intrinsic mechanical flexibility and compatibility with large-area, low-cost fabrication techniques make them particularly attractive for next-generation electronic and optoelectronic applications [3]. Organic semiconductors are already widely used in technologies such as organic light-emitting diodes (OLEDs), organic field-effect transistors (OFETs), and organic solar cells [4–7]. In particular, OLED technology has become standard in modern displays, including smartphones, televisions, and emerging flexible or foldable devices, highlighting the growing technological relevance of these materials [8].

Despite their technological success, organic semiconductors also present fundamental challenges. Their electronic properties are governed not only by the motion of charge carriers but also by the intricate interplay between molecular structure, intermolecular interactions, and the dynamic nature of

the lattice. The weak van der Waals bonding between molecules leads to significant thermal motion, which strongly influences electronic coupling and transport properties [9, 10]. Understanding how charge carriers move in such environments is therefore essential both for improving device performance and for advancing the broader understanding of transport phenomena in condensed matter systems.

This thesis is devoted to the study of charge transport in organic molecular systems, with particular emphasis on how interactions between charge carriers and their local environment give rise to different transport regimes. Before introducing the theoretical framework in detail, it is useful to first examine the structural and physical properties of organic semiconductors that distinguish them from their inorganic counterparts.

1.1 Organic molecular semiconductors

Organic semiconductors are materials composed of molecules built primarily from carbon and hydrogen atoms arranged in conjugated π-electron structures where carbon atoms form alternating single and double bonds. In such systems, carbon atoms typically adopt sp^2 hybridization, forming three equivalent sp^2 orbitals and one remaining $2p_z$ orbital. The sp^2 orbitals form strong σ-bonds with neighboring atoms, establishing the structural backbone of the molecule, often in planar ring configurations. The remaining unhybridized $2p_z$ orbitals are oriented perpendicular to this molecular plane and overlap to form weak π bonds. A double carbon-carbon bond thus consists of one strong σ and one weak π bond. The alternating pattern of single and double bonds in conjugated systems leads to extended π-electron states that are delocalized across the molecule. From a molecular orbital perspective, this results in the formation of bonding (π) and antibonding (π^*) orbitals, commonly referred to as the highest occupied molecular orbital (HOMO) and lowest unoccupied molecular orbital (LUMO). The energy difference between these orbitals plays a role analogous to the band gap between the valence and conduction bands in inorganic semiconductors and is central to the electronic properties of organic materials. In general, as the conjugated system extends over a larger number of connected carbon atoms, the HOMO–LUMO gap decreases [3, 10–12].

A fundamental building block of many organic semiconductors is the aromatic molecule, such as benzene, in which carbon atoms form planar ring-like structures with delocalized π-electron orbitals. These molecules typically exhibit a high degree of symmetry and planarity, which facilitates intermolecular π–π interactions when brought into proximity. In molecular solids, such aromatic units can stack or arrange in various geometries, allowing π-orbitals from adjacent molecules to overlap. This intermolecular overlap provides the primary pathway for charge transport in organic materials [3, 10, 11]. Representative molecular structures of organic materials are shown in Fig. 1.1, illustrating the progression from simple aromatic units to extended conjugated systems and more complex macromolecular architectures.

Unlike inorganic crystals, where atoms are connected through strong covalent bonds into rigid three-dimensional lattices, organic molecular solids consist of discrete molecules held together by relatively weak van der Waals interactions. As a consequence, organic crystals typically exhibit lattice constants on the order of 1 nm, comparable to molecular size, while in inorganic crystals lattice spacings are significantly smaller and determined by atomic dimensions. The relatively large intermolecular separation results in weak orbital overlap and small electronic coupling between neighboring molecules. Consequently, the electronic properties of organic semiconductors depend not only on the structure of individual molecules but also sensitively on their arrangement within the crystal [2, 10, 11].

The molecular nature of these materials has several important consequences. Organic molecules are relatively large, often consisting of tens to hundreds of atoms, and possess many internal degrees of freedom. These include vibrational modes associated with bond stretching, bending, and torsional motion, as well as rotational and translational motion of entire molecules within the crystal. The large

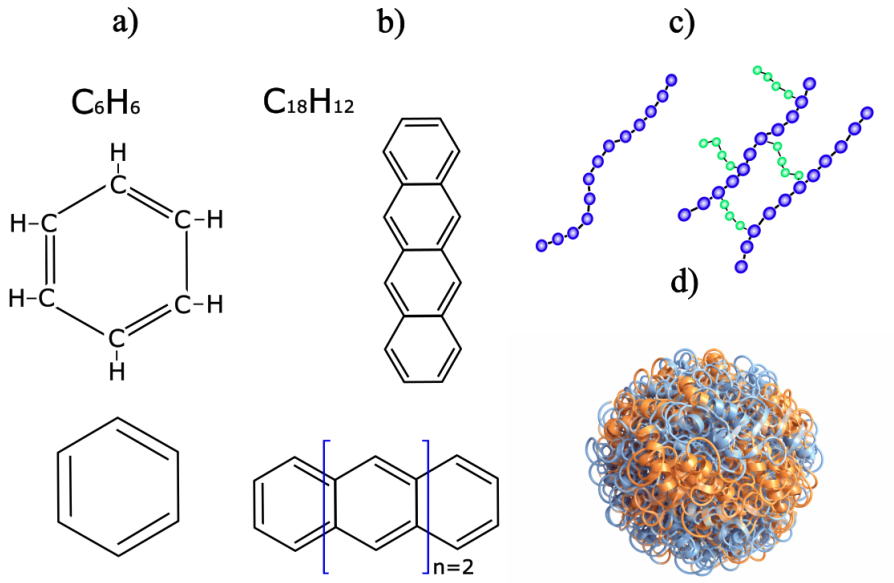

Figure 1.1: Representative molecular building blocks of organic materials. a) Benzene molecule as a fundamental aromatic unit; b) tetracene - polyacene consisting of four fused benzene rings; c) schematic polymer chain featuring repeating molecular units; d) schematic representation of a biomolecule-like structure showing enhanced structural complexity.

number of such degrees of freedom gives rise to a rich spectrum of lattice excitations that strongly influence the electronic properties of the material [9, 10].

Another key characteristic of organic molecules is their high polarizability. The electronic charge distribution is spatially extended and relatively soft, allowing the electron cloud to be easily distorted. When an electron or hole is introduced into the system, it modifies the local electrostatic environment and induces a rearrangement of charge density and molecular geometry in its surroundings. This strong coupling between charge carriers and their local environment is a defining feature of organic semiconductors and plays a central role in determining their transport properties [11, 13].

Charge carriers in these materials can be generated in several ways. In electronic devices, carriers are typically injected from metallic electrodes, while in optoelectronic applications they can be created through photoexcitation. The energy required to add or remove an electron from a molecule is determined by its ionization energy and electron affinity, typically on the order of a few electronvolts. Since thermal energy at room temperature is much smaller than this scale, free carriers are generally not present in significant numbers unless they are externally injected, optically generated, or introduced through doping [3, 11].

The weak intermolecular bonding, which decays rapidly with intermolecular distance (approximately as $1/R^6$), leads to relatively soft crystal structures. As a consequence, thermal motion at room temperature produces significant fluctuations in both the positions and orientations of molecules. Because the electronic coupling between neighboring molecules depends sensitively on their relative arrangement, even small displacements can lead to substantial variations in orbital overlap. Charge transport in organic semiconductors is therefore inherently sensitive to lattice dynamics [9, 10].

The arrangement of molecules within the crystal, commonly referred to as molecular packing, is a central factor in determining transport properties. Different packing motifs, such as slipped-stack, herringbone, or brick-wall structures, lead to distinct patterns of orbital overlap and define preferred pathways for charge motion. In many organic crystals, electronic coupling is significantly stronger along certain directions than others, resulting in strongly anisotropic transport. In some cases, charge carriers effectively propagate along a dominant direction, giving rise to quasi-one-dimensional transport behavior [3, 10, 11]. Representative molecular packing motifs are illustrated in Fig. 1.2,

highlighting how different arrangements give rise to anisotropic charge transport.

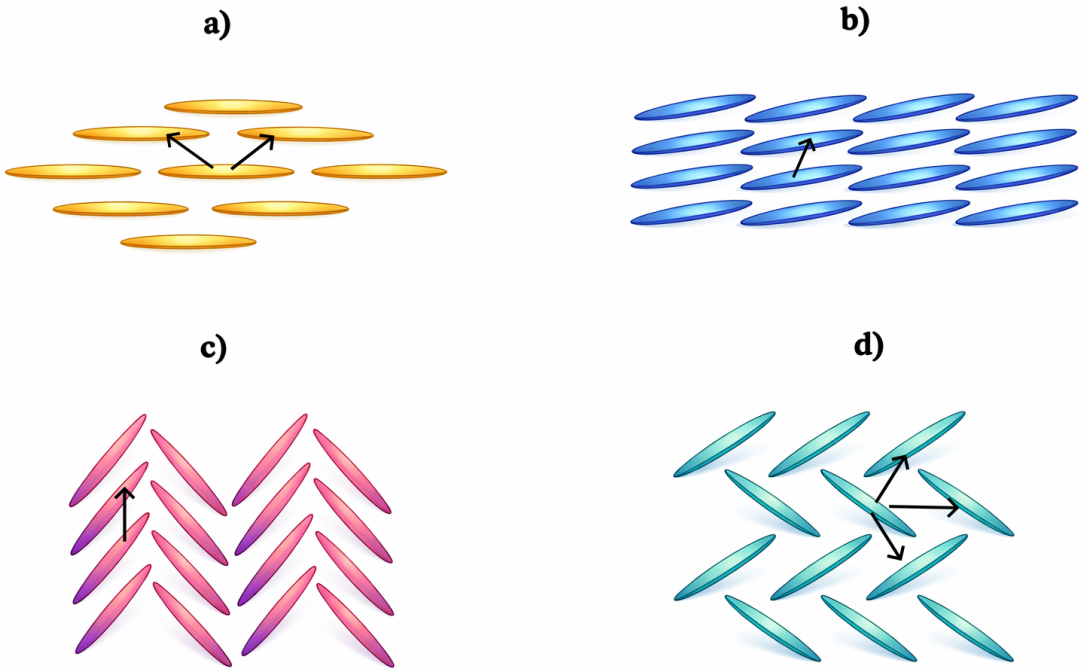

Figure 1.2: Representative molecular packing motifs commonly found in organic crystals. a) Brickwall packing; b) slipped-stack packing; c) slipped-π stack arrangement; d) herringbone packing. The arrows indicate the directions of the dominant intermolecular electronic coupling (transfer integral). The schematic representation of molecular packing motifs follows commonly observed structures reported in the literature [10].

A particularly illustrative example is the organic semiconductor rubrene, which exhibits some of the highest charge carrier mobilities among organic materials. Its crystal structure enables favorable π-orbital overlap along specific crystallographic directions, leading to enhanced electronic coupling and improved transport properties along those directions. At the same time, coupling remains much weaker in other directions, resulting in pronounced anisotropy. This example highlights how molecular packing directly governs transport behavior in organic crystals [10, 14]. The molecular structure of rubrene and its characteristic slipped π–π stacking arrangement are illustrated in Fig. 1.3, together with the direction of strongest intermolecular electronic coupling, which determines the anisotropy of charge transport.

It is instructive to compare the charge carrier mobilities of organic semiconductors with those of inorganic materials. High-quality silicon crystals exhibit electron mobilities on the order of 10^3 cm^2/Vs, while materials such as graphene can reach even higher values. In contrast, typical mobilities in organic semiconductors range from 10^{-3} to 10^1 cm^2/Vs. Although significantly lower, these values remain sufficient for many applications where flexibility, low cost, and large-area fabrication are more important than ultrafast electronic performance. At the same time, improving carrier mobility remains one of the central challenges in the development of organic electronic materials. A representative comparison across different material classes is summarized in Table 1.1 [7, 9, 10].

Another important distinction between organic and inorganic semiconductors lies in the comparable magnitude of several key energy scales. The electronic coupling between molecules, the energies of relevant vibrational modes, and the strength of their interaction typically all fall within the range of tens to hundreds of millielectronvolts. In particular, low-frequency intermolecular vibrational modes, associated with the relative motion of neighboring molecules, play a dominant role in modulating the

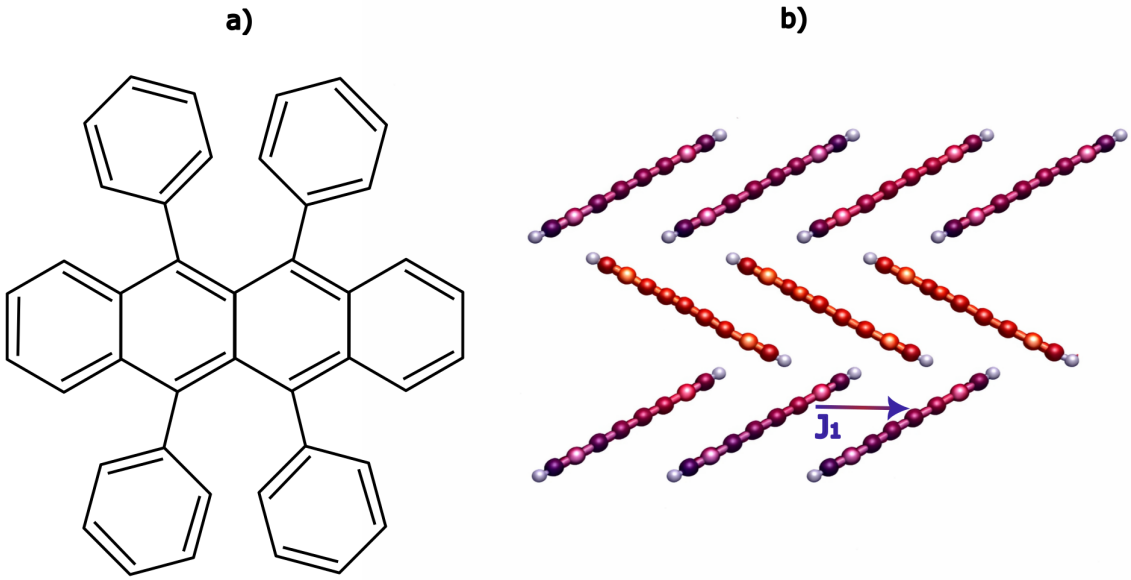

Figure 1.3: Structure and molecular packing of rubrene. a) Chemical structure of the rubrene molecule. b) Schematic representation of the slipped π–π stacking arrangement in rubrene crystals. The arrow indicates the direction of the dominant electronic coupling between neighboring molecules. The illustrated molecular packing motifs are based on structural arrangements that are frequently described in the literature [10].

Table 1.1: Representative charge carrier mobilities for different classes of semiconducting materials. Values are approximate and depend on material quality, temperature, and measurement conditions [4, 9–11, 14].

Material Class	**Example Material**	**Mobility (cm^2/Vs)**
Inorganic semiconductors		
Monocrystalline elemental semiconductor	Si (single crystal)	$\sim 10^3$
Amorphous elemental semiconductor	a-Si	$10^{-1} - 1$
Compound semiconductor	GaAs	$\sim 10^3 - 10^4$
Transition metal dichalcogenide	MoS_2	$10^1 - 10^2$
Low-dimensional / nanomaterials		
Graphene (suspended)	Graphene	$10^4 - 10^6$
Graphene (supported)	Graphene on SiO_2	$10^3 - 10^4$
Carbon nanotubes	CNTs	$10^3 - 10^5$
Organic semiconductors		
Small-molecule crystal	Rubrene	$1 - 20$
High-mobility OSC	DNTT, BTBT derivatives	$1 - 10$
Polymer semiconductor	P3HT	$10^{-4} - 10^{-1}$
Amorphous organic film	Disordered OSC	$10^{-6} - 10^{-3}$

electronic coupling. As a result, even modest thermal fluctuations can significantly influence charge transport [9, 11, 13].

These considerations demonstrate that charge transport in organic semiconductors cannot be understood solely in terms of static electronic structure. Instead, it is governed by a dynamic interplay between electronic motion and molecular vibrations. In the following section, this interplay is examined in more detail, with emphasis on how it gives rise to different transport mechanisms.

1.2 Charge transport in organic crystals

The problem of charge transport in solids has been a central topic in condensed matter physics since the early development of quantum theory. In the first half of the twentieth century, the emergence of band theory provided a successful framework for describing electronic motion in crystalline solids, particularly metals and inorganic semiconductors. Soon after, it became clear that interactions between charge carriers and the lattice play an essential role in many materials. Early theoretical work by Landau and Pekar introduced the concept of a charge carrier interacting with its surrounding medium, forming a composite object whose properties differ from those of a free electron. This idea was later developed in models describing the interaction between electrons and lattice vibrations, including the work of Fröhlich and, subsequently, Holstein, who formulated a model particularly suited for molecular crystals [15–19].

In inorganic semiconductors, the motion of charge carriers is often well described within the framework of band theory. When atoms are arranged in a periodic lattice and their electronic orbitals strongly overlap, the discrete energy levels of individual atoms broaden into continuous energy bands. In this picture, an electron is no longer associated with a single atom but is instead delocalized over the entire crystal, propagating as a Bloch wave through the periodic structure. This type of motion, commonly referred to as band transport, is characterized by relatively high mobility, with the carrier dynamics primarily limited by scattering from lattice vibrations or impurities. A typical signature of such transport is a decrease in mobility with increasing temperature, as enhanced lattice vibrations lead to more frequent scattering events [11, 20].

This physical picture relies on strong overlap between neighboring orbitals, which is a direct consequence of the rigid, closely packed atomic structure found in inorganic crystals. In contrast, organic molecular crystals are composed of relatively large molecules held together by weak intermolecular forces. As a result, the overlap between electronic orbitals on neighboring molecules is much smaller and highly sensitive to their relative positions. Furthermore, because the molecules are not rigidly fixed, they undergo significant thermal motion, continuously fluctuating around their equilibrium positions and orientations. These fluctuations dynamically modulate the already small orbital overlap, leading to narrow electronic bands or, in some cases, to states that are effectively localized on individual molecules [9, 11, 21, 22].

To describe these effects more precisely, it is useful to introduce the concept of phonons, which represent quantized modes of lattice vibrations. In organic materials, these include both internal molecular vibrations and intermolecular modes associated with the relative motion of entire molecules. Because of the weak binding and large molecular size, many of these modes occur at relatively low energies which can strongly influence electronic motion, as even small molecular displacements can significantly modify intermolecular orbital overlap [9, 11, 22, 23].

When a charge carrier moves through such a deformable and polarizable environment, it interacts with these lattice vibrations as well as with the surrounding molecular structure. Instead of moving independently of the lattice, the carrier modifies its local environment, and this modified environment in turn influences the carrier dynamics. In many cases, this mutual interaction leads to the formation of a polaron, a quasiparticle consisting of the charge carrier together with the lattice deformation it induces. Compared to a free carrier in a conventional band, a polaron behaves as an effectively heavier object, reflecting the fact that its motion is accompanied by the reorganization of the surrounding lattice [11, 15, 16, 18, 19, 24].

The nature of this coupling depends on its strength. In the case of relatively weak interaction, the carrier remains largely delocalized, and the lattice deformation extends over many sites, forming what is commonly referred to as a large polaron. In stronger coupling regimes, the deformation becomes more localized, and the carrier becomes effectively confined to a small region of the lattice, forming a small polaron. This distinction has important consequences for transport: while large polarons may still exhibit band-like motion, small polarons are typically associated with localized behavior [11, 17–19, 24].

A key consequence of strong coupling between the carrier and its environment is the possibility of self-trapping. In this case, the carrier induces a local lattice distortion that lowers its energy, effectively creating a potential well in which it resides. Unlike trapping by impurities or defects, which arises from external disorder, this localization is intrinsic, as it is generated by the carrier itself. Motion to a neighboring site requires the carrier to overcome this local binding, which typically occurs through interaction with lattice vibrations [11, 19, 24].

This mechanism leads to thermally activated hopping transport. Instead of moving continuously through the crystal, the carrier resides on a given molecular site and transitions to neighboring sites when it acquires sufficient energy from lattice vibrations to overcome the local binding potential. As temperature increases, these fluctuations become stronger and more frequent, facilitating such transitions. Consequently, the mobility in this regime typically increases with temperature, in contrast to band transport. This behavior is characteristic of processes governed by thermal activation over an energy barrier and is commonly described within polaron hopping and Marcus-type theories [11, 19, 22, 25].

Experimental studies of organic molecular crystals reveal signatures of both transport mechanisms. In highly ordered systems, such as high-quality single crystals, the mobility often decreases with increasing temperature, indicating that carriers retain a degree of coherent, band-like motion. In contrast, in less ordered systems or at higher temperatures, the mobility frequently increases with temperature, reflecting thermally activated hopping between localized states. These contrasting behaviors have been observed in a wide range of materials and experimental conditions and highlight the sensitivity of charge transport to structural order and thermal fluctuations. Together, these observations suggest that organic semiconductors often operate in an intermediate regime, where neither purely band-like nor purely hopping descriptions are fully adequate [2, 8, 9, 11, 26].

The origin of this complexity lies in the comparable magnitude of several key energy scales in these materials. The electronic coupling between neighboring molecules, the energies associated with lattice vibrations, and the strength of their interaction with charge carriers often fall within the same energy range ($10-100$ meV). As a result, even modest thermal motion, such as small displacements or reorientations of molecules, can significantly alter orbital overlap and, consequently, charge transport. In this sense, transport in organic semiconductors is inherently dynamic, continuously influenced by the fluctuating structure of the lattice [9, 11, 22, 23, 27].

Recent theoretical and experimental work has emphasized that charge carriers in such systems may occupy states that are neither fully localized nor completely delocalized. Instead, the carrier can transiently access more extended states while still interacting strongly with its environment, a picture often referred to as transient localization. This framework provides a useful way to understand transport behavior that lies between the traditional limits of band transport and hopping conduction [8, 9, 28].

To capture these effects theoretically, it is necessary to use models that explicitly include the interaction between electronic motion and lattice degrees of freedom. Among these, the Holstein model has become one of the most widely used frameworks for describing charge transport in molecular crystals. In this model, a charge carrier moves between discrete sites while interacting locally with vibrational modes associated with each site. Despite its simplicity, the model captures key features such as polaron formation, bandwidth renormalization, and the crossover between different transport regimes [11, 18, 19, 24].

Although simplified, Holstein-type models provide valuable insight into the fundamental mechanisms governing charge transport in organic semiconductors and serve as a foundation for many modern theoretical and numerical approaches. In the following chapter, a detailed theoretical description of polaron formation and transport based on this framework is presented, with particular emphasis on regimes relevant for organic molecular systems.

1.3 Theoretical and numerical approaches to electron-phonon coupled systems

The theoretical description of charge transport in systems where charge carriers interact strongly with their surrounding lattice remains a challenging problem that has been studied for many decades [18, 24]. The difficulty arises from the need to treat electronic and lattice degrees of freedom on equal footing, as their interplay can give rise to qualitatively different physical behavior depending on the interaction strength and the relevant energy scales [9, 11]. As a result, a wide range of theoretical and computational approaches have been developed, each applicable within a specific regime and based on different approximations [12, 29].

One of the earliest and most widely used approaches is based on band theory combined with a perturbative treatment of interactions [20]. Within this framework, electronic states remain largely delocalized, while lattice vibrations enter as a weak perturbation that gives rise to scattering processes [30]. Such approaches are highly successful in inorganic semiconductors, where the electronic bandwidths are large and the carrier-lattice coupling is relatively weak [20]. However, in organic molecular systems, where intermolecular electronic coupling is small and lattice fluctuations are significant, these methods often fail to capture essential features such as carrier localization and strong renormalization of transport properties [9, 11, 12].

An alternative class of approaches is provided by semiclassical transport theories, in which charge carriers are treated quantum mechanically, while lattice degrees of freedom are described classically [30]. Examples include Boltzmann transport equations and extensions that incorporate dynamic disorder [12, 27]. These methods offer useful insight into intermediate regimes, particularly when lattice fluctuations act as a time-dependent disorder potential [9, 27]. However, their applicability becomes limited when the quantum effects of lattice vibrations are important or when carrier–lattice coupling leads to the formation of composite quasiparticles [11, 29].

In the opposite limit of strong localization, transport is commonly described within the framework of hopping models [19, 24, 31]. In this picture, the system is viewed as a network of localized sites, and charge transport proceeds via transitions between them. The rates of these transitions depend on the coupling to lattice vibrations and the associated energy changes. A well-established example is the Marcus theory, which has been widely used to describe charge transfer in molecular systems [25]. Although such approaches successfully capture thermally activated transport and are particularly effective in disordered or high-temperature regimes, they inherently assume localized carriers and are therefore unable to describe coherent or partially delocalized motion [31].

To bridge the gap between these limiting descriptions, various polaron theories have been developed. Models such as the Holstein and Fröhlich Hamiltonians describe how charge carriers become coupled to lattice distortions, forming composite quasiparticles whose properties differ significantly from those of free carriers [17, 31, 32]. Depending on the coupling strength and the relative time scales of electronic and lattice motion, these models can describe both large and small polarons, as well as the crossover between coherent and incoherent transport regimes [24, 31]. However, analytical treatments are typically restricted to limiting cases, and approximate methods are required to address realistic parameter ranges [24].

The limitations of analytical approaches have motivated the development of a variety of numerical and semi-analytical methods for treating electron–phonon coupled systems. A large class of these methods relies on controlled or, in some cases, uncontrolled approximations, which makes them computationally efficient and applicable to complex or extended systems, but also limits their range of validity. This trade-off between efficiency and accuracy is well recognized in the study of electron–phonon models, where different approximate techniques often yield consistent results only within specific parameter regimes [33].

Among these approaches, diagrammatic and Green's-function-based methods such as the cumulant expansion and dynamical mean-field theory (DMFT) provide nonperturbative insight into spectral and

transport properties. In particular, DMFT becomes exact in the limit of infinite lattice coordination and allows one to capture the crossover from coherent band-like motion to incoherent hopping transport in polaronic systems. However, such approaches typically neglect nonlocal correlations and may fail in low-dimensional systems or in regimes with strong spatial fluctuations [34–38].

Another class of approximate methods is based on variational and diagrammatic resummation techniques. Variational approaches, including those based on systematically constructed Hilbert spaces or generalized Lang–Firsov transformations, can provide highly accurate results for ground-state and low-energy properties across a wide parameter range, but are often limited in their ability to describe dynamical quantities or finite-temperature behavior [39, 40]. Related diagrammatic approximations, such as the momentum-average method, sum large classes of self-energy diagrams in an efficient manner and yield accurate results for Green's functions and spectral properties over broad parameter regimes, while remaining computationally inexpensive [41–44].

Stochastic approaches, such as kinetic Monte Carlo, provide an effective framework for simulating charge transport in disordered systems by describing the carrier motion as a sequence of thermally activated transitions between localized states. Despite their widespread use in the modeling of organic semiconductors, these methods inherently assume localized carriers and classical hopping dynamics and, therefore, cannot capture effects of quantum coherence or partial delocalization in intermediate regimes [45].

To overcome the limitations of approximate approaches, a variety of numerically exact or systematically controllable methods have been developed for electron–phonon systems. These methods aim to solve the model Hamiltonian without introducing uncontrolled approximations, at the cost of significantly increased computational effort.

Among these, wavefunction-based techniques such as exact diagonalization (ED) and density matrix renormalization group (DMRG) provide numerically exact results for finite systems. ED allows direct access to both ground-state and dynamical properties, but is restricted to small system sizes due to the exponential growth of the Hilbert space [46]. DMRG, on the other hand, enables simulations of much larger one-dimensional systems by efficiently truncating the Hilbert space and has proven highly successful in describing polaron formation and crossover behavior across different coupling regimes [47]. Extensions such as time-dependent DMRG further allow the investigation of real-time dynamics and finite-temperature properties in complex systems [48–51]. Complementary approaches based on open quantum system techniques, such as hierarchical equations of motion (HEOM), provide an alternative route to numerically exact dynamics by systematically incorporating system–bath correlations [48, 52–56].

Another important class of numerically exact methods is based on quantum Monte Carlo (QMC) techniques. These methods provide unbiased results for thermodynamic and dynamical quantities by statistically sampling the configurations of the system. Early implementations based on discrete path-integral formulations demonstrated that electron–phonon problems can be treated accurately by integrating out phonon degrees of freedom and sampling electron trajectories [57, 58]. Subsequent developments, including continuous-time QMC algorithms, eliminated systematic errors associated with time discretization and enabled simulations across a wide range of parameters and dimensionalities [59, 60]. More advanced approaches, such as diagrammatic Monte Carlo, directly sample Feynman diagram expansions of Green's functions and can, in principle, yield exact results in the thermodynamic limit [61–63].

These methods are naturally formulated within the path integral framework of quantum mechanics, in which quantum statistical properties are expressed as sums over all possible trajectories of the system. Within this formalism, QMC techniques enable the stochastic evaluation of path integrals, allowing interacting quantum systems to be treated at finite temperature without relying on perturbative assumptions. In particular, path-integral QMC approaches are well suited for studying electron–lattice interaction models, as they incorporate both quantum fluctuations and thermal effects on equal footing and provide numerically exact results within statistical uncertainty [64–66].

Compared to many approximate methods, quantum Monte Carlo approaches offer the important

advantage of being numerically exact within statistical uncertainty. In particular, they do not rely on uncontrolled approximations regarding the interaction strength or the degree of carrier localization. This makes them especially valuable for systems such as organic semiconductors, where electronic coupling, lattice dynamics, and their mutual interaction occur on comparable energy scales and cannot be treated independently.

At the same time, these approaches are not without limitations. Their computational cost can be significant, and certain formulations, particularly those involving real-time evolution, may suffer from the dynamical sign problem, which severely restricts accessible timescales [67–70]. In addition, extracting transport properties often requires analytic continuation from imaginary-time data, an ill-posed problem that can introduce additional uncertainties [71–77]. Nevertheless, for a broad class of electron–phonon coupled systems, path-integral quantum Monte Carlo methods provide a powerful and reliable framework for investigating equilibrium properties and transport-related quantities.

In this thesis, a path integral quantum Monte Carlo approach is employed to study charge transport in systems described by electron–phonon interaction models. This framework enables a consistent treatment of quantum and thermal fluctuations and allows different transport regimes to be explored on equal footing, without restricting the analysis to a particular limiting case. In the following chapters, this approach is applied to investigate the behavior of charge carriers in model systems relevant to organic molecular semiconductors and to analyze the conditions under which different transport mechanisms emerge.

1.4 Motivation and thesis outline

The study of charge transport in organic semiconductors is motivated by both technological demands and fundamental scientific questions. On the applied side, these materials offer unique advantages such as mechanical flexibility, low-cost fabrication, and compatibility with large-area devices, making them promising candidates for next-generation electronic and optoelectronic technologies. However, their performance remains limited by relatively low charge carrier mobility compared to inorganic semiconductors. Improving transport properties therefore requires a deeper understanding of the microscopic mechanisms governing carrier motion in these systems.

From a fundamental perspective, organic molecular crystals represent a class of materials in which several key energy scales, including electronic coupling, lattice dynamics, and their mutual interaction, are of comparable magnitude. This leads to a rich variety of transport regimes that cannot be fully captured by traditional theories developed for inorganic semiconductors. Instead, charge carriers in these materials exhibit behavior ranging from coherent band-like motion to thermally activated hopping, with intermediate regimes that remain an active area of research. Understanding how these regimes emerge and how they depend on microscopic parameters is one of the central challenges in the field.

To address these questions, it is useful to adopt simplified theoretical models that capture the essential physical mechanisms while remaining tractable for detailed analysis. The Holstein model provides such a framework, describing a charge carrier locally coupled to vibrational degrees of freedom. This model is particularly well suited for organic molecular systems, where charge transport occurs via the overlap of molecular orbitals and where the interaction between the carrier and local molecular distortions plays a dominant role. Furthermore, the pronounced anisotropy of many organic crystals, arising from their molecular packing, often leads to transport that is effectively confined to one preferred direction. This motivates the use of a one-dimensional formulation of the model as a minimal yet physically meaningful representation of such systems.

A central difficulty in studying electron–phonon coupled systems lies in the fact that different theoretical approaches are typically valid only in limiting cases. Weak-coupling theories describe nearly free carriers, while strong-coupling approaches capture localized behavior. However, the intermediate regime, in which electronic coupling, lattice fluctuations, and their interaction are of

comparable magnitude, is particularly challenging because it cannot be reliably described by simple approximations. This regime is especially relevant for organic semiconductors, where these energy scales naturally coincide.

Charge transport in such systems can be investigated using a path integral quantum Monte Carlo (QMC) approach. This method enables a non-perturbative treatment of electron–phonon coupled systems and provides a consistent description across a wide range of coupling strengths and temperatures. In contrast to approaches that are restricted to specific regimes, the path integral formulation allows direct access to the intermediate regime, where many standard approximations break down. Within this framework, quantum and thermal fluctuations are treated on equal footing, enabling a detailed analysis of transport behavior and the emergence of different transport regimes. The numerical exactness of the method, within statistical uncertainty, makes it particularly well suited for studying the interplay between charge carriers and lattice dynamics in organic semiconductors.

The results presented in this thesis are divided into two parts. In the first part, a path integral quantum Monte Carlo approach is developed for evaluating charge transport properties of the Holstein polaron. Within this framework, a methodology for calculating carrier mobility is established and validated by reproducing known results obtained using independent theoretical methods. This provides a reliable foundation for studying transport across a wide range of interaction strengths and temperatures.

In the second part, this methodology is applied to a systematic investigation of the Holstein polaron model. By analyzing the dependence of the transport properties on the temperature, interaction strength, and phonon energy, distinct regimes of carrier motion are identified and the crossover between coherent and incoherent transport is examined. The results provide a unified picture of the transport behavior across a wide range of parameters, including the intermediate regime, where different mechanisms compete.

The structure of the thesis is as follows.

Chapter 2 provides the theoretical foundation for the study of charge transport in electron–phonon coupled systems and establishes the formal framework underlying the path-integral quantum Monte Carlo methodology. It introduces the Holstein model and the linear response formalism used to describe transport properties, with particular emphasis on the current–current correlation function as the central quantity governing transport. The polaron picture is then presented, together with an overview of the main transport mechanisms, including hopping, band, and polaron band transport. In addition, the path-integral formulation of quantum statistical mechanics is introduced, along with key mathematical tools required for its treatment. The chapter concludes with an overview of quantum Monte Carlo methods, including the path-integral approach employed in this work, the associated dynamical sign problem, and the analytic continuation procedure used to extract real-time transport quantities from imaginary-time data.

Chapter 3 presents the development of the computational methodology used to evaluate transport properties of the Holstein polaron within the path-integral quantum Monte Carlo framework. The path-integral representation of time-correlation functions is derived, where the quantum statistical problem is formulated in terms of discretized imaginary- and real-time evolution operators using the Trotter–Suzuki decomposition. Two complementary formulations are considered, based on the electron momentum and position representations. The analytic continuation procedure used to extract dc mobility from real- and imaginary-time correlation functions is then described and illustrated. The chapter concludes with the presentation of numerical results, including current–current correlation functions, analysis of statistical uncertainties, and the temperature dependence of the Holstein polaron mobility, demonstrating good agreement with independent theoretical approaches.

Chapter 4 presents the main results of this thesis, focusing on the identification of transport regimes in the one-dimensional Holstein model. Effective approximate theoretical descriptions corresponding to the three relevant transport mechanisms, namely hopping, band, and polaron band transport, are introduced and analyzed. The corresponding expressions for current–current correlation functions and dc mobility are presented and compared, providing insight into the crossover between different trans-

port regimes. Criteria for identifying transport regimes are then established based on the agreement between numerically exact quantum Monte Carlo results and the approximate theoretical descriptions. These criteria are applied through a systematic comparison of imaginary-time correlation functions and dc mobility, allowing for the identification of the regions of parameter space where each transport mechanism is applicable. The chapter concludes with the construction of the transport regime diagram for the one-dimensional Holstein model.

Chapter 5 provides a discussion of the results presented in Chapters 3 and 4, focusing on their physical interpretation and their relation to existing theoretical and experimental studies. The implications for charge transport in organic semiconductors are considered in the context of relevant literature.

Chapter 6 summarizes the main findings of the thesis and outlines their significance. The broader implications of the results are discussed, and possible directions for future research are briefly indicated.

Chapter 2

Theoretical background

The theoretical description of charge transport in organic molecular systems requires a framework capable of capturing the interplay between electronic motion and lattice dynamics. As discussed in the Introduction, this interplay gives rise to a rich variety of transport regimes, ranging from band-like motion to thermally activated hopping, as well as intermediate regimes where neither description is fully adequate.

A central challenge in developing such a framework lies in the comparable magnitude of the relevant energy scales. In organic semiconductors, the electronic coupling between neighboring molecules, the characteristic energies of lattice vibrations, and the strength of electron–phonon interaction are often of the same order. As a result, the motion of charge carriers cannot be treated independently of the lattice, and standard perturbative approaches become insufficient.

To address these challenges, it is necessary to adopt microscopic models that explicitly incorporate the coupling between electronic and vibrational degrees of freedom. Among these, the Holstein model has emerged as one of the most widely used minimal models for describing charge transport in molecular crystals. Despite its relative simplicity, it captures the essential physics of local electron–phonon interaction and provides a unified framework for studying different transport regimes.

In addition to selecting an appropriate model, it is equally important to employ theoretical and numerical methods capable of treating electron–phonon coupled systems across a broad range of parameters. In particular, approaches that do not rely on assumptions about the nature of transport, such as whether it is band-like or hopping, are especially valuable in regimes where multiple mechanisms compete. In this work, we adopt a path-integral quantum Monte Carlo approach, which enables a numerically exact treatment of the coupled electron–lattice system within statistical uncertainty.

In this chapter, we establish the theoretical framework used throughout this work. We begin by introducing the Holstein polaron model, which serves as a minimal microscopic description of charge carriers interacting with lattice vibrations in molecular systems. We then present the formalism of linear response theory and the Kubo formula, which provide the connection between microscopic dynamics and experimentally measurable transport coefficients such as electrical conductivity and mobility.

Building on this foundation, we discuss the principal transport mechanisms relevant for electron–phonon coupled systems, including band transport, thermally activated hopping, and polaron band transport, and outline the conditions under which each regime is expected to occur. We then introduce the path-integral formulation of quantum mechanics, which offers a natural framework for treating systems with coupled electronic and lattice degrees of freedom. Finally, we present the quantum Monte Carlo methodology employed in this work, with particular emphasis on path-integral Monte Carlo techniques used to evaluate current–current correlation functions. Special attention is given to key methodological aspects, including the dynamical sign problem that limits real-time simulations and the analytic continuation procedure required to extract real-frequency transport quantities from imaginary-time data. Together, these elements form the computational framework that enables a numerically exact evaluation of transport properties across a wide range of parameters.

2.1 Holstein polaron model

Charge transport in molecular and organic semiconductors is strongly influenced by the interaction between charge carriers and lattice vibrations. Due to the pronounced anisotropy and partial localization of electronic wave functions in such materials, charge motion is often adequately described within a tight-binding framework with local electron-phonon coupling. A minimal microscopic model capturing these effects is provided by the Holstein molecular crystal model, originally introduced by T. Holstein in the late 1950s.

The Holstein Hamiltonian is written as

$$H = H_{\mathrm{e}} + H_{\mathrm{ph}} + H_{\mathrm{e-ph}} \,, \tag{2.1}$$

where H_{e} describes the electronic kinetic energy, H_{ph} the lattice degrees of freedom and $H_{\mathrm{e-ph}}$ accounts for the electron-phonon coupling [24, 32].

Within the nearest-neighbor tight-binding approximation, the electronic part for a one-dimensional lattice reads

$$H_{\mathrm{e}} = -J \sum_{n} \sum_{\gamma=\pm 1} c_{n+\gamma}^{\dagger} c_n \,, \tag{2.2}$$

where $c_n^{\dagger}$ and c_n are fermionic creation and annihilation operators at the lattice site n, and J is the electron transfer integral. The corresponding bare electronic bandwidth is $W = 4J$. In the absence of electron-phonon interaction, the eigenstates are Bloch waves with dispersion $\varepsilon(k) = -2J\cos k$, describing coherent band-like transport [24, 78].

The lattice is modeled as a set of independent, dispersionless optical phonons of frequency ω_0, reflecting the local character of intramolecular vibrational modes. In coordinate representation, the phonon Hamiltonian is

$$H_{\mathrm{ph}} = \sum_{n} \left[\frac{p_n^2}{2M} + \frac{1}{2} M \omega_0^2 x_n^2 \right] \,, \tag{2.3}$$

where x_n and p_n denote the displacement and conjugate momentum operators of an oscillator of mass M at the site n. Equivalently, the phonon Hamiltonian in second-quantization reads

$$H_{\mathrm{ph}} = \hbar\omega_0 \sum_{n} b_n^{\dagger} b_n \,, \tag{2.4}$$

where $b_n^{\dagger}$ and b_n are phonon creation and annihilation operators at site n. The zero point energy $\hbar\omega_0/2$ has been omitted as an irrelevant constant energy shift. The two representations are related through operator relations

$$x_n = \sqrt{\frac{\hbar}{2M\omega_0}} (b_n^{\dagger} + b_n) \,, \quad p_n = \mathrm{i}\sqrt{\frac{\hbar M\omega_0}{2}} (b_n^{\dagger} - b_n) \,, \tag{2.5}$$

which satisfy the canonical commutation relations $[x_n, p_m] = \mathrm{i}\hbar\delta_{nm}$ [24, 78].

The electron-phonon interaction in the Holstein model is purely local, coupling the electronic density at a given site to the lattice displacement at the same site. In second-quantization, the interaction Hamiltonian is

$$H_{\mathrm{e-ph}} = G \sum_{n} c_n^{\dagger} c_n (b_n^{\dagger} + b_n) \,, \tag{2.6}$$

where G is the electron-phonon coupling constant with dimensions of energy. Using the coordinate representation for phonon operators, the interaction term can be written as

$$H_{\mathrm{e-ph}} = \alpha \sum_{n} c_n^{\dagger} c_n x_n \,, \tag{2.7}$$

with $\alpha = G\sqrt{2M\omega_0/\hbar}$. This representation is especially useful in the path-integral formalism, where phonon degrees of freedom naturally appear as lattice displacement fields and can be integrated out [24, 57, 78].

The properties of the model are governed by the competition between electronic movement and lattice response. Two dimensionless parameters are commonly used to characterize the system. The first is the adiabaticity ratio $J/(\hbar\omega_0)$, which compares the electronic hopping scale to the phonon energy. It distinguishes between the adiabatic regime, $J \gg \hbar\omega_0$, where lattice dynamics is slow compared to electronic motion, and the non-adiabatic regime, $J \ll \hbar\omega_0$, where quantum lattice fluctuations dominate. The second parameter is the dimensionless electron–phonon coupling strength $\lambda = 2G^2/(\hbar\omega_0 W)$, which measures the ratio of polaron binding energy $E_p = G^2/(\hbar\omega_0)$ to half electronic bandwidth $W/2$. In the weak coupling regime, $\lambda \ll 1$, the carrier remains relatively delocalized and forms a large polaron with moderate mass renormalization and predominantly band-like transport. In the strong coupling regime, $\lambda \gtrsim 1$, the electron becomes self-trapped by the lattice distortion it induces, forming a small polaron. In this regime, the effective bandwidth is exponentially reduced and charge transport is typically governed by thermally activated hopping [24, 31].

Over the past decades, the Holstein polaron model has been studied using a wide variety of theoretical and numerical methods, each suited to different parameter regimes. Approaches range from perturbative treatments in the weak-coupling limit to variational and canonical transformation techniques for intermediate coupling, and to nonperturbative methods such as exact diagonalization, density-matrix renormalization group, diagrammatic Monte Carlo, and path-integral Monte Carlo. The diversity of these methods reflects both the fundamental importance of the Holstein model and the intrinsic complexity of strongly coupled electron–phonon systems, especially in regimes where neither weak nor strong coupling approximations are quantitatively reliable.

The Holstein model thus provides a unified microscopic framework that continuously connects coherent band transport and incoherent hopping, making it particularly suitable for quantitative investigations of polaron dynamics over a broad range of temperatures, coupling strengths, and phonon frequencies. Although the model can be extended straightforwardly to higher spatial dimensions, in the present work, we restrict our analysis to the one-dimensional case. Even in one dimension, the Holstein Hamiltonian remains highly nontrivial and does not admit a general exact analytical solution.

2.2 Linear response theory and Kubo formula

Although theoretical descriptions of transport in terms of charge carriers, phonons, and their mutual interactions may appear abstract, the ultimate objective is to establish a direct connection between microscopic dynamics and experimentally measurable observables. In the context of charge transport, the relevant observable is the electrical current. More precisely, the material property of interest is the electrical conductivity, which characterizes the response of a system to an applied electric field and can be measured directly in experiments.

When a material is subjected to an external perturbation, such as an electric or magnetic field, pressure, or a temperature gradient, it exhibits a measurable response. In the regime of weak perturbations, the response is linear in the applied field. This statement constitutes the foundation of linear response theory. The proportionality factor relating the induced response to the perturbation defines a transport coefficient that encodes intrinsic properties of the material.

In the presence of an external electric field, the induced quantity is the electrical current density $J(\mathbf{r}, t)$. Within linear response theory, the current is related to the total electric field $E(\mathbf{r}, t)$ as

$$J_i(\mathbf{r}, t) = \int \mathrm{d}\mathbf{r}' \int_{-\infty}^{t} \mathrm{d}t' \sigma_{ij}(\mathbf{r}, \mathbf{r}'; t - t') E_j(\mathbf{r}', t') \ . \tag{2.8}$$

Here, $i, j = x, y, z$ denote spatial components and summation over repeated indices is implied. The conductivity tensor σ_{ij} depends on the time difference $t - t'$ due to time-translation invariance of the equilibrium system, while the restriction $t' \leq t$ reflects causality. The response is necessarily retarded with respect to the perturbation.

For a homogeneous system, the conductivity depends only on coordinate differences, $\sigma_{ij}(\mathbf{r}, \mathbf{r}'; t - t') \equiv \sigma_{ij}(\mathbf{r} - \mathbf{r}'; t - t')$. In crystalline solids, translational invariance allows one to perform a Fourier transformation to momentum-frequency space, yielding

$$J_i(\mathbf{q}, \omega) = \sigma_{ij}(\mathbf{q}, \omega) E_j(\mathbf{q}, \omega) \ . \tag{2.9}$$

A perturbation at frequency ω generates a response at that same frequency. In the linear regime, the different frequency components act independently and do not mix [78, 79].

2.2.1 Kubo formula for electric conductivity

The microscopic formulation of conductivity was originally introduced by Kubo in 1957 [78, 80]. The central result, commonly known as the Kubo formula, expresses the conductivity in terms of the autocorrelation functions of the current operator.

To establish a microscopic expression for conductivity, consider a system described by the Hamiltonian $H(t) = H_0 + H'(t)$, where H_0 is the unperturbed interacting part of the Hamiltonian and the term $H'(t)$ represents an external perturbation. In the nonrelativistic limit, the interaction of a system with an external electromagnetic field is given by $H'(t) = -\int \mathrm{d}\mathbf{r}\ j(\mathbf{r}) \cdot A(\mathbf{r}, t)$, where $A(\mathbf{r}, t)$ is the vector potential and $j(\mathbf{r})$ is the current density operator. The total induced current is obtained as the average velocity of charged particles in the system. The velocity operator of a particle with charge q and mass m in the presence of a vector potential is given by [78]

$$v_i = \frac{1}{m} \left(p_i - q A(r_i, t) \right) \ . \tag{2.10}$$

The total current density is proportional to the average charge velocity. For a system with n carriers of charge q, the induced current density can be written as

$$J_i(\mathbf{r}, t) = nq \langle v_i(\mathbf{r}, t) \rangle \ . \tag{2.11}$$

Substituting the velocity operator and using $q = -\mathrm{e}$ for the electron yields

$$J_i(\mathbf{r}, t) = -\frac{n\mathrm{e}}{m} \langle p_i(\mathbf{r}, t) \rangle - \frac{n\mathrm{e}^2}{m} A_i(\mathbf{r}, t) \ . \tag{2.12}$$

It is convenient to introduce the paramagnetic current density operator

$$j_i(\mathbf{r}, t) = -\frac{\mathrm{e}}{m} p_i(\mathbf{r}, t) \ , \tag{2.13}$$

which allows the induced current to be written in the form

$$J_i(\mathbf{r}, t) = \langle j_i(\mathbf{r}, t) \rangle - \frac{n\mathrm{e}^2}{m} A_i(\mathbf{r}, t) \ . \tag{2.14}$$

The first term represents the paramagnetic current, while the second term describes the diamagnetic contribution proportional to the vector potential.

Within the first-order time-dependent perturbation theory, the average value of the current density operator depends only on the perturbation Hamiltonian H'

$$\langle j_i(\mathbf{r}, t) \rangle \simeq -\frac{\mathrm{i}}{\hbar} \int_{-\infty}^{t} \mathrm{d}t' \ \langle [j_i(\mathbf{r}, t), H'(t')] \rangle \ . \tag{2.15}$$

where the expectation value is taken in thermal equilibrium with respect to the non-perturbed Hamiltonian. Substituting the perturbation Hamiltonian $H'(t') = -\int \mathrm{d}\mathbf{r}'\ j_k(\mathbf{r}', t')A_k(\mathbf{r}', t')$, one obtains

$$\langle j_i(\mathbf{r}, t)\rangle = \frac{\mathrm{i}}{\hbar}\int_{-\infty}^{t} \mathrm{d}t' \int \mathrm{d}\mathbf{r}'\langle[j_i(\mathbf{r}, t), j_k(\mathbf{r}', t')]\rangle A_k(\mathbf{r}', t') \ . \tag{2.16}$$

To express the response in terms of electric field, it is convenient to transform to momentum-frequency space. In general, the electric field is related to the vector and scalar potential as

$$E(\mathbf{r}, t) = -\frac{\partial A(\mathbf{r}, t)}{\partial t} - \nabla\phi(\mathbf{r}, t) \ . \tag{2.17}$$

Choosing the gauge $\phi = 0$ and Fourier transforming to momentum-frequency representation gives

$$E(\mathbf{q}, \omega) = \mathrm{i}\omega A(\mathbf{q}, \omega) \ , \tag{2.18}$$

and equivalently

$$A(\mathbf{q}, \omega) = \frac{E(\mathbf{q}, \omega)}{\mathrm{i}\omega} \ . \tag{2.19}$$

Using this relation and expressing the average of the current density operator in momentum-frequency space, one obtains

$$\langle j_i(\mathbf{q}, \omega)\rangle = \frac{1}{\hbar\omega V}\int_{-\infty}^{t} \mathrm{d}t' \mathrm{e}^{\mathrm{i}\omega(t-t')}\Big\langle\ [j_i(-\mathbf{q}, t), j_k(\mathbf{q}, t')]\ \Big\rangle E_k(\mathbf{q}, \omega) \tag{2.20}$$

The proportionality coefficient between the induced current and the applied electric field defines the conductivity tensor. Including both the paramagnetic contribution and the diamagnetic term from Eq.(2.14), one obtains the Kubo formula for the conductivity[78–80]

$$\sigma_{ik}(\mathbf{q}, \omega) = \frac{1}{\hbar\omega V}\int_{0}^{\infty} \mathrm{d}t\ \mathrm{e}^{\mathrm{i}\omega t}\left\langle\left[j_i^\dagger(\mathbf{q}, t), j_k(\mathbf{q}, 0)\right]\right\rangle + \mathrm{i}\frac{n\mathrm{e}^2}{m\omega}\delta_{ik} \ , \tag{2.21}$$

where the Hermiticity of the current operator implies $j(-\mathbf{q}, t) = j^\dagger(\mathbf{q}, t)$. The integrand in the first term of the Kubo formula can be identified with the retarded autocorrelation function of the current operator j_i which is defined as [78, 79]

$$C_{ik}^{\mathrm{R}}(\mathbf{q}, t - t') = -\frac{\mathrm{i}}{\hbar V}\theta(t - t')\langle[j_i^\dagger(t), j_k(t')]\rangle \ , \tag{2.22}$$

where V denotes the total volume of the system and $\theta(t)$ is the Heaviside step function indicating the time order of events $t > t'$. After Fourier transformation to frequency space, some cyclic permutations and time variable substitution $(t - t') \to t$, one obtains the retarded correlator in frequency representation

$$C_{ik}^{R}(\mathbf{q}, \omega) = \frac{-\mathrm{i}}{\hbar V}\int_{0}^{\infty} \mathrm{d}t\ \left\langle\left[j_i^\dagger(\mathbf{q}, t), j_k(\mathbf{q}, 0)\right]\right\rangle \ . \tag{2.23}$$

Consequently, the Kubo formula is expressed in terms of the retarded current-current correlation function

$$\sigma_{ik}(\mathbf{q}, \omega) = \frac{\mathrm{i}}{\omega}\left[C_{ik}^{R}(\mathbf{q}, \omega) - \frac{n\mathrm{e}^2}{m}\delta_{ik}\right] \ . \tag{2.24}$$

The principal quantity of interest in transport theory is the dc conductivity, obtained in the long-wavelength and zero-frequency limit,

$$\lim_{\omega\to 0}\lim_{\mathbf{q}\to 0}\sigma_{ik}(\mathbf{q},\omega)\ . \tag{2.25}$$

The order of limits is important as reversing them corresponds to a static electric field and yields no net current. The dc conductivity is a real quantity and after taking the limit $\mathbf{q}\to 0$ it reads as

$$\sigma_{ik}|_{\omega\to 0}\propto -\lim_{\omega\to 0}\frac{1}{\omega}\mathrm{Im}C^{\mathrm{R}}_{ik}(\omega)\ . \tag{2.26}$$

To make the structure of the correlation function explicit, one introduces its spectral representation. The imaginary part of the retarded correlation function is related to the spectral function according to $\mathrm{Im}C_{ik}(\omega)=-\frac{1}{2}R(\omega)$, where $R_{ik}(\omega)$ is the spectral function defined as [78]

$$R_{ik}(\omega)=2\pi\left(1-\mathrm{e}^{-\beta\hbar\omega}\right)\frac{1}{Z}\sum_{n,m}\mathrm{e}^{-\beta E_n}\langle n|j_i^\dagger|m\rangle\langle m|j_k|n\rangle\delta(\hbar\omega+E_n-E_m)\ . \tag{2.27}$$

Here, $\{|n\rangle\}$ denotes the eigenstates of the full Hamiltonian with the corresponding energies E_n and $Z=\sum_n\exp(-\beta E_n)$ is the partition function.

Substituting the spectral representation into the conductivity expression Eq. (2.21) and taking the limit $\omega\to 0$ yields the Kubo formula for dc conductivity [78]

$$\sigma_{ik}|_{\omega=0}=\frac{\pi\beta\hbar}{V}\frac{1}{Z}\sum_{n,m}\mathrm{e}^{-\beta E_n}\langle n|j_i^\dagger|m\rangle\langle m|j_k|n\rangle\delta(E_n-E_m)\ . \tag{2.28}$$

This expression shows that the dc conductivity is determined by transitions between states that are very close in energy.

In macroscopic systems with finite carrier density n, electrical transport is characterized by conductivity $\sigma=ne\mu$, where μ denotes mobility. In the small carrier concentration limit, relevant in polaron physics, conductivity vanishes proportionally to $n\to 0$, while mobility remains a well-defined intrinsic transport coefficient.

An alternative representation of the transport coefficient can be obtained by invoking the fluctuation-dissipation theorem, which relates the spectral representation above to equilibrium time-correlation functions. Using the symmetry properties of equilibrium correlation functions, the dc conductivity can be expressed as a time integral of the current-current correlation function

$$\sigma_{ik}=\frac{\beta}{V}\int_0^\infty \mathrm{d}t\langle j_i(t)j_k(0)\rangle\ , \tag{2.29}$$

where $j_i(t)\equiv j_i(\mathbf{q}=0,t)$. Dividing this expression by the carrier density yields the Green-Kubo relation for mobility [80, 81]

$$\mu_{ik}=\frac{\beta}{neV}\int_0^\infty \mathrm{d}t\langle j_i(t)j_k(0)\rangle\ . \tag{2.30}$$

Thus, mobility is determined by the time integral of the equilibrium current-current correlation function.

The equivalence of this form with the previously obtained Kubo expression Eq.(2.28) can be demonstrated by explicitly evaluating the correlation function in the eigenbasis of the Hamiltonian. In general, the conductivity is a tensor quantity, as indicated in Eq. (2.28), reflecting the possibility of anisotropic transport in different spatial directions. However, for the one-dimensional systems considered in this work, charge transport is confined to a single spatial direction. In this case, it

is sufficient to consider the longitudinal response, corresponding to the diagonal components of the conductivity tensor. Accordingly, in the following, the analysis is restricted to a single transport direction, with $i = k$ implicitly assumed, and explicit spatial indices omitted for notational simplicity.

Consider the current-current correlation function $C(t) = \langle j(t)j(0)\rangle$. Using the Heisenberg representation for time operators and inserting a complete set of Hamiltonian eigenstates, the correlation function can be written in the spectral form as

$$C(t) = Z^{-1} \sum_{n,m} \mathrm{e}^{-\beta E_n} \mathrm{e}^{\frac{\mathrm{i}}{\hbar}(E_n - E_m)t} |\langle n|j|m\rangle|^2 \,, \tag{2.31}$$

where $Z = \sum_n \mathrm{e}^{-\beta E_n}$ is the partition function and E_n are the eigenvalues of the Hamiltonian. Integrating this expression over time yields

$$\int_{-\infty}^{\infty} \mathrm{d}t \; C(t) = 2\pi\hbar Z^{-1} \sum_{n,m} \mathrm{e}^{-\beta E_n} |\langle n|j|m\rangle|^2 \delta(E_n - E_m) \,. \tag{2.32}$$

This result closely resembles the Kubo expression for dc conductivity Eq.(2.28), but to retrieve that exact expression one should consider the symmetry properties of correlation functions. For Hermitian operators such as the current operator,

$$C(-t) = C(t)^* \,. \tag{2.33}$$

Since the dc transport coefficient depends only on the real part of the correlation function, one effectively has $C(-t) = C(t)$. Consequently, the time integral over positive times can be written symmetrically as

$$\int_0^{\infty} \mathrm{d}t \; C(t) = \frac{1}{2} \int_{-\infty}^{\infty} \mathrm{d}t \; C(t) \,. \tag{2.34}$$

Substituting this into the Green-Kubo formula gives

$$\mu_{\mathrm{dc}} = \frac{\beta}{2n\mathrm{e}V} \int_{-\infty}^{\infty} \mathrm{d}t \langle j(t)j(0)\rangle = \frac{\hbar\beta\pi}{n\mathrm{e}V} Z^{-1} \sum_{n,m} \mathrm{e}^{-\beta E_n} |\langle n|j|m\rangle|^2 \delta(E_n - E_m) \,, \tag{2.35}$$

which is equivalent to the Kubo expression in Eq.(2.28), up to the factor $n\mathrm{e}$, with the understanding that only diagonal (longitudinal) components of the current operator are considered.

The Kubo formalism thus establishes a rigorous connection between equilibrium quantum fluctuations at the microscopic level and experimentally measurable transport coefficients. The mobility can be determined entirely from equilibrium current-current correlation functions, without requiring explicit knowledge of the system's eigenstates.

The Green–Kubo relation demonstrates that electrical transport is fundamentally governed by the temporal correlations of microscopic currents in thermal equilibrium. In practice, the evaluation of the current-current correlation function depends on the microscopic model describing the charge carriers and their interaction with the lattice. In systems with significant electron–phonon interaction, the appropriate quasiparticle description is that of a polaron. The dynamical properties of this quasiparticle determine the time evolution of the current operator and therefore the resulting transport coefficients.

The microscopic transport properties of a system are encoded in the time dependence of the current-current correlation function appearing in the Kubo formula. Different physical mechanisms of carrier motion produce distinct temporal behaviors of this correlation function and consequently lead to different transport regimes. In the following sections, the principal theoretical descriptions of polaron transport are introduced. Although the underlying microscopic description is provided

by the Holstein model introduced earlier, the resulting transport behavior depends sensitively on the electron-phonon coupling strength and the adiabaticity ratio. These parameters determine whether charge transport occurs predominantly through band motion, thermally activated hopping, or within a regime characterized by a renormalized polaron band. Understanding the conditions under which each of these regimes emerges is central to the theoretical description of charge transport in electron-phonon coupled systems.

2.2.2 Current-current correlation function

Since this study is based on the Holstein Hamiltonian presented in the preceding section, the explicit form of the current operator within this model should be defined.

For a tight-binding system, the current operator can be derived directly from the Heisenberg equation of motion applied to the polarization operator [78]

$$P = \mathrm{e} \sum_n (an) c_n^\dagger c_n \ , \tag{2.36}$$

where an denotes the lattice site position. The current operator is defined as the time derivative of polarization,

$$j = \frac{\partial P}{\partial t} = \frac{\mathrm{i}}{\hbar} [H, P] \ , \tag{2.37}$$

where the commutator is evaluated using the full interacting Hamiltonian.

For the one-dimensional Holstein model introduced in the previous section, this procedure yields

$$j = \mathrm{i}J \frac{\mathrm{e}a}{\hbar} \sum_n (c_{n+1}^\dagger c_n - c_n^\dagger c_{n+1}) \ . \tag{2.38}$$

Therefore, the current operator is a Hermitian operator. The electron-phonon interaction term does not contribute explicitly to the current operator, as it is local in space. However, it strongly affects the dynamics of $j(t)$ through the full interacting Hamiltonian.

The current-current correlation function is defined as the expectation value of the product of two current operators. It is a two-particle correlation function, since each current operator is itself composed of one creation operator and one annihilation operator. Thus, the current-current correlation function characterizes two correlated microscopic processes, each involving the annihilation of a particle in one state and its creation in another. Because the particle is the charge carrier, these microscopic processes together underlie the electrical conductivity.

There are multiple ways to define time-correlation functions. Among them, the retarded correlation function, which appears in the Kubo formula expression Eq.(2.21), is the most physically intuitive, as it explicitly reflects the causality of physical processes. For numerous analytical applications, it is also convenient to define the advanced correlation function,

$$C^{\mathrm{A}}(t) = \frac{\mathrm{i}}{\hbar} \theta(-t) \langle [j(t), j(0)] \rangle \ , \tag{2.39}$$

where the time argument and the imaginary unit appear with signs opposite to those in the retarded function. Another important formulation is the time-ordered correlation function appearing in the Green–Kubo relation for mobility, Eq.(2.30), given by $C(t) = \langle j(t) j(0) \rangle$, where $t \geq 0$. The standard definitions of correlation functions are related to each other through their spectral representations. These spectral representations also exhibit a number of useful analytic properties, which are discussed in detail in [79].

The central quantity examined in this thesis is the time-ordered current-current correlation function, defined as the thermal average

$$C(t) = \langle j(t) j(0) \rangle = Z^{-1} \mathrm{Tr} \left[\mathrm{e}^{-\beta H} \mathrm{e}^{\frac{\mathrm{i}}{\hbar} tH} j \mathrm{e}^{-\frac{\mathrm{i}}{\hbar} tH} j \right] \ , \tag{2.40}$$

where $Z = \mathrm{Tr}\left[\mathrm{e}^{-\beta H}\right]$ is the canonical partition function and the time dependence of the operators is given in the Heisenberg representation. This formulation is particularly well suited to path-integral and Monte Carlo methods [78, 79].

For numerical approaches based on imaginary-time path integrals, it is convenient to introduce the imaginary-time current–current correlation function obtained by substitution $t \longrightarrow -\mathrm{i}\tau$, where both t and τ are real. The imaginary time correlation function reads [79, 82]

$$C(\tau) = \langle j(\tau) j(0) \rangle \ , \quad 0 \leq \tau \leq \hbar\beta \ , \tag{2.41}$$

where τ takes values in the interval $[0, \hbar\beta]$ and the imaginary-time correlation function is periodic in imaginary time with period $\hbar\beta$. The τ-dependence is defined through the Heisenberg relations

$$j(\tau) = \exp\left(-\frac{\tau}{\hbar} H\right) j \exp\left(\frac{\tau}{\hbar} H\right) \ . \tag{2.42}$$

The quantity $C_{jj}(\tau)$ can typically be determined straightforwardly in path-integral quantum Monte Carlo simulations. The dc mobility is obtained from a zero-frequency limit of the real-frequency mobility, which requires analytic continuation of $C(\tau)$ from imaginary time to real frequencies [75]. The ill-posed nature of this inversion procedure constitutes a central numerical challenge in studying quantum system dynamics.

2.3 Transport theories for polarons

The electron-phonon (e-ph) interaction constitutes one of the fundamental interactions in condensed matter physics. The coupling between the charge carriers and lattice vibrations plays a decisive role in determining the dynamical and transport properties of solids and strongly influences their electrical, thermal, and optical response. When this interaction becomes significant, the motion of a carrier can no longer be described independently of the lattice degrees of freedom. Instead, the appropriate quasiparticle description is that of a polaron rather than a bare carrier [24, 78].

The term polaron was introduced by Pekar in the 1940s [16], although the underlying idea of a charge carrier interacting with a polarizable medium had already been formulated earlier by Landau [15]. Subsequent microscopic theories were developed by Fröhlich for large (continuum) polarons [17] and by Holstein for small (lattice) polarons [18, 19] in the 1950s. These pioneering works established the theoretical framework within which electron-phonon coupled systems are understood today[24].

A polaron represents a composite quasiparticle consisting of a charge carrier together with the lattice deformation it induces through the e-ph interaction. The presence of the carrier locally polarizes the surrounding medium, modifying the equilibrium positions of the ions. Rather than treating the carrier as moving through a dynamically fluctuating lattice, it is therefore more appropriate to regard the carrier and its accompanying lattice distortion as a single entity. The carrier thus propagates together with a phonon cloud, whose spatial extent and dynamical properties determine the nature of the polaron [24, 31, 83].

The primary distinction between different types of polarons is based on the spatial extent of the lattice deformation associated with the charge carrier. In the case of a large polaron, the deformation extends over many lattice sites and the carrier remains relatively delocalized. Such behavior typically arises in the regime of weak e-ph coupling ($\lambda < 1$) or when the interaction is long-ranged. By contrast, a small polaron is characterized by a highly localized lattice distortion confined to one or a few lattice sites. In this case, strong e-ph coupling ($\lambda \gtrsim 1$) leads to partial or complete self-trapping of the carrier. The resulting spatial confinement substantially increases the effective mass of the polaron quasiparticle and strongly modifies its transport properties [24, 31].

The transport properties in these two limits differ qualitatively. Large polarons generally move coherently through the crystal in a band-like manner. Their motion can be described in terms of

delocalized Bloch states, while the mobility is primarily limited by scattering processes involving phonons or other sources of disorder. As a consequence, the mobility of large polarons typically decreases with increasing temperature due to enhanced phonon scattering. In contrast, small polarons propagate predominantly through thermally assisted hopping between localized states [18, 19]. In this regime, the carrier motion is largely incoherent, and the corresponding mobility often exhibits activated behavior of Arrhenius type. The temperature dependence of the mobility therefore provides an important indicator of the dominant transport mechanism [24, 83].

It is important to emphasize, however, that the nature of charge transport is not determined solely by the spatial extent of the polaron. While large polarons are often associated with coherent band-like motion and small polarons with incoherent hopping, this correspondence is not universal. Strong scattering by lattice vibrations or disorder may significantly reduce the carrier mean free path, leading to incoherent transport even when the electronic states remain relatively delocalized. Conversely, localized states may still support coherent motion under suitable conditions. As a result, many realistic materials exhibit transport behavior that lies between the two limiting pictures of band conduction and thermally activated hopping, reflecting the complex interplay between e-ph coupling, lattice dynamics, and thermal fluctuations [24, 31].

From a microscopic standpoint, the character of polaron motion is governed by the competition between the electronic transfer integral J and the phonon energy scale $\hbar\omega_0$, commonly expressed through the adiabaticity ratio $J/(\hbar\omega_0)$. In the adiabatic regime, $J \gg \hbar\omega_0$, the carrier can continuously adjust to the instantaneous lattice configuration, which favors coherent motion. In the non-adiabatic regime, $J \ll \hbar\omega_0$, the carrier cannot follow rapid lattice fluctuations and transport becomes increasingly incoherent. Together with the e-ph coupling strength λ, these parameters determine whether the system exhibits band transport, hopping transport, or an intermediate regime characterized by a narrow polaronic band [24].

In the following subsections, the principal theoretical descriptions of polaron transport are reviewed. Starting with the hopping transport mechanism characteristic of strongly localized small polarons, followed by band transport in the weak-coupling regime and finally polaron band transport, which describes coherent motion of small polarons at sufficiently low temperatures.

2.3.1 Hopping transport

In the strong-coupling limit of the short-range e-ph interaction, a charge carrier tends to become self-trapped by the local lattice distortion it induces. The resulting quasiparticle, known as a small polaron, is spatially localized around a lattice site with a characteristic extent of the order of the lattice constant. In this regime, the electronic wavefunction is strongly coupled to the lattice degrees of freedom, and coherent propagation through the crystal lattice is strongly suppressed. Instead, charge transport occurs through occasional transitions between localized states centered on neighboring lattice sites. Because each transition requires a rearrangement of the surrounding lattice distortion, the elementary transport process is intrinsically coupled to phonon dynamics and the resulting motion is largely incoherent. In the simplest approximation, this dynamics may be described as a Markovian random walk of independent hopping events [18, 24, 83].

A key physical aspect of small-polaron hopping is that the lattice deformation associated with the carrier must be transferred from one site to another during a hop. In general, the equilibrium lattice configurations corresponding to a carrier localized on neighboring sites differ from one another, and direct tunneling between them would violate energy conservation. Hopping therefore becomes possible only during rare lattice fluctuations that temporarily bring the energies of the two configurations into resonance. These so-called coincidence configurations play a central role in small-polaron transport. Once such a configuration is reached, the carrier may tunnel between the two sites with an amplitude determined by the electronic transfer integral. After the transition, the lattice relaxes toward the new equilibrium configuration around the final state. Because the formation of coincidence configurations

requires thermal lattice fluctuations, the hopping rate typically exhibits thermally activated behavior [19, 24, 31, 83].

An important consequence of the Green-Kubo relation is that microscopic transport processes enter the conductivity through the time dependence of the current-current correlation function [78]. In systems where transport proceeds via localized charge carriers, the decay of correlation function is governed by the stochastic hopping events between neighboring sites. In this situation the current operator changes only when a carrier performs a hop, and the temporal decay of the current-current correlation function is directly related to the hopping transition rate.

Within this framework, the carrier mobility can be related to the characteristic hopping rate that governs the diffusion of carriers through the lattice. The derivation presented below for a two-site system provides a simple microscopic illustration of this connection [19, 83, 84]. In this approach, the hopping rate obtained from Fermi's golden rule is expressed as a time integral of a correlation function of the perturbation operator. This correlation function can be directly related to the current-current correlation function appearing in the Kubo formalism. This derivation therefore demonstrates how the microscopic dynamics of phonon-assisted hopping processes determine the macroscopic transport coefficients. The following derivation of the hopping rate for a two-site system closely follows the treatment presented in Ref.[84], adapted here to the notation used in the present work.

The essential physics of small-polaron hopping can be illustrated by the minimal model of a carrier transferring between two identical sites [19, 84]. In this picture, the carrier is strongly localized and a transition between sites becomes possible only when lattice fluctuations allow for a phonon-assisted process that conserves the total energy of the system. From a quantum-mechanical perspective, the electronic transfer integral J is assumed to be small compared to the other energy scales of the problem, allowing the hopping term of the tight-binding Hamiltonian to be treated as a perturbation. For a two-site system ($n = 2$), the Holstein Hamiltonian can therefore be written in the form

$$H = H_1 + H_2 + V = H_0 + V \ , \tag{2.43}$$

where H_0 represents the unperturbed Hamiltonian and V denotes the hopping perturbation. The two contributions read

$$H_n = \hbar\omega_0 b_n^\dagger b_n + G c_n^\dagger c_n (b_n^\dagger + b_n), \quad n = 1, 2 \ , \tag{2.44}$$

$$V = -J(c_1^\dagger c_2 + c_2^\dagger c_1) \ , \tag{2.45}$$

where c_n are electron operators, b_n are phonon operators, G is the e-ph coupling constant, and ω_0 is the phonon frequency.

The hopping rate between two sites n and m is obtained from Fermi's golden rule [19, 84],

$$w = \frac{2\pi}{\hbar} \sum_n p_n \sum_m |V_{nm}|^2 \delta(E_n - E_m), \tag{2.46}$$

where p_n is the probability of occupying the initial state n, and E_n and E_m are the eigenenergies of the unperturbed Hamiltonian $H_0 = H_1 + H_2$. The central task is therefore the evaluation of matrix elements of the perturbation operator V.

Using the integral representation of the delta function,

$$\delta(E_n - E_m) = \frac{1}{2\pi\hbar} \int_{-\infty}^{\infty} \mathrm{d}t \ \mathrm{e}^{\frac{\mathrm{i}}{\hbar}(E_n - E_m)t} \ , \tag{2.47}$$

the hopping rate can be rewritten as

$$w = \frac{1}{\hbar^2} \int_{-\infty}^{\infty} \mathrm{d}t \ \sum_n p_n \sum_m \mathrm{e}^{\frac{\mathrm{i}}{\hbar}(E_n - E_m)t} \langle n|V|m\rangle \langle m|V|n\rangle. \tag{2.48}$$

Equivalently, introducing the time-dependent perturbation operator $V(t)$, the hopping rate may be written in the form

$$w = \frac{1}{\hbar^2}\int_{-\infty}^{\infty} \mathrm{d}t \ \sum_n p_n \sum_m \langle n|\mathrm{e}^{\frac{\mathrm{i}}{\hbar}H_0 t} V \mathrm{e}^{-\frac{\mathrm{i}}{\hbar}H_0 t}|m\rangle\langle m|V|n\rangle = \frac{1}{\hbar^2}\int_{-\infty}^{\infty} \mathrm{d}t \ \sum_n p_n \sum_m \langle n|V(t)|m\rangle\langle m|V|n\rangle, \tag{2.49}$$

where $|n\rangle$ denotes the full direct-product state of the electronic and phonon degrees of freedom, $|n\rangle = |\text{electron}\rangle|\text{phonon}\rangle$. This representation expresses the hopping rate as the time integral of a correlation function of the perturbation operator [19, 84].

To evaluate the transition rate, it is convenient to diagonalize the unperturbed Hamiltonian H_0 so that the electronic and phononic degrees of freedom become separated. This can be achieved by performing the unitary Lang-Firsov transformation [85], defined by

$$U = \exp\left(\frac{G}{\hbar\omega_0}\sum_n c_n^\dagger c_n (b_n^\dagger - b_n)\right). \tag{2.50}$$

Using the Baker-Campbell-Hausdorff formula, the transformed operators and the corresponding transformed Hamiltonian can be obtained. In the transformed representation, the unperturbed Hamiltonian becomes

$$\tilde{H}_0 = -\frac{G^2}{\hbar\omega_0}\sum_n c_n^\dagger c_n + \hbar\omega_0 \sum_n b_n^\dagger b_n \ = \tilde{H}_e + \tilde{H}_{ph}, \tag{2.51}$$

which explicitly separates the electronic and phononic contributions. The e-ph interaction is thus removed from the unperturbed part of the Hamiltonian and reappears as phonon-dependent dressing factors in the hopping perturbation [19, 85].

The transformed hopping operator becomes

$$\tilde{V} = -J\left[c_1^\dagger c_2 \mathrm{e}^{\frac{G}{\hbar\omega_0}(b_1^\dagger - b_1)} \mathrm{e}^{-\frac{G}{\hbar\omega_0}(b_2^\dagger - b_2)} + c_2^\dagger c_1 \mathrm{e}^{-\frac{G}{\hbar\omega_0}(b_1^\dagger - b_1)} \mathrm{e}^{\frac{G}{\hbar\omega_0}(b_2^\dagger - b_2)}\right]. \tag{2.52}$$

The corresponding time-dependent perturbation operator is

$$\tilde{V}(t) = \mathrm{e}^{\frac{\mathrm{i}}{\hbar}\tilde{H}_0 t}\tilde{V}\mathrm{e}^{-\frac{\mathrm{i}}{\hbar}\tilde{H}_0 t} = \mathrm{e}^{\frac{\mathrm{i}}{\hbar}\tilde{H}_e t}\mathrm{e}^{\frac{\mathrm{i}}{\hbar}\tilde{H}_{ph} t}\tilde{V}\mathrm{e}^{-\frac{\mathrm{i}}{\hbar}\tilde{H}_e t}\mathrm{e}^{-\frac{\mathrm{i}}{\hbar}\tilde{H}_{ph} t}. \tag{2.53}$$

Since the eigenstates of the unperturbed Hamiltonian factorize into electronic and phononic parts, $|n\rangle = |n\rangle_e|n\rangle_{ph}$, and the electronic Hamiltonian satisfies $H_e|n\rangle_e = \varepsilon_n|n\rangle_e$, the corresponding matrix element becomes

$$\langle n|\tilde{V}(t)|m\rangle = \mathrm{e}^{\frac{\mathrm{i}}{\hbar}(\varepsilon_n - \varepsilon_m)t}\langle n|\mathrm{e}^{\frac{\mathrm{i}}{\hbar}\tilde{H}_{ph} t}\tilde{V}\mathrm{e}^{-\frac{\mathrm{i}}{\hbar}\tilde{H}_{ph} t}|m\rangle. \tag{2.54}$$

For two identical lattice sites, the unperturbed electronic states are degenerate, so that $\varepsilon_n = \varepsilon_m$ and the electronic phase factor reduces to unity. The hopping rate is therefore determined entirely by the phonon contribution. Introducing the phonon statistical weights p_n^{ph}, the transition rate can be written as

$$w = \frac{1}{\hbar^2}\int_{-\infty}^{\infty} \mathrm{d}t \ \sum_n p_n^{ph} \sum_m \langle n|\mathrm{e}^{\frac{\mathrm{i}}{\hbar}\tilde{H}_{ph} t}\tilde{V}\mathrm{e}^{-\frac{\mathrm{i}}{\hbar}\tilde{H}_{ph} t}|m\rangle\langle m|\tilde{V}|n\rangle \ , \tag{2.55}$$

which can be rewritten as

$$w = \frac{1}{\hbar^2}\int_{-\infty}^{\infty} \mathrm{d}t \ \sum_n p_n^{ph} \langle n|\mathrm{e}^{\frac{\mathrm{i}}{\hbar}\tilde{H}_{ph} t}\tilde{V}\mathrm{e}^{-\frac{\mathrm{i}}{\hbar}\tilde{H}_{ph} t}\tilde{V}|n\rangle \ . \tag{2.56}$$

In compact form, the hopping rate becomes

$$w = \frac{1}{\hbar^2}\int_{-\infty}^{\infty} \mathrm{d}t \ \langle \mathrm{e}^{\frac{\mathrm{i}}{\hbar}\tilde{H}_{ph} t}\tilde{V}'\mathrm{e}^{-\frac{\mathrm{i}}{\hbar}\tilde{H}_{ph} t}\tilde{V}'\rangle, \tag{2.57}$$

where

$$\tilde{V}' = -J\left[\exp\left(\frac{G}{\hbar\omega_0}(b_1^\dagger - b_1 - b_2^\dagger + b_2)\right) + \exp\left(-\frac{G}{\hbar\omega_0}\left(b_1^\dagger - b_1 - b_2^\dagger + b_2\right)\right)\right] \tag{2.58}$$

represents the phonon-dependent part of the perturbation.

The required thermodynamic averages are evaluated using standard bosonic occupation numbers,

$$\langle b_n\rangle = \langle b_n^\dagger\rangle = 0\ , \tag{2.59}$$

$$\langle b_n^\dagger b_n\rangle = n_{ph} = (\mathrm{e}^{\beta\hbar\omega_0} - 1)^{-1}\ , \tag{2.60}$$

$$\langle b_n b_n^\dagger\rangle = n_{ph} + 1\ . \tag{2.61}$$

This yields the hopping rate in the form

$$w = \frac{J^2}{\hbar^2}\int_{-\infty}^{\infty}\mathrm{d}t\ \exp\left[-2\frac{G^2}{\hbar\omega_0}(2n_{ph} + 1 - (n_{ph}+1)\mathrm{e}^{-\mathrm{i}\omega_0 t} - n_{ph}\mathrm{e}^{\mathrm{i}\omega_0 t})\right]. \tag{2.62}$$

The transition rate is therefore expressed as a time integral of a correlation function of the perturbation operator. In this representation the hopping rate can be directly related to the current-current correlation function C_{jj}, so that formally

$$w = \frac{1}{2}\int_{-\infty}^{\infty}\mathrm{d}t\ C_{jj}(t)\ . \tag{2.63}$$

For the isolated two-site system considered here, however, the correlation function is periodic in time and the dc limit of the Kubo formula is not well defined. A meaningful transport coefficient emerges only in the thermodynamic limit or when dissipative processes are included [20, 30, 78].

Despite this limitation, the two-site model remains useful because it yields a transparent limiting expression under well-controlled approximations. In the high-temperature limit $\beta\hbar\omega_0 \ll 1$, the phonon occupation number reduces to

$$n_{ph} \simeq 1/(\beta\hbar\omega_0)\ . \tag{2.64}$$

Moreover, in the strong-coupling, high-temperature regime, the dominant contributions arise from short real times, allowing the expansion $\exp(\mathrm{i}\omega_0 t) \simeq 1 + \mathrm{i}\omega_0 t - \frac{1}{2}\omega_0^2 t^2$. Under these approximations the current-current correlation function decays sufficiently rapidly for the integral to converge, and the hopping rate reduces to the well-known Marcus formula,

$$w = \frac{J^2}{\hbar}\sqrt{\frac{\beta\pi}{\Lambda}}\exp\left(-\frac{\beta\Lambda}{4}\right) \tag{2.65}$$

where $\Lambda = \dfrac{2G^2}{\hbar\omega_0}$ is the lattice reorganization energy.

The Marcus formula shows that small-polaron hopping is governed by the interplay between the electronic transfer integral J and the lattice reorganization energy Λ, which represents the energy required to transfer the accompanying lattice distortion from the initial site to the final one [19, 31, 83, 84].

The corresponding current-current correlation function takes the form

$$C_{jj}(t) = 2J^2\exp\left(-\frac{1}{\hbar^2}\sigma_0^2 t^2\right)\exp\left(-\frac{\mathrm{i}}{\hbar}\beta\sigma_0^2 t\right), \tag{2.66}$$

where

$$\sigma_0^2 = \frac{2G^2}{\beta\hbar\omega_0} = \Lambda/\beta\ . \tag{2.67}$$

The Gaussian factor describes the decay of the current-current correlation function caused by thermal lattice fluctuations, whereas the oscillatory phase reflects the energy shift associated with lattice reorganization during the hopping process.

Within the random-walk picture, charge transport proceeds through a sequence of statistically independent hopping events between neighboring lattice sites. In this limit, the carrier motion can be described as a diffusion process characterized by the diffusion coefficient

$$D = a^2 w \ , \tag{2.68}$$

where a denotes the hopping distance and w the transition rate between adjacent sites. Using the Einstein diffusion relation for mobility $\mu = \mathrm{e}\beta D = \mathrm{e}a^2\beta w$ [30, 78], the mobility can therefore be expressed as

$$\mu = \frac{\mathrm{e}a^2\beta J^2}{\hbar}\sqrt{\frac{\beta\pi}{\Lambda}}\exp\left(-\frac{\beta\Lambda}{4}\right). \tag{2.69}$$

Although this result is derived from a minimal toy model, it captures the central feature of small-polaron transport, namely its thermally activated character. The exponential factor in Eq.(2.69) implies an Arrhenius-type temperature dependence with activation energy $\Lambda/4$.

The quantity Λ represents the lattice reorganization energy associated with transferring the local lattice distortion from one site to another. Within the Holstein model, this energy is directly related to the polaron binding energy, $\Lambda = 2E_p$, and reflects the lattice deformation that must be created at the target site before the carrier can successfully complete the hop. The activation barrier therefore arises from the energetic cost of rearranging the surrounding lattice configuration during the hopping process [19, 83].

An additional complication arises from the fact that individual hopping events do not necessarily contribute equally to long-range transport. In a realistic lattice environment, a carrier may repeatedly hop back and forth between two neighboring sites before eventually escaping to a different site. Such correlated hopping processes increase the number of microscopic transitions without producing a proportional increase in the net diffusion of the carrier. Consequently, the diffusion constant and the resulting mobility depend not only on the local hopping rate but also on the probability that a hop leads to escape from the local potential environment. This effect becomes particularly important at elevated temperatures, where lattice fluctuations increase the hopping frequency but also enhance the probability of rapid back-and-forth transitions [83].

While the two-site derivation and its high-temperature Marcus limit provide a physically transparent description of activated hopping, they rely on several simplifying assumptions, including strong e-ph coupling, classical phonon statistics, and a short-time decay of the current-current correlation function. Outside this regime, the transport cannot, in general, be reduced to a simple Arrhenius law.

At intermediate temperatures and for more general phonon spectra, the temporal evolution of lattice fluctuations entering the current-current correlation function becomes nontrivial. These fluctuations determine the probability that the lattice reaches coincidence configurations and may substantially modify the activation behavior.

A more general description of charge transport can be formulated within the framework of linear-response theory, where transport coefficients are obtained from the current-current correlation function through the Kubo formula [78, 80]. Within this approach, the correlation function can be expressed in terms of electronic Green's functions. Different approximation schemes correspond to different diagrammatic truncations of the resulting expressions. The simplest treatment corresponds to the so-called bubble approximation, which retains only single-particle Green's functions, while more refined descriptions include vertex corrections arising from correlated scattering processes. This formalism provides a systematic framework for describing transport beyond the simple activated hopping limit and allows one to interpolate between incoherent hopping and more coherent transport regimes[24, 78].

2.3.2 Band transport

In the weak e-ph coupling regime, the lattice distortion induced by a charge carrier extends over many lattice sites and does not lead to self-trapping. The carrier therefore remains delocalized and its motion can be described in terms of extended Bloch states. In crystalline materials, the overlap of electronic orbitals on neighboring sites leads to the formation of energy bands, within which the electronic states are coherent superpositions of localized atomic or molecular orbitals. As a result, the carrier propagates through the lattice as a quasiparticle characterized by a well-defined momentum and an increased effective mass [20, 78]. In this regime the lattice deformation associated with the carrier acts primarily as a weak perturbation that scatters the otherwise delocalized electronic states, rather than localizing the carrier into a small polaron [31].

In realistic crystalline structures, the motion of the carrier is interrupted by occasional scattering processes that change its momentum. The dominant scattering mechanism include interactions with phonons, structural disorders and impurities in the lattice. Consequently, the carrier propagates coherently only over a finite time between successive scattering events. This situation is commonly described within the semiclassical Boltzmann transport framework, where the carrier dynamics are characterized by an average scattering time between collisions [30, 78].

Under the assumption of weak electric field, as considered in linear response theory, the distribution function of carriers with momentum k acquires a small deviation from equilibrium. The nonequilibrium distribution can therefore be written as

$$f_k = f_k^0 + \delta f_k \ , \tag{2.70}$$

where f_k^0 is the equilibrium distribution and δf_k represents the small correction induced by the electric field. In thermal equilibrium, the occupation of Bloch states is given by the Fermi-Dirac distribution

$$f_k^0 = \left(\mathrm{e}^{\beta(\varepsilon_k - \mu)} + 1\right)^{-1} \ , \tag{2.71}$$

where ε_k is the band dispersion and μ is the chemical potential.

Within the relaxation-time approximation, the stationary Boltzmann equation in one dimension takes the form [30, 78]

$$f_k = f_k^0 - \frac{1}{\hbar}\mathrm{e}\tau_k E \frac{\partial}{\partial k} f_k^0 = f_k^0 - \mathrm{e}v_k \tau_k E \frac{\partial f_k^0}{\partial \varepsilon_k} \ , \tag{2.72}$$

where

$$v_k = \frac{1}{\hbar}\frac{\partial \varepsilon_k}{\partial k} \tag{2.73}$$

is the band velocity and τ_k is the transport relaxation time.

The electric current density is proportional to the average velocity of the carriers. In thermal equilibrium, where no external electric field is present, the distribution function is symmetric in momentum, and the net current therefore vanishes. Consequently, only the nonequilibrium correction δf_k contributes to the electric current. The electric current density is then given by

$$J = \frac{\mathrm{e}^2}{V} \sum_k \tau_k v_k^2 \left(-\frac{\partial f_k^0}{\partial \varepsilon_k}\right) E \ . \tag{2.74}$$

The conductivity is defined as the proportionality factor between the current density and the applied electric field, which yields

$$\sigma = \frac{\mathrm{e}^2}{V} \sum_k \tau_k v_k^2 \left(-\frac{\partial f_k^0}{\partial \varepsilon_k}\right) \ . \tag{2.75}$$

Finally, using the relation $\sigma = n\mathrm{e}\mu$, the carrier mobility can be written as

$$\mu = \frac{\mathrm{e}}{nV} \sum_k \tau_k v_k^2 \left(-\frac{\partial f_k^0}{\partial \varepsilon_k}\right) \ , \tag{2.76}$$

where n is the carrier density.

In the low carrier concentration limit relevant for polaron transport, the chemical potential lies well below the band edge, $\mu_{\text{chem}} \to -\infty$, and the Fermi-Dirac distribution reduces to the Maxwell-Boltzmann form

$$f_k^0 \simeq \mathrm{e}^{-\beta(\varepsilon_k - \mu_{\text{chem}})} \ . \tag{2.77}$$

The derivative of the distribution function with respect to energy then becomes

$$-\frac{\partial f_k^0}{\partial \varepsilon_k} = \beta f_k^0 = \beta \mathrm{e}^{-\beta\varepsilon_k} \mathrm{e}^{\beta\mu_{\text{chem}}} \ . \tag{2.78}$$

The carrier density can be written explicitly as

$$n = \frac{1}{V}\sum_k f_k^0 = \frac{1}{V}\sum_k \mathrm{e}^{-\beta\varepsilon_k} \mathrm{e}^{\beta\mu_{\text{chem}}} \ . \tag{2.79}$$

Substituting these expressions into the mobility formula shows that the factors containing the chemical potential cancel between the numerator and denominator. As a result, the mobility becomes independent of the chemical potenital and depends only on the Boltzmann weights of the band states.

The standard band-transport mobility formula in low carrier density limit therefore takes the form [30, 78]

$$\mu = \mathrm{e}\beta \frac{\sum_k n_k \tau_k v_k^2}{\sum_k n_k} \ , \tag{2.80}$$

where $n_k = \exp(-\beta\varepsilon_k)$ is the Boltzmann factor. For a one-dimensional tight-binding system with dispersion $\varepsilon_k = -2J\cos(ka)$, the corresponding band velocity is $v_k = 2Ja\sin(ka)/\hbar$.

The same expression for the mobility as in Eq. (2.80) can also be obtained from the Kubo formula Eq. (2.30) by evaluating the current-current correlation function within a single-particle framework [78], as will be described in the following text.

In momentum representation, the current operator can be written as [20, 78]

$$j = \mathrm{e}\sum_k v_k a_k^\dagger a_k, \tag{2.81}$$

where $a_k^\dagger$ and a_k are creation and annihilation operators of an electron with momentum k, and v_k denotes the band velocity. Substituting this operator into the current-current correlation function leads to a four-operator average

$$C(t) = \langle j(t) j(0)\rangle = \mathrm{e}^2 \sum_{k,q} v_k v_q \left\langle a_k^\dagger(t) a_k(t) a_q^\dagger(0) a_q(0)\right\rangle \ . \tag{2.82}$$

This correlation function describes the correlated propagation of two fermionic lines and therefore contains, in general, all many-body scattering processes induced by the e-ph interaction. In diagrammatic approach, its exact evaluation involves an infinite series of diagrams in which the two current vertices are connected by dressed single-particle propagators. In addition, vertex corrections appear that account for correlated multi-phonon scattering processes [78].

In the weak-coupling regime, where the carrier remains a quasiparticle with well-defined momentum and scattering events are relatively rare, the dominant contribution arises from diagrams that neglect vertex corrections and retain only the product of two single-particle propagators. This approximation is known as the bubble approximation, since its diagrammatic representation consists of two propagator lines connecting the two current vertices and forming a closed loop [31, 78].

Within this approximation, the four-operator average factorizes into a product of two-operator averages corresponding to single-particle Green's functions,

$$\left\langle a_k^\dagger(t) a_k(t) a_q^\dagger(0) a_q(0)\right\rangle \approx \delta_{k,q} \left\langle a_k^\dagger(t) a_k(0)\right\rangle \left\langle a_k(t) a_k^\dagger(0)\right\rangle \ , \tag{2.83}$$

and the current-current correlation function reduces to

$$C(t) \simeq \mathrm{e}^2 \sum_k v_k^2 \left\langle a_k^\dagger(t) a_k(0) \right\rangle \left\langle a_k(t) a_k^\dagger(0) \right\rangle \ . \tag{2.84}$$

Physically, this approximation assumes that the current response is governed by the independent propagation of quasiparticles dressed by phonons, while correlated processes that modify the coupling between the external and the quasiparticles are neglected. The effects of electron-phonon scattering are incorporated through the self-energy entering the single-particle Green's function [78].

The two-point correlation functions appearing in the current-current correlator can be expressed in terms of the spectral function $A_k(\omega)$. Using the spectral representation of the single-particle Green's functions, one obtains [78]

$$\left\langle a_k^\dagger(t) a_k(0) \right\rangle = \frac{1}{2\pi} \int_{-\infty}^{\infty} \mathrm{d}\omega \mathrm{e}^{\mathrm{i}\omega t} A_k(\omega) f(\hbar\omega) \ , \tag{2.85}$$

$$\left\langle a_k(t) a_k^\dagger(0) \right\rangle = \frac{1}{2\pi} \int_{-\infty}^{\infty} \mathrm{d}\omega \mathrm{e}^{-\mathrm{i}\omega t} A_k(\omega) \left(1 - f(\hbar\omega)\right) \ , \tag{2.86}$$

where

$$f(E) = \left(\mathrm{e}^{\beta(E-\mu_{\mathrm{chem}})} + 1\right)^{-1} \tag{2.87}$$

is the Fermi-Dirac distribution.

It is also convenient to express the particle number as $N = \sum_k \left\langle a_k^\dagger a_k \right\rangle$, with

$$\left\langle a_k^\dagger a_k \right\rangle = \frac{1}{2\pi} \int_{-\infty}^{\infty} \mathrm{d}\omega A_k(\omega) f(\hbar\omega) \ . \tag{2.88}$$

Substituting these expressions into the current-current correlation function in the Green-Kubo relation for mobility,Eq. (2.30), and using the identity

$$\int_{-\infty}^{\infty} \mathrm{d}t \ \mathrm{e}^{\mathrm{i}(\omega_1-\omega_2)t} = 2\pi\delta(\omega_1 - \omega_2) \ , \tag{2.89}$$

one obtains the dc mobility in the form

$$\mu = \frac{\beta \mathrm{e}}{2nV} \sum_k v_k^2 \int \frac{\mathrm{d}\omega}{2\pi} A_k(\omega)^2 f(\hbar\omega) \left(1 - f(\hbar\omega)\right) \ . \tag{2.90}$$

Using the identity

$$f(E)(1 - f(E)) = -\frac{1}{\beta} \frac{\partial f(E)}{\partial E} \ , \tag{2.91}$$

this expression can be rewritten as

$$\mu = \frac{\mathrm{e}}{nV} \sum_k v_k^2 \int \frac{\mathrm{d}\omega}{2\pi} A_k(\omega)^2 \left(-\frac{1}{\beta} \frac{\partial f(E)}{\partial E} \bigg|_{E=\hbar\omega} \right) \ . \tag{2.92}$$

The spectral function is related to the retarded Green's function by [78]

$$A_k(\omega) = -2\mathrm{Im} \ G_k^R(\omega) \ . \tag{2.93}$$

The retarded Green's function itslef is determined by the Dyson equation [78]

$$G_k^R(\omega) = \left[\hbar\omega - (\varepsilon_k - \mu_{\mathrm{chem}}) - \Sigma_k^R(\omega)\right]^{-1} \ , \tag{2.94}$$

where $\Sigma_k^R(\omega)$ is the retarded self-energy.

In the weak e-ph interaction limit, scattering processes are relatively rare and the spectral function is narrow and sharply peaked around the quasiparticle energy [31, 78]. In this case it can be approximated by delta function,

$$A_k(\omega) \simeq 2\pi\delta(\hbar\omega - \varepsilon_k) \ . \tag{2.95}$$

and the square of spectral function in this limit behaves as

$$A_k(\omega)^2 = \frac{\pi}{-\mathrm{Im}\ \Sigma_k^R(\omega)}\delta\left(\hbar\omega - \varepsilon_k\right) \ , \tag{2.96}$$

where ε_k denotes the renormalized quasiparticle excitation energy.

The dc mobility then takes the form

$$\mu = \frac{\mathrm{e}}{nV}\sum_k v_k^2\tau_k\left(-\frac{\partial f(\varepsilon_k)}{\partial\varepsilon_k}\right) \ , \tag{2.97}$$

where the scattering relaxation time is identified with the imaginary part of the retarded self-energy,

$$\tau_k^{-1} = -\frac{2}{\hbar}\mathrm{Im}\ \Sigma_k^R(\omega)\Big|_{\hbar\omega=\varepsilon_k-\mu_{\mathrm{chem}}} \ . \tag{2.98}$$

The imaginary part of the self-energy determines the linewidth of the spectral peak and therefore the inverse lifetime of the quasiparticle excitation, while the real part of the self-energy represents the renormalization shift of quasiparticle energy caused by interactions [78]. In this way the microscopic scattering processes induced by the e-ph interaction enter the transport coefficients through the self-energy of the single-particle Green's function [31, 78].

In the low carrier concentration limit relevant for polaron transport, the Fermi-Dirac distribution reduces to the Maxwell-Boltzmann form [30, 78]

$$f(\varepsilon_k - \mu_{\mathrm{chem}}) \approx \exp(-\beta(\varepsilon_k - \mu_{\mathrm{chem}})) \ . \tag{2.99}$$

The particle number entering the mobility equation becomes

$$nV \equiv N \simeq \sum_k \exp(-\beta(\varepsilon_k - \mu_{\mathrm{chem}})) \ . \tag{2.100}$$

Because the chemical potential appears in both the numerator and denominator, the corresponding factors cancel. As a result, the mobility obtained from the Kubo formalism reduces to the same expression as derived previously within the semiclassical Boltzmann apporach,

$$\mu = \mathrm{e}\beta\frac{\sum_k n_k v_k^2\tau_k}{\sum_k n_k} \ , \tag{2.101}$$

where $n_k = \exp\left(-\beta\varepsilon_k\right)$ is the Boltzmann factor.

Within the band-transport picture, the charge carrier propagates through the lattice as a delocalized quasiparticle whose motion is periodically interrupted by scattering on thermally excited phonons. As the temperature increases, the phonon population grows and scattering processes become more frequent, leading to a gradual reduction of the carrier mobility. This temperature dependence is a characteristic feature of band transport and is commonly observed in systems where electron-phonon interaction is relatively weak and the electronic bandwidth remains large compared to the characteristic phonon energy [30, 78].

When the e-ph interaction becomes stronger, however, the lattice distortion accompanying the carrier can no longer be treated as a small perturbation. The carrier then becomes strongly dressed by phonons and forms a polaronic quasiparticle. At sufficiently low temperatures such quasiparticles may still propagate coherently through the lattice, but with a substantially renormalized bandwidth [24, 31]. This intermediate regime, in which transport remains coherent but the electronic motion is strongly influenced by lattice dressing, is commonly reffered to as polaron band transport and is discussed in the following subsection.

2.3.3 Polaron band transport

In the strong e-ph coupling limit, the lattice distortion accompanying the charge carrier becomes sufficiently large that the polaron binding energy $E_p = G^2/(\hbar\omega_0)$ exceeds half the bare electronic bandwidth. For the one-dimensional Holstein model, the electronic dispersion is $\varepsilon_k = -2J\cos(ka)$, corresponding to a bandwidth $W = 4J$, so the condition for strong coupling may be written as $E_p > W/2 = 2J$ [18, 24].

Under these conditions, the carrier forms a small polaron, in which the electronic state is strongly dressed by a local lattice deformation. Despite the strong coupling, coherent motion of the carrier may still occur at very low temperatures in a perfect crystal without impurities. In this regime, the carrier is not confined to a single lattice site but instead forms delocalized Bloch states associated with a narrow polaronic band. The resulting transport mechanism is commonly referred to as polaron band transport [18, 24, 83].

In contrast to the incoherent hopping mechanism discussed in the previous subsection, the motion of the carrier in this regime remains coherent and adiabatic. The lattice distortion accompanying the carrier moves together with the electron as it propagates through the lattice, forming a composite quasiparticle whose dynamics reflect the interplay between electronic motion and the accompanying lattice deformation [24, 31].

A convenient theoretical description of this regime is obtained by applying the canonical Lang-Firsov transformation applied to the Holstein Hamiltonian, defined by the unitary transformation [18, 24, 85]

$$\tilde{H} = \mathrm{e}^{S} H \mathrm{e}^{-S} \ . \tag{2.102}$$

The Hamiltonian is written as $H = H_e + H_{e\text{-}ph} + H_{ph}$, with H_e the tight-binding electronic term, H_{ph} describes the phonons, and $H_{e\text{-}ph}$ represents the e-ph interaction. The transformation is generated by the operator

$$S = \frac{G}{\hbar\omega_0} \sum_n c_n^\dagger c_n \left(b_n^\dagger - b_n \right) \ . \tag{2.103}$$

This transformation shifts the equilibrium positions of the lattice oscillators and eliminates the explicit e-ph interaction from the unperturbed Hamiltonian. The transformed Hamiltonian can then be written as

$$\tilde{H} = \tilde{H}_0 + \tilde{V} \ . \tag{2.104}$$

The first term describes a localized polaron together with the phonon bath, while the second term represents the phonon-assisted hopping between neighboring lattice sites. The transformed terms are given as

$$\tilde{H}_0 = -E_p \sum_n c_n^\dagger c_n + \hbar\omega_0 \sum_n b_n^\dagger b_n \ , \tag{2.105}$$

$$\tilde{V} = -J \sum_n c_{n+1}^\dagger c_n X_{n+1}^\dagger X_n + \text{h.c.} \ , \tag{2.106}$$

where the polaron binding energy is

$$E_p = \frac{G^2}{\hbar\omega_0} \ , \tag{2.107}$$

and the phonon dressing operator is

$$X_n = \exp\left(-\frac{G}{\hbar\omega_0} (b_n^\dagger - b_n) \right) \ . \tag{2.108}$$

The operator X_n describes the phonon cloud accompanying the carrier and accounts for the overlap between lattice distortions associated with neighboring sites. In the transformed representation, the hopping term therefore acquires phonon-dependent dressing factors that renormalize the effective electronic transfer integral.

In the strong-coupling regime, the polaron binding energy E_p greatly exceeds the electronic transfer energy J. For the one-dimensional tight-binding band $\varepsilon_k = -2J\cos(ka)$ with bandwidth $W = 4J$, the dimensionless coupling parameter may be written as

$$\lambda = \frac{E_p}{W/2} \, . \tag{2.109}$$

Consequently, the ratio $J/E_p \sim 1/\lambda$ is small, allowing the hopping term $\tilde{V}$ to be treated perturbatively. This forms the basis of the $1/\lambda$ expansion commonly used in small-polaron theory [18, 24].

The unperturbed Hamiltonian $\tilde{H}_0$ describes a polaron localized on a lattice site with the associated lattice deformation. The corresponding ground state localized at the n-th site can be written as

$$|n\rangle = c_n^\dagger |0\rangle_e |0\rangle_{ph} \, , \tag{2.110}$$

where $|0\rangle_e$ and $|0\rangle_{ph}$ denote the electronic and phononic vacuum states, respectively. All states $|n\rangle$ are degenerate with energy $-E_p$. The perturbation $\tilde{V}$ lifts this degeneracy and produces a coherent polaron band.

To first order in perturbation theory, the effective hopping amplitude between neighboring localized polaron states is given by

$$\langle n+1|\tilde{V}|n\rangle = -J\langle 0|X_{n+1}^\dagger X_n|0\rangle \, . \tag{2.111}$$

At zero temperature the phonon vacuum expectation value evaluates to

$$\langle 0|X_{n+1}^\dagger X_n|0\rangle = \mathrm{e}^{-g^2} \, , \tag{2.112}$$

where $g = G/(\hbar\omega_0)$. The hopping integral is therefore renormalized to

$$\tilde{J} = J\mathrm{e}^{-g^2} \, . \tag{2.113}$$

Using the relation $g^2 = E_p/(\hbar\omega_0)$, the renormalized hopping amplitude may also be written as

$$\tilde{J} = J \, \exp\left(-\frac{E_p}{\hbar\omega_0}\right) \, . \tag{2.114}$$

The coherent small-polaron band is then

$$\tilde{\varepsilon}_k = -2\tilde{J}\cos(ka) \, , \tag{2.115}$$

with corresponding bandwidth

$$\tilde{W} = W\mathrm{e}^{-g^2} = W\exp\left(-\frac{E_p}{\hbar\omega_0}\right) \, . \tag{2.116}$$

This result shows that the reduction of the electronic bandwidth is controlled by the ratio of the polaron binding energy to the phonon energy scale. When the lattice deformation energy greatly exceeds the characteristic phonon energy $\hbar\omega_0$, the overlap between the neighboring phonon clouds becomes exponentially small, leading to a very narrow polaron band.

The exponential reduction of the hopping amplitude directly implies a strong renormalization of the quasiparticle dispersion and its effective mass. The effective mass of a quasiparticle is determined from the curvature of the dispersion relation at the band minimum,

$$\frac{1}{m^*} = \frac{1}{\hbar^2}\frac{\partial^2\varepsilon_k}{\partial k^2}\bigg|_{k=0} \, . \tag{2.117}$$

For the bare tight-binding dispersion $\varepsilon_k = -2J\cos(ka)$, the electronic effective mass is

$$m^* = \frac{\hbar^2}{2Ja^2} \ . \tag{2.118}$$

Using the renormalized small-polaron dispersion $\tilde{\varepsilon}_k = -2\tilde{J}\cos(ka)$ gives

$$\tilde{m}^* = m^* \mathrm{e}^{g^2} = m^* \exp\left(\frac{E_p}{\hbar\omega_0}\right) \ . \tag{2.119}$$

The effective mass of the small polaron therefore increases exponentially with the e-ph coupling strength. Compared with the bare band mass, relevant for conventional band transport, the small-polaron mass is exponentially larger, which strongly suppresses the mobility of coherent small polarons. In the limit of very strong e-ph coupling, the coherent polaron bandwidth collapses and the efective mass diverges, indicating that the carrier becomes effectively localized. Under such conditions coherent band motion is no longer possible, even at very low temperatures, and charge transport proceeds through incoherent hopping[24, 31].

In the coherent small-polaron regime, the lattice distortion surrounding the carrier moves together with the electron as it propagates through the crystal. Because the polaron motion is slow compared to the characteristic phonon dynamics, the phonon bath remains close to equilibrium. Under these conditions, the phonon operators in the transformed hopping term can be replaced by their thermal expectation value. Evaluating this average yields

$$\langle X_{n+1}^\dagger X_n \rangle = \exp\left(-g^2(2n_{ph}+1)\right) \ , \tag{2.120}$$

where $n_{ph} = \left(\mathrm{e}^{\beta\hbar\omega_0} - 1\right)^{-1}$ is the phonon occupation number [19, 24]. This approximation makes the effective hopping integral temperature dependent,

$$\tilde{J}(T) = J\mathrm{e}^{-g^2(2n_{ph}+1)} \ . \tag{2.121}$$

The polaron dispersion therefore becomes

$$\tilde{\varepsilon}_k(T) = -2\tilde{J}(T)\cos(ka) = -2J\,\exp\left(-\frac{E_p}{\hbar\omega_0}(2n_{ph}+1)\right)\cos(ka) \ , \tag{2.122}$$

with bandwidth

$$\tilde{W}(T) = 4\tilde{J}(T) = 4J\,\exp\left(-\frac{E_p}{\hbar\omega_0}(2n_{ph}+1)\right) \ . \tag{2.123}$$

The polaron bandwidth therefore decreases exponentially with temperature, reflecting the increasing strength of thermal lattice fluctuations surrounding the carrier.

The temperature dependence of mobility in the polaron band regime therefore differs qualitatively from both conventional band transport and thermally assisted hopping. At very low temperatures, the polaron propagates coherently through the lattice with a strongly renormalized effective mass. As the temperature increases, thermal lattice fluctuations progressively disrupt the coherence of the polaron motion and reduce the effective transfer integral through the temperature-dependent narrowing of the polaron band. Consequently, the bandwidth continues to shrink and the delocalized polaron picture eventually breaks down. Under such conditions, the carrier motion becomes dominated by phonon-assisted transitions between localized configurations, and transport crosses over to the incoherent hopping regime.

The theoretical frameworks discussed in this section illustrate how the charge transport in e-ph coupled systems emerges from the interplay bwteen coherent electronic mootion and the dynamical response of the lattice. Depending on the strength of the e-ph interaction and the temperature of the

system, transport may occur through distinct mechanisms ranging from band-like motion of weakly dressed carriers, to coherent propagation of heavy polarons withing a narrow band, and finally to incoherent hopping between localized lattice configurations. Understanding the conditions under which these regimes arise is essential for interpreting transport properties in materials where e-ph interaction plays a dominant role, and provides the theoretical foundation for the analysis of polaron dynamics within the Holstein model presented in the following chapters.

2.4 Path-Integral formalism

The path integral formalism represents a fundamental formulation of quantum mechanics [79, 86–88], complementary to the canonical approach based on operator algebra and wave functions. Although the formalism is most commonly associated with the work of Feynman, its conceptual roots can be traced to earlier developments in both classical probability theory and quantum mechanics [89–91]. These early contributions laid the groundwork for a formulation of quantum theory in which physical processes are described in terms of ensembles of trajectories in phase space rather than an individual deterministic path.

One of the earliest appearances of something that resembles the integrals over paths arose in the work of Wiener, who studied the Brownian motion as a stochastic process [86, 91, 92]. Brownian motion can be viewed as a continuum limit of a Markovian random walk with discrete time steps. In Wiener's construction, the probability for a particle initially located at position x_0 at time t_0 to be found at position x_n at a later time t_n is described by a set of integrals over all possible variables x_i, $i = 0, 1, \ldots, n$, reflecting the absence of a unique trajectory in stochastic motion.

$$P(x_n, x_0) = \int \mathrm{d}x_1 \mathrm{d}x_2 \ldots \mathrm{d}x_{n-1}\; p(x_n - x_{n-1}) \ldots p(x_2 - x_1) p(x_1 - x_0)\ .$$

In the continuum limit $n \to \infty$, this construction leads to a probability measure defined over a space of continuous paths, known as the Wiener measure. A key feature of Wiener's formulation is that the probability weight $p(x' - x)$ with which each path contributes to the total probability measure is determined by a Gaussian distribution $\exp(-(x - x')^2/2)$. This result follows from the central limit theorem, which ensures that the cumulative effect of an infinitely large number of random steps converges to a Gaussian process. Although Wiener's work was purely classical and probabilistic in nature, it introduced mathematical structures that later proved essential for the development of path integrals in quantum mechanics [88, 89].

Around the same period, Dirac introduced ideas that pointed toward a path-based formulation of quantum dynamics. Dirac considered the quantum time-evolution operator and expressed it as a product of infinitesimal evolution operators over discrete time intervals [93]. This representation implicitly suggests a decomposition of quantum evolution into a sequence of short-time transitions, each contributing to the total amplitude. Although Dirac did not explicitly formulate a sum over continuous paths, his approximation of the evolution operator provided a crucial conceptual step toward the discretized time-slicing approach that underlies the path integral formulation [88, 90].

Closely related ideas also appeared in the work of Wentzel, who studied transition amplitudes in quantum optics [86]. Wentzel proposed that transition probability amplitudes could be expressed as sums over possible paths, each weighted by a phase factor determined by the action. In this picture, destructive interference suppresses contributions from paths that deviate strongly from the classical equations of motion, while constructive interference occurs near classical trajectories. This insight foreshadowed a central principle of the path integral formulation [88, 89]. The classical behavior emerges not from the exclusion of non-classical paths, but from the coherent cancelation of their contributions.

Building on these ideas, Feynman formulated the path integral approach as a complete and self-consistent framework for quantum mechanics [89, 90]. In this formulation, the transition amplitude

between an initial and a final state is expressed as a sum over all possible trajectories connecting the two configurations. Each trajectory contributes with a phase determined by the classical action S, typically through a factor of the form $\exp(\mathrm{i}S/\hbar)$. Unlike classical mechanics, which singles out a unique trajectory determined by the equations of motion and conservation laws, quantum mechanics admits contributions from an infinite set of paths [79, 86, 88]. Observable quantities arise from the coherent superposition of these contributions, rather than from a single deterministic history.

This multiplicity of contributing paths reflects a fundamental distinction between classical and quantum descriptions of motion. In classical mechanics, conservation laws constrain the system's evolution locally and single out a unique trajectory. In quantum mechanics, by contrast, the uncertainty principle limits the simultaneous specification of conjugate variables, so that the transition amplitude receives contributions from configurations that do not correspond to classical solutions at intermediate times [89]. While energy is conserved globally, the energy–time uncertainty relation allows non-classical configurations to contribute to the quantum amplitude over sufficiently short time intervals, rendering classically forbidden processes dynamically relevant. In the classical limit $\hbar \to 0$, only paths in close proximity to the classical trajectory contribute constructively, and classical mechanics is recovered [87, 88].

The role of non-classical paths becomes particularly evident in quantum tunneling phenomena [88]. Classically, a particle encountering a potential barrier with energy lower than the barrier height cannot access the forbidden region. However, quantum mechanically, the uncertainty principle allows configurations in which the particle explores regions that are classically inaccessible. In the path integral picture, tunneling arises from trajectories that traverse the forbidden region and contribute coherently to the transition amplitude. The finite tunneling probability thus emerges naturally from the sum over histories, without invoking any explicit modification of classical laws.

A defining structural feature of the path integral formalism is its reliance on classical Lagrangian mechanics as the starting point for quantization [88, 90]. Rather than introducing operator commutation relations as fundamental postulates, the formalism begins with the classical action functional and constructs quantum amplitudes by summing over histories weighted by that action. This approach is particularly advantageous for systems with constraints or nontrivial configuration spaces, where canonical quantization may be ambiguous. It also provides a natural route to the quantization of fields [94, 95], in which the dynamical variables are continuous functions of space and time.

The principal strength of the path integral formalism emerges in the description of systems with many degrees of freedom. In quantum field theory and quantum statistical physics, operator-based approaches often become cumbersome, whereas the path integral formulation offers a unified and flexible framework [79, 82]. Physical observables are expressed as expectation values, that is, statistical averages over ensembles of paths or configurations, closely paralleling the structure of classical statistical mechanics.

A crucial step in connecting quantum dynamics with statistical physics is the introduction of imaginary time [79, 86, 88, 89]. The unitary time-evolution operator,

$$U(t) = \exp\left(-\frac{\mathrm{i}}{\hbar}Ht\right) ,$$

describes the evolution of a system described by a Hamiltonian H in real time t. The path integral representation of evolution operator in real time suffers from highly oscillatory character due to the imaginary part in the exponent. This imaginary (or complex) nature of the exponent makes both the analytic and numerical evaluation of the transition amplitudes quite problematic. By performing the Wick rotation $t \to -\mathrm{i}\tau$, one obtains an evolution operator in imaginary time,

$$U(t) = \exp\left(-\frac{1}{\hbar}H\tau\right) ,$$

which closely resembles the statistical operator of equilibrium quantum mechanics $\exp(-\beta H)$, where $\beta = 1/\mathrm{k_B}T$ is the inverse temperature [96]. This correspondence allows the path integral formulation

to be applied directly to the quantum partition function $Z = \mathrm{Tr}\exp(-\beta H)$, with the Euclidean action S_E replacing the real-time action and serving as a weighting factor for each configuration [86, 88, 89]. In the zero-temperature limit $\beta \to \infty$, the statistical operator projects on the ground state of the system, establishing a direct connection between imaginary-time evolution and the properties of the ground state of the system [82, 86]. This correspondence is of particular importance in low-energy quantum systems, where ground-state correlations dominate the physical behavior.

In the remainder of this chapter, the focus is on the explicit construction of the path-integral representation of the quantum transition amplitude for a general single-particle Hamiltonian of the form $H = p^2/2m + V$, as well as the path integral formulation of the many-body partition function. The presentation largely follows the exposition of Altland and Simons [79], with notation and emphasis adapted to the present context. Complementary treatments of path-integral methods can be found in Refs. [86–88].

2.4.1 Derivation of the path integral from the quantum transition amplitude

The time evolution of an autonomous quantum system is described by the time-dependent Schrödinger equation [97]:

$$\mathrm{i}\hbar\frac{\partial}{\partial t}|\Psi(t)\rangle = H|\Psi(t)\rangle \ , \tag{2.124}$$

where $|\Psi(t)\rangle$ denotes the system's wave function and H is the (time-independent) Hamiltonian. A formal solution of this equation over a finite time interval defines the time-evolution operator $U(t', t)$ through [79, 93, 97]

$$|\Psi(t')\rangle = U(t', t)|\Psi(t)\rangle \ , \qquad U(t', t) = \exp\left(-\frac{\mathrm{i}}{\hbar}H(t' - t)\right)\Theta(t' - t) \ . \tag{2.125}$$

The unitary operator $U(t', t)$ describes the dynamical evolution of the system from time t to t'. The inclusion of the Heaviside step function $\Theta(t' - t)$ emphasizes forward time evolution with $t' > t$.

For a single-particle system governed by the Hamiltonian H, the particle may evolve from a position eigenstate $|q\rangle$ at time t to another position eigenstate $|q'\rangle$ at time t'. The probability amplitude for this transition is given by the matrix element of the evolution operator $\langle q'|U(t', t)|q\rangle = \langle q'|\mathrm{e}^{\left(-\frac{\mathrm{i}}{\hbar}H(t'-t)\right)}|q\rangle$, which is commonly referred to as the propagator of the system [90].

The central idea behind Feynman's path integral approach is to simplify the calculation of the propagator by first considering an infinitesimally small time interval Δt, rather than attempting to evaluate the propagator over a finite time interval directly [90, 93]. Such a direct calculation can be highly nontrivial, depending on the form of the Hamiltonian. Introducing a sufficiently small time step Δt in the exponential of the evolution operator enables the use of series expansions and perturbative approaches. To extend this idea to a general propagation time, the total time interval is divided into N equal slices, $t = N\Delta t$. For simplicity, the notation t is used to denote the time interval $t' - t$, since only the duration of the interval is relevant. In the limit $N \to \infty$, the continuum description of time is restored. With this time slicing, the evolution operator can be written as [90]

$$\mathrm{e}^{-\mathrm{i}Ht/\hbar} = \left(\mathrm{e}^{-\mathrm{i}H\Delta t/\hbar}\right)^N \ . \tag{2.126}$$

The introduction of a small time step is particularly useful for Hamiltonians of the simple but general form [88, 90]

$$H = \frac{p^2}{2m} + V(q) \ , \tag{2.127}$$

which consist of a kinetic and a potential energy term. For a Hamiltonian of this form and a sufficiently small time step Δt, the short-time evolution operator can be factorized as

$$\mathrm{e}^{-\mathrm{i}H\Delta t/\hbar} \simeq \mathrm{e}^{-\mathrm{i}p^2\Delta t/2m\hbar}\mathrm{e}^{-\mathrm{i}V(q)\Delta t/\hbar} + O(\Delta t^2) \ . \tag{2.128}$$

This factorization follows from the Baker-Campbell-Hausdorff formula [86, 88, 90]. The higher-order commutator terms that involve $\left[p^2, V(q)\right]$ can be neglected, since they contribute only on the order of $(\Delta t)^2$. This factorization of the short-time evolution operator allows the kinetic and potential energy operators to act independently on their respective eigenstates. The full evolution operator over a finite time interval may be expressed as a product of short-time evolution operators.

The corresponding transition amplitude can be expressed as

$$\langle q_f| \left(\mathrm{e}^{-\mathrm{i}H\Delta t/\hbar}\right)^N |q_i\rangle = \langle q_f|(I_q I_p)\mathrm{e}^{-\mathrm{i}H\Delta t/\hbar}(I_q I_p)\ldots(I_q I_p)\mathrm{e}^{-\mathrm{i}H\Delta t/\hbar}|q_i\rangle \ , \tag{2.129}$$

where $|q_i\rangle$ and $|q_f\rangle$ denote the initial and final position eigenstates, respectively. Here, resolutions of the identity in terms of position and momentum eigenstates [90], defined as

$$I_q = \int \mathrm{d}q_n |q_n\rangle\langle q_n|, \qquad I_p = \int \mathrm{d}p_n |p_n\rangle\langle p_n|, \tag{2.130}$$

have been inserted before each short-time evolution operator in the product. The index $n = 1, \ldots, N$ labels the intermediate time slices, with equalities $q_i \equiv q_0$ and $q_f \equiv q_N$.

Employing the standard dyadic product of position and momentum eigenstates

$$\langle q|p\rangle = \langle p|q\rangle^* = \frac{1}{\sqrt{2\pi\hbar}}\mathrm{e}^{\mathrm{i}qp/\hbar} \ , \tag{2.131}$$

together with the short-time factorization of the evolution operator given in Eq. (2.128), the transition amplitude can be written in the form

$$\langle q_f|\mathrm{e}^{-\mathrm{i}Ht/\hbar}|q_i\rangle \simeq \int \prod_{n=1}^{N-1} \mathrm{d}q_n \prod_{n=1}^{N} \frac{\mathrm{d}p_n}{2\pi\hbar} \exp\left[-\mathrm{i}\frac{\Delta t}{\hbar}\sum_{n=0}^{N-1}\left(V(q_n) + \frac{{p_{n+1}}^2}{2m} - p_{n+1}\frac{q_{n+1}-q_n}{\Delta t}\right)\right] \ . \tag{2.132}$$

In this representation, the propagator is expressed as a $(2N-1)$-dimensional integral over discrete phase space variables (q_n, p_n) [79, 88, 90]. The discretization of time, $\Delta t = t/N$, induces a corresponding discretization of a path in phase space. To describe the propagator in terms of continuous paths, the continuum limit $N \to \infty$ is taken [79, 86, 88]. In this limit, the discrete set of phase-space points (q_n, p_n) approaches a smooth curve $Q(t) \equiv (q(t), p(t))$.

Accordingly, sums over discrete time slices become integrals, and finite differences become time derivatives,

$$\Delta t \sum_{n=0}^{N-1} \to \int_0^t \mathrm{d}t' \ , \qquad \frac{q_{n+1}-q_n}{\Delta t} \to \partial_t q(t) \equiv \dot{q}(t) \ . \tag{2.133}$$

The terms in the exponent corresponding to the kinetic and potential energies combine into the classic Hamiltonian $H(p,q) = (p(t))^2/2m + V(q(t))$, which is now a functional of the phase-space variables $q(t)$ and $p(t)$.

In the continuum limit, this motivates the definition of the functional integration measure as [79, 86, 94]

$$\lim_{N\to\infty} \int \prod_{n=1}^{N-1} \mathrm{d}q_n \prod_{n=1}^{N} \frac{\mathrm{d}p_n}{2\pi\hbar} \to \int_{q(0)=q_i}^{q(t)=q_f} \mathrm{D}q\mathrm{D}p = \int_{q(0)=q_i}^{q(t)=q_f} \mathrm{D}Q \ . \tag{2.134}$$

Summarizing these results yields the Hamiltonian form of the path integral representation of the propagator [79, 88, 90],

$$\langle q_f|\mathrm{e}^{-\mathrm{i}Ht/\hbar}|q_i\rangle = \int_{q_i=q(0)}^{q_f=q(t)} \mathrm{D}Q \, \exp\left[\frac{\mathrm{i}}{\hbar}\int_0^t \mathrm{d}t' \, (p\dot{q} - H(p,q))\right] \ . \tag{2.135}$$

The functional integration extends over all phase-space paths that begin at q_i and end at q_f. Each path contributes with a weight determined by the exponential of the classical action. The classical action is defined as the time integral of the Lagrangian [90, 93],

$$S(p,q) = \int_0^t \mathrm{d}t'\, L(p,q) = \int_0^t \mathrm{d}t'\, \left(p\dot{q} - H(p,q)\right) . \tag{2.136}$$

In this way, the path integral formulation of the quantum transition amplitude is expressed directly in terms of classical phase-space variables, providing a natural bridge to classical mechanics.

For the class of Hamiltonians considered here, where the kinetic and potential energy terms are separated and the potential $V(q)$ is independent of the momentum, the momentum integration can be performed explicitly. In this case, the propagator can be written as

$$\langle q_f|\mathrm{e}^{-\mathrm{i}Ht/\hbar}|q_i\rangle = \int_{q_i=q(0)}^{q_f=q(t)} \mathrm{D}q\; \mathrm{e}^{-\frac{\mathrm{i}}{\hbar}\int_0^t \mathrm{d}t'\, V(q)} \int \mathrm{D}p\, \exp\left[-\frac{\mathrm{i}}{\hbar}\int_0^t \mathrm{d}t' \left(\frac{p^2}{2m} - p\dot{q})\right)\right] . \tag{2.137}$$

Since the Hamiltonian is quadratic in the momentum, the integral over the momentum variables is of Gaussian form and can be calculated straightforwardly [86, 90]. Upon performing the momentum integration, the phase-space path integral reduces to a coordinate-space path integral, and the transition amplitude may be written as

$$\langle q_f|\mathrm{e}^{-\mathrm{i}Ht/\hbar}|q_i\rangle = \int_{q(0)=q_i}^{q(t)=q_f} \mathrm{D}q\, \exp\left[\frac{\mathrm{i}}{\hbar}\int_0^t \mathrm{d}t' L(q,\dot{q})\right] , \tag{2.138}$$

where the Lagrangian is given by

$$L(q,\dot{q}) = \frac{m\dot{q}^2}{2} - V(q) . \tag{2.139}$$

This expression defines the path integral as an infinite-dimensional integral over trajectories in coordinate space that connect the initial position q_i to the final position q_f within the time interval t, with each trajectory weighted by the exponential of the classical action [86, 88]. The resulting numerical factors arising from momentum integration are absorbed into the constant included in the formal functional integration measure $\mathrm{D}q$. Such constants are typically irrelevant for normalized transition amplitudes and expectation values, where they cancel by construction. The evaluation of integrals of Gaussian type, such as the one appearing in Eq. (2.137), will be addressed in a subsequent subsection, after introducing the path integral representation of the quantum partition function.

2.4.2 Path-integral representation of quantum partition function

In quantum statistical physics, the partition function plays a central role, as it provides direct access to all equilibrium thermodynamic properties of a system [82, 86]. Fundamental physical quantities such as internal energy, free energy, entropy, and correlation functions can be obtained from appropriate derivatives of the partition function. In the context of interacting many-body systems, it serves as the primary object from which the collective and emergent behavior arises.

The canonical partition function of a quantum system is defined as the trace of the statistical operator [82, 86]

$$Z = \mathrm{Tr}\left(\mathrm{e}^{-\beta H}\right) , \tag{2.140}$$

where $\beta = 1/(\mathrm{k_B}T)$ is the inverse temperature and H is the Hamiltonian of the system. The trace is taken over the full Hilbert space of the system, and any complete set of basis states can be chosen to evaluate it.

For quantum many-body systems, a natural choice of basis is the set of coordinate eigenstates $\{|q_n\rangle\}$, where state q_n denotes the configuration of the n-th degree of freedom [86, 88, 90]. In this representation, the partition function can be written as

$$Z = \sum_n \int \mathrm{d}q_n \langle q_n | \mathrm{e}^{-\beta H} | q_n \rangle. \tag{2.141}$$

The construction of a path-integral representation of the partition function closely parallels the derivation of the quantum transition amplitude discussed in the previous section [88, 90]. In both cases, the central object is a matrix element of the exponential operator, either the time-evolution operator $\exp(-\mathrm{i}tH)$ or the statistical operator $\exp(-\beta H)$. The essential difference lies in the nature of the exponent. Whereas real-time evolution involves a purely imaginary exponent, the statistical operator is governed by a real and negative exponent.

This distinction has important mathematical and practical consequences. In real time, the path integral is weighted by an oscillatory phase factor of the form $\mathrm{e}^{\mathrm{i}S/\hbar}$, where S is the classical action. Such oscillatory integrals are not absolutely convergent and are therefore mathematically ill-defined without additional prescriptions [86, 88]. Their highly oscillatory nature also poses severe difficulties for numerical evaluation.

A standard procedure to overcome these issues is the Wick-rotation from real to imaginary time [79, 88, 98], defined by the transformation

$$t \to -\mathrm{i}\tau \ , \qquad (\tau \in \mathbb{R}), \tag{2.142}$$

which may be interpreted as a rotation by $\pi/2$ in the complex time plane. Under this transformation, the oscillatory phase factor $\exp(\mathrm{i}S/\hbar)$ is replaced by a real damping factor $\mathrm{e}^{-S_E/\hbar}$, where S_E is the Euclidean action [86, 90]. For a single-particle system with the Hamiltonian $H = p^2/(2m) + V(q)$, the Euclidean action takes the form [86, 88]

$$S_E = \int \mathrm{d}\tau \ \left(m\dot{q}^2/2 + V(q) \right) \ . \tag{2.143}$$

Compared to the real-time action, the potential energy term enters with the opposite sign. The resulting path integral is well defined and convergent, making it suitable for both analytical treatment and numerical evaluation. Real-time quantities can subsequently be recovered by analytic continuation from imaginary to real time.

The connection between imaginary time evolution and statistical mechanics becomes explicit by identifying the total extent of imaginary time with the inverse temperature according to $\tau = \beta\hbar$ [79, 82, 90]. With this identification, the statistical operator $\exp(-\beta H)$ may be interpreted as an evolution operator in imaginary time over an interval of length $\beta\hbar$ [82, 86, 94]. The matrix element $\langle q_n | \mathrm{e}^{-\beta H} | q_n \rangle$ therefore corresponds to an imaginary-time propagator that begins and ends in the same configuration.

Taking the trace over all states enforces this identification of initial and final configurations and naturally leads to periodic boundary conditions in imaginary time, $q(0) = q(\beta)$. The partition function can therefore be expressed in path-integral form as [86, 88, 90]

$$Z = \sum_n \int_{q(0)=q(\beta\hbar)} \mathrm{D}q \mathrm{e}^{-S_E[q]/\hbar} \ , \tag{2.144}$$

where the Euclidean action is given by

$$S_E = \sum_n \int_0^{\beta\hbar} \mathrm{d}\tau \ \left(\frac{m}{2} (\dot{q}_n)^2 + V(q_n) \right) \ . \tag{2.145}$$

In this representation, the quantum partition function is expressed as an integral over closed trajectories in coordinate space, with each path weighted by the exponential of the Euclidean action [82, 88].

This formulation establishes a direct and transparent connection between quantum statistical mechanics and the path-integral formalism. It provides a natural framework for the description of interacting many-body systems and forms the basis for both analytical approximations and numerical methods [82, 86]. In later sections, this formalism will be specialized to the Holstein Hamiltonian, with particular emphasis on discretized path-integral techniques relevant for numerical applications.

2.4.3 Gaussian integrals

Gaussian integrals play a central role as a technical tool in the evaluation of path integrals in quantum and statistical physics [86, 94]. They arise whenever the exponent contains a quadratic form, which occurs naturally in the action functionals underlying the path-integral formulation. As already encountered in the derivation of the path-integral representations of the quantum transition amplitude and the partition function for Hamiltoninans of the form $H = p^2/2m + V(q)$, the momentum-dependent contributions typically appear as quadratic terms. More generally, Gaussian structures characterize non-interacting theories, harmonic approximations to interacting systems, and fluctuations around classical or mean-field solutions [82, 88]. For these reasons, Gaussian integrals constitute a fundamental building block of the path-integral formalism.

The simplest Gaussian integral is of the form [79, 86, 94]

$$\int_{-\infty}^{\infty} \mathrm{d}x\ \mathrm{e}^{-ax^2} = \sqrt{\frac{\pi}{a}}\ , \tag{2.146}$$

where x is a real variable and $a > 0$ is a real positive constant. This result generalizes straightforwardly to a quadratic form with linear terms $-ax^2 + bx + c$,

$$\int_{-\infty}^{\infty} \mathrm{d}x\ \exp\left(-ax^2 + bx + c\right) = \sqrt{\frac{\pi}{a}}\exp\left(\frac{b^2}{4a} + c\right)\ , \tag{2.147}$$

where $a > 0$ and b and c are real parameters. This expression is obtained by completing the square in the exponent [79, 86]. Quadratic forms of this type commonly arise when external sources or constraints are introduced to the system.

Another family of integrals that frequently appears is the one that involves the polynomial factor next to the exponential. This type of integrals can be generated by the differentiation with respect to auxiliary parameters in Gaussian exponent. For example, integrals of the form

$$\int_{-\infty}^{\infty} \mathrm{d}x\ x^{2n}\mathrm{e}^{-ax^2} \tag{2.148}$$

can be obtained by differentiation of the basic Gaussian integral given in Eq. (2.146) with respect to the parameter a [79, 88]. This property is widely used in perturbative expansions and in the computation of correlation functions [82, 94]. Due to symmetry of the integrand, only integrals with even powers of x evaluate as non-zero.

Gaussian integrals over complex variables are equally important in quantum and statistical field theories [79, 86, 94]. Let $z = x + \mathrm{i}y$ be a complex variable and let w be a complex number with $\mathrm{Re}(w) > 0$. The complex Gaussian integral then evaluates

$$\int \mathrm{d}(z^*, z)\mathrm{e}^{-z^*wz} = \frac{\pi}{w}\ , \tag{2.149}$$

where $z^* = x - \mathrm{i}y$ and the integration measure is defined as $\mathrm{d}(z^*, z) = \mathrm{d}x\mathrm{d}y$. Under this parameterization, the quadratic form reduces to $w(x^2 + y^2)$, and the complex Gaussian integral becomes equivalent

to a two-dimensional real Gaussian integral. Including linear source terms yields

$$\int \mathrm{d}(z^*, z)\mathrm{e}^{-z^*wz+u^*z+z^*v} = \frac{\pi}{w}\exp\left(\frac{u^*v}{w}\right) , \tag{2.150}$$

where u and v are, in general, independent complex numbers and $\mathrm{Re}(w) > 0$ ensures convergence.

These results generalize naturally to multivariate Gaussian integrals [79, 82, 86]. For a set of N real variables collected in a vector $\mathbf{v} = (v_1, v_2, \ldots, v_N)^T$ and a real, symmetric, positive-definite matrix A, the N-dimensional Gaussian integral is given by

$$\int \mathrm{d}^N v \, \exp\left(-\frac{1}{2}\mathbf{v}^T\mathbf{A}\mathbf{v} + \mathbf{j}^T\mathbf{v}\right) = \frac{(2\pi)^{N/2}}{\sqrt{\mathrm{det}\mathbf{A}}}\exp\left(\frac{1}{2}\mathbf{j}^T\mathbf{A}^{-1}\mathbf{j}\right) , \tag{2.151}$$

where $\mathbf{j}$ is arbitrary N-component source vector. The appearance of the determinant $\mathrm{det}\mathbf{A}$ follows from the diagonalization of the quadratic form. Since $\mathbf{A}$ is real and symmetric, it can be decomposed as $\mathbf{A} = \mathbf{O}^T\mathbf{D}\mathbf{O}$, where $\mathbf{O}$ is an orthogonal matrix, and $\mathbf{D}$ is diagonal with positive elements [94]. A change in variables $\mathbf{v}' = \mathbf{O}\mathbf{v}$ reduces the integral to a product of N independent one-dimensional Gaussian integrals, producing the stated result.

The formula given in Eq. (2.151) serves as a generating functional for correlation functions [82, 86]. By differentiating with respect to the components of the source vector j_i, one obtains expectation values, for example $\langle v_i v_k\rangle = A^{-1}_{i,k}$. Interpreting the Gaussian weight as a probability distribution, these expectation values are given by

$$\langle \ldots \rangle = \frac{\mathrm{det}\mathbf{A}^{1/2}}{(2\pi)^{N/2}} \int \mathrm{d}\mathbf{v} \; \mathrm{e}^{-\frac{1}{2}\mathbf{v}^T\mathbf{A}\mathbf{v}}(\ldots) \; . \tag{2.152}$$

By differentiating the generating functional $2n$ times with respect to the source vector $\mathbf{j}$, one obtains higher-order correlation functions, which directly leads to Wick's theorem for bosonic fields [79, 86, 98]. Wick's theorem states that the expectation value of a product of $2n$ bosonic fields can be represented as a sum over all possible pairings into 2-point contractions, such as $\langle v_i v_k\rangle$. As an illustration, the four-point function $\langle v_m v_n v_p v_q\rangle$ can be computed from the multivariate Gaussian integral and yields $\langle v_m v_n v_p v_q\rangle = A^{-1}_{mn}A^{-1}_{pq} + A^{-1}_{mp}A^{-1}_{qn} + A^{-1}_{mq}A^{-1}_{np}$. Recognizing that each matrix element represents a corresponding contraction, this expression can equivalently be written as

$$\langle v_m v_n v_p v_q\rangle = \langle v_m v_n\rangle\langle v_p v_q\rangle + \langle v_m v_p\rangle\langle v_n v_q\rangle + \langle v_m v_q\rangle\langle v_n v_p\rangle,$$

which coincides precisely with the result given by Wick's theorem.

Multivariate Gaussian integrals can also be extended to include complex vectors and matrices [94]. If $\mathbf{v}$ is a complex N-component vector and $\mathbf{A}$ is a positive-definite Hermitian matrix, one obtains

$$\int \mathrm{d}(\mathbf{v}^\dagger\mathbf{v}) \; \mathrm{e}^{-\mathbf{v}^\dagger\mathbf{A}\mathbf{v}} = \pi^N \mathrm{det}\mathbf{A}^{-1} \; , \tag{2.153}$$

where $\mathbf{v}^\dagger$ denotes the Hermitian conjugate of $\mathbf{v}$. As in the real case, diagonalization of quadratic form by unitary transformation reduces the problem to a product of independent integrals. Gaussian integrals can also be generalized to certain non-Hermitian matrices, provided the quadratic form can be brought into diagonalizable form with convergent eigenvalues.

Finally, Gaussian integration extends to infinite-dimensional functional integrals, where the integration variables are continuous fields $\phi(x)$ [86, 88]. For a quadratic action, the functional Gaussian integral takes the formal form

$$\begin{aligned}\int \mathrm{D}\phi(x) \, \exp\left[-\frac{1}{2}\int \mathrm{d}x\mathrm{d}x' \; \phi(x)A(x,x')\phi(x') + \int \mathrm{d}x \; J(x)\phi(x)\right] \\ \propto (\mathrm{det}A)^{-1/2}\exp\left[\frac{1}{2}\int \mathrm{d}x\mathrm{d}x' \; J(x)A^{-1}(x,x')J(x')\right] ,\end{aligned} \tag{2.154}$$

where the inverse operator satisfies $\int \mathrm{d}x'\ A(x.x')A^{-1}(x', x") = \delta(x - x")$. The overall normalization factor is ommited, as it is divergent in the infinite-dimensional limit and cancels in normalized obsevrables [86]. This integral can be generalized to the case with complex fields and Hermitian operators. With this discussion, the use of the continuum limit in defining the path integral for the transition amplitude is validated, as is the momentum integration appearing in the final expression for the path integral. These functional integrals provide the basis for the path-integral formalism and for continuum field theories. However, in this thesis, the emphasis will be on finite-dimensional Gaussian integrals, reflecting the inherently discrete character of computational numerical methods.

2.5 Quantum Monte Carlo methods

The path-integral approach to studying quantum many-body systems naturally leads to the evaluation of extremely high-dimensional integrals. Upon discretization of the time or imaginary-time interval, the partition function or time-dependent correlation functions are expressed as integrals over configurations defined on the discretized time grid. The dimensionality of these integrals grows rapidly with the number of time slices and the number of degrees of freedom in the system. As a result, direct deterministic numerical evaluation of such integrals becomes computationally impractical as the discretization is refined. In this context, Monte Carlo stochastic integration techniques offer an efficient alterantive [99, 100].

The term *Monte Carlo* was introduced in the early 1940s at the Los Alamos Laboratory by Stanislaw Ulam, in collaboration with John von Neumann and others, in the context of nuclear physics calculations[101–103]. The name reflects the central role of randomness in the method and was inspired by games of chance. Although initially regarded primarily as a tool for obtaining approximate numerical estimates, Monte Carlo methods gained widespread acceptance with the advent of digital computing [99, 100] and have since become an essential computational technique in many areas of science. In physics, Monte Carlo methods are particularly valuable for the study of classical and quantum many-body systems, where high-dimensional integrals arise naturally.

The basic idea underlying Monte Carlo methods can be illustrated by a simple example. Consider a unit circle inscribed within a square of unit side length. The ratio of the area of the circle to that of the square is equal to $\pi/4$. By uniformly sampling points within the square and counting the fraction that fall inside the circle, this ratio, or equivalently the value of π, can be estimated statistically. As the number of sampled points increases, the estimate approaches the true value. Since the method is probabilistic in nature, the estimate is never exact for a finite number of samples. However, it can be made sufficiently accurate by increasing the sample size.

The value of a definite integral can be estimated in a similar way. Monte Carlo integration is primarily based on drawing random samples from the integration domain and then taking the average of the integrand's values at the sampled points. Unlike deterministic quadrature methods, which rely on structured grids and whose computational cost grows rapidly with the dimensionality of the integral, Monte Carlo integration employs probabilistic sampling and remains effective in high-dimensional settings. The trade-off associated with this probabilistic approach is the presence of an intrinsic statistical error in the estimator. Nevertheless, this statistical uncertainty is controllable as the Monte Carlo error decreases inversely with the square root of the number of samples [99, 100].

To make this discussion more explicit, consider a definite integral of a real-valued function $f(x)$ over a domain $x \in \Omega$,

$$I = \int_{\Omega} \mathrm{d}x\ f(x)\ . \tag{2.155}$$

The integrand can be written in the form $f(x) = P(x)f(x)P(x)^{-1} = P(x)F(x)$, where $P(x)$ is a non-negative function defined over a domain $\Omega_0 \supseteq \Omega$, normalized such that $\int_{\Omega_0} \mathrm{d}x\ P(x) = 1$. The

integral I can then be rewritten as

$$I = \int_\Omega \mathrm{d}x\ P(x)F(x) \equiv \langle F \rangle_P\ , \tag{2.156}$$

where $\langle \dots \rangle_P$ denotes an expectation value with respect to the probability density $P(x)$. To estimate the value of the integral I, a set of N random variables $\{x_i\} \in \Omega$ is sampled from the distribution $P(x)$ and the Monte Carlo estimator is defined as

$$I_N = \frac{1}{N} \sum_{i=1}^{N} F(x_i)\ . \tag{2.157}$$

If the expectation value of $F(x)$ with respect to the probability density $P(x)$ exists, the Monte Carlo estimator is unbiased, meaning that its expectation value satisfies $\langle I_N \rangle = I$. For any finite number of samples, a particular realization of the estimator fluctuates around the exact value and can therefore be written as $I_N = I + \epsilon$, where ϵ denotes the statistical error. The magnitude of these fluctuations is characterized by the variance of the estimator, defined as $\sigma^2 = \langle F^2 \rangle_P - \langle F \rangle_P^2$, whose square root σ is the standard deviation. For N statistically independent samples, the standard deviation of the estimator decreases as $\epsilon \sim \sigma/\sqrt{N}$, explicitly demonstrating how the statistical error decreases with increasing sample size [99, 100].

While increasing the number of samples reduces the statistical uncertainty, this approach is often computationally inefficient, particularly for high-dimensional integrals. A more effective strategy is to reduce the variance of the estimator itself, thereby achieving a desired accuracy with fewer samples. Since the variance depends explicitly on the choice of the probability density function, it can be minimized by selecting a sampling distribution that reflects the structure of the integrand. This principle, known as importance sampling, forms the basis of most practical Monte Carlo algorithms [99, 100].

All Monte Carlo evaluations are based on random number generation. To obtain reliable convergence and accurate statistical estimates, it is essential to use high-quality random samples. Standard programming environments provide random number generators for uniformly distributed random numbers in the interval $[0, 1]$, and often also include generators for specific distributions such as the normal distribution. It is important to note that all random numbers generated on a computer are pseudo-random, as truly random numbers arise only from inherently stochastic physical processes. Pseudo-random number generators produce sequences of random numbers based on an initial input known as the *seed*. Changing the seed results in a different sequence, while fixing it allows for reproducibility of numerical simulations [99, 100, 104].

Given a generator for uniformly distributed random numbers, samples from other distributions can be generated using various transformation techniques. In the simplest case, when the target distribution is specified by a continuous probability density function $f_Y(y)$, one may generate a uniformly distributed random variable $0 \leq x \leq 1$ with density $f_X(x)$ and define a deterministic mapping $y = y(x)$. If this mapping is known and invertible, the target distribution follows from the change of variables formula

$$f_Y(y) = f_X(x) \left| \frac{\mathrm{d}y}{\mathrm{d}x} \right|^{-1}\ . \tag{2.158}$$

In cases where the target distribution cannot be expressed analytically or Jacobian $|\mathrm{d}y/\mathrm{d}x|$ cannot be evaluated, alternative sampling methods are used. One such method is rejection sampling. The basic idea is to enclose the target distribution within a larger known distribution from which samples can be easily drawn. Random points are generated from this enclosing distribution and accepted if they fall under the curve of the target distribution and rejected otherwise. While conceptually simple, this method can be inefficient, particularly in high-dimensional spaces, as a large fraction of proposed samples may be rejected. Its efficiency improves when the enclosing distribution closely approximates the target distribution while remaining everywhere larger than it [99, 100, 104].

In many physical applications, however, the optimal sampling distribution is not known a priori or cannot be sampled from directly. In such cases, sample configurations are generated using Markov Chain Monte Carlo methods, in which a sequence of correlated samples is constructed to reproduce the desired probability distribution. The most widely used algorithm in this class is the Metropolis acceptance-rejection method, which provides an efficient and general procedure for importance sampling without requiring explicit knowledge of the normalization constant of the target distribution function [99–101, 105].

The Metropolis algorithm generates configurations distributed according to a target probability density $P(X)$ defined over a configuration space of dimension d. Starting from an initial configuration point $X \equiv \{x_i\} = (x_1, x_2, \ldots, x_d)$, a trial configuration $X' \equiv \{x_i'\}$ is proposed by introducing a small change to one or more components of X. The new proposed configuration X' is accepted with probability

$$r = \min\left(1, \frac{P(X')}{P(X)}\right) . \tag{2.159}$$

If $P(X') > P(X)$, the new configuration is accepted with probability one. Otherwise, it is accepted with probability equal to $P(X')/P(X)$. In practice, this acceptance rule is implemented by drawing a random number n uniformly from the interval $[0, 1]$. The proposed move is accepted if $n < r$. If this condition is not met, the move is rejected, and the system remains in its original configuration [99–101].

This acceptance probability follows from the requirement of detailed balance with respect to the target distribution $P(X)$, under the assumption that the proposal probabilities for moves $X \to X'$ and $X' \to X$ are symmetric. Provided that the proposal moves are ergodic, the resulting Markov chain converges to the stationary distribution $P(X)$ independently of the initial configuration [99–101].

Because successive configurations are generated by local updates, the samples produced by the Metropolis algorithm are generally correlated. These correlations are particularly strong during the initial stages of the simulation, when the system has not yet equilibrated. Furthermore, the arbitrary choice of the initial configuration may cause early samples to deviate significantly from the target distribution. To mitigate these effects, it is standard practice to discard an initial portion of the Markov chain, referred to as the thermalization or "warm up" period, during which the algorithm is allowed to reach equilibrium [99, 100].

To reduce correlations between sampled configurations, one may retain only every n-th configuration generated by the algorithm, discarding the intermediate ones. Although this increases the total number of Monte Carlo steps required for a given number of effective samples, it improves the statistical independence of the data. As a result, the Metropolis algorithm typically constitutes the most computationally demanding part of a Monte Carlo simulation. Nevertheless, it remains highly efficient and well suited to many problems in physics, where the stochastic dynamics of the algorithm naturally mirrors the behavior of the underlying physical system [99, 100, 105].

Convergence of a Monte Carlo simulation is an essential prerequisite for obtaining reliable and physically meaningful results. In practice, convergence tests are performed by examining the behavior of measured observables as functions of Monte Carlo time and by comparing results obtained using different thermalization lengths, sampling intervals, and total numbers of samples [99, 100, 105].

The general framework of Monte Carlo sampling can be applied directly to the discretized paths introduced in the path-integral formulation. In this approach, each path represents a configuration of the system along the real or imaginary-time axis, and the probability weight of a configuration is determined by the corresponding action functional. The resulting Path Integral Monte Carlo (PIMC) method allows for efficient stochastic evaluation of quantum statistical averages in high-dimensional configuration spaces [58, 106, 107].

2.5.1 Path integral Monte Carlo

In the path-integral formulation introduced in the previous section, quantum partition functions and correlation functions are expressed as sums or integrals over discretized trajectories defined on a time or imaginary-time grid. Upon discretization into N time slices, a configuration X corresponds to a specific realization of the system variables on each time slice, collectively defining a discretized path. Each configuration is assigned a statistical weight proportional to $\exp(-S[X])$, where $S[X]$ is the action associated with the path [58, 106, 107]. Monte Carlo algorithms generate configurations distributed according to this weight, allowing the stochastic evaluation of otherwise intractable high-dimensional integrals.

Physical observables are evaluated as ensemble averages over sampled configurations. For an observable O defined on the discretized path, its expectation value is given as

$$\langle O \rangle = \frac{1}{Z} \sum_{\{x\}} O(\{x\}) \mathrm{e}^{-S[\{x\}]} \approx \frac{1}{N_s} \sum_{i=1}^{N_s} O(X_i) \ ,$$

where the right-hand side represents the Monte Carlo estimator, X_i is a configuration generated by the Monte Carlo simulation, and N_s is the total number of sampled paths. This thesis focuses particularly on time correlation functions

$$C(t) = \langle A(t)A(0) \rangle = \frac{1}{Z} \mathrm{Tr} \left[\mathrm{e}^{-\beta H} \mathrm{e}^{\mathrm{i}tH} A(0) \mathrm{e}^{-\mathrm{i}tH} A(0) \right] \ , \tag{2.160}$$

where the trace is expanded in a complete basis. The choice of basis determines the form of the action functional and influences the optimal sampling distribution for the correlation function. As discussed previously, the real time variable can be transformed to imaginary time via $t \rightarrow -\mathrm{i}\tau$, yielding the corresponding imaginary-time correlation function. Imaginary-time correlation function can then be analytically continued to real-time or real-frequency quantities [59, 108]. This illustrates how path-integral Monte Carlo allows direct computation of quantum correlation functions in high-dimensional systems, including many-body polaron models [66, 109].

A schematic of the path-integral Monte Carlo algorithm, widely used in the literature and relevant to this work, proceeds as follows. A path configuration X_0 is initialized. At each Monte Carlo step, a trial move X' is proposed by introducing a local modification to one or more time slices of the current path. The corresponding change in action, $\Delta S = S[X'] - S[X]$, is evaluated, and the trial configuration is accepted with probability $\min(1, \mathrm{e}^{-\Delta S})$. This ensures the convergence of the Markov chain to the stationary distribution defined by the path-integral weight [57, 109]. Because successive configurations generated in this manner are generally correlated, an initial thermalization period is discarded and the observables $O(X)$ are sampled at selected intervals to reduce the correlations between successive configurations. This process is repeated until a sufficient number of statistically independent samples have been collected to estimate expectation values with the desired accuracy. In practice, the efficiency of the Metropolis algorithm can be reduced if the Markov chain becomes trapped in local minima of configuration space, resulting in poor phase space exploration, long autocorrelation times and significantly biased estimates even for long simulation times.

While the Metropolis acceptance-rejection algorithm is widely used method in path-integral Monte Carlo simulations, it is not the only approach. Depending on the system under study and the desired efficiency, alternative path sampling strategies can be employed. These include multi-level or bisection moves [58], staging and normal-mode updates [106], worm algorithms [107], and continuous-time formulations [68], among others. Each method is designed to efficiently explore the path configuration space while respecting the statistical weights defined by the action, and can be combined with importance sampling or other variance-reduction techniques. The choice of algorithm often depends on the dimensionality of the system, the nature of the interactions, and the observables of interest [57, 58, 68, 106, 107, 109].

Implementing path-integral Monte Carlo methods in practice requires careful attention to discretization errors and convergence. The number of time slices N must be sufficient to accurately approximate the continuous path integral. Convergence should be verified by testing the stability of sampled observables against the number of Monte Carlo steps, thermalization period, and sampling intervals. In many-body systems, the configuration space grows rapidly with system size, making importance sampling essential for efficient exploration of relevant paths [68, 110].

Path integral Monte Carlo has been successfully applied to a variety of condensed-matter systems, including lattice and continuum polarons, electrons coupled to phonon baths and strongly correlated lattice models [57–59, 66, 107–109]. Its combination of stochastic integration and path discretization provides a versatile framework that naturally extends to evaluating real-time correlation functions either directly or via analytic continuation, making it a central tool in the methodology employed in this thesis.

2.5.2 Dynamical sign problem

The Monte Carlo framework described previously relies fundamentally on the existence of a non-negative, normalizable weight that can be interpreted as a probability density. In imaginary-time Path Integral formulations, this requirement is typically satisfied, as the Euclidean action is real and the associated weight $\mathrm{e}^{-S[X]}$ is positive. This property underlies the success of Path Integral Monte Carlo methods for equilibrium and thermodynamic quantities[57, 58, 106].

The situation changes qualitatively when one considers real-time dynamics. Real-time correlation functions and dynamical observables are expressed in terms of path integrals weighted by the real-time action, leading to oscillatory integrands of the form

$$w[X] = \mathrm{e}^{\mathrm{i}S[X]} \ . \tag{2.161}$$

Since this weight is complex in general, it cannot be interpreted as a probability density and the direct application of standard Monte Carlo sampling methods is therefore not valid[68, 111].

A common formal workaround is to introduce a positive reference distribution by separating the magnitude and phase of the weight, $w[X] = |w[X]|\mathrm{e}^{\mathrm{i}\theta[X]}$[68, 111]. The expectation values of the observables may then be written as

$$\langle O \rangle = \frac{\langle O \ \mathrm{e}^{\mathrm{i}\theta} \rangle_{|w|}}{\langle \mathrm{e}^{\mathrm{i}\theta} \rangle_{|w|}} \ , \tag{2.162}$$

where $\langle \dots \rangle_{|w|}$ denotes an average with respect to the positive weight $|w[X]|$. While this reweighting restores a probabilistic sampling procedure, it introduces a severe numerical difficulty. The phase factor $\exp(\mathrm{i}\theta[X])$ exhibits strong fluctuations across configuration space, leading to extensive cancellations between sampled contributions[106].

This phenomenon is commonly reffered to as the dynamical sign problem or phase problem[68, 111]. In contrast to the fermionic sign problem encountered in equilibrium simulations[112], the dynamical sign problem is intrinsic to real-time evolution and arises irrespective of particle statistics. Its severity increases rapidly with the real time extent of the path integral as the accumulated phase fluctuations grow with propagation time leading to exponential growth of the variance of Monte Carlo estimators[68, 110, 113]. Achieving a fixed statistical accuracy therefore requires a number of samples that increases exponentially with the real-time propagation length. As a result, the real-time Monte Carlo simulations become impractical beyond relatively short time lengths.

Over the past decades, a variety of approaches have been proposed to mitigate the dynamical sign problem and to extend the accessible real-time regime. Early studies of real-time path-integral Monte Carlo already identified the exponential growth of statistical noise as a fundamental limitation of direct sampling schemes [57, 58, 68, 111].

Significant progress was achieved for quantum dissipative systems through the use of influence-functional techniques, where enviromental degrees of freedom are analytically integrated out, leading

to effective non-local actions with finite memory. These approaches allow controlled real-time simulations up to intermediate times by systematically truncating bath-induced correlations[107, 109, 113, 114].

Other strategies include reformulations of real-time correlation functions aimed at reducing phase cancellations, as well as stochastic sampling schemes with modified estimators [106, 110]. While such approaches can substantially improve convergence for specific models and parameter regimes, the statistical error in real-time Monte Carlo simulations generally continues to grow rapidly with propagation time. As a result, no universally applicable solution to the dynamical sign problem is currently known.

A widely adopted way to circumvent this difficulty is to avoid explicit real-time sampling altogether by formulating the problem in imaginary time and subsequently performing an analytic continuation to real frequencies or times[57, 106]. This approach eliminates the dynamical sign problem at the level of Monte Carlo sampling at the cost of introducing an ill-posed inversion problem. The principles and limitations of this strategy will be discussed in the following subsection.

2.5.3 Analytic continuation

As discussed in the previous subsection, direct Monte Carlo evaluation of real-time dynamical observables is severely limited by the dynamical sign problem. A widely adopted alternative strategy is therefore to reformulate the problem in imaginary time, where Path Integral Monte Carlo methods are well controlled, and to subsequently recover real-time or real-frequency information via analytic continuation [72, 75, 106].

In the imaginary-time formalism, dynamical correlation functions are defined along the imaginary-time axis $\tau \in [0, \beta]$, where $\beta = 1/(k_B T)$. Under transformation $t \to -i\tau$, the oscillatory real-time weight $e^{iS[X]}$ is converted into a non-negative real Euclidean weight $e^{-S[X]}$. As a result, imaginary-time correlation functions can be sampled efficiently using standard Monte Carlo techniques without encountering the dynamical sign problem [57, 106].

The connection between imaginary-time and real-time dynamics is established through analytic continuation. Formally, correlation functions defined in imaginary time correspond to values of an analytic function evaluated along the imaginary axis in the complex-time plane. Real-time or real-frequency observables are obtained by continuing this function to the real axis. In the frequency domain, this relation is usually formulated using integral transforms that link imaginary-time data to real-frequency spectral functions through specific kernels. Schematically, this relation may be written as

$$G(\tau) = \int_0^\infty \mathrm{d}\omega \; K(\tau, \omega) A(\omega) \; , \tag{2.163}$$

where $G(\tau)$ denotes the imaginary-time correlation function, $A(\omega)$ is the corresponding real-frequency spectral function, and $K(\tau, \omega)$ is a known kernel determined by the statistical ensemble and the definition of the observable. The problem of analytic continuation then amounts to reconstructing $A(\omega)$ from noisy and discretized data for $G(\tau)$. Owing to the structure of the integral transform,the kernel $K(\tau, \omega)$ acts as a smoothing operator that suppresses the high-frequency features of $A(\omega)$, so that the fine structures in the spectral function contribute only weakly to $G(\tau)$. As a result, their reconstruction is extremely sensitive to statistical noise and discretization errors [106, 115, 116]. In the absence of statistical noise and discretization, this correspondence is exact and uniquely defines the real-time dynamics.

In practice, however, Monte Carlo simulations provide correlation functions at a finite number of discrete points with statistical uncertainty. Analytic continuation then becomes an ill-posed inverse problem, in which small fluctuations in the input data can result in large variations in the continued function. A key aspect underlying this instability is the limited information content of the available data. For analytic continuation to be meaningful and stable, the known portion of the function must contain sufficient structure, in the sense that it exhibits significant variation relative to the extent of

the domain on which it is known. Data that are nearly featureless, slowly varying, or dominated by statistical noise carry little information about the analytic structure of the function and therefore provide only weak constraints on its continuation [75, 117].

From this perspective, the quality of an analytic continuation is not determined solely by the length of the imaginary-time interval or the number of sampled points, but rather by how sensitively the data reflect the underlying functional dependence. Correlation functions that display pronounced curvature, decay, or other nontrivial behavior in imaginary time impose stronger constraints on the continuation than those that are nearly linear or constant over the sampled range. Conversely, large statistical errors can obscure such features and further reduce the effective information content available for continuation.

While analytic continuation is often discussed in the context of purely imaginary-time data, the procedure is not fundamentally restricted to this case. More generally, analytic continuation may be performed from data known along contours in the complex-time plane, which may include combinations of imaginary and real time data [71, 118, 119]. In such formulations, additional information obtained away from the imaginary axis can, in principle, improve the conditioning of the continuation problem by providing stronger constraints on the analytic structure of the underlying function. However, in practice, acquiring reliable data at complex times is often challenging, and the benefits depend sensitively on the accuracy and coverage of the sampled domain.

A variety of numerical techniques have been developed to address the ill-posed nature of analytic continuation, each introducing regularization or additional constraints to stabilize the inversion. Maximum Entropy (MaxEnt) methods formulate analytic continuation as a Bayesian inference problem in which a spectral function is chosen to maximize the information entropy subject to consistency with the imaginary-time data. This approach incorporates prior knowledge such as positivity and sum rules and is among the most widely used and robust methods for spectra extraction, although it can sometimes oversmooth fine features of the spectrum [71–76, 120]. Padé approximants reconstruct the Green's function or correlation function by fitting a rational function (ratio of polynomials) to the imaginary-time or Matsubara data and analytically continuing this fit to real frequencies. When data are highly precise, Padé can capture sharper spectral structures, but it is particularly sensitive to statistical noise and can produce spurious poles, limiting its reliability for typical Monte Carlo results [73, 77, 116, 121]. Stochastic continuation techniques parametrize the spectral function using an ensemble of basis functions, such as delta functions, and sample this space using Monte Carlo or other statistical criteria, generating an average spectrum along with an uncertainty estimate. Such methods can resolve sharp features and provide explicit error quantification, but are more computationally intensive and require careful sampling strategies [122, 123].

The singular value decomposition (SVD) method provides a linear-algebraic approach to regularization. The Kernel matrix is decomposed into singular values and corresponding vectors. By discarding the contributions associated with small singular values that amplify noise, one obtains a regularized estimate of the spectral function. Schematically, this can be expressed as

$$G = \mathbf{K} \cdot \rho \quad \xrightarrow{\text{SVD: } \mathbf{K}=\mathbf{U}\mathbf{\Sigma}\mathbf{V}^T} \quad \rho_{\text{reg}} = \sum_i \frac{\mathbf{U}_i^T \cdot G}{\sigma_i} \mathbf{V}_i \ , \quad \sigma_i > \sigma_{\text{cut}} \ , \tag{2.164}$$

where vector G holds discretized imaginary time data, ρ is unknown spectral density and kernel matrix $\mathbf{K}$ is decomposed into orthogonal matrices $\mathbf{U}$ and $\mathbf{V}$ and diagonal matrix $\mathbf{\Sigma}$ whose entries are called singular values σ_i. The regularized spectral density ρ_{reg} is obtained by summing only over singular values larger than the cut-off σ_{cut}, effectively filtering out components that would otherwise amplify noise of data contained in G [66, 74, 115, 124, 125]. Among these methods, SVD provides a transparent and flexible regularization framework that will be exploited in the context of Kubo formula in the next chapter of this thesis.

More recent developments include Bayesian parametric analytic continuation, sparse modeling techniques, and machine-learning or neural-network approaches, which introduce alternative regularization strategies beyond classic MaxEnt or Padé methods [126–130]. Each technique has strengths

and limitations, depending on quality of the input data and the functional features of the underlying correlation function. Nevertheless, all these approaches illustrate the central challenge of analytic continuation which is balancing fidelity to noisy or incomplete input data with the stability and physical plausibility of the continued solution. The choice of continuation method and the handling of statistical noise are therefore crucial considerations in any practical implementation.

Chapter 3

Path-Integral Quantum Monte Carlo method for obtaining polaron mobility

The evaluation of charge transport properties in electron–phonon coupled systems requires a framework that connects microscopic dynamics with experimentally measurable quantities such as electrical conductivity and mobility. Within linear response theory (Sec. 2.2), these transport coefficients are expressed in terms of current–current correlation functions. In the present work, the microscopic description is provided by the Holstein model (Sec. 2.1), while the corresponding quantum statistical problem is formulated within the path-integral approach introduced in Sec. 2.4.

The central quantity of interest is the current–current correlation function, which encodes the transport properties of the system. In interacting electron–phonon systems, this quantity cannot generally be evaluated analytically, which requires the use of numerical methods. As discussed in Sec. 2.5.1, path-integral quantum Monte Carlo provides a numerically exact approach for computing such correlation functions at finite temperature. Here, this framework is extended to evaluate both real-time and imaginary-time correlation functions within a unified formalism, enabling access to dynamical properties relevant for charge transport. Based on this formulation, the current–current correlation function of the Holstein polaron is evaluated through stochastic sampling, and the corresponding carrier mobility is obtained either by direct integration or by analytic continuation.

The first step of this procedure is the construction of a path-integral representation of the current–current correlation function. This is achieved by expressing the quantum evolution operators in a discretized form using the Trotter–Suzuki decomposition, which allows the exponential of the Hamiltonian to be factorized into short-time propagators corresponding to its non-commuting components. Within this representation, two complementary formulations are considered, corresponding to the choice of basis for the electronic degrees of freedom: the electron momentum basis and the electron position basis. Although these formulations are formally equivalent, the choice of basis influences the statistical properties of the Monte Carlo sampling, leading to different levels of numerical efficiency and uncertainty.

The second step involves the extraction of transport coefficients from the computed correlation functions. In the present approach, both real-time and imaginary-time correlation functions are obtained. However, the accessible real-time interval is limited by the dynamical sign problem, which restricts the direct evaluation of long-time behavior of correlation functions. To address this limitation, the real-time data are complemented by imaginary-time data. The charge carrier mobility is then extracted from the combined real and imaginary correlation function data using an analytic continuation procedure. This procedure plays a central role in the methodology and is outlined in the main text, while its technical details are presented in Appendix B.

The numerical implementation is based on stochastic sampling of electron trajectories within the path-integral formalism. The Monte Carlo scheme used to evaluate the current–current correlation function was developed specifically for this work. Detailed aspects of the implementation, including the simulation algorithm and its numerical realization, are presented in Appendix C.

3.1 Path integral representation for current-current correlation functions

The starting point of the calculation is the current–current correlation function, defined as the thermal expectation value of the product of current operators evaluated at different times,

$$C(t) = \langle j(t)j(0)\rangle = Z^{-1}\mathrm{Tr}\left[\mathrm{e}^{-\beta H}\mathrm{e}^{\mathrm{i}Ht}j\mathrm{e}^{-\mathrm{i}Ht}j\right] , \tag{3.1}$$

where $Z = \mathrm{Tr}\,(\exp(-\beta H))$ is the partition function, $\beta = 1/T$ is the inverse temperature and

$$j(t) = \mathrm{e}^{\mathrm{i}Ht}j\mathrm{e}^{-\mathrm{i}Ht} , \tag{3.2}$$

denotes the current operator in the Heisenberg picture with $j(0) \equiv j$.

To obtain a representation suitable for numerical evaluation, this expression is reformulated within the path-integral framework by discretizing both imaginary- and real-time evolution. This is achieved using the Trotter–Suzuki decomposition [57, 131],

$$\mathrm{e}^{H_1+H_2+\cdots+H_P} = \lim_{n\to\infty}\left[\mathrm{e}^{H_1/n}\mathrm{e}^{H_2/n}\ldots\mathrm{e}^{H_P/n}\right]^n , \tag{3.3}$$

where H_p denote generally non-commuting contributions to the Hamiltonian. This decomposition allows the exponential of the Hamiltonian to be expressed as a product of short-time evolution operators.

The physical system considered consists of a single electron interacting locally with lattice vibrations and is described by the Holstein model. Throughout this chapter, a system of units is used in which the lattice constant a and the fundamental constants $\hbar$, e_0 and k_B are equal to unity, and periodic boundary conditions are assumed. In the presentation of results, energies are expressed in units of the electronic transfer integral J, which sets the natural energy scale of the problem.

The Holstein Hamiltonian, introduced in Sec. 2.1, is written as the sum of the electronic, phononic, and electron–phonon interaction contributions. In order to apply the Trotter–Suzuki decomposition, it is convenient to rewrite the Hamiltonian in a form that separates contributions according to their operator structure,

$$H = H_0 + H_1 + H_2, \tag{3.4a}$$

$$H_0 = \sum_n \frac{P_n^2}{2M}, \tag{3.4b}$$

$$H_1 = \sum_n \left(\sqrt{2M\omega_n}Gc_n^\dagger c_n X_n + \frac{1}{2}M\omega_n^2 X_n^2\right), \tag{3.4c}$$

$$H_2 = -J\sum_n \left(c_n^\dagger c_{n+1} + c_{n+1}^\dagger c_n\right). \tag{3.4d}$$

This representation enables efficient evaluation of the short-time propagators. Here, the index n runs from 0 to $N-1$, where N is the number of lattice sites. The parameter J denotes the electronic transfer integral between neighboring sites. The operators $c_n^\dagger$ (c_n) are electron creation and annihilation operators, while X_n and P_n are phonon position and momentum operators. The phonon frequency at site n is denoted by ω_n and M is the oscillator mass. The electron-phonon interaction strength is represented by constant G.

The term H_2 is diagonal in electron momentum representation and can be written as

$$H_2 = \sum_k \varepsilon(k)c_k^\dagger c_k , \tag{3.5}$$

where the bare electronic dispersion is given as $\varepsilon(k) = -2J\cos(k)$.

To discretize the problem, the imaginary-time interval of length β and the real-time interval of length t are divided into small slices. Using the Trotter–Suzuki decomposition, the correlation function is expressed as a trace over a sequence of short-time evolutions. This discretized formulation maps the quantum-mechanical problem onto a multidimensional integral over configurations defined along a contour consisting of imaginary and real time segments, which can be evaluated using Monte Carlo sampling.

3.1.1 Path integral with momentum representation for electrons

In order to construct the path-integral representation, a specific basis is chosen in which the short-time evolutions can be evaluated efficiently. In the present case, a mixed representation is used, consisting of electron momentum states and phonon states in the coordinate representation,

$$|q; \{X_n\}\rangle \equiv |q\rangle|\{X_n\}\rangle. \tag{3.6}$$

The electron momentum takes discrete values $q = 2n\pi/N$, while the phonon coordinates are continuous real variables $X_n \in \mathbb{R}$.

To obtain a form suitable for numerical evaluation of current-current correlation function given with Eq. (3.1), the imaginary-time interval β is divided into m subintervals, while the real-time interval t is divided into Q subintervals. The corresponding time steps are defined as $\tau = \beta/m$ and $\Delta t = t/Q$.

Applying the Trotter–Suzuki decomposition to the correlation function, the trace can be expressed as

$$\langle j(t)j\rangle = \lim_{m,Q\to\infty} Z_m^{-1} Tr\left[\left(e^{-\tau H_0}e^{-\tau H_1}e^{-\tau H_2}\right)^m \left(e^{i\Delta t H_0}e^{i\Delta t H_1}e^{i\Delta t H_2}\right)^Q j \left(e^{-i\Delta t H_0}e^{-i\Delta t H_1}e^{-i\Delta t H_2}\right)^Q j\right], \tag{3.7}$$

where $\lim_{m\to\infty} Z_m = Z$.

In this representation, the correlation function is expressed as a product of short-time evolution operators, which enables the subsequent insertion of resolutions of identity in the chosen basis and the construction of the path-integral formulation

The trace of an operator O and the completeness relation in the basis defined in Eq. (3.6) are given by

$$Tr(O) = \sum_{q\in BZ} \int \left(\prod_{n=0}^{N-1} dX_n\right) \langle\{X_n\}; q|O|q; \{X_n\}\rangle, \tag{3.8a}$$

$$1 = \sum_{q\in BZ} \int \left(\prod_{n=0}^{N-1} dX_n\right) |q; \{X_n\}\rangle\langle\{X_n\}; q|. \tag{3.8b}$$

The trace from expression (3.7) from now on will be denoted with $C_{jj}^{m,Q}$. By using Eq. (3.8a) it can be written as

$$C_{jj}^{m,Q} = \sum_{q\in BZ} \int \left(\prod_{n=0}^{N-1} dX_n^0\right) \langle\{X_n^0\}; q_0| \left(\rho(-\tau)\right)^m \left(\rho(i\Delta t)\right)^Q j \left(\rho(-i\Delta t)\right)^Q j|q_0; \{X_n^0\}\rangle, \tag{3.9}$$

where the introduction of index "0" on electron momentum and phonon coordinate variables will be clarified in following text. The shorthand notation was introduced for exponential operators

$$\rho(z) = e^{zH_0}e^{zH_1}e^{zH_2}, \tag{3.10}$$

where $z = -\tau, -i\Delta t, i\Delta t$ is the complex time variable .

For notational convenience, the phonon coordinates and integration measure are denoted as

$$\{X_n^i\} \to X^i,$$

$$\prod_{n=0}^{N-1} \mathrm{d}X_n^i \to \mathrm{D}X^i.$$

To evaluate the trace, resolutions of identity given in Eq. (3.8b) are inserted between all operators $\rho(z)$ and j. This procedure introduces independent integration variables at each time slice and transforms the trace into a multidimensional sum and integral over all intermediate configurations. As a result, the correlation function takes the form

$$\begin{aligned} C_{jj}^{m,Q} = \sum_{q_0,\ldots,q_{m+2Q+1}} \int \prod_{i=0}^{m-1} \mathrm{D}X^i \prod_{p=m}^{m+Q} \mathrm{D}X^p \prod_{l=m+Q+1}^{m+2Q+1} \mathrm{D}X^l \left(\prod_{i=0}^{m-1} \langle X^i; q_i | \rho(-\tau) | q_{i+1}; X^{i+1} \rangle \right) \\ \left(\prod_{p=m}^{m+Q-1} \langle X^p; q_p | \rho(\mathrm{i}\Delta t) | q_{p+1}; X^{p+1} \rangle \right) \langle X^{m+Q}; q_{m+Q} | j | q_{m+Q+1}; X^{m+Q+1} \rangle \\ \left(\prod_{l=m+Q+1}^{m+2Q} \langle X^l; q_l | \rho(-\mathrm{i}\Delta t) | q_{l+1}; X^{l+1} \rangle \right) \langle X^{m+2Q+1}; q_{m+2Q+1} | B | q_0; X^0 \rangle, \end{aligned} \tag{3.11}$$

where the resolutions of identity are indexed in increasing order as "1","2",...,"$m + 2Q + 1$" from left to right.

The matrix elements appearing in the above expression can now be evaluated. Since the current operator acts only on the electronic degrees of freedom, it does not affect the phonon coordinates. As a result, the matrix elements factorize as

$$\langle X^{m+Q}; q_{m+Q} | j | q_{m+Q+1}; X^{m+Q+1} \rangle = \prod_{n=0}^{N-1} \delta \left(X_n^{m+Q+1} - X_n^{m+Q} \right) \langle q_{m+Q} | j | q_{m+Q+1} \rangle \,, \tag{3.12a}$$

$$\langle X^{m+2Q+1}; q_{m+2Q+1} | j | q_0; X^0 \rangle = \prod_{n=0}^{N-1} \delta \left(X_n^0 - X_n^{m+2Q+1} \right) \langle q_{m+2Q+1} | j | q_0 \rangle \,. \tag{3.12b}$$

The current operator in the momentum representation is given by

$$j = -2J \sum_k c_k^\dagger c_k \sin(k), \tag{3.13}$$

where $c_k^\dagger$ (c_k) are electron creation (annihilation) operators in momentum space. The diagonal structure of the current operator in momentum space significantly simplifies the evaluation of the corresponding matrix elements which take the form

$$\begin{aligned} \langle q_{m+Q} | j | q_{m+Q+1} \rangle &= -2J \sin(q_{m+Q+1}) \delta_{q_{m+Q}, q_{m+Q+1}} \,, \\ \langle q_{m+2Q+1} | j | q_0 \rangle &= -2J \sin(q_0) \delta_{q_0, q_{m+2Q+1}} \,. \end{aligned} \tag{3.14}$$

To evaluate the matrix elements of the form $\langle X^i; q_i | \rho(z) | q_{i+1}; X^{i+1} \rangle$, it is necessary to determine how the exponential operators act on the chosen basis states.

The operator e^{zH_2} acts only on the electronic degrees of freedom and is diagonal in the momentum representation. Its action is given by

$$\mathrm{e}^{zH_2} | q_{i+1}; X^{i+1} \rangle = \mathrm{e}^{z\varepsilon(q_{i+1})} | q_{i+1}; X^{i+1} \rangle, \tag{3.15}$$

where $\varepsilon(q)$ is the electronic dispersion.

The operator e^{zH_1}, which contains the e-ph interaction and phonon potential terms, is diagonal in the phonon coordinate representation but couples different electronic momentum states. Its action on the basis states can be written as

$$e^{zH_1}|q_{i+1};X^{i+1}\rangle = e^{z\frac{M}{2}\sum_n \omega_n^2 (X_n^{i+1})^2}\frac{1}{N}\sum_k\sum_r e^{-ir\cdot(q_{i+1}-k)+z\sum_n \sqrt{2M\omega_n}GX_n^{i+1}\delta_{n,m}}|k;X^{i+1}\rangle. \tag{3.16}$$

Since the operator e^{zH_0} depends the phonon momentum, its action is most conveniently evaluated in the momentum representation of the phonon degrees of freedom. This requires inserting a resolution of identity in the phonon momentum basis. After performing the resulting Gaussian integration over the phonon momenta, the matrix elements can be expressed in terms of the phonon coordinates alone. The resulting expressions for matrix elements entering $C_{jj}^{m,Q}$ take the form

$$\langle X^i;q_i|\rho(-\tau)|q_{i+1};X^{i+1}\rangle = C_1\ f_{q_{i+1},q_i}(-\tau;X^{i+1})e^{-\tau\sum_n\left(\frac{M}{2}\omega_n^2(X_n^{i+1})^2+\frac{M}{2}\frac{(X_n^{i+1}-X_n^i)^2}{\tau^2}\right)}, \tag{3.17}$$

$$\langle X^p;q_p|\rho(i\Delta t)|q_{p+1};X^{p+1}\rangle = C_2\ f_{q_{p+1},q_p}(i\Delta t;X^{p+1})e^{i\Delta t\sum_n\left(\frac{M}{2}\omega_n^2(X_n^{p+1})^2+\frac{M}{2}\frac{(X_n^{p+1}-X_n^p)^2}{(i\Delta t)^2}\right)}, \tag{3.18}$$

$$\langle X^l;q_l|\rho(-i\Delta t)|q_{l+1};X^{l+1}\rangle = C_3\ f_{q_{l+1},q_l}(-i\Delta t;X^{l+1})e^{i\Delta t\sum_n\left(\frac{M}{2}\omega_n^2(X_n^{l+1})^2+\frac{M}{2}\frac{(X_n^{l+1}-X_n^l)^2}{(i\Delta t)^2}\right)}, \tag{3.19}$$

where C_1,C_2 and C_3 are constants arising from the Gaussian integration over phonon momenta.

The functions $f_{q_i,q_j}(z;X^i)$ can be interpreted as effective fermionic propagators between momentum states q_i and q_j over a time interval z, which may correspond to either imaginary or real time. They are given by

$$f_{q_i,q_j}(z;X^i) = e^{z\varepsilon(q_i)}\frac{1}{N}\sum_m e^{-im\cdot(q_i-q_j)+z\sqrt{2M\omega_m}GX_m^i}. \tag{3.20}$$

This function describes the propagation of an electron coupled to lattice vibrations, i.e. a dressed (polaronic) quasiparticle, with the propagation amplitude determined by the instantaneous phonon configuration at a given time slice.

The path-integral representation of the correlator $C_{jj}^{m,Q}$ can now be written in the form

$$\begin{aligned}C_{jj}^{m,Q} = C\int\prod_{i=0}^{m-1}DX^i\prod_{p=m}^{m+Q}DX^p\prod_{l=m+Q+1}^{m+2Q+1}DX^l\ e^{-S_1[\tau;X^i]}e^{-S_2[-i\Delta t;X^p]}e^{-S_3[i\Delta t;X^l]}\times\\ \times\sum_{\{q\}}\prod_{i=0}^{m-1}f_{q_{i+1},q_i}(-\tau;X^{i+1})\prod_{p=m}^{m+Q-1}f_{q_{p+1},q_p}(i\Delta t;X^{p+1})\prod_{l=m+Q+1}^{m+2Q}f_{q_{l+1},q_l}(-i\Delta t;X^{l+1})\times\\ \times\langle X^{m+Q};q_{m+Q}|j|q_{m+Q+1};X^{m+Q+1}\rangle\langle X^{m+2Q+1};q_{m+2Q+1}|j|q_0;X^0\rangle\ ,\end{aligned} \tag{3.21}$$

where C is a constant resulting from the Gaussian integration over phonon momenta, and $\sum_{\{q\}}$ denotes summation over all intermediate momentum variables.

The exponential terms define an effective discretized phonon action along the contour composed of imaginary-time evolution, followed by forward and backward real-time propagation. The corresponding contributions are given by

$$\begin{aligned}S_1[\tau;X^i] &= \tau\sum_{i=0}^{m-1}\sum_n\left[\frac{M}{2}\omega_n^2(X_n^{i+1})^2+\frac{M}{2}\frac{(X_n^{i+1}-X_n^i)^2}{\tau^2}\right],\\ S_2[-i\Delta t;X^p] &= -i\Delta t\sum_{p=m}^{m+Q-1}\sum_n\left[\frac{M}{2}\omega_n^2(X_n^{p+1})^2+\frac{M}{2}\frac{(X_n^{p+1}-X_n^p)^2}{(i\Delta t)^2}\right],\\ S_3[i\Delta t;X^l] &= i\Delta t\sum_{l=m+Q+1}^{m+2Q}\sum_n\left[\frac{M}{2}\omega_n^2(X_n^{l+1})^2+\frac{M}{2}\frac{(X_n^{l+1}-X_n^l)^2}{(i\Delta t)^2}\right].\end{aligned} \tag{3.22}$$

This representation provides the basis for the Monte Carlo evaluation of the correlation function.

In order to obtain a form suitable for numerical calculation, the trace $C_{jj}^{m,Q}$ is rewritten in a compact matrix form by introducing a vector variable that collects all phonon coordinates along the discretized contour,

$$C_{jj}^{m,Q} = C \int \mathrm{D}\mathbf{Y}\ \mathrm{e}^{-\frac{1}{2}\mathbf{Y}^T \mathcal{D}\mathbf{Y}} F(\mathbf{Y}), \tag{3.23}$$

where the vector $\mathbf{Y}$ is defined as

$$\begin{aligned}\mathbf{Y} &= \left(Y^0, Y^1, \ldots, Y^{m+2Q-1}\right)^T \\ &= \left(X^1, X^2, \ldots, X^{m+Q-1}, X^{m+Q+1}, \ldots, X^{m+2Q-1}, X^{m+2Q}, X^0\right)^T \ .\end{aligned} \tag{3.24}$$

The identification of variables, such as $X^{m+Q} = X^{m+Q+1}$, follows from the delta functions in Eqs. (3.12a) and (3.12b). Each component X^j (and correspondingly Y^j) is itself an N-dimensional vector,

$$X^j = (X_0^j, X_1^j, \ldots, X_{N-1}^j)^T \ . \tag{3.25}$$

The matrix $\mathcal{D}$ represents the discretized phonon action in the coordinate basis $\mathbf{Y}$ and its explicit form can be derived from Eq. (3.21).

An analogous change of variables is introduced for the electronic momentum indices,

$$\left(k^0, k^1, \ldots, k^{m+2Q-1}\right)^T = \left(q^1, q^2, \ldots, q^{m+Q-1}, q^{m+Q+1}, \ldots, q^{m+2Q-1}, q^{m+2Q}, q^0\right)^T \tag{3.26}$$

In this representation, the function $F(\mathbf{Y})$ is given by

$$\begin{aligned}F(\mathbf{Y}) = \sum_{k_0} \cdots \sum_{k_{m+2Q-1}} & f_{k_0,k_{m+2Q-1}}(-\tau; Y^0) \prod_{i=1}^{m-1} f_{k_i,k_{i-1}}(-\tau; Y^i) \prod_{p=m}^{m+Q-2} f_{k_p,k_{p-1}}(\mathrm{i}\Delta t; Y^p) \times \\ \times\, \tilde{f}_{k_{m+Q-1},k_{m+Q-2}}(\mathrm{i}\Delta t; Y^{m+Q-1}) & \prod_{l=m+Q}^{m+2Q-2} f_{k_l,k_{l-1}}(-\mathrm{i}\Delta t; Y^l)\ \tilde{f}_{k_{m+2Q-1},k_{m+2Q-2}}(-\mathrm{i}\Delta t; Y^{m+2Q-1}),\end{aligned} \tag{3.27}$$

where

$$\tilde{f}_{k_j,k_l}(z; Y^j) = -2J \sin(k_j) f_{k_j,k_l}(z; Y^j) \ . \tag{3.28}$$

To evaluate the real-time correlation function, the following estimator is used:

$$\langle j(t) j \rangle^{m,Q} = \frac{1}{C_{11}^{m,Q}}\ C_{jj}^{m,Q} \tag{3.29}$$

where $C_{11}^{m,Q}$ is obtained from (3.21) by replacing the current operator with the identity operator. This quanitity serves as a normalization factor. In this formulation, the constant C cancels between numerator and denominator and does not need to be evaluated explicitly.

For sufficiently large values of m and Q, the estimator converges to the real correlation function $\langle j(t) j \rangle$.

The integrals appearing in $C_{jj}^{m,Q}$ are evaluated using a Monte Carlo approach by sampling configurations of the phonon variables according to the quadratic form defined by the phonon action,

$$S[\mathbf{Y}] = \frac{1}{2}\mathbf{Y}^T \mathcal{D}\mathbf{Y}. \tag{3.30}$$

The matrix $\mathcal{D}$ is a complex symmetric with positive definite real part, which ensures that the corresponding Gaussian form is well-defined. In the present formulation, the matrix $\mathcal{D}$ is found to be diagonalizable, yielding a decomposition of the form

$$\mathcal{D} = Q \Lambda Q^T \ , \tag{3.31}$$

where Λ is a diagonal matrix containing the eigenvalues of $\mathcal{D}$, and $QQ^T = I$, i.e. Q is a complex orthogonal matrix whose columns are the corresponding eigenvectors. This decomposition is used to transform the quadratic form into a sum of independent contributions, enabling efficient sampling of phonon configurations. The validity of this decomposition has been verified numerically for the matrices appearing in the calculation.

Introducing the change of variables

$$Z = \Lambda^{1/2} Q^T Y \,, \tag{3.32}$$

the quadratic form becomes

$$\mathbf{Y}^T \mathcal{D} \mathbf{Y} = \mathbf{Y}^T Q \Lambda Q^T \mathbf{Y} = \mathbf{Z}^T \mathbf{Z} = \sum_k Z_k^2 \,. \tag{3.33}$$

In this representation, the components Z_k are independent variables and can be sampled directly. The original variables $\mathbf{Y}$ are then obtained via the inverse transformation

$$\mathbf{Y} = Q \Lambda^{-1/2} \mathbf{Z} \,. \tag{3.34}$$

Once a configuration $\mathbf{Y}$ is generated, the function $F(\mathbf{Y})$ can be evaluated. The summation over electronic momenta in $F(\mathbf{Y})$ can be expressed as the trace over products of matrices, leading to the representation

$$\begin{aligned} F(\mathbf{Y}) = Tr \Big[&\mathcal{F}(-\tau; Y^0) \cdot \mathcal{F}(-\tau; Y^1) \ldots \mathcal{F}(-\tau; Y^{m-1}) \cdot \mathcal{F}(\mathrm{i}\Delta t; Y^m) \cdot \cdots \cdot \mathcal{F}(\mathrm{i}\Delta t; Y^{m+Q-2}) \cdot \\ &\cdot \mathcal{G}(\mathrm{i}\Delta t; Y^{m+Q-1}) \cdot \mathcal{F}(-\mathrm{i}\Delta t; Y^{m+Q}) \ldots \mathcal{F}(-\mathrm{i}\Delta t; Y^{m+2Q-2}) \cdot \mathcal{G}(-\mathrm{i}\Delta t; Y^{m+2Q-1}) \Big] \,, \end{aligned} \tag{3.35}$$

where the matrices are defined as

$$\begin{aligned} [\mathcal{F}(-\tau; Y^k)]_{l,j} &= \mathrm{e}^{-\tau\varepsilon(2\pi j/N)} \frac{1}{N} \sum_{n=0}^{N-1} \mathrm{e}^{-\mathrm{i}n\cdot(j-l)\frac{2\pi}{N} - \tau\sqrt{2M\omega_n} G Y_n^k} \,, \\ [\mathcal{G}(\mathrm{i}\Delta t; Y^{m+Q-1})]_{l,j} &= -2J \sin(2\pi j/N) \mathrm{e}^{\mathrm{i}\Delta t\varepsilon(2\pi j/N)} \frac{1}{N} \sum_{n=0}^{N-1} \mathrm{e}^{-\mathrm{i}n\cdot(j-l)\frac{2\pi}{N} + \mathrm{i}\Delta t\sqrt{2M\omega_n} G Y_n^{m+Q-1}} \,, \\ [\mathcal{G}(-\mathrm{i}\Delta t; Y^{m+2Q-1})]_{l,j} &= -2J \sin(2\pi j/N) \mathrm{e}^{-\mathrm{i}\Delta t\varepsilon(2\pi j/N)} \frac{1}{N} \sum_{n=0}^{N-1} \mathrm{e}^{-\mathrm{i}n\cdot(j-l)\frac{2\pi}{N} - \mathrm{i}\Delta t\sqrt{2M\omega_n} G Y_n^{m+2Q-1}} \,. \end{aligned} \tag{3.36}$$

In the case of $C_{11}^{m,Q}$ the matrices $\mathcal{G}$ are replaced by the matrices $\mathcal{F}$.

This completes the construction of the path-integral representation in the momentum basis. The detailed evaluation of the exponential operator actions and the explicit construction of the matrix $\mathcal{D}$ are provided in Appendix A.

3.1.2 Path integral with position representation for electrons

In this case, a basis consisting of direct product states of electron position and phonon coordinates is used,

$$|r; \{X_n\}\rangle \equiv |r\rangle |\{X_n\}\rangle \,, \tag{3.37}$$

where the electron position index takes values $r = 0, \ldots, N-1$, and the phonon coordinates satisfy $X_n \in \mathbb{R}$.

The expressions for the trace of an operator O and the resolution of identity in this basis are given by

$$Tr(O) = \sum_r \int \left(\prod_{n=0}^{N-1} \mathrm{d}X_n \right) \langle \{X_n\}; r|O|r; \{X_n\} \rangle, \tag{3.38a}$$

$$1 = \sum_r \int \left(\prod_{n=0}^{N-1} \mathrm{d}X_n \right) |r; \{X_n\}\rangle\langle \{X_n\}; r|. \tag{3.38b}$$

Following the same procedure as in the previous subsection, the trace $C_{jj}^{m,Q}$ can be written in a form analogous to Eq. (3.11),

$$\begin{aligned} \mathrm{C}_{jj}^{m,Q} = \sum_{r_0,\ldots,r_{m+2Q+1}} \int & \left(\prod_{j=0}^{m-1} \mathrm{D}X^j \right) \left(\prod_{p=m}^{m+Q} \mathrm{D}X^p \right) \left(\prod_{l=m+Q+1}^{m+2Q+1} \mathrm{D}X^l \right) \left(\prod_{j=0}^{m-1} \langle X^j; r_j|\rho(-\tau)|r_{j+1}; X^{j+1}\rangle \right) \times \\ & \times \left(\prod_{p=m}^{m+Q-1} \langle X^p; r_p|\rho(\mathrm{i}\Delta t)|r_{p+1}; X^{p+1}\rangle \right) \langle X^{m+Q}; r_{m+Q}|j|r_{m+Q+1}; X^{m+Q+1}\rangle \times \\ & \times \left(\prod_{l=m+Q+1}^{m+2Q} \langle X^l; r_l|\rho(-\mathrm{i}\Delta t)|r_{l+1}; X^{l+1}\rangle \right) \langle X^{m+2Q+1}; r_{m+2Q+1}|j|r_0; X^0\rangle \ . \end{aligned} \tag{3.39}$$

Evaluating the matrix elements and taking into account that the current operator acts only on the electronic degrees of freedom, the expression simplifies to

$$\begin{aligned} \mathrm{C}_{jj}^{m,Q} = C \sum_{r_0,\ldots,r_{m+2Q+1}} & \langle r_{m+Q}|j|r_{m+Q+1}\rangle\langle r_{m+2Q+1}|j|r_0\rangle \left(\prod_{j=0}^{m-1} I(\tau; r_{j+1} - r_j) \right) \times \\ & \times \left(\prod_{p=m}^{m+Q-1} I(-\mathrm{i}\Delta t; r_{p+1} - r_p) \right) \left(\prod_{l=m+Q+1}^{m+2Q} I(\mathrm{i}\Delta t; r_{l+1} - r_l) \right) \times \\ & \times \int \left(\prod_{j=0}^{m-1} \mathrm{D}X^j \right) \left(\prod_{p=m}^{m+Q-1} \mathrm{D}X^p \right) \left(\prod_{l=m+Q+1}^{m+2Q} \mathrm{D}X^l \right) \mathrm{e}^{-S_1[\tau;X^j]} \mathrm{e}^{-S_2[-\mathrm{i}\Delta t;X^p]} \mathrm{e}^{-S_3[\mathrm{i}\Delta t;X^l]} \ . \end{aligned} \tag{3.40}$$

The corresponding phonon actions are given by

$$\begin{aligned} S_1[\tau; X^j] &= \tau \sum_{j=0}^{m-1} \sum_n \left[\frac{M}{2} \omega_n^2 (X_n^{j+1})^2 + \frac{M}{2} \frac{(X_n^{j+1} - X_n^j)^2}{\tau^2} + \sqrt{2M\omega_n} G \delta_{n,r_j} X_n^{j+1} \right], \\ S_2[-\mathrm{i}\Delta t; X^p] &= -\mathrm{i}\Delta t \sum_{p=m}^{m+Q-1} \sum_n \left[\frac{M}{2} \omega_n^2 (X_n^{p+1})^2 + \frac{M}{2} \frac{(X_n^{p+1} - X_n^p)^2}{(\mathrm{i}\Delta t)^2} + \sqrt{2M\omega_n} G \delta_{n,r_p} X_n^{p+1} \right], \\ S_3[\mathrm{i}\Delta t; X^l] &= \mathrm{i}\Delta t \sum_{l=m+Q+1}^{m+2Q} \sum_n \left[\frac{M}{2} \omega_n^2 (X_n^{l+1})^2 + \frac{M}{2} \frac{(X_n^{l+1} - X_n^l)^2}{(\mathrm{i}\Delta t)^2} + \sqrt{2M\omega_n} G \delta_{n,r_l} X_n^{l+1} \right]. \end{aligned} \tag{3.41}$$

The constant C results from Gaussian integration in the matrix elements.

The main difference in this representation is the appearance of the functions $I(z; r_{j+1} - r_j)$, which correspond to electron propagators transformed to coordinate space. In contrast to the momentum representation, where the propagators $f_{q_i,q_j}(z; X^i)$ depend explicitly on the phonon coordinates, the functions $I(z; r_{j+1} - r_j)$ are independent of the phonon variables. This property allows the integration over phonon coordinates in Eq. (3.40) to be carried out analytically.

These Fourier-transformed propagators are defined as

$$I(z; r_{j+1} - r_j) = \frac{1}{N} \sum_{k=0}^{N-1} \cos\left(\frac{2\pi}{N} k (r_{j+1} - r_j)\right) \exp\left(2zJ \cos(2\pi k/N)\right) \ . \tag{3.42}$$

As in the previous subsection, a vector variable for the phonon coordinates is introduced, allowing the expression to be written as

$$\begin{aligned} f(\{r\}) &= \int \left(\prod_{j=0}^{m-1} \mathrm{D}X^j\right) \left(\prod_{p=m}^{m+Q-1} \mathrm{D}X^p\right) \left(\prod_{l=m+Q+1}^{m+2Q} \mathrm{D}X^l\right) \mathrm{e}^{-S_1[\tau; X^j]} \mathrm{e}^{-S_2[-\mathrm{i}\Delta t; X^p]} \mathrm{e}^{-S_3[\mathrm{i}\Delta t; X^l]} \\ &= \int \mathrm{D}\mathbf{Y} \mathrm{e}^{-S[\mathbf{Y}]} \end{aligned} \tag{3.43}$$

where $\mathbf{Y}$ is defined in Eq. (3.24). The resulting action takes the form of a quadratic expression with an additional linear term,

$$S[\mathbf{Y}] = \frac{1}{2} \mathbf{Y}^T \mathcal{D} \mathbf{Y} + \mathbf{Y}^T \mathbf{d} \ , \tag{3.44}$$

where the vector $\mathbf{d}$ contains the contributions arising from the electron–phonon interaction terms in the actions given in Eq. (3.41).

To evaluate the integral over phonon coordinates, a shift of variables is introduced,

$$\mathbf{Z} = \mathbf{Y} + \mathcal{D}^{-1} \mathbf{d} \ , \tag{3.45}$$

which leaves the integration measure invariant. The action then transforms as

$$-\frac{1}{2} \mathbf{Y}^T \mathcal{D} \mathbf{Y} - \mathbf{Y}^T \cdot \mathbf{d} = -\frac{1}{2} \mathbf{Z}^T \mathcal{D} \mathbf{Z} + \frac{1}{2} \mathbf{d}^T \mathcal{D}^{-1} \mathbf{d}. \tag{3.46}$$

The integral over phonon coordinates can now be evaluated in closed form,

$$f(\{r\}) = \exp\left(\frac{1}{2} \mathbf{d}^T \mathcal{D}^{-1} \mathbf{d}\right) \int \mathrm{D}\mathbf{Z} \ \exp\left(-\frac{1}{2} \mathbf{Z}^T \mathcal{D} \mathbf{Z}\right) , \tag{3.47}$$

yielding

$$f(\{r\}) = (2\pi)^{\frac{N_{\mathrm{tot}}}{2}} \left[\det\left(\mathcal{D}\right)\right]^{-\frac{1}{2}} \exp\left(\frac{1}{2} \mathbf{d}^T \mathcal{D}^{-1} \mathbf{d}\right) \ , \tag{3.48}$$

where $N_{\mathrm{tot}} = (m + 2Q)N$ denotes the total number of phonon degrees of freedom in the vector $\mathbf{Y}$. Since the matrix $\mathcal{D}$ is complex symmetric with a positive definite real part, the integral is well-defined and yields the standard expression proportional to $[\det(\mathcal{D})]^{-1/2}$. This result is obtained by analytic continuation of the standard Gaussian integral for real symmetric positive-definite matrices [79].

This analytical integration over phonon coordinates reduces the problem to a sum over electron trajectories, which forms the basis of the Monte Carlo sampling in the position representation.

The trace $C_{jj}^{m,Q}$ can be written in the form:

$$\mathrm{C}_{jj}^{m,Q} = C \sum_{\{r\}} w(\{r\}) F(\{r\}), \tag{3.49}$$

where the weight function $w(\{r\})$ is real and non-negative, while the function $F(\{r\})$ contains the remaining phase factors and contributions arising from the current operators and the electron–phonon interaction. These functions are defined as

$$w(\{r\}) = \left(\prod_{j=0}^{m-1} I(\tau; r_{j+1} - r_j)\right) \left(\prod_{p=m}^{m+Q-1} |I(-\mathrm{i}\Delta t; r_{p+1} - r_p)|\right) \left(\prod_{l=m+Q+1}^{m+2Q} |I(\mathrm{i}\Delta t; r_{l+1} - r_l)|\right), \tag{3.50}$$

$$F(\{r\}) = \langle r_{m+Q}|j|r_{m+Q+1}\rangle\langle r_{m+2Q+1}|j|r_0\rangle \exp\left(\frac{1}{2}\mathbf{d}(\{r\})^T \cdot \mathcal{D}^{-1} \cdot \mathbf{d}(\{r\})\right) \times \prod_{p=m}^{m+Q-1} \mathrm{e}^{\mathrm{i}\phi(-\mathrm{i}\Delta t; r_{p+1}-r_p)} \prod_{l=m+Q+1}^{m+2Q} \mathrm{e}^{\mathrm{i}\phi(\mathrm{i}\Delta t; r_{l+1}-r_l)} , \tag{3.51}$$

where the residual phase is defined as $\phi(z; r_i - r_j) = \arg\left[I(z; r_i - r_j)\right]$.

The real-time correlation function is then evaluated using the same estimator $\langle j(t)j\rangle^{m,Q}$ as in the previous subsection. This representation allows the correlation function to be computed by Monte Carlo sampling over configurations $\{r\}$, which are interpreted as electron trajectories along the discretized time contour. Configurations are generated with probability proportional to the weight $w(\{r\})$, and the estimator is obtained by averaging the corresponding values of $F(\{r\})$. The locality of the weight function in terms of differences $r_{j+1} - r_j$ enables efficient sampling using local updates.

The matrix elements of the current operator,

$$j = \mathrm{i}J \sum_{n=0}^{N-1} \left(c_n^\dagger c_{n+1} - c_{n+1}^\dagger c_n\right) , \tag{3.52}$$

are nonzero only for nearest-neighbor positions. Explicitly,

$$\langle r_i|j|r_j\rangle = \begin{cases} \mathrm{i}J, & r_i = r_j - 1, \\ -\mathrm{i}J, & r_i = r_j + 1, \\ 0, & \text{otherwise}, \end{cases} \tag{3.53}$$

where the equalities are understood modulo N due to periodic boundary conditions.

The path integral representation in imaginary time is obtained by replacing the real-time evolution with imaginary-time evolution, $t \to -\mathrm{i}t$, which corresponds to the substitution $\Delta t \to -\mathrm{i}\Delta t$ in the discretized real-time expressions. It should be emphasized that this imaginary-time step is distinct from the thermal imaginary time $\tau = \beta/m$ introduced through the Boltzmann factor.

In this case, the weight function from Eq. (3.50) reduces to

$$w(\{r\}) = \prod_{j=0}^{m-1} I(\tau; r_{j+1} - r_j) \prod_{p=m}^{m+Q-1} I(-\Delta t; r_{p+1} - r_p) \prod_{l=m+Q+1}^{m+2Q} I(\Delta t; r_{l+1} - r_l) \ , \tag{3.54}$$

so that all contributions are real and non-negative.

In addition, the matrix $\mathcal{D}$ becomes real symmetric and the residual phase factors vanish. This significantly simplifies the numerical evaluation as the sign problem is absent in imaginary time.

This completes the construction of the path-integral representation of the current–current correlation function in both real and imaginary time in the position basis. The explicit construction of the matrix $\mathcal{D}$, the vector $\mathbf{d}$, and the implementation details of the sampling procedures are presented in Appendices A and C.

3.2 Analytic continuation procedure for obtaining dc mobility

The path-integral quantum Monte Carlo methodology described in the previous section provides access to the current–current correlation function $\langle j(z)j(0)\rangle$ evaluated either at imaginary times ($z = -\mathrm{i}t$, $0 \le t \le \beta$) or at short real times ($z = t$, $t \ge 0$). The quantity of primary interest, however, is the dc mobility $\mu = \mu(\omega = 0)$. The relation between the correlation function and the frequency-dependent mobility $\mu(\omega)$ follows from the standard Kubo formalism introduced in Sec. 2.2.1,

$$\langle j(z)j(0)\rangle = \int_{-\infty}^{\infty} \mathrm{d}\omega \frac{1}{\pi} \frac{\omega \mathrm{e}^{-\mathrm{i}\omega z}}{1 - \mathrm{e}^{-\beta\omega}} \mathrm{Re}\mu(\omega) \ . \tag{3.55}$$

In the quantum many-body literature, this problem is typically addressed by evaluating the correlation function in imaginary time, where the sign problem is absent, and subsequently performing analytic continuation in order to obtain $\mathrm{Re}\mu(\omega)$. Among the analytic continuation methods discussed in Sec. 2.5.3, the singular value decomposition (SVD) method is adopted.

Particular emphasis is placed on the combined use of imaginary-time and real-time data within the analytic continuation procedure. In addition to imaginary-time correlation functions, real-time data are incorporated only over time intervals for which the sign problem is not yet pronounced, such that the correlation function can be evaluated with sufficient accuracy. The analytic continuation procedure is therefore constructed using both imaginary-time and short real-time information obtained from the path-integral Monte Carlo simulations. This combined approach constitutes an important aspect of the present work, as it improves the stability and resolution of the continuation procedure compared to the use of imaginary-time data alone.

Since the analytic continuation procedure was not developed as part of the original contribution of this thesis, its technical details are presented in Appendix B for completeness. The method and its implementation follow the approach developed by Nenad Vukmirović [132], while a concise overview is provided here.

The singular value decomposition (SVD) method is employed to perform the analytic continuation. Upon discretization of Eq. (3.55), the problem is reduced to a linear system of the form

$$\mathbf{j} = \mathbf{K} \cdot \mathbf{m}, \tag{3.56}$$

where $\mathbf{K}$ is a known kernel matrix obtained from the discretization of Eq. (3.55). The vector $\mathbf{j}$ contains the values of the current–current correlation function at the discretized time points, while the vector $\mathbf{m}$ represents the unknown discrete form of $\mathrm{Re}\mu(\omega)$. All quantities can be expressed in terms of real numbers by separating real and imaginary parts, allowing the problem to be treated within a real-valued linear algebra framework.

Any real matrix admits a singular value decomposition of the form

$$\mathbf{K} = \mathbf{U}\mathbf{S}\mathbf{V}^T, \tag{3.57}$$

where $\mathbf{U}$ and $\mathbf{V}$ are orthogonal matrices, and $\mathbf{S}$ is a diagonal matrix whose entries s_k are the singular values. The solution for $\mathbf{m}$ can then be formally written as

$$\mathbf{m} = \sum_k \frac{\mathbf{U}^T_{.,k} \cdot \mathbf{j}}{s_k} \mathbf{V}_{.,k} \ , \tag{3.58}$$

where $\mathbf{U}^T_{.,k}$ and $\mathbf{V}_{.,k}$ are the k-th column vectors of matrix $\mathbf{U}^T$ and $\mathbf{V}$ respectively.

The main difficulty in reconstructing $\mathbf{m}$ from Eq. (3.58) arises from the presence of very small singular values. These lead to a strong amplification of statistical noise originating from Monte Carlo sampling, as well as numerical errors present in the data contained in the vector $\mathbf{j}$. In practice, the summation in Eq. (3.58) is therefore truncated, and only contributions corresponding to sufficiently large singular values are retained.

It should be emphasized that combining real- and imaginary-time data is not exclusive to the SVD approach and can likewise be integrated into other analytic continuation methods. The SVD approach is adopted here due to its transparency, which allows for a clear illustration of the intrinsic difficulties associated with the analytic continuation procedure.

The performance of the analytic continuation procedure, including the effect of singular value truncation and the role of real-time data, is demonstrated in the following subsection.

3.2.1 Assessment of the SVD analytic continuation procedure

In this subsection, the analytic continuation procedure is assessed using controlled test data. In order to evaluate the accuracy and limitations of the method, it is advantageous to consider a case in which

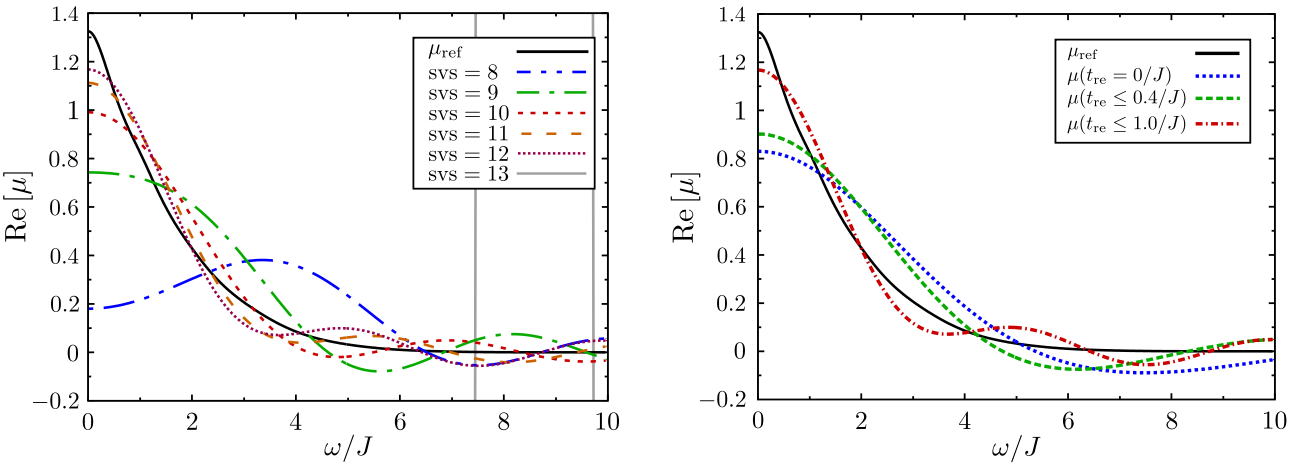

Figure 3.1: Examples illustrating the analytic continuation procedure. (a) Comparison between the reference mobility μ_{ref} and reconstructed results obtained using different numbers of singular values. (b) Comparison between μ_{ref} and reconstructed results obtained using imaginary-time data only (denoted as $\mu(t_{\mathrm{re}} = 0)$), as well as using combined imaginary- and real-time data up to $t_{\mathrm{re}} \leq 0.4/J$ and $t_{\mathrm{re}} \leq 1/J$, respectively. Results are shown for $\omega_0/J = 1$, $G/J = 1$, and $T/J = 1$. Only positive frequencies are displayed, since $\mathrm{Re}, \mu(\omega) = \mathrm{Re}, \mu(-\omega)$.

the exact frequency dependence of the mobility is known. This allows a direct comparison between the reconstructed and exact results.

For this purpose, the procedure is not applied to Monte Carlo data. Instead, the frequency-dependent mobility obtained in Ref. [133] is used as a reference, denoted by μ_{ref}. Based on this reference mobility, the corresponding current–current correlation function is constructed in both imaginary and real time using Eq. (3.55). To mimic realistic conditions, statistical noise is then added to these data, with an amplitude comparable to that observed in the Monte Carlo simulations.

The analytic continuation procedure described in the previous section is subsequently applied to the noisy correlation function, yielding the reconstructed mobility $\mathrm{Re}\mu_{\mathrm{ac}}(\omega)$. By comparing $\mathrm{Re}\mu_{\mathrm{ac}}(\omega)$ with the reference result $\mathrm{Re}\mu_{\mathrm{ref}}(\omega)$, the performance of the continuation procedure can be quantitatively assessed. Since the primary quantity of interest is the dc mobility, particular attention is given to the value at $\omega = 0$.

The results are presented for model parameters $\omega_0/J = 1$, $G/J = 1$ and $T/J = 1$ in Fig. 3.1. This choice corresponds to an intermediate regime in which the electron–phonon coupling, phonon energy, and temperature are all of comparable magnitude, avoiding both weak- and strong-coupling limits as well as low- and high-temperature regimes. In Fig. 3.1a, the reconstruction is performed using imaginary-time data up to $0.6/J$ and real-time data up to $1/J$. The imaginary-time range is chosen to slightly exceed $\beta/2$, beyond which the correlation function does not provide additional independent information due to its symmetry in imaginary time. The real-time range is selected to reflect the typical time window accessible in Monte Carlo simulations, thereby mimicking the typical range over which reliable real-time data can be obtained in Monte Carlo simulations. In Fig. 3.1b, the same imaginary-time data are used, while the range of included real-time data is varied, as specified in the figure caption.

Figure 3.1a illustrates the effect of the number of singular values retained in the truncated sum of Eq. (3.58). If too many singular values are included (e.g., svs = 13), the reconstructed mobility becomes dominated by amplified noise. Conversely, if too few singular values are retained (e.g., svs = 8, 9, 10), the reconstruction lacks sufficient information and fails to reproduce the qualitative features of the reference mobility. In practice, an optimal choice corresponds to retaining the largest possible number of singular values before the onset of noise amplification.

Figure 3.1b demonstrates the effect of incorporating real-time data into the analytic continuation procedure. When only imaginary-time data are used, the reconstructed mobility deviates significantly

from the reference result. By progressively including real-time data over increasing time intervals, the reconstruction improves and approaches the reference mobility. This clearly indicates that the combined use of imaginary- and real-time data enhances the stability and accuracy of the analytic continuation procedure, particularly in the low-frequency domain relevant for dc mobility.

To quantify the accuracy of the analytic continuation procedure, an estimate of the associated reconstruction error is introduced. This estimate is based on a comparison between the reconstructed mobility and the known reference result at zero frequency.

The relative error is defined as

$$\delta = \frac{\mathrm{Re}\mu_{\mathrm{ac}}\,(\omega = 0) - \mathrm{Re}\mu_{\mathrm{ref}}\,(\omega = 0)}{\mathrm{Re}\mu_{\mathrm{ref}}\,(\omega = 0)}\,, \tag{3.59}$$

and is used as a quantitative measure of the accuracy of the analytic continuation procedure.

This estimate is subsequently employed to assign an uncertainty to the dc mobility values obtained from Monte Carlo data. For each set of model parameters, the same discrete time grid (both imaginary and real) used in the Monte Carlo calculations is applied to the reference mobility, allowing the error introduced by the analytic continuation procedure to be evaluated under conditions that closely match those of the actual simulations.

In this way, the error estimate reflects the combined effect of limited time-domain data, discretization, and statistical noise, and provides a realistic assessment of the uncertainty associated with the reconstructed dc mobility. It is further observed that the reconstructed values $\mathrm{Re}\mu_{\mathrm{ac}}\,(\omega = 0)$ systematically underestimate the reference values $\mathrm{Re}\mu_{\mathrm{ref}}\,(\omega = 0)$. This indicates that, within the present implementation and for finite data sets, the analytic continuation procedure introduces a bias towards lower mobility values.

3.3 Choice of parameters values in QMC calculations

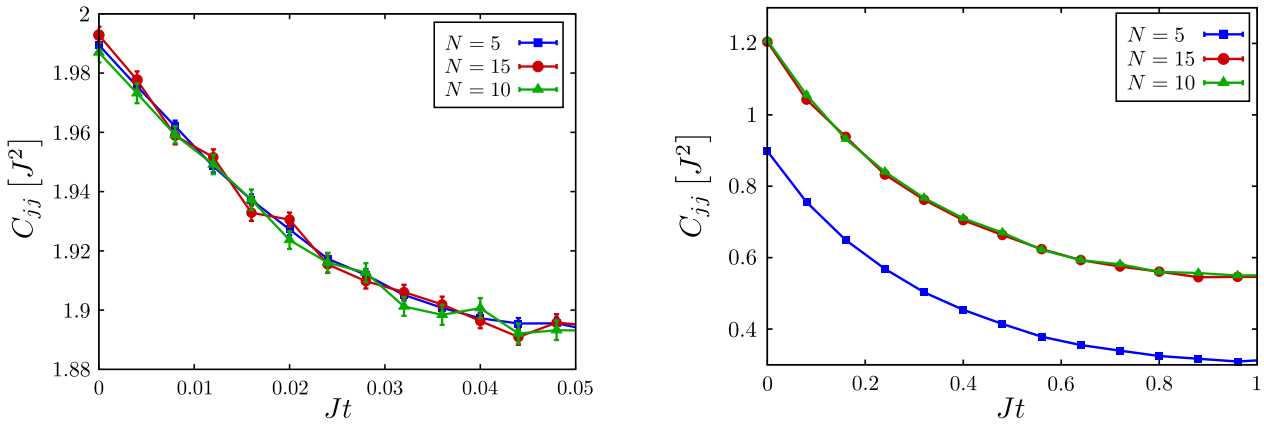

Figure 3.2: Dependence of the imaginary-time current–current correlation function on the system size N for $\omega_0/J = 1$ and $G/J = 1$. (a) High temperature, $T/J = 10$; (b) low temperature, $T/J = 0.5$. Results are shown for $0 \le t \le \beta/2$, exploiting the symmetry $C_{jj}(t) = C_{jj}(\beta - t)$. Error bars represent the estimated standard deviation.

In order to ensure the reliability of the quantum Monte Carlo (QMC) results, particular attention was devoted to the choice of simulation parameters. These parameters were determined based on systematic convergence tests, with the aim of achieving high numerical accuracy while maintaining computational efficiency.

The statistical accuracy of the results was controlled by the number of Monte Carlo samples and independent repetitions. In most cases, 10^6 Monte Carlo samples were generated, while smaller

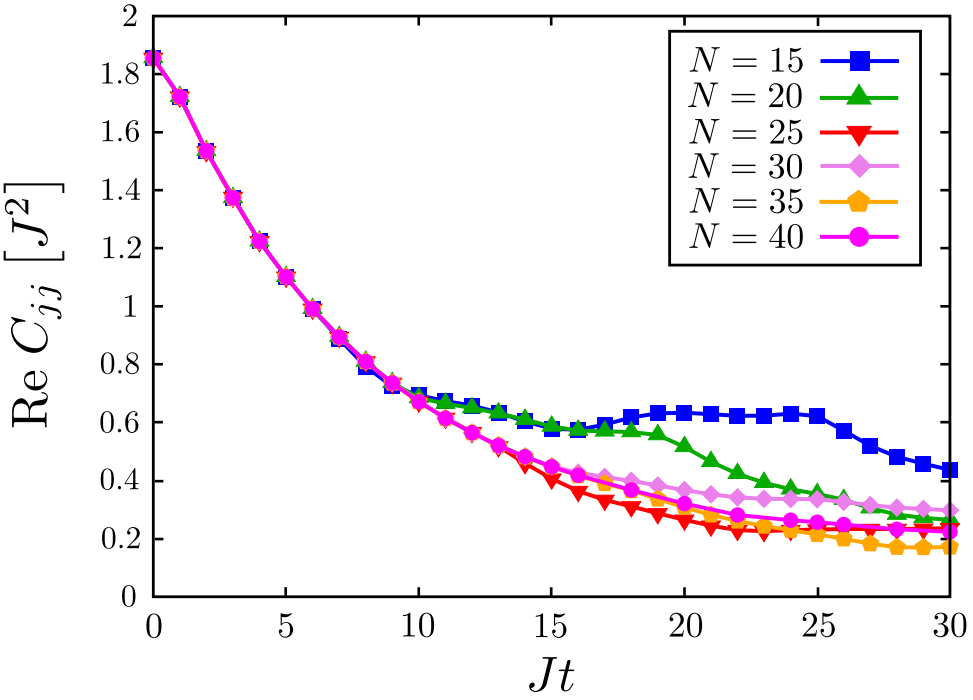

Figure 3.3: Real part of the real-time current–current correlation function for different system sizes N. Results are shown for $\omega_0/J = 1$, $G/J = 0.141$, and $T/J = 2.5$.

or larger sample sizes were used when required by the parameter regime. Each simulation was repeated 100 times. These repetitions improve the statistical reliability of the results by allowing for averaging over independent realizations, and enable the estimation of statistical uncertainties through the standard deviation. The number of samples was adjusted as needed to ensure that the relative standard deviation of the computed quantities remains below approximately 1% of the corresponding mean value.

The discretization of both imaginary and real time introduces additional numerical parameters, namely the time steps τ and Δt. Convergence tests show that the choice $\tau = \Delta t = \frac{0.1}{J}$ is sufficient, as further reduction of the time step does not lead to a significant change in the results. However, the time discretization was adjusted depending on the parameter regime and the time interval considered. In cases involving small temperatures (large β) or longer real-time intervals, slightly larger time steps were employed when verified to have no impact on the results. Conversely, for shorter time intervals or smaller β, smaller time steps were used in order to achieve adequate resolution of the correlation functions. In practice, the time intervals were discretized so as to include a sufficient number of data points, typically exceeding 15, ensuring both numerical stability and accurate representation of the time dependence.

A key parameter in the simulations is the system size, determined by the number of lattice sites N. The objective is to obtain results representative of the thermodynamic limit, $N \to \infty$. In practice, this is achieved by selecting N large enough such that further increases do not affect the computed correlation functions.

The dependence of the imaginary-time current–current correlation function on the system size is shown in Fig. 3.2 for $\omega_0/J = 1$ and $G/J = 1$, at both high temperature ($T/J = 10$) and low temperature ($T/J = 0.5$). It is observed that at high temperature, a relatively small system size ($N = 5$) is sufficient to reach convergence, whereas at low temperature a larger system ($N = 10$) is required. This behavior reflects the reduction of spatial correlations at higher temperatures, where the system becomes more local and finite-size effects are less pronounced.

The influence of system size on real-time correlation functions is illustrated in Fig. 3.3 for the case of weak electron–phonon interaction ($G/J = 0.141$), $\omega_0/J = 1$, and $T/J = 2.5$. In this regime, the carrier mean free path is large, and correspondingly larger system sizes are required to accurately

capture the dynamics. The results indicate that a system with $N = 30$ sites is necessary to obtain reliable data for times up to $Jt \approx 15$.

In practice, for each set of model parameters, short convergence checks were performed in which the system size and the time discretization were varied within a narrow range around estimated optimal values. This procedure was sufficient to verify that the chosen parameters do not affect the resulting correlation functions.

In order to reduce computational cost, simulations at shorter times were performed using smaller system sizes, as justified by these convergence tests. This is particularly advantageous since the computational effort increases rapidly with system size. In the path-integral formulation, the dimensions of the matrices and vectors grow with both the number of time slices and the number of lattice sites N resulting in a substantial increase in numerical cost for larger systems. For example, $N = 20$ was used for the time interval $5 \leq Jt \leq 10$, while $N = 30$ was used for $10 \leq Jt \leq 15$. This approach allows for efficient calculations without compromising the accuracy of the results.

Additional implementation details of the Monte Carlo simulations, including the algorithmic procedure and pseudocode, as well as a detailed overview of the parameter choices used in individual calculations (such as system size, time discretization, and number of samples), are provided in Appendix C.

3.4 Results

3.4.1 Current-current correlation function

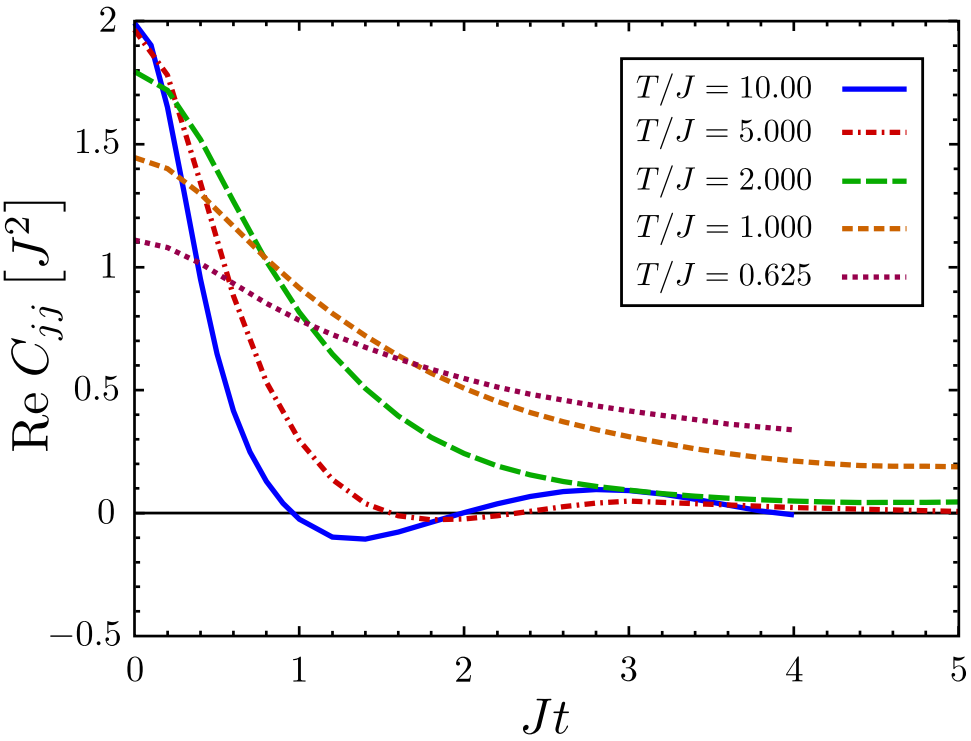

Figure 3.4: Time decay of the real part of the current–current correlation function at different temperatures. Results are shown for $\omega_0/J = 1$ and $G/J = 0.5$.

The time dependence of the current–current correlation function provides direct insight into the transport properties of the system. In this subsection, the time evolution of the correlation function in both real and imaginary time is analyzed as a function of temperature and electron–phonon interaction strength. The resulting behavior reflects the underlying transport mechanisms and determines how reliably the mobility can be extracted, as discussed in the following subsection.

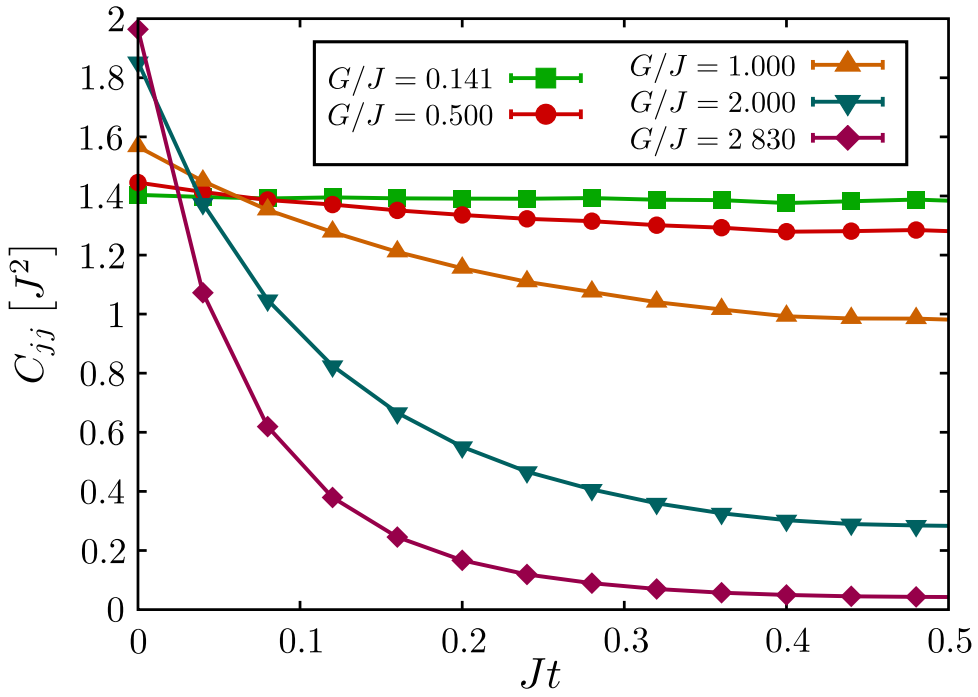

Figure 3.5: Imaginary-time current–current correlation function for different interaction strengths. Results are shown for $T/J = 1$ and $\omega_0/J = 1$. The data are presented for $0 \leq t \leq \beta/2$, exploiting the symmetry $C_{jj}(t) = C_{jj}(\beta - t)$.

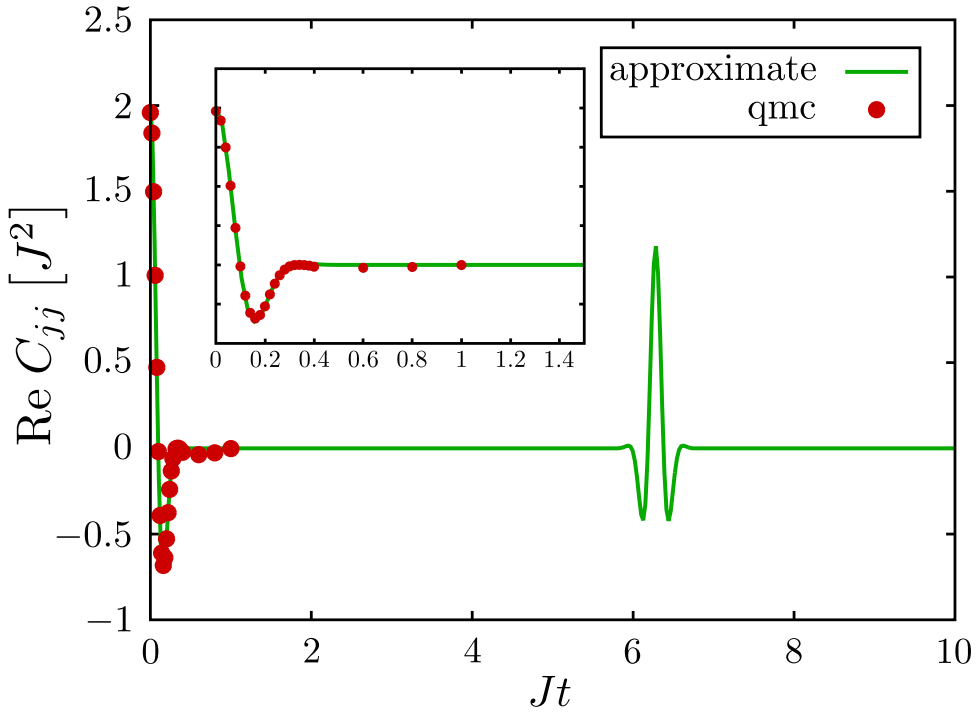

Figure 3.6: Time dependence of the real part of the current–current correlation function for $G/J = 2.83$. Results are shown for $T/J = 2$, obtained using an approximate method from Ref. [133] (labeled "approximate") and from QMC calculations (labeled "qmc"). The inset shows a detailed view for times $Jt \leq 1.5$.

The time decay of the real part of the real-time current–current correlation function for $\omega_0/J = 1$ and $G/J = 0.5$ is shown in Fig. 3.4 for a range of temperatures from low (T/J=0.625) to high (T/J=10). The results are displayed as continuous lines to highlight their functional dependence on time, and the statistical uncertainty is below 1%, making it invisible at the scale of the figure. The chosen interaction strength $G/J = 0.5$ allows both rapid decay at high temperatures and slow decay at low temperatures to be clearly observed within the accessible time intervals.

At higher temperature ($T/J \geq 2$), the correlation function decays rapidly and reaches zero within the accessible simulation time window, indicating that the relevant dynamics are confined to short times. In this regime, the full time dependence is captured, which enables a direct evaluation of the dc mobility via the Kubo formula,with the uncertainty determined primarily by the small statistical error of the data. For the highest temperature ($T/J = 10$), it is observed that the correlation function crosses zero, exhibits a shallow minimum, and then converges back to zero. This type of behavior is also observed at stronger electron–phonon interactions, as shown in Fig. 3.6.

At lower temperatures ($T/J < 2$), the decay of the correlation function becomes significantly slower, and within the accessible time interval the correlation function appears nearly asymptotic to zero, indicating that a significant portion of the long-time behavior is not captured. These contributions cannot be fully resolved as the dynamical sign problem becomes increasingly pronounced, limiting the accessible time range. The data are therefore shown only up to times where the statistical uncertainty remains controlled. As a result, the correlation function is only partially captured, and direct integration of the Kubo formula would lead to a substantial underestimation of the mobility. For weaker interactions, this effect is even more pronounced, as the decay is slower and the full time dependence is generally inaccessible except at the highest temperatures. In contrast, for stronger interactions the decay becomes faster and more structured, but the accessible time interval is more severely restricted. The chosen interaction strength ($G/J = 0.5$) considered here therefore provides a representative balance between these two cases .

The time dependence of the current–current correlation function in imaginary time is shown in Fig. 3.5 for $T/J = 1$ and $\omega_0/J = 1$, for a range of interaction strengths. The results are presented as data points connected by lines to illustrate the functional dependence on imaginary time, while statistical uncertainties remain negligible on the scale of the figure. A clear qualitative difference is observed between weak and strong electron–phonon coupling. For weak interactions ($G/J = 0.141$), the correlation function exhibits only a very weak dependence on imaginary time and appears nearly constant over the entire interval. With increasing interaction strength, the variation with imaginary time becomes more pronounced, indicating a stronger functional dependence.

This behavior directly reflects the amount of information contained in the imaginary-time data. In the weak-coupling regime, the nearly constant behavior provides only limited information on the underlying dynamics, making analytic continuation based on imaginary-time data alone highly unreliable. In this case, the real-time correlation functions remain accessible over longer time intervals and therefore provide the main source of information. In contrast, for stronger interactions, the pronounced variation in imaginary time provides a more informative input for analytic continuation. Temperature, in this case, primarily affects the overall time scale and magnitude of the correlation function, while the qualitative behavior remains governed by the interaction strength.

Additional insight into the behavior of the real-time correlation function at strong coupling is provided in Fig. 3.6, shown for $G/J = 2.83$ and $T/J = 2$, where the QMC results are compared with those obtained by an approximate method from Ref. [133]. A good qualitative agreement is observed, confirming that the QMC results capture the main features of the correlation function. In particular, the approximate result exhibits a sequence of oscillatory peaks at times $t_n = n\frac{2\pi}{\omega_0}$ ($n \geq 1$) each accompanied by smaller minima. The QMC data reproduce the initial peak around $Jt = 0$, which has a similar structure to that observed at weaker interaction strength in Fig. 3.4.

The accessible time interval in the QMC calculations is limited by the dynamical sign problem, and therefore only the short-time behavior is reliably captured. As a result, the additional peaks present at longer times in the approximate solution are not resolved in the QMC data. This comparison demonstrates that while the essential short-time structure of the correlation function is accurately reproduced, longer-time contributions remain inaccessible within the simulation.

3.4.2 Standard deviation of QMC results depending on choice of electron basis

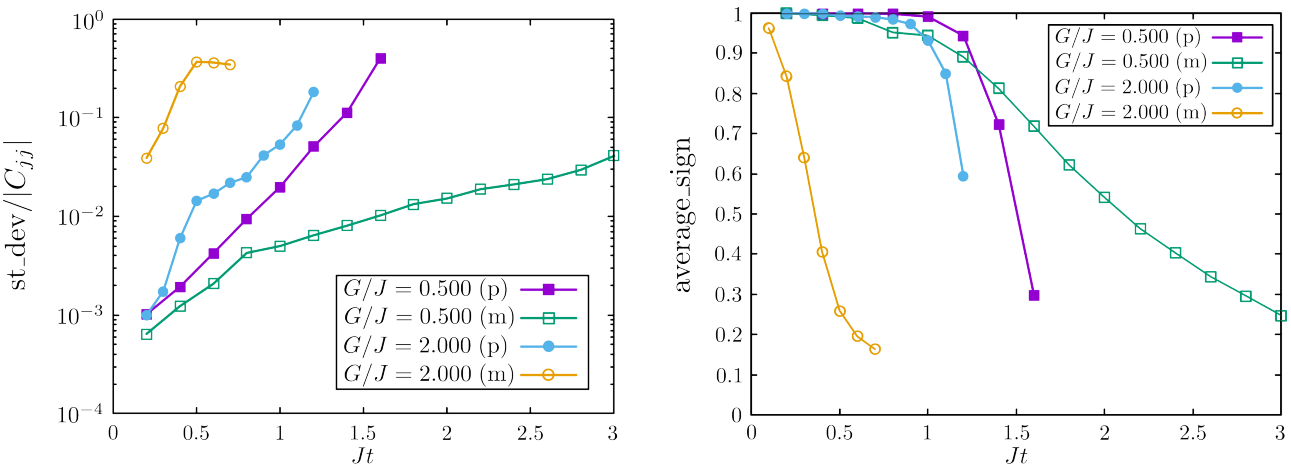

(a) **(b)**

Figure 3.7: Real-time dependence of the relative standard deviation and the average sign of the current–current correlation function. Results are shown for $\omega_0/J = 1$ and $T/J = 2$. Panel (a) corresponds to the relative standard deviation and panel (b) to the average sign. The label "m" denotes results obtained in the momentum representation, while "p" denotes results obtained in the position representation.

In this subsection, the influence of the choice of electron basis on the statistical accuracy of QMC calculations and the severity of the sign problem is examined quantitatively. This is illustrated in Fig. 3.7, where the relative standard deviation of the current–current correlation function, defined as the ratio of the standard deviation to its absolute value, is shown as a function of real time for calculations performed in both the momentum and position representations.

The results are presented up to times where the statistical uncertainty becomes comparable to the value of the correlation function. A clear dependence on both interaction strength and choice of basis is observed. For weak electron–phonon interaction ($G/J = 0.5$), the momentum representation yields significantly smaller statistical fluctuations. In contrast, for stronger interaction ($G/J = 2$), the position representation becomes more favorable, resulting in a noticeably reduced standard deviation. This demonstrates that the efficiency of the Monte Carlo sampling strongly depends on the basis in which the electronic degrees of freedom are represented.

To clarify the origin of this behavior, the average sign of the Monte Carlo estimator is shown in Fig. 3.7(b) for the same set of parameters. The average sign is defined as

$$s_{\mathrm{av}} = \left| \left\langle \frac{A_i}{|A_i|} \right\rangle \right| , \tag{3.60}$$

where A_i denotes the individual contributions to the Monte Carlo sum. The value $s_{\mathrm{av}} = 1$ corresponds to the absence of a sign problem, while $s_{\mathrm{av}} = 0$ indicates a completely random distribution of phases and thus a severe sign problem.

A direct correlation between the average sign and the statistical uncertainty is observed. In regimes where the average sign remains close to unity, the standard deviation is small and reliable results can be obtained. As the average sign decreases, the statistical fluctuations increase rapidly, and the results become unreliable once the standard deviation becomes comparable to the result. This confirms that the observed dependence of the statistical accuracy on the choice of basis originates from the severity of the sign problem in the corresponding representation.

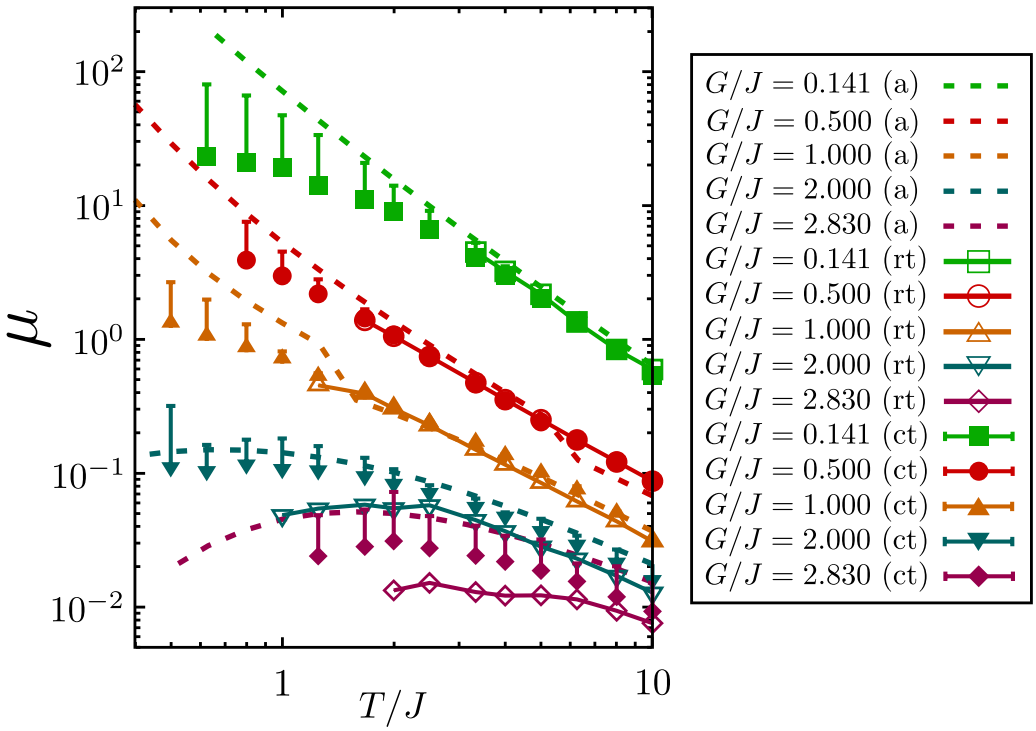

Figure 3.8: Temperature dependence of the Holstein polaron mobility obtained from path-integral QMC calculations for different electron–phonon interaction strengths at $\omega_0/J = 1$. Results labeled "ct" are obtained by analytic continuation from combined real- and imaginary-time data. Results labeled "rt" are obtained by direct integration of the real-time current–current correlation function (full lines are guides to the eye). Results labeled "a" correspond to approximate calculations from Ref. [133]..

3.4.3 Temperature dependence of Holstein polaron mobility

In this subsection, the temperature dependence of the polaron mobility is presented as the main result of the analysis developed in the preceding sections. The temperature dependence of mobility for the one dimensional Holstein model is shown in Fig. 3.8 for e-ph interaction strengths ranging from weak ($G/J = 0.141$) to strong ($G/J = 2.830$) at $\omega_0/J = 1$.

The results labeled "ct" correspond to mobilities obtained using the analytic continuation procedure, which combines imaginary-time data with real-time data up to times where the QMC results remain reliable. The associated error bars are estimated following the procedure introduced in the previous subsection. In brief, the relative error of analytic continuation is first evaluated using reference correlation functions constructed from the dynamic mobility obtained in Ref. [133]. This relative error, defined by Eq. (3.59), is then used as an estimate for the uncertainty when the procedure is applied to QMC data for the same set of parameters, which is justified by the close similarity of the approximate and QMC correlation functions. The resulting relative error is subsequently converted into an estimate of the absolute error of the mobility. It is observed that analytic continuation systematically tends to underestimate the mobility. For this reason, the error bars shown in Fig. 3.8 are presented as one-sided.

The results labeled "rt" are obtained by direct integration of the real-time current–current correlation function over the time interval where reliable data are available. The corresponding statistical uncertainty is very small and remains negligible on the scale of the results. For comparison, results from the approximate method of Ref. [133], labeled "a", are also shown.

The reliability of the obtained results depends strongly on both interaction strength and temperature. The most accurate results are obtained for relatively weak interactions $G/J \lesssim 1$ and higher temperatures $T/J \gtrsim 2$, where the full time decay of the correlation function can be captured and direct integration yields reliable values of mobility. In this regime, analytic continuation produces results consistent with those obtained from real-time integration. For stronger interactions ($G/J > 1$)

at higher temperatures, reasonably accurate results can still be obtained, although the accessible time interval becomes more restricted. In contrast, at low temperatures ($T/J < 1$), the slow decay of the correlation function and the severity of the sign problem significantly limit the accuracy of both approaches.

A comparison with the results of Ref. [133] shows good overall agreement across the parameter range considered. In most cases, the reference results lie within the estimated error bars of the QMC-based results. The consistency between two independent approaches provides mutual validation of the obtained results. In particular, since the QMC method employed here is numerically exact within statistical uncertainty, this agreement further supports the reliability of the approximate method used in Ref. [133] in describing the temperature dependence of the mobility.

The choice of electronic basis in the path-integral calculations is influenced by the interaction strength. For weak electron–phonon coupling ($G/J < 1$), the momentum representation is used in real-time calculations. In this case, the residual phase appearing in the estimator for the real-time current–current correlation function is proportional to the factor $\Delta t G$, and remains sufficiently small for efficient Monte Carlo sampling. As the interaction strength G increases, however, the dynamical sign problem becomes more pronounced, making this representation less effective. This limitation is further exacerbated at low temperatures, where longer time intervals become relevant, as discussed in the previous subsection.

The position representation is used for the evaluation of the current–current correlation function in imaginary time for all interaction strengths, and in real time for stronger interactions ($G/J \geq 1$), where it provides a more stable numerical approach. Additional details on the calculations for each parameter set shown in Fig. 3.8, including the choice of basis, are provided in Appendix C.

A comparison is also made with the results of Ref. [66], which, to the best of current knowledge, represents the only study of the temperature dependence of Holstein polaron mobility obtained using a methodology that is, in principle, numerically exact. For the weakest interaction ($G/J = 0.141$), good agreement is observed within the temperature range where the estimated error of the present results remains small. However, for stronger interactions ($G/J = 1, 2, 2.83$), the values reported in Ref. [66] are consistently lower than those obtained here.

For example, at $G/J = 2.83$, $\omega_0/J = 1$ and $T/J = 2$, mobility values in the range $\mu \in (2.8, 8.1) \times 10^{-3}$ are reported in Ref. [66], while the present results show $\mu \in (3.1, 7.2) \times 10^{-2}$. It is noted that direct integration of the QMC current-current correlation function over the first peak alone (for $0 \leq Jt \leq 1$, see Fig. 3.6) already gives $\mu \approx 1.5 \cdot 10^{-2}$, while contributions from subsequent peaks can only increase this value.

The results of Ref. [66] are obtained using analytic continuation based solely on imaginary-time data. As discussed previously, the limited information content of imaginary-time correlation functions in certain parameter regimes can lead to an underestimation of the mobility. This is therefore considered a plausible explanation for the observed discrepancy between the two sets of results.

In this chapter, the temperature dependence of the polaron mobility in the one-dimensional Holstein model has been obtained using a path-integral quantum Monte Carlo approach combined with analytic continuation. The analysis of current–current correlation functions in both real and imaginary time has enabled a detailed understanding of the regimes in which reliable results can be achieved. The methodology is shown to provide accurate results for weak to intermediate interaction strengths and higher temperatures, while its applicability becomes limited at low temperatures due to the dynamical sign problem and the restricted accessible time intervals. These findings establish a consistent framework for the calculation of transport properties within the considered model and provide the basis for further analysis presented in the following chapter.

Chapter 4

Transport regimes of Holstein polaron

The Holstein model represents a prototypical framework for studying systems with electron–phonon interaction. Despite its simplicity, a complete understanding of its transport properties across the full parameter space remains an open problem. In the preceding chapters, the theoretical framework for describing charge transport in such systems has been established, and a numerically exact path-integral quantum Monte Carlo (QMC) method has been developed to evaluate current–current correlation functions and carrier mobility.

As discussed in Chapter 2, the mobility of charge carriers in systems with electron–phonon interaction is governed by the interplay between coupling strength and temperature, which gives rise to qualitatively different transport regimes (see Section 2.3). In the weak-coupling limit, carriers remain delocalized and transport is well described within the band transport picture (Section 2.3.2). In contrast, in the regime of strong coupling and sufficiently high temperatures, carriers become localized and propagate via thermally activated hopping processes (Section 2.3.1), while at low temperatures a coherent but strongly renormalized motion may occur within a narrow polaron band (Section 2.3.3). These regimes form the basis of most theoretical descriptions of charge transport in such systems.

However, these transport theories are typically derived under restrictive assumptions and are valid only within limited regions of parameter space. In practice, approaches based on band or hopping transport are often applied beyond their formal range of validity, particularly in situations where the relevant energy scales are comparable and the dominant transport mechanism is not known a priori. At the same time, numerically exact methods that do not rely on such assumptions are generally restricted by computational limitations and can typically be applied only within a limited range of parameters.

For this reason, it is of interest to examine the range of validity of the different transport regimes and to assess whether they provide a consistent description of transport behavior across the parameter space of the Holstein model. In principle, this could be achieved by comparing numerically exact results for dynamical quantities, such as current–current correlation functions or carrier mobility, with the predictions of the corresponding transport theories. In practice, however, numerically exact approaches based on real-time or real-frequency formulations are computationally demanding and therefore limited in their applicability, primarily due to the dynamical sign problem and the need for analytic continuation.

In contrast, imaginary-time quantities can be evaluated reliably over a much broader range of parameters within the path-integral QMC framework developed in Chapter 3. In the present chapter, path-integral QMC calculations of the imaginary-time current–current correlation function are used as a primary tool for analyzing transport behavior. For the same set of parameters, the corresponding quantities are evaluated within the approximate descriptions of band transport, hopping transport, and polaron band transport. This enables a direct comparison between the QMC results and the corresponding approximate descriptions, allowing the regions of validity of these transport regimes to be examined.

In cases where the comparison of imaginary-time correlation functions does not provide a conclusive classification, the analysis can be further supplemented by considering real-time correlation

functions or by comparison with available numerically exact results for dc mobility, providing an additional basis for examining the transport regimes across the parameter space. Based on this analysis, a transport regime diagram for the Holstein model can be constructed.

4.1 Current-current correlation function and dc mobility in different transport regimes

The different transport regimes are associated with distinct microscopic mechanisms of carrier motion, which are reflected in the temporal behavior of the current–current correlation function. The analysis in this section is therefore formulated in terms of these correlation functions and the corresponding expressions for dc mobility.

In the strong-coupling regime, where small polarons are formed, transport may proceed either through coherent motion within a narrow polaron band at low temperatures or through thermally activated hopping between localized states at higher temperatures. In contrast, in the weak-coupling regime, transport is governed by band-like motion of delocalized carriers, with scattering by lattice vibrations determining the temperature dependence of mobility.

These qualitatively different mechanisms give rise to distinct forms of the current–current correlation function, which in turn determine the corresponding transport coefficients within the Kubo formalism. In the following subsections, the expressions for the current–current correlation function and the associated dc mobility are presented for the three relevant regimes, namely hopping transport of small polarons, coherent transport within a narrow polaron band, and conventional band transport of large polarons.

4.1.1 Hopping transport at all temperatures and in high-temperature limit

In the strong-coupling regime of the Holstein model, charge carriers form small polarons, whose transport is governed by thermally activated hopping between localized states, as discussed in Section 2.3.1. In this regime, the electronic transfer integral is treated as a perturbation, while the coupling to lattice vibrations determines the dynamics of the hopping process.

Following the derivation presented in Chapter 2, the transition rate between two neighboring sites is obtained within Fermi's golden rule framework and can be written as [84, 134, 135]

$$W = J^2 \int_{-\infty}^{\infty} \mathrm{d}t \; \mathrm{e}^{-2(\frac{G}{\omega_0})^2[2n_{\mathrm{ph}}+1-(n_{\mathrm{ph}}+1)\mathrm{e}^{-\mathrm{i}\omega_0 t}-n_{\mathrm{ph}}\mathrm{e}^{\mathrm{i}\omega_0 t}]}, \tag{4.1}$$

where $n_{\mathrm{ph}} = (\mathrm{e}^{\beta\omega_0} - 1)^{-1}$ denotes the phonon occupation number.

The corresponding current–current correlation function takes the form [136]

$$C_{jj}(t) = 2J^2\mathrm{e}^{-2(\frac{G}{\omega_0})^2[2n_{\mathrm{ph}}+1-(n_{\mathrm{ph}}+1)\mathrm{e}^{-\mathrm{i}\omega_0 t}-n_{\mathrm{ph}}\mathrm{e}^{\mathrm{i}\omega_0 t}]}. \tag{4.2}$$

In the high-temperature limit, these expressions reduce to the Marcus form of the hopping rate [137–141],

$$W = J^2\sqrt{\frac{\beta\pi}{\lambda}}\mathrm{e}^{-\frac{\beta\lambda}{4}} \; , \tag{4.3}$$

with $\lambda = \frac{2G^2}{\omega_0}$. The corresponding mobility is then given by

$$\mu = \beta J^2\sqrt{\frac{\beta\pi}{\lambda}}\mathrm{e}^{-\frac{\beta\lambda}{4}} \; . \tag{4.4}$$

In this limit, the current–current correlation function assumes a Gaussian form [136],

$$C_{jj}(t) = 2J^2\mathrm{e}^{-\sigma_0^2 t^2}\mathrm{e}^{-\mathrm{i}\beta\sigma_0^2 t} \; , \tag{4.5}$$

where $\sigma_0^2 = \frac{2G^2}{\beta\omega_0}$.

However, for the Holstein model with a single dispersionless phonon mode, the expression in Eq. (4.1) leads to a divergence of the hopping rate and the corresponding dc mobility. This behavior originates from the fact that the correlation function in Eq. (4.2) does not decay to zero in the long-time limit, reflecting the implicit assumption of infinitely long-lived small-polaron states.

To account for finite lifetimes, an improved description can be obtained by including self-energy corrections that introduce a broadening of polaron states. This removes the unphysical long-time behavior of the correlation function and provides a more realistic description of hopping dynamics. Following the approach presented in Ref. [136], the current–current correlation function is modified to

$$C_{jj}(t) = g(t)\mathrm{e}^{-2(\frac{G}{\omega_0})^2[2n_{\mathrm{ph}}+1-(n_{\mathrm{ph}}+1)\mathrm{e}^{-i\omega_0 t}-n_{\mathrm{ph}}\mathrm{e}^{\mathrm{i}\omega_0 t}]}\,, \tag{4.6}$$

where the prefactor $g(t)$ accounts for the finite lifetime effects and introduces an effective decay of the correlation function. It is given by

$$g(t) = 2J^2\frac{\beta}{t(\beta-\mathrm{i}t)}\frac{1}{\sqrt{c_0}}\frac{I_1\left(-2(\beta-\mathrm{i}t)\sqrt{c_0}\right)J_1(2t\sqrt{c_0})}{I_1(-2\beta\sqrt{c_0})}\,, \tag{4.7}$$

with I_1 and J_1 denoting the modified and ordinary Bessel functions of the first kind, respectively, both of order 1. The parameter c_0 is defined as

$$c_0 = 2J^2\mathrm{e}^{-2(\frac{G}{\omega_0})^2(2n_{\mathrm{ph}}+1)}I_0(\alpha), \tag{4.8}$$

$$\alpha = 4(\frac{G}{\omega_0})^2\sqrt{n_{\mathrm{ph}}(n_{\mathrm{ph}}+1)}. \tag{4.9}$$

The corresponding dc mobility, obtained with the Kubo formula (Eq. (2.30)), is then given by

$$\mu = 2J^2\beta\pi\mathrm{e}^{-2(\frac{G}{\omega_0})^2(2n_{\mathrm{ph}}+1)}\frac{\sum_{l=-\infty}^{\infty}\int \mathrm{d}\omega\; e^{-\beta\omega}A(\omega)A(\omega+l\omega_0)I_l(\alpha)e^{-\frac{l\omega_0\beta}{2}}}{\int \mathrm{d}\omega\; e^{-\beta\omega}A(\omega)}, \tag{4.10}$$

where the spectral function $A(\omega)$ is given by

$$A(\omega) = \frac{\sqrt{4c_0-\omega^2}}{2\pi c_0}\theta(4c_0-\omega^2), \tag{4.11}$$

and I_l denotes the modified Bessel function of order l. This expression provides a finite and well-defined mobility by incorporating the broadening of polaron states.

In the following, Eqs. (4.6) and (4.10) are used as the reference expressions for the current–current correlation function and dc mobility in the hopping regime. Their high-temperature limits, given by Eqs. (4.5) and (4.4), are used for comparison. Imaginary-time correlation functions are obtained by the substitution $t \to -\mathrm{i}\tau$.

For the presentation of results, all energies are expressed in units of the transfer integral J, while the electron–phonon interaction strength is parameterized by the dimensionless coupling $\lambda = G^2/(2J\omega_0)$.

As shown in Fig. 4.1, the mobility obtained from Eq. (4.10) approaches the high-temperature result given by Eq. (4.4) with increasing temperature, and the two expressions eventually converge. This behavior reflects the expected crossover to the Marcus regime at sufficiently high temperatures.

The influence of the phonon frequency is also clearly visible. Comparison of Figs. 4.1a and 4.1b shows that for smaller values of ω_0/J, the high-temperature Marcus limit is reached at lower temperatures, while for larger phonon frequencies this shift occurs at higher temperatures. This reflects the fact that the onset of high-temperature effects is controlled by the ratio of thermal energy to the phonon energy scale.

The current–current correlation functions shown in Fig. 4.2 exhibit good agreement between the full expressions and their high-temperature limits at elevated temperatures, both in imaginary time

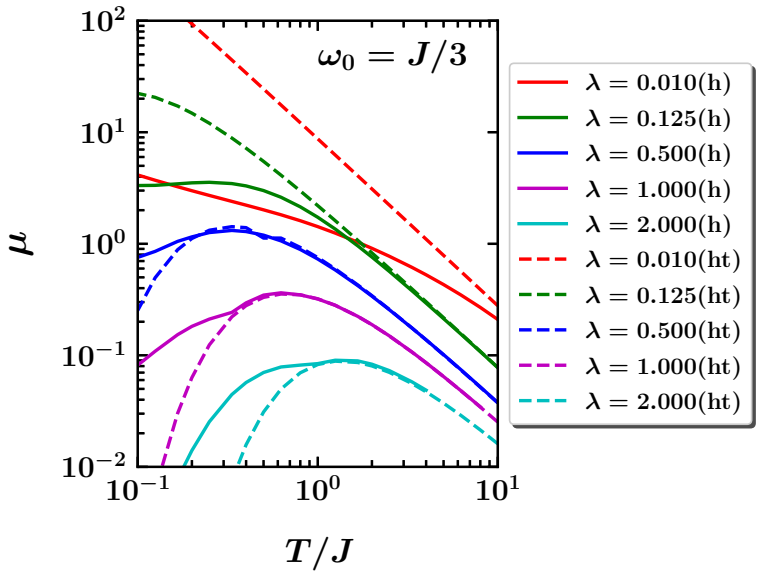

(a)

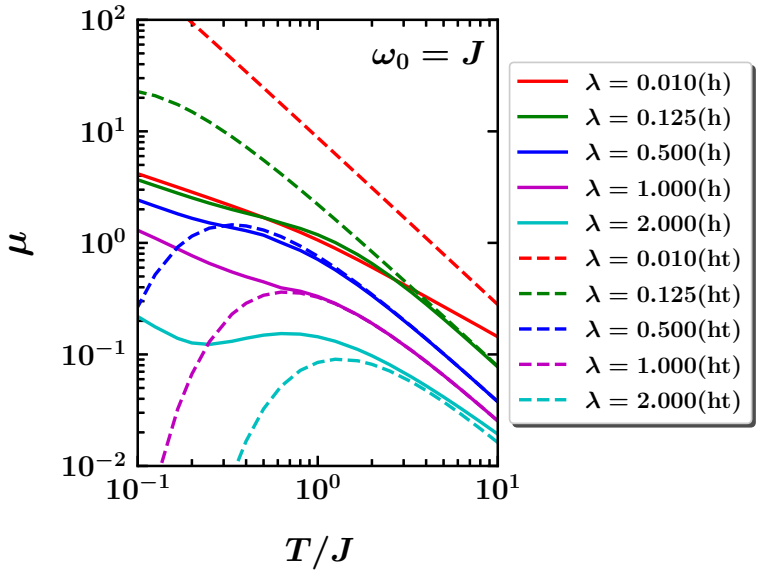

(b)

Figure 4.1: Temperature dependence of the hopping mobility for different interaction strengths λ. Results obtained from Eq. (4.10) are shown with solid lines (label "h"), while the high-temperature approximation given by Eq. (4.4) is shown with dashed lines (label "ht"). Panel (a) corresponds to $\omega_0 = J/3$ and panel (b) to $\omega_0 = J$.

and in the real parts of the real-time correlation functions, while clear deviations appear at lower temperatures. This behavior is consistent with the trends observed for the mobility, where agreement with the high-temperature limit is likewise obtained only in the appropriate temperature range.

Such agreement confirms that the high-temperature approximation captures the essential transport behavior in the appropriate regime. At the same time, the deviations observed at lower temperatures highlight the limitations of the Marcus description outside its range of validity.

Overall, these results are consistent with the theoretical expectations established in Section 2.3.1, where the hopping transport picture is shown to reduce to the Marcus form in the high-temperature limit.

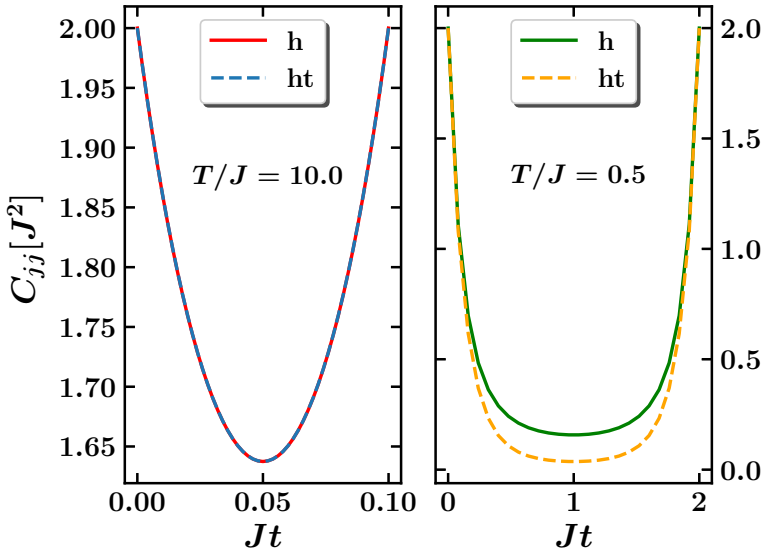

(a)

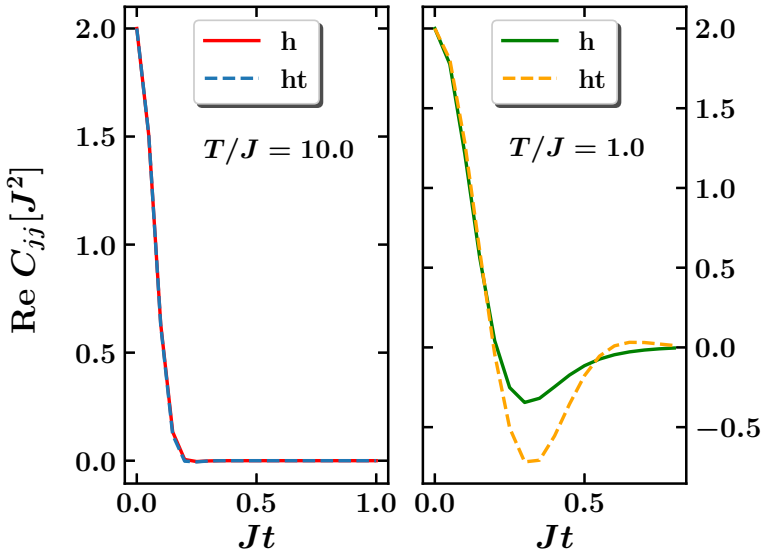

(b)

Figure 4.2: Imaginary-time and real-time current–current correlation functions in the hopping regime. Panel (a) shows the imaginary-time correlation function, while panel (b) shows the real part of the real-time correlation function. Solid lines (label "h") correspond to Eq. (4.6), while dashed lines (label "ht") correspond to its high-temperature limit, Eq. (4.5). Results are shown for $\omega_0 = 3J$ and $\lambda = 2.000$, with temperatures $T/J = 10.0$ and $T/J = 0.5$ in (a), and $T/J = 10.0$ and $T/J = 1.0$ in (b

4.1.2 Polaron band transport and crossover to hopping regime

In the strong-coupling regime at low temperatures, charge carriers form polarons that retain a degree of coherence and propagate within a narrow polaron band, as discussed in Section 2.3.3. This regime is commonly referred to as polaron band transport and is characterized by a strong renormalization of the electronic bandwidth due to the coupling to lattice vibrations.

A convenient description of this regime is obtained within the Lang–Firsov transformed framework introduced in Section 2.3.3, in which the Hamiltonian is expressed in terms of polaron quasiparticles. The transformed Hamiltonian describes a renormalized band with dispersion

$$\tilde{\varepsilon}_k = -\frac{G^2}{\omega_0} - 2\tilde{J}\cos k, \tag{4.12}$$

where the effective transfer integral is given by

$$\tilde{J} = J\mathrm{e}^{-(2n_{\mathrm{ph}}+1)\frac{G^2}{\omega_0^2}}. \tag{4.13}$$

In this representation, the Hamiltonian can be written as $\tilde{H} = \tilde{H}_0 + \tilde{V}$, where $\tilde{H}_0$ describes noninteracting polarons, while $\tilde{V}$ contains residual coupling between polarons and lattice fluctuations. These residual interactions give rise to a finite lifetime of polaron states and are treated perturbatively. Their effect is incorporated at the level of the self-energy, while the dominant coherent contributions to transport are treated explicitly, following the approach of Ref. [133].

Within this framework, the current–current correlation function can be expressed in terms of single-particle Green's functions and an interaction-dependent vertex contribution [136]. The resulting expression contains contributions from both coherent processes, in which no phonons are exchanged, and incoherent phonon-assisted processes. In the polaron band transport regime, coherent processes are dominant. Accordingly, only the leading contribution is retained, corresponding to the independent-particle (bubble) approximation.

Within this approximation, the current–current correlation function takes the form

$$C_{jj}(t) = \frac{\sum_{k_1k_2}\langle a_{k_1}^\dagger(t)a_{k_1}\rangle\langle a_{k_2}(t)a_{k_2}^\dagger\rangle Y_{k_1k_2}(t)}{\sum_k\langle a_k^\dagger a_k\rangle}. \tag{4.14}$$

The quantity $Y_{k_1k_2}(t)$ encodes the phonon dressing of the current operator, which arises from the Lang–Firsov transformation. Its explicit form follows from the evaluation of phonon correlation functions associated with the transformed hopping operators and has been derived in Ref. [133]. It can be written as

$$Y_{k_1k_2}(t) = -\frac{\tilde{J}^2}{N}\sum_{X,Y=\pm1}\sum_Z XY\mathrm{e}^{\mathrm{i}k_1(X+Z)}\mathrm{e}^{\mathrm{i}k_2(X-Z)}\theta_{XYZ}(t), \tag{4.15}$$

where X, Y, and Z denote lattice-site displacements entering the transformed hopping processes, and $\theta_{XYZ}(t)$ describes the corresponding phonon correlations.

To distinguish between coherent and incoherent contributions, the function $\theta_{XYZ}(t)$ is decomposed as

$$\theta_{XYZ}(t) = \theta_{XYZ}^{(0)} + \theta_{XYZ}^{(1)}(t). \tag{4.16}$$

The term $\theta_{XYZ}^{(1)}(t)$ contains oscillatory factors of the form $\mathrm{e}^{\mathrm{i}l\omega_0 t}$, corresponding to processes involving phonon emission and absorption. Since polaron band transport is dominated by coherent motion, such processes are neglected, and only the static contribution $\theta_{XYZ}^{(0)}$ is retained in the following.

The expectation values entering the correlation function can be expressed in terms of the polaron spectral function $\tilde{A}_k(\omega)$ as

$$\langle a_k^\dagger(t)a_k\rangle = \int \mathrm{d}\omega\ \mathrm{e}^{\mathrm{i}\omega t}\tilde{A}_k(\omega)\mathrm{e}^{-\beta\omega}, \tag{4.17}$$

$$\langle a_k(t)a_k^\dagger\rangle = \int \mathrm{d}\omega\ \mathrm{e}^{-\mathrm{i}\omega t}\tilde{A}_k(\omega). \tag{4.18}$$

Using the Kubo formalism, the dc mobility can then be expressed in terms of the spectral function and the renormalized band velocity $\tilde{v}_k = -2\tilde{J}\sin k$. In the low-temperature regime relevant for polaron band transport, the phonon occupation number is small, and the Bessel-function contributions entering $\theta_{XYZ}^{(0)}$ can be approximated by unity, so that multi-phonon processes are effectively suppressed and the dominant coherent contribution is retained. This leads to the simplified expression

$$\mu_{\mathrm{dc}} = \pi\beta\frac{\sum_k \tilde{v}_k^2\int \mathrm{d}\omega\ \tilde{A}_k(\omega)^2\mathrm{e}^{-\beta\omega}}{\sum_k \tilde{n}_k}, \tag{4.19}$$

where $\tilde{n}_k = \mathrm{e}^{-\beta\tilde{\varepsilon}_k}$.

Assuming a narrow spectral function, which corresponds to long-lived quasiparticles with weak scattering, the integral can be evaluated as

$$\int \mathrm{d}\omega\ \tilde{A}_k(\omega)^2 \mathrm{e}^{-\beta\omega} = -\frac{\mathrm{e}^{-\beta\omega}}{2\pi \mathrm{Im}\Sigma_k(\omega)}\bigg|_{\omega=\tilde{\varepsilon}_k} = \frac{\tilde{n}_k \tilde{\tau}_k}{\pi}, \tag{4.20}$$

where $\tilde{\tau}_k$ denotes the polaron lifetime, determined by the imaginary part of the self-energy (see Section 2.3). The explicit form of the self-energy $\Sigma_k(\omega)$ is provided in Appendix D.

The dc mobility then takes the form

$$\mu_{\mathrm{dc}} = \beta \frac{\sum_k \tilde{n}_k \tilde{\tau}_k \tilde{v}_k^2}{\sum_k \tilde{n}_k}, \tag{4.21}$$

which has the same formal structure as the band transport expression derived in Section 2.3.2, with all quantities replaced by their renormalized counterparts.

To evaluate the imaginary-time current–current correlation function, an additional approximation can be introduced by treating the spectral function as sharply peaked, $\tilde{A}_k(\omega) \approx \delta(\omega - \tilde{\varepsilon}_k)$, effectively neglecting lifetime effects and retaining only the quasiparticle energy. While this approximation is not sufficient for describing real-time dynamics or dc mobility, it is adequate for imaginary-time quantities, which are primarily sensitive to the energy distribution rather than the detailed spectral broadening.

The corresponding correlation function is then given by

$$C_{jj}(z) = \frac{\sum_{k_1 k_2} \mathrm{e}^{-\beta\tilde{\varepsilon}_{k_1}} \mathrm{e}^{\mathrm{i}(\tilde{\varepsilon}_{k_1} - \tilde{\varepsilon}_{k_2})z} Y^{(0)}_{k_1 k_2}}{\sum_k \mathrm{e}^{-\beta\tilde{\varepsilon}_k}}\ , \tag{4.22}$$

where $z = -\mathrm{i}\tau$ ($0 \le \tau \le \beta$), and $Y^{(0)}_{k_1 k_2}$ denotes the contribution corresponding to coherent processes, obtained from Eq. (4.15) by replacing θ_{XYZ} with $\theta^{(0)}_{XYZ}$.

As discussed in Section 2.3, polaron band transport is expected to dominate at low temperatures in the strong-coupling regime. To compare the two transport mechanisms, the mobility obtained from Eq. (4.21) is considered alongside the hopping mobility given by Eq. (4.10). The intersection of the corresponding curves can be used as a rough estimate of the crossover between the two transport mechanisms.

The comparison between the mobilities obtained within the polaron band and hopping transport descriptions is shown in Fig. 4.3. A clear trend can be observed as the interaction strength λ increases: the intersection between the polaron band and hopping mobilities progressively shifts towards lower temperatures. This indicates that, for stronger electron–phonon coupling, the system transitions to hopping transport already at relatively low temperatures. In this regime, the increased coupling leads to stronger localization of charge carriers, which suppresses coherent motion within the polaron band and favors thermally activated hopping processes.

The role of the phonon frequency is also evident from the figure. As ω_0 increases, the crossover shifts to higher temperatures. This behavior is consistent with the trend already observed in the hopping regime and reflects the fact that larger phonon energies require higher thermal energy for incoherent, phonon-assisted processes to become dominant. In other words, for higher phonon frequencies, the system remains in the coherent, band-like regime over a wider temperature range.

Finally, it is important to emphasize that this comparison is physically meaningful primarily in the strong-coupling regime. For weaker interaction strengths, the assumptions underlying both the hopping and the polaron band descriptions are not strictly satisfied, and the interpretation of the crossover becomes less reliable. For this reason, only results corresponding to sufficiently large interaction strengths (e.g., $\lambda \gtrsim 0.5$) are considered when identifying the crossover between polaron band and hopping transport.

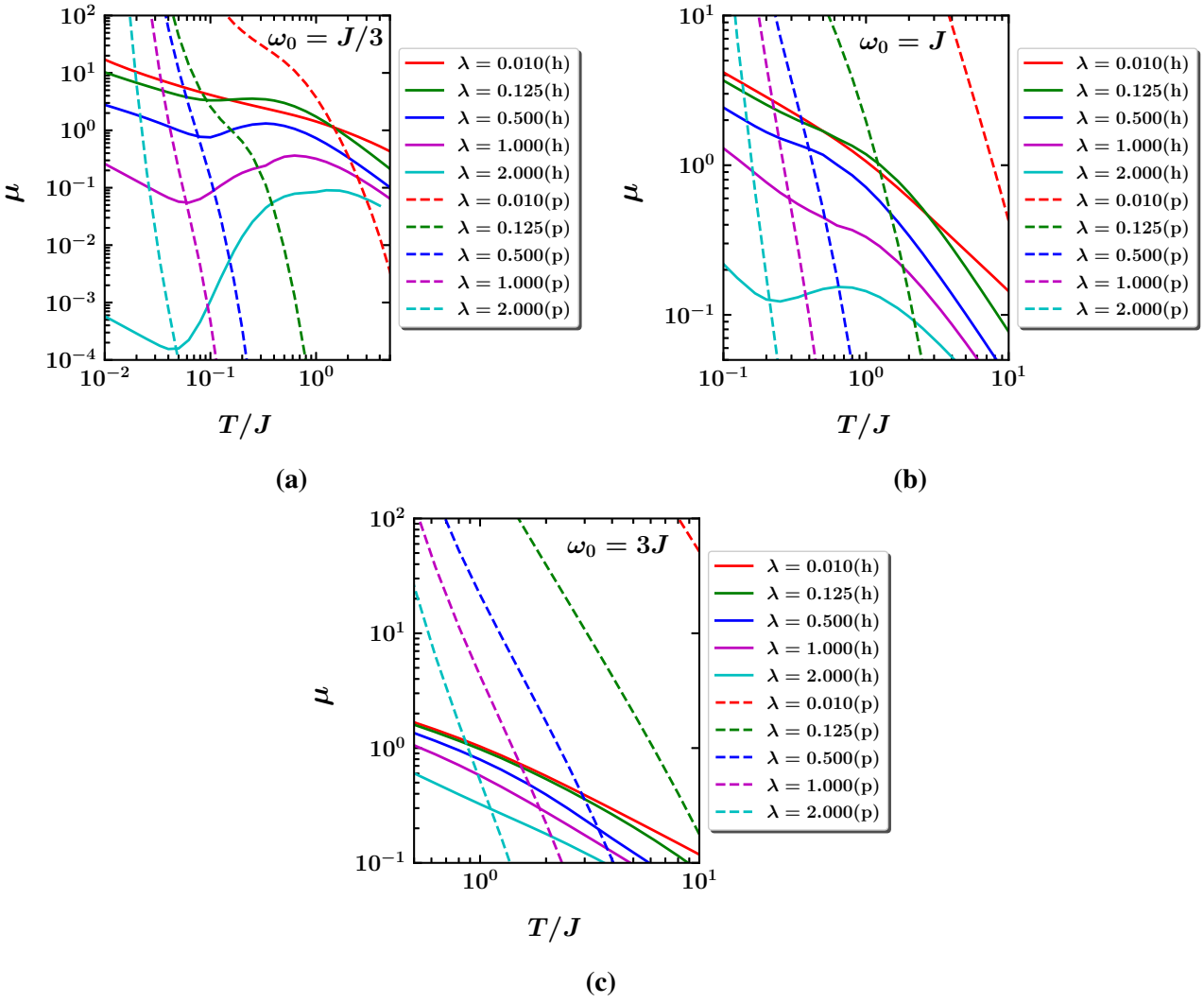

Figure 4.3: Temperature dependence of the mobility in the hopping and polaron band transport regimes for different interaction strengths λ. Solid lines (label "h") correspond to hopping transport (Eq. (4.10)), while dashed lines (label "p") correspond to polaron band transport (Eq. (4.21)). Panels (a)–(c) correspond to $\omega_0 = J/3$, $\omega_0 = J$, and $\omega_0 = 3J$, respectively.

4.1.3 Band transport regime and crossover to hopping regime

Transport in the weak-coupling regime is well described within the conventional band transport picture, as outlined in Section 2.3.2. In this regime, charge carriers remain delocalized over many lattice sites and form large polarons, whose spatial extent is significantly larger than the lattice spacing. Their motion therefore retains a coherent, band-like character and can be described in terms of Bloch states associated with a relatively wide electronic band. The electron–phonon interaction leads only to a weak renormalization of this band, resulting in a moderate increase of the effective mass, so that the polaron behaves similarly to a nearly free particle with only slight dressing by lattice vibrations.

At the same time, coupling to phonons introduces scattering processes that limit the lifetime of these delocalized states. The probability of such scattering events increases with temperature due to the growing phonon population, leading to a progressive suppression of coherent motion. In contrast to the strong-coupling regime, where the bandwidth is strongly reduced and carriers become localized, the relatively large bandwidth in this case still allows for extended motion across the lattice. The resulting transport behavior is therefore governed by the interplay between coherent band propagation and temperature-dependent phonon scattering.

In the band transport picture, the current operator is diagonal in momentum space, so that charge

transport can be expressed in terms of contributions from individual momentum states. As a result, the current–current correlation function naturally takes a momentum-resolved form, which can be written as

$$C_{jj}(t) = \frac{\sum_{k,k'} v_k v_{k'} \langle a_k^\dagger(t) a_k(t) a_{k'}^\dagger, a_{k'} \rangle}{\sum_k \langle a_k^\dagger a_k \rangle}. \tag{4.23}$$

For sufficiently weak electron–phonon interaction, the current–current correlation function can be evaluated within the independent-particle (bubble) approximation. In this approximation, scattering processes are weak enough that different momentum states evolve independently, so that the two-particle correlation function factorizes into a product of two single-particle expectation values. The four-operator average then reduces to the form adopted in Ref. [136],

$$\langle a_k{}^\dagger(t) a_k(t) a_{k'}^\dagger, a_{k'} \rangle = \delta_{kk'} \langle a_k^\dagger(t) a_k \rangle \langle a_k(t) a_k^\dagger \rangle, \tag{4.24}$$

which yields

$$C_{jj}(t) = 4J^2 \frac{\sum_k \langle a_k^\dagger(t) a_k \rangle \langle a_k(t) a_k^\dagger \rangle \sin^2(k)}{\sum_k \langle a_k^\dagger a_k \rangle}. \tag{4.25}$$

The expectation values entering the current–current correlation function can be expressed in terms of the electronic spectral function as

$$\langle a_k^\dagger(t) a_k \rangle = \int_{-\infty}^{\infty} \mathrm{d}\omega \; \mathrm{e}^{\mathrm{i}\omega t} A_k(\omega) \mathrm{e}^{-\beta\omega} \; , \tag{4.26}$$

$$\langle a_k(t) a_k^\dagger \rangle = \int_{-\infty}^{\infty} \mathrm{d}\omega \; \mathrm{e}^{-\mathrm{i}\omega t} A_k(\omega) \; . \tag{4.27}$$

The spectral function is defined as

$$A_k(\omega) = -\frac{1}{\pi} \mathrm{Im} \; G_k^R(\omega) \; , \tag{4.28}$$

where $G_k^R(\omega)$ denotes the retarded Green's function, which incorporates the effects of the electron–phonon interaction through the self-energy and is related to it through the Dyson equation,

$$G_k^R(\omega) = \frac{1}{\omega - \varepsilon_k - \Sigma_k(\omega)} \; . \tag{4.29}$$

Within the weak-coupling regime, the self-energy $\Sigma_k(\omega)$ is evaluated within the Migdal approximation, where only processes involving a single phonon line are retained. The self-energy is then written as [37, 142]

$$\Sigma_k(\omega) = \frac{G^2}{N} \sum_q \left[(n_{\mathrm{ph}} + 1) G_{k-q}^{(0)}(\omega - \omega_0) + n_{\mathrm{ph}} G_{k-q}^{(0)}(\omega + \omega_0) \right] \; , \tag{4.30}$$

where $G_k^{(0)}(\omega) = (\omega - \varepsilon_k + \mathrm{i}0^+)^{-1}$ denotes the Green's function of a free particle. Performing the summation over momentum yields

$$\Sigma(\omega) = G^2 (n_{\mathrm{ph}} + 1) S(\omega - \omega_0) + G^2 n_{\mathrm{ph}} S(\omega + \omega_0) \; , \tag{4.31}$$

where the function $S(\omega)$ corresponds to the contribution of single-phonon processes and is given by

$$S(\omega) = \begin{cases} \dfrac{\mathrm{sgn}(\omega)}{\sqrt{\omega^2 - 4J^2}} \; , & \text{if } \left| \dfrac{\omega}{2J} \right| > 1 \; , \\ \dfrac{-\mathrm{i}}{\sqrt{4J^2 - \omega^2}} \; , & \text{if } \left| \dfrac{\omega}{2J} \right| < 1 \; . \end{cases} \tag{4.32}$$

Details of the evaluation of Eq. (4.30), as well as the derivation of the resulting expressions, are provided in Appendix D.

It is important to note that, for $\omega > 2J$, energy conservation restricts single-phonon scattering processes for certain momenta. In this case, the imaginary part of the self-energy vanishes within the Migdal approximation, implying an infinite quasiparticle lifetime and, consequently, a divergent mobility. This indicates that the present approximation becomes insufficient in this regime, and that higher-order processes must be taken into account. In particular, contributions involving two phonon lines restore a finite scattering rate and provide a consistent description of carrier dynamics. The corresponding expressions are presented in Appendix D.

With these considerations in mind, the dc mobility in the band transport regime is given by the standard expression [133]

$$\mu_{\mathrm{dc}} = \beta \frac{\sum_k n_k \tau_k v_k^2}{\sum_k n_k} \,, \tag{4.33}$$

where $n_k = \mathrm{e}^{-\beta\varepsilon_k}$ denotes the occupation of electronic states and the scattering time is defined as $\tau_k^{-1} = -2\,\mathrm{Im}\Sigma_k(\omega)|_{\omega=\varepsilon_k}$.

This expression has the same formal structure as that obtained for polaron band transport (Eq. (4.21)), with the key difference that the quantities entering the expression correspond to the bare electronic band. In contrast to the strong-coupling regime, where transport is governed by localized or strongly renormalized states, the mobility here reflects the dynamics of delocalized carriers subject to phonon-induced scattering.

Even in the weak-coupling regime, a crossover from band transport to hopping transport may occur at sufficiently high temperatures. As the temperature increases, phonon scattering becomes more pronounced, leading to a rapid decrease of the band mobility. In contrast, the hopping mobility exhibits a weaker temperature dependence in this regime, so that the two transport mechanisms become comparable at elevated temperatures.

This behavior is illustrated in Fig. 4.4. With increasing temperature, the hopping mobility gradually approaches the band mobility, and the two curves eventually intersect. This intersection provides a rough estimate of the crossover from coherent band-like transport to incoherent hopping dynamics at high temperatures.

It should be emphasized that this comparison is meaningful primarily in the weak-coupling regime. For larger interaction strengths, the assumptions underlying the band transport description are no longer valid, and the interpretation of the crossover becomes less reliable. For this reason, only results corresponding to sufficiently small interaction strengths (e.g., $\lambda \lesssim 0.5$) are considered when analyzing this behavior.

4.2 Identification of the transport regimes in parameter space of Holstein model based on numerically exact calculations

The analysis presented in the previous section establishes the expected ranges of validity of the different transport regimes across the parameter space of the one-dimensional Holstein model. In particular, at low temperatures and strong electron–phonon coupling, transport is expected to occur through coherent motion within a narrow polaron band. In contrast, at high temperatures and strong coupling, thermally activated hopping becomes the dominant transport mechanism. For weak electron–phonon interaction, transport is generally well described within the conventional band picture, although deviations may arise at sufficiently high temperatures.

To identify these regimes in a more precise manner and determine their ranges of validity in parameter space, it is necessary to compare the approximate descriptions introduced in the previous section with numerically exact results obtained without assuming a specific transport mechanism.

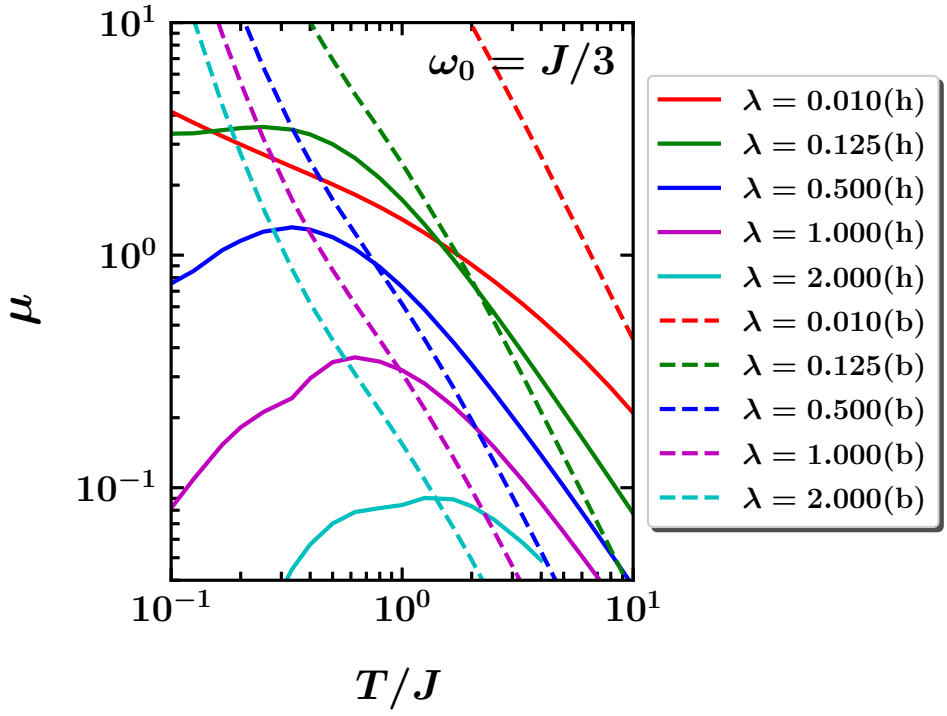

Figure 4.4: Temperature dependence of the mobility in the band and hopping transport regimes for several interaction strengths λ at $\omega_0 = J/3$. The band transport results [Eq. (4.33)] are shown as solid lines (labeled "b"), while the hopping results [Eq. (4.10)] are shown as dashed lines (labeled "h")

To this end, numerically exact results for the imaginary-time current–current correlation function are obtained using the path-integral quantum Monte Carlo (QMC) method developed in Chapter 3. These results are compared with the corresponding expressions derived for each transport regime. The calculations are performed over a broad region of parameter space, covering temperatures in the range $0.1 \leq T/J \leq 10$, interaction strengths $0.01 \leq \lambda \leq 2.0$, and three representative phonon frequencies, $\omega_0/J = 1/3$, $\omega_0/J = 1$, and $\omega_0/J = 3$.

A direct comparison at the level of real-time correlation functions or dc mobility would be desirable, but such numerically exact results are not available over the full parameter range due to computational limitations. For a restricted set of parameters where these quantities can be evaluated, additional comparisons are performed. In particular, the dc mobility obtained within the different transport regimes is compared with numerically exact results reported in Ref. [33], obtained using the hierarchical equations of motion (HEOM) method, as well as with real- and imaginary-time QMC results presented in Chapter 3.

4.2.1 Imaginary time current-current correlation function in different regimes compared to QMC results

To compare the imaginary-time current–current correlation functions obtained from approximate transport theories with the numerically exact QMC results, a quantitative measure of the deviation between the two is introduced.

For the hopping and conventional band transport regimes, a numerical criterion is introduced to quantify the deviation between an approximate correlation function $C_{jj}^{(\mathrm{a})}(t)$ and the numerically exact result $C_{jj}^{\mathrm{QMC}}(t)$, defined as

$$\mathcal{D}_{C_{jj}} = \frac{\int \mathrm{d}t \left| C_{jj}^{\mathrm{QMC}}(t) - C_{jj}^{(\mathrm{a})}(t) \right|}{\left| \int \mathrm{d}t \, C_{jj}^{\mathrm{QMC}}(t) \right|} , \tag{4.34}$$

where C_{jj}^{QMC} is taken as the reference. The two functions are considered to be in agreement when $\mathcal{D}_{C_{jj}} < 0.2$. This tolerance is chosen to be sufficiently small to ensure meaningful agreement, while still being large enough to account for numerical uncertainties and the inherent limitations of the approximate theoretical descriptions.

In the case of polaron band transport, a different numerical criterion must be employed. This is because the approximate expressions derived for this regime retain only coherent contributions, corresponding to processes within a narrow energy window determined by the renormalized bandwidth (see Section 4.1.2). In contrast, the exact correlation function obtained from QMC calculations contains additional contributions arising from multiphonon processes at higher energies. As a result, a direct comparison over the full time domain does not provide a reliable measure of agreement.

Instead, the comparison is performed at imaginary time $t = -\mathrm{i}\beta/2$, which selectively probes the low-frequency part of the spectrum [73, 143]. As discussed in these works, the imaginary-time correlation function at $\tau = \beta/2$ is predominantly sensitive to frequencies around $\omega = 0$, with a resolution set by temperature. This makes it particularly suitable for assessing the low-energy behavior relevant for dc transport. Consequently, this choice directly targets the frequency range governing polaron band transport. The corresponding deviation is defined as

$$\mathcal{D}_{Cjj} = \frac{\left| C_{jj}^{\mathrm{QMC}}(-\mathrm{i}\beta/2) - C_{jj}^{(\mathrm{p})}(-\mathrm{i}\beta/2) \right|}{\left| C_{jj}^{\mathrm{QMC}}(-\mathrm{i}\beta/2) \right|} \,. \tag{4.35}$$

A threshold value $\mathcal{D}_{C_{jj}} < 0.5$ is chosen to identify the polaron band transport regime. This criterion is less restrictive than in the cases of hopping and band transport, reflecting both the stronger approximations underlying the polaron band description and the fact that the approximate and exact correlation functions include different contributions. Despite this, the chosen threshold remains sufficiently stringent to identify the regime where the approximate description captures the relevant low-energy behavior.

In the limit of weak electron–phonon interaction, the expressions for polaron band transport and conventional band transport coincide. In this limit, the interaction-dependent factors reduce to their noninteracting values, and the correlation function simplifies to

$$C_{jj}(z) = 4J^2 \frac{\sum_k \mathrm{e}^{-\beta\varepsilon_k} \sin^2 k}{\sum_k \mathrm{e}^{-\beta\varepsilon_k}} \,. \tag{4.36}$$

This expression is identical to that obtained for band transport. Consequently, in parameter regions where both numerical criteria indicate agreement with polaron band and conventional band transport, the system is assigned to the conventional band transport regime.

The deviation $\mathcal{D}_{C_{jj}}$ across the parameter space for all three transport regimes is shown in Fig. 4.5. Agreement between the approximate and numerically exact correlation functions is identified using the numerical criterion $\mathcal{D}_{C_{jj}} < 0.2$ for hopping and band transport.

To clarify the interpretation of this criterion, representative imaginary-time correlation functions for QMC, hopping, and band transport are shown in Fig. 4.6 for $\omega_0 = J/3$ and $\lambda = 0.5$. At high temperature ($T/J = 10.0$), the QMC results closely follow the hopping transport correlation function. This behavior is consistent with the small values of $\mathcal{D}_{C_{jj}}$ observed in Fig. 4.5, indicating that the hopping description captures the dominant transport mechanism in this regime.

At low temperature ($T/J = 0.1$), the situation is quite different. Neither the hopping nor the band transport expressions reproduce the QMC results, and clear deviations are visible over the entire time interval. This is reflected in Fig. 4.5, where the deviation exceeds the chosen threshold for both regimes, indicating that neither approximation provides a reliable description in this region of parameter space.

Certain regions of the parameter space are not covered in Fig. 4.5. In particular, the absence of data at low temperatures and strong coupling reflects the increasing difficulty of QMC calculations in

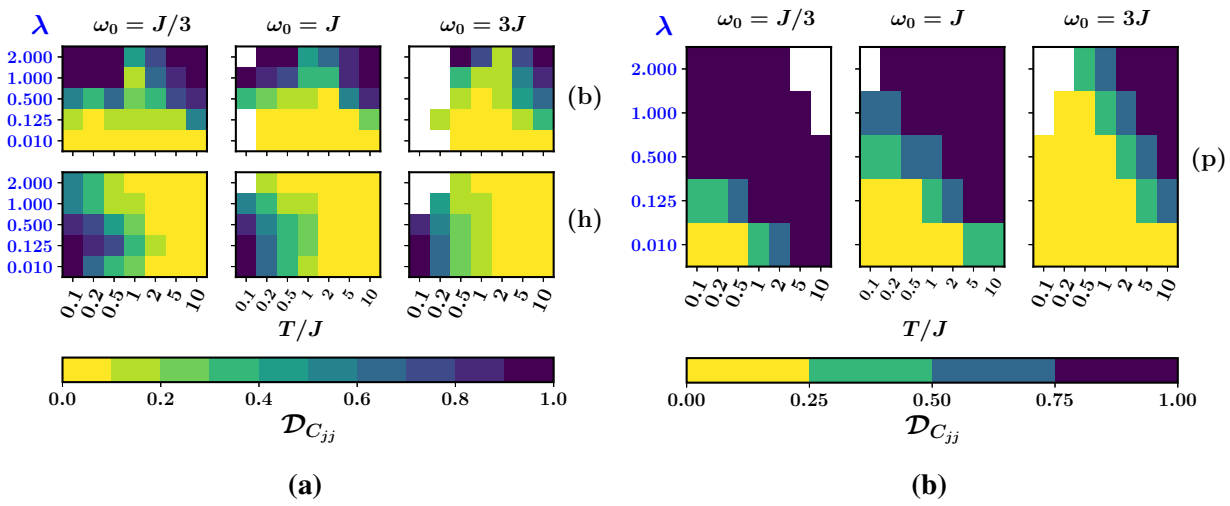

Figure 4.5: Relative deviation $\mathcal{D}_{C_{jj}}$ between approximate and numerically exact (QMC) imaginary-time current–current correlation functions as a function of temperature T and interaction strength λ for different phonon frequencies ω_0. Each column corresponds to a different value of ω_0. Panel (a) shows results for band transport ("b") and hopping transport ("h"), while panel (b) shows results for polaron band transport ("p").

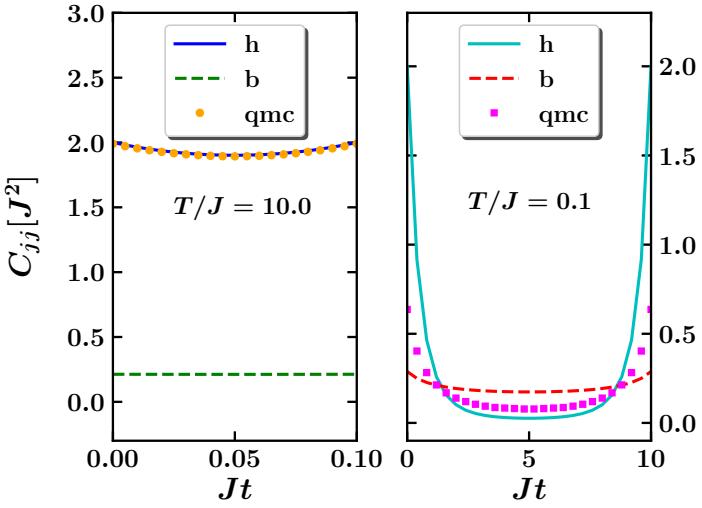

Figure 4.6: Imaginary-time current–current correlation functions for $\omega_0 = J/3$ and $\lambda = 0.5$. Panels (a) and (b) correspond to temperatures $T/J = 10.0$ and $T/J = 0.1$, respectively. Results for hopping transport (denoted by "h") and band transport (denoted by "b") are compared with numerically exact QMC results (points).

this regime. Additional limitations arise in the evaluation of the approximate correlation functions. For band transport, the spectral function becomes extremely narrow at low temperatures, which makes its numerical treatment increasingly challenging. In the case of polaron band transport, numerical instabilities related to the evaluation of Bessel functions appear at high temperatures and strong coupling for $\omega_0 = J/3$. However, this corresponds to a parameter region where this transport regime is not expected to play a significant role.

Figure 4.5 is therefore used as a basis for identifying the dominant transport mechanisms across a broad region of the parameter space. In most cases, the numerical criterion provides a clear indication of which transport description is applicable. However, there are regions where more than one transport regime appears to be consistent with the chosen criterion. In such cases, the classification is further refined by incorporating additional information from real-time correlation functions and dc mobility. This combined analysis provides a more complete characterization of the transport behavior and enables a clear reconstruction of the transport regime diagram in the following sections.

4.2.2 DC mobility in different transport regimes compared to numerically exact results

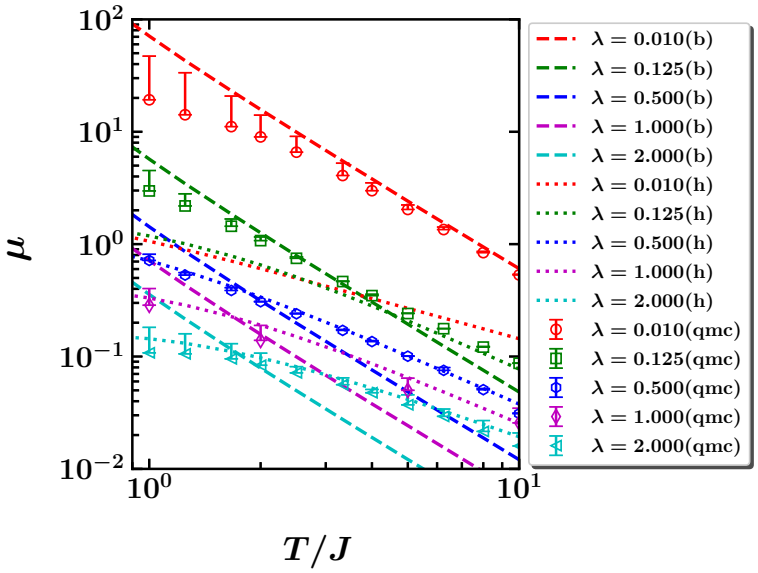

(a)

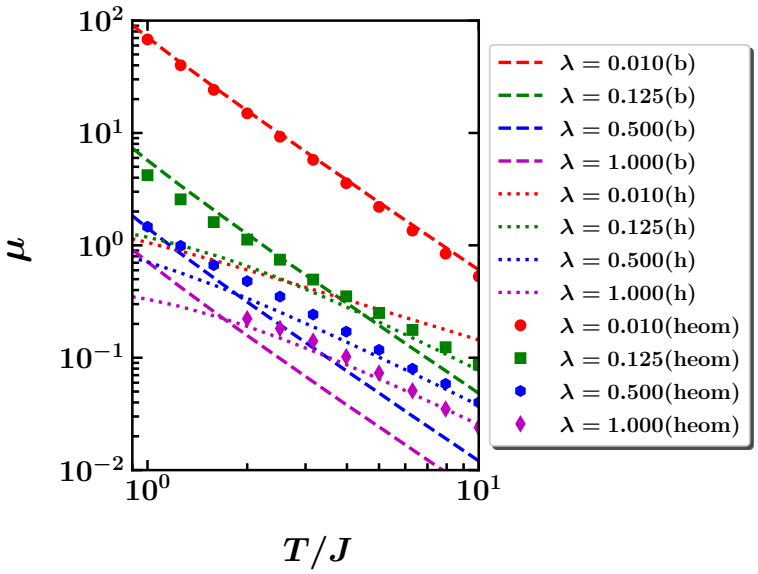

(b)

Figure 4.7: Temperature dependence of the mobility for hopping and band transport at $\omega_0/J = 1$. Results labeled "h" and "b" are compared with numerically exact data from (a) QMC and (b) HEOM, shown as symbols. Error bars for the QMC results are estimated as described in the previous chapter.

Figure 4.7 shows the temperature dependence of the mobility for different interaction strengths at $\omega_0 = J$. This value of phonon frequency is chosen because comprehensive and reliable numerically exact results are available from both QMC and HEOM [33] methods. The solid lines correspond to the approximate expressions for mobility derived in previous section, while the symbols represent the numerical data.

A clear level of agreement between the approximate and numerically exact results is observed within the parameter regions where the respective transport descriptions are expected to be valid. In the weak-coupling regime, the band transport expression, given with Eq. (4.33), follows the numerical data over the entire temperature range considered, reflecting the fact that charge carriers remain delocalized and retain a coherent, band-like character.

With increasing interaction strength, this behavior gradually changes. The coupling to lattice vibrations becomes more pronounced, leading to stronger renormalization and reduced carrier mobility. In this regime, the numerical results are more closely captured by the hopping transport expression, defined in Eq. (4.10), particularly at elevated temperatures, where transport is governed by thermally activated, incoherent motion between localized states.

These results confirm that the approximate transport theories capture the correct limiting behavior in their respective regimes. At the same time, they reveal the limitations of the criterion based on imaginary-time correlation functions, shown in Fig. 4.5, when distinguishing between band and hopping transport in certain regions of the parameter space. In particular, for weak interaction strengths at high temperatures, both approximate descriptions may appear consistent with the correlation-function-based criterion ($\mathcal{D}_{C_{jj}} < 0.2$), even though the mobility comparison clearly favors the band transport picture. This illustrates that the imaginary-time correlation-function-based criterion alone is not sufficient to unambiguously distinguish between these regimes in this parameter range.

Due to the difficulty of obtaining numerically exact results at very low temperatures, the crossover from polaron band transport to hopping transport is not visible in Fig. 4.7. However, as discussed in the previous section, the position of this crossover depends on the phonon frequency. For larger phonon frequencies, the crossover shifts to higher temperatures, where it becomes accessible within the range of the present calculations.

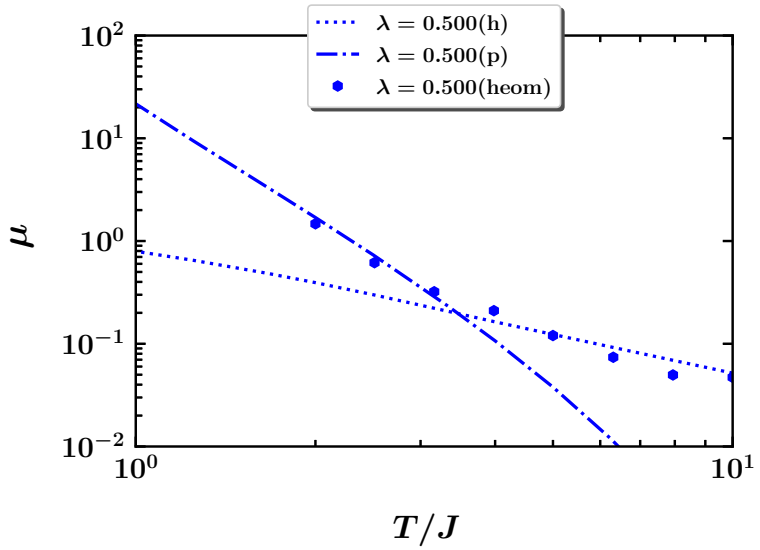

Figure 4.8: Temperature dependence of the mobility for hopping and polaron band transport at $\omega_0 = 3J$ and $\lambda = 0.5$. Hopping ("h") and polaron band transport ("p") results are compared with numerically exact HEOM data (symbols).

The crossover between polaron band and hopping transport is illustrated in Fig. 4.8. In this case, the intersection between the two approximate expressions occurs within the temperature range accessible to numerically exact calculations. The numerical data follow the polaron band transport curve at lower temperatures, while at higher temperatures they approach the hopping transport curve, with the crossover occurring in the vicinity of their intersection. This behavior provides direct support for identifying the crossover based on the intersection of the respective approximate mobility curves, as discussed in the previous section.

The combined analysis of imaginary-time correlation functions and dc mobility thus provides a consistent picture of transport across a broad region of the parameter space. While the imaginary-time correlation-function-based criterion offers a useful first indication of the relevant transport regime, the comparison of mobility allows for a more refined identification, particularly in regions where different descriptions appear to overlap. Taken together, these results establish a reliable basis for mapping out

the transport regimes of the Holstein model, which is presented in the following section in the form of a transport regime diagram.

4.2.3 Transport regime diagram for one-dimensional Holstein model

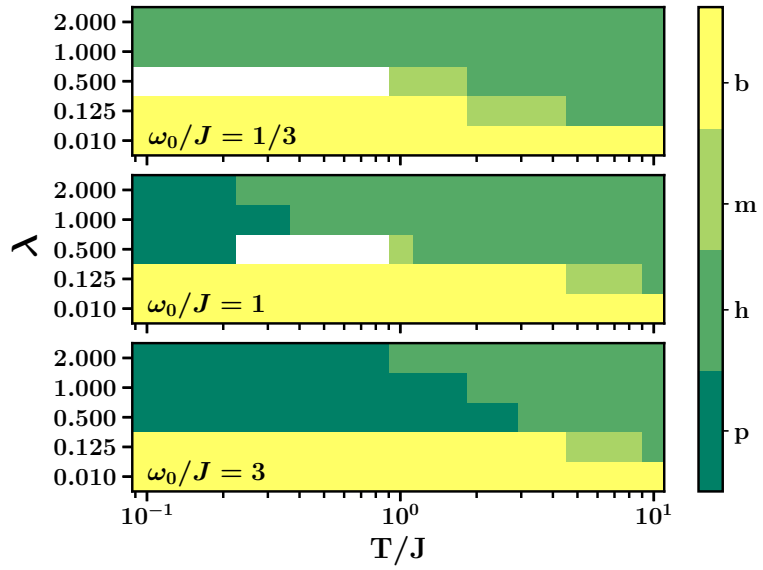

Figure 4.9: Transport regime diagram of the one-dimensional Holstein model for different phonon frequencies ω_0/J. The results are shown in the $(T/J, \lambda)$ parameter space. The regimes are labeled as conventional band transport ("b"), hopping transport ("h"), and polaron band transport ("p"). Regions marked as "m" indicate an intermediate regime where no single transport theory provides a fully consistent description.

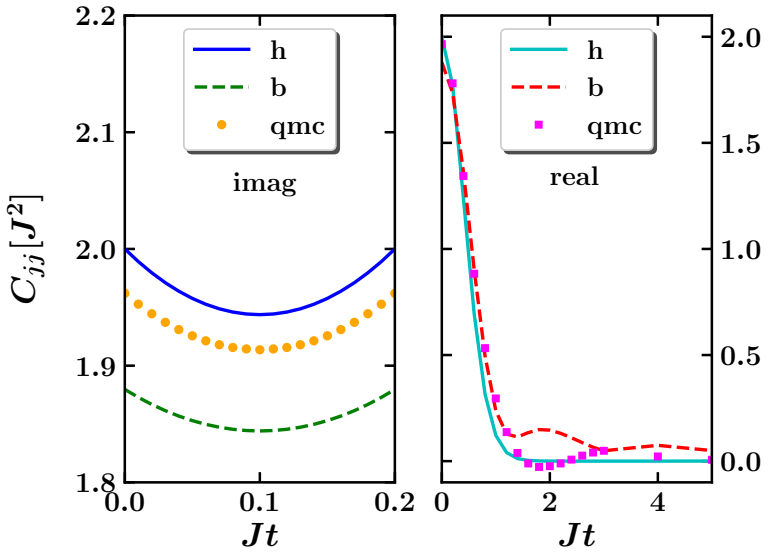

Figure 4.10: Imaginary- and real-time current–current correlation functions for $\omega_0 = J$, $\lambda = 0.125$, and $T/J = 5.0$. Results for hopping transport ("h") and band transport ("b") are compared with numerically exact QMC data (points).

The transport regime diagram obtained from the combined analysis is shown in Fig. 4.9. In the following, the construction of this diagram is described in detail for the representative case $\omega_0 = J$, while analogous results for other phonon frequencies are presented in Appendix E.

The identification of the different transport regimes proceeds by combining the information from the numerical criterion $\mathcal{D}_{C_{jj}}$ shown in Fig. 4.5 with the mobility comparison in Fig. 4.7. From

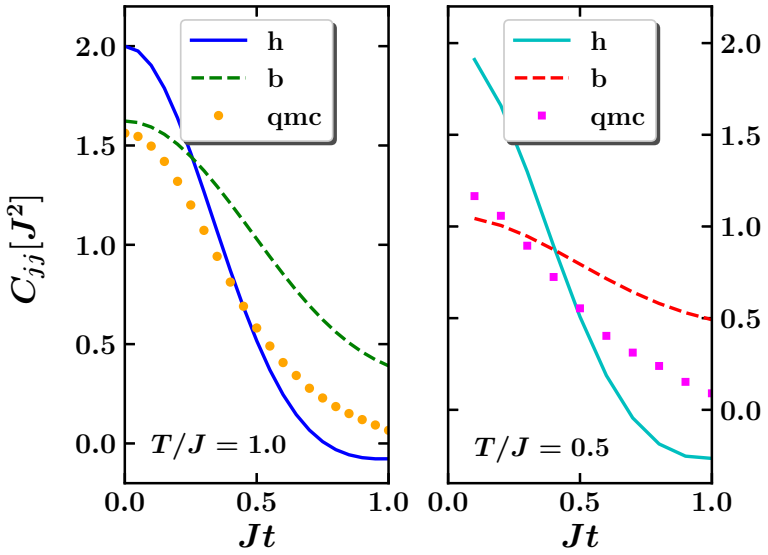

Figure 4.11: Real-time current–current correlation functions for $\omega_0 = J$, $\lambda = 0.5$, and temperatures $T/J = 1.0$ and $T/J = 0.5$. Results for hopping transport ("h") and band transport ("b") are compared with numerically exact QMC data (points)

Fig. 4.5, it is evident that the band transport regime dominates at low temperatures and weak interaction strengths. As the temperature increases, the deviation measure $\mathcal{D}_{C_{jj}}$ indicates that both band and hopping transport may be consistent with the numerically exact results, leading to an ambiguous classification in this region.

This ambiguity is resolved by considering the mobility. For the weakest interaction strength, the numerical data follow the band transport expression over the entire temperature range, and no intersection between the band and hopping mobility curves is observed. This confirms that transport remains governed by the band transport regime in this region of parameter space.

For the next interaction strength, $\lambda = 0.125$, the distinction between band and hopping transport becomes less clear. As shown in Fig. 4.7, both approximate expressions yield very similar results and remain consistent with the numerically exact data. This ambiguity is also reflected in the comparison of real-time correlation functions in Fig. 4.10, where both transport descriptions provide a comparable level of agreement with the QMC results.

This behavior indicates that the system cannot be unambiguously assigned to a single transport regime in this region, and it is therefore identified as an intermediate regime between band and hopping transport. At the highest temperatures, however, a transition toward hopping behavior is indicated, as the imaginary-time correlation function for the band transport approximation begins to deviate from the QMC results.

For stronger interaction strength, $\lambda = 0.500$, Fig. 4.5 indicates that hopping transport dominates at temperatures above $T/J \approx 2.0$, while at low temperatures ($T/J \lesssim 0.2$) the system is found in the polaron band transport regime. In the intermediate temperature range, the numerical criterion $\mathcal{D}_{C_{jj}}$ suggests possible agreement with band transport. However, the real-time correlation functions shown in Fig. 4.11 reveal that, although band transport provides a better approximation than hopping, noticeable deviations from the QMC results persist.

This indicates that neither description is fully adequate in this region, and it is therefore classified as an undefined regime. In Fig. 4.9, regions shown in white correspond to parameter ranges where none of the considered transport descriptions are in satisfactory agreement with the numerical results. In contrast, the region around $T/J \approx 1.0$ is denoted as an intermediate band–hopping regime, where both band and hopping transport provide a comparable level of agreement with the numerical data.

For $\lambda = 1.000$, Fig. 4.5 clearly identifies hopping transport as the dominant mechanism for temperatures $T/J \gtrsim 0.5$. The crossover between polaron band and hopping transport is estimated

from the intersection of the corresponding mobility curves (Fig. 4.3), which occurs in the range $T/J \approx 0.2$–0.3. In this case, the intersection of the approximate expressions is used as an indicator of the crossover between the two regimes. As discussed in the previous analysis, this approach is supported by the comparison with numerically exact results, where the crossover is found to occur in the vicinity of the intersection point (see Fig. 4.8). Below this temperature range, transport is therefore assigned to the polaron band regime.

The same reasoning applies to the case $\lambda = 2.000$, where the crossover occurs at slightly lower temperatures, reflecting the stronger electron–phonon coupling and the enhanced localization of charge carriers.

The results confirm the anticipated limiting behavior, showing that band transport prevails for weak coupling at low temperatures, hopping transport becomes dominant at strong coupling and high temperatures, while at strong coupling and low temperatures, transport proceeds via a polaronic band mechanism. These three regimes are found to account for the transport behavior over most of the parameter space considered in this work, which spans a broad and physically relevant range of conditions, from low to high temperatures ($0.1 \leq T/J \leq 10$) and from weak to strong interaction strengths ($0.01 \leq \lambda \leq 2$).

Only a limited portion of the parameter space exhibits intermediate or undefined behavior, corresponding to parameter ranges in which the relevant energy scales are of comparable magnitude. In the present case, this occurs for temperatures of the order $T/J \sim 1$ and interaction strengths around $\lambda \sim 0.5$. In this regime, no single transport theory provides a fully consistent description, which reflects the intrinsic difficulty of capturing transport in this crossover region.

Nevertheless, even in this case, the combined analysis allows for a consistent characterization of transport behavior across the physically relevant part of the parameter space, particularly in the region around $T/J \sim 1$ and intermediate interaction strengths $\lambda \sim 0.5$–1.0. In addition, a systematic shift of temperature effects with phonon frequency is observed. For larger phonon frequencies, the crossover between polaron band and hopping transport occurs at higher temperatures, allowing the full transition to be resolved, as in the case $\omega_0 = 3J$. For smaller phonon frequencies, such as $\omega_0 = J/3$, the same crossover is shifted beyond the accessible temperature range, leading to a competition between band and hopping transport expected at high temperatures.

For intermediate phonon frequency $\omega_0 = J$, all three transport regimes are captured and provide a consistent description over nearly the entire parameter space, with only a small region around $\lambda \sim 0.5$ and $T/J \sim 1$ exhibiting intermediate or undefined behavior. This parameter range closely corresponds to the regime relevant for molecular crystals, indicating that the transport behavior in these systems can, to a large extent, be described within the theoretical framework considered in this work.

These results provide a consistent and physically grounded description of transport across the relevant parameter space of the one-dimensional Holstein model, completing the identification of transport regimes in this system.

Chapter 5

Conclusions

This thesis has presented a comprehensive study of charge transport in electron–phonon coupled systems within the framework of the Holstein model, with particular emphasis on the development and application of a numerically exact path-integral quantum Monte Carlo (QMC) methodology. The central objective was to establish a consistent and unbiased framework for the calculation of current–current correlation functions and the corresponding dc mobility, and to apply this approach to the investigation of transport properties over a broad range of parameters.

A key outcome of this work is the formulation and implementation of current–current correlation functions within the path-integral QMC framework and their use for the determination of dc mobility. By combining imaginary-time and real-time correlation functions, and by employing both the electron position basis and the momentum basis in the path-integral formulation, a methodology has been developed that mitigates the limitations imposed by the dynamical sign problem and improves the outcome of the analytic continuation procedure. This approach enables the determination of current–current correlation functions and mobility with controlled accuracy, and provides a consistent and quantitatively supported description of the dynamical behavior of charge carriers across different transport regimes.

The capabilities of this approach are demonstrated through its application to the calculation of dc mobility and the analysis of transport behavior across the parameter space of the Holstein model.

The results for the dc mobility obtained in Chapter 3 of this thesis show very good agreement with those reported in Ref. [133]. For almost all parameter values studied, the results of that reference, obtained using an unrelated approximate method, fall within the error bars of the QMC results presented in Chapter 3 (see Fig. 3.8). This level of agreement indicates that the approach of Ref. [133] provides a reliable description within the corresponding parameter ranges. At the same time, this comparison highlights the role of numerically exact QMC results as a benchmark for a broad class of approximate and computational methods. Although the QMC approach employed in this thesis remains limited by the dynamical sign problem and the challenges of analytic continuation, the extension to longer accessible real-time intervals, together with the achieved statistical precision, provides sufficiently reliable data over a broad portion of parameter space, making it well suited for such benchmarking purposes.

A similar comparison can be made with the results reported in Ref. [66], which presents the temperature dependence of the Holstein polaron mobility obtained using a similar unbiased numerical approach. For the weakest interaction ($G/J = 0.141$) and higher temperatures, the results of Ref. [66] are in good agreement with those obtained in Chapter 3 (see Fig. 3.8). These parameter regimes correspond to the cases in which the path-integral QMC method developed in this thesis achieves its highest accuracy, as the full real-time decay of the current–current correlation function can be captured within the accessible time window. Under these conditions, the mobility can be determined by direct integration of the real-time correlation function in accordance with the Kubo formula, yielding results with negligible uncertainty determined by the statistical error of the correlation function.

For stronger interactions and lower temperatures, clear differences emerge. In these regimes,

capturing the full time decay of the correlation function requires longer real-time intervals, while the analytic continuation procedure requires sufficiently extended and reliable data to reconstruct the real-time behavior faithfully. In this case, the comparison with Ref. [66] shows that the mobility values reported in that reference are consistently lower. For example, for the strongest interaction considered in Chapter 3, $G/J = 2.83$ and temperature $T/J = 2$, the method developed in this thesis yields mobility values in the range $\mu \in (3.1 \times 10^{-2}, 7.2 \times 10^{-2})$ (see Fig. 3.8), whereas Ref. [66] reports values in the range $\mu \in (2.8 \times 10^{-3}, 8.1 \times 10^{-3})$, i.e., approximately one order of magnitude smaller.

This difference can be understood by examining the structure of the current–current correlation function. For strong interactions, the correlation function exhibits multiple resonant peaks at times corresponding to integer multiples of the phonon period $2\pi/\omega_0$, with amplitudes that decrease with increasing time. This behavior is visible in the approximate results of Ref. [133] (see Fig. 3.6). The QMC method employed in this thesis captures the first and largest peak with high precision. Integration over this initial peak alone already yields a contribution of approximately 1.5×10^{-2} to the mobility, while inclusion of subsequent peaks would further increase the final value.

The lower values reported in Ref. [66] can therefore be attributed to the limitations of the analytic continuation procedure employed in that reference, which relies exclusively on imaginary-time QMC data. This provides a clear illustration of the limitations associated with analytic continuation procedures based solely on imaginary-time input, as the lack of direct real-time information restricts the accuracy of the reconstructed real-time dynamics. In contrast, the approach developed in this thesis incorporates additional input from real-time data, and even the simple SVD-based continuation scheme used here leads to a noticeable improvement in the resulting mobility values, indicating that the inclusion of real-time information plays an important role in improving the outcome of analytic continuation.

The results presented in Chapter 4 further demonstrate the role of the numerically exact QMC data obtained in this thesis as a benchmarking reference, in this case for established theoretical descriptions of polaron transport. The detailed analysis of current–current correlation functions and mobilities shows that almost the entire studied parameter space can be adequately described within the framework of three well-known transport mechanisms: hopping transport, conventional band transport, and polaron band transport. This represents an important result, as it confirms that the transport properties of the Holstein polaron can, to a large extent, be understood within existing theoretical frameworks, thereby reducing the need for computationally demanding methods in regimes where these theories are applicable.

The findings of Chapter 4 can be further compared with those reported in Refs. [49] and [144]. In Ref. [49], a Holstein–Peierls model, also relevant for organic semiconductors, is considered. That reference examines transport regimes as functions of electronic coupling strength and non-local electron–phonon interaction. However, temperature dependence is not explicitly addressed. Due to these differences in both the form of the Hamiltonian and the parameters considered, a direct quantitative comparison with the results obtained in this thesis is not possible. Nevertheless, the general conclusions of Ref. [49], namely the identification of band-like transport at large electronic coupling and phonon-assisted (hopping-type) transport at small electronic coupling, are in qualitative agreement with the results obtained in Chapter 4.

In Ref. [144], a two-site Holstein model is studied and crossovers between different transport regimes are analyzed as they evolve in time for various values of the adiabaticity ratio. The identified regimes include polaronic transport, soft-gating, and transient localization. The analysis presented in Chapter 4 of this thesis provides a complementary perspective to the results reported in these references. In particular, the analysis in this thesis systematically investigates the effect of temperature over a broad range, which is not considered in Ref. [49]. Furthermore, while Ref. [144] focuses on short-range transport in a two-site system, the results of this thesis address long-range charge transport thereby extending the scope of the analysis.

The results obtained in this work establish a numerically exact and internally consistent framework

for the investigation of charge transport in electron–phonon coupled systems. The combination of path-integral QMC methods with a correlation-function-based analysis enables a unified description of transport across different regimes of Holstein polaron model.

An important outcome of this work is the demonstration that numerically exact QMC data provide a reliable benchmark for assessing the validity of approximate theoretical and computational approaches. Such benchmarking is particularly valuable in parameter regimes where the assumptions underlying simplified models are no longer valid, while at the same time allowing the identification of regimes in which computationally less demanding methods can be applied with confidence.

The developed methodology also offers clear directions for future work. The combination of different representations in the path-integral formalism and the joint analysis of imaginary- and real-time data can be extended to other model Hamiltonians and, potentially, to more realistic systems. In particular, the application of this approach to Hamiltonians derived from ab initio calculations represents a promising route toward connecting microscopic modeling with material-specific transport properties.

Furthermore, the strategy of combining imaginary- and real-time data for analytic continuation is not limited to the specific numerical scheme employed in this work and can be integrated with other continuation methods. This suggests that improvements in analytic continuation may be achieved not only through algorithmic developments, but also through the inclusion of additional physically relevant input data.

In conclusion, this thesis provides both methodological advances and physical insight into charge transport in electron–phonon coupled systems. The developed framework enables a consistent interpretation of transport behavior across different regimes and establishes a foundation for future theoretical and computational studies in this field.

Bibliography

[1] C. Groves, "Simulating charge transport in organic semiconductors and devices: a review", Rep. Prog. Phys. **80**, 026502 (2016).

[2] S. R. Forrest, "The path to ubiquitous and low-cost organic electronic appliances on plastic", Nature **428**, 911–918 (2004).

[3] J. D. Myers and J. Xue, "Organic semiconductors and their applications in photovoltaic devices", Polym, Rev. **52**, 1–37 (2012).

[4] J. Yu, Y. Zheng, and J. Huang, "Towards high performance organic photovoltaic cells: a review of recent development in organic photovoltaics", Polymers **6**, 2473–2509 (2014).

[5] H. Sirringhaus, "25th anniversary article: organic field-effect transistors: the path beyond amorphous silicon", Adv. Mater. **26**, 1319–1335 (2014).

[6] Y. Qian, X. Zhang, L. Xie, D. Qi, B. K. Chandran, X. Chen, and W. Huang, "Stretchable organic semiconductor devices", Adv. Mater. **28**, 9243–9265 (2016).

[7] G. Schweicher, G. Garbay, R. Jouclas, F. Vibert, F. Devaux, and Y. H. Geerts, "Molecular semiconductors for logic operations: dead-end or bright future?", Adv. Mater. **32**, 1905909–1905909 (2020).

[8] M. Muccini, "A bright future for organic field-effect transistors", Nat. Mater. **5**, 605–613 (2006).

[9] S. Fratini, D. Mayou, and S. Ciuchi, "The transient localization scenario for charge transport in crystalline organic materials", Adv. Funct. Mater. **26**, 2292–2315 (2016).

[10] S. Fratini, M. Nikolka, A. Salleo, G. Schweicher, and H. Sirringhaus, "Charge transport in high-mobility conjugated polymers and molecular semiconductors", Nat. Mater. **19**, 491–502 (2020).

[11] V. Coropceanu, J. Cornil, D. da Silva Filho, Y. Olivier, R. Silbey, and J.-L. Brédas, "Charge transport in organic semiconductors", Chem. Rev. **107**, 926–952 (2007).

[12] A. Troisi, "Charge transport in high mobility molecular semiconductors: classical models and new theories", Chem. Soc. Rev. **40**, 2347–2358 (2011).

[13] H. Sato, S. A. Abd. Rahman, Y. Yamada, H. Ishii, and H. Yoshida, "Conduction band structure of high-mobility organic semiconductors and partially dressed polaron formation", Nat. Mater. **21**, 910–916 (2022).

[14] J. Nitta, K. Miwa, N. Komiya, E. Annese, J. Fujii, S. Ono, and K. Sakamoto, "The actual electronic band structure of a rubrene single crystal", Sci. Rep. **9**, 9645 (2019).

[15] L. D. Landau, "On the motion of electrons in a crystal lattice", Physikalische Zeitschrift der Sowjetunion **3**, 664–665 (1933).

[16] S. I. Pekar, *Research in electron theory of crystals* (US AEC Translation, 1963).

[17] H. Fröhlich, "Electrons in lattice fields", Advances in Physics **3**, 325–361 (1954).

[18] T. Holstein, "Studies of polaron motion: part i. the molecular-crystal model", Annals of Physics **8**, 325–342 (1959).

[19] T. Holstein, "Studies of polaron motion: part ii. the "small" polaron", Annals of Physics **8**, 343–389 (1959).

[20] N. W. Ashcroft and N. D. Mermin, *Solid state physics* (Harcourt, Orlando, 1976).

[21] A. Troisi, "Charge transport in high mobility molecular semiconductors: classical models and new theories", Chem. Soc. Rev. **40**, 2347–2358 (2011).

[22] V. Coropceanu, R. S. Sánchez-Carrera, P. Paramonov, G. M. Day, and J.-L. Brédas, "Interaction of charge carriers with lattice vibrations in organic molecular semiconductors: naphthalene as a case study", J. Phys. Chem. C. **113**, 4679–4686 (2009).

[23] G. Schweicher, G. D'Avino, M. T. Ruggiero, D. J. Harkin, K. Broch, D. Venkateshvaran, G. Liu, A. Richard, C. Ruzié, J. Armstrong, A. R. Kennedy, K. Shankland, K. Takimiya, Y. H. Geerts, J. A. Zeitler, S. Fratini, and H. Sirringhaus, "Chasing the "killer" phonon mode for the rational design of low-disorder, high-mobility molecular semiconductors", Adv. Mater. **31**, 1902407 (2019).

[24] A. S. Alexandrov and J. T. Devreese, *Advances in polaron physics* (Springer, Berlin, Heidelberg, 2010).

[25] R. A. Marcus, "On the theory of oxidation-reduction reactions involving electron transfer. i", The Journal of Chemical Physics **24**, 966–978 (1956).

[26] W. F. da Cunha, P. H. de Oliveira Neto, R. Gargano, and G. Magela e Silva, "Temperature effects on polaron stability in polyacetylene", Int. J. Quantum Chem. **108**, 2448–2453 (2008).

[27] A. Troisi and G. Orlandi, "Charge-transport regime of crystalline organic semiconductors: diffusion limited by thermal off-diagonal electronic disorder", Phys. Rev. Lett. **96**, 086601 (2006).

[28] G. De Filippis, V. Cataudella, A. S. Mishchenko, N. Nagaosa, A. Fierro, and A. de Candia, "Crossover from super- to subdiffusive motion and memory effects in crystalline organic semiconductors", Phys. Rev. Lett. **114**, 086601 (2015).

[29] F. Ortmann, F. Bechstedt, and K. Hannewald, "Charge transport in organic crystals: interplay of band transport, hopping and electron–phonon scattering", New J. Phys. **12**, 023011 (2010).

[30] J. M. Ziman, *Electrons and phonons* (Oxford University Press, Oxford, 1960).

[31] D. Emin, *Polarons* (Cambridge University Press, Cambridge, 2013).

[32] T. Holstein, "Studies of polaron motion", Ann. Phys. **8**, 343 (1959).

[33] V. Janković, "Holstein polaron transport from numerically "exact" real-time quantum dynamics simulations", J. Chem. Phys. **159**, 094113 (2023).

[34] S. Fratini and S. Ciuchi, "Dynamical mean-field theory of transport of small polarons", Phys. Rev. Lett. **91**, 256403 (2003).

[35] S. Ciuchi, F. de Pasquale, S. Fratini, and D. Feinberg, "Dynamical mean-field theory of the small polaron", Phys. Rev. B **56**, 4494–4512 (1997).

[36] A. Georges, "Strongly correlated electron materials: dynamical mean-field theory and electronic structure", AIP Conference Proceedings **715**, 3–74 (2004).

[37] P. Mitrić, V. Janković, N. Vukmirović, and D. Tanasković, "Cumulant expansion in the Holstein model: spectral functions and mobility", Phys. Rev. B **107**, 125165 (2023).

[38] A. Georges, G. Kotliar, W. Krauth, and M. J. Rozenberg, "Dynamical mean-field theory of strongly correlated fermion systems and the limit of infinite dimensions", Rev. Mod. Phys. **68**, 13–125 (1996).

[39] D. R. Yarkony and R. Silbey, "Variational approach to exciton transport in molecular crystals", The Journal of Chemical Physics **67**, 5818–5827 (1977).

[40] R. Silbey and R. W. Munn, "General theory of electronic transport in molecular crystals. i. local linear electron–phonon coupling", The Journal of Chemical Physics **72**, 2763–2773 (1980).

[41] G. Wellein and H. Fehske, "Self-trapping problem of electrons or excitons in one dimension", Phys. Rev. B **58**, 6208–6218 (1998).

[42] J. Bonča, S. A. Trugman, and I. Batistić, "Holstein polaron", Phys. Rev. B **60**, 1633–1642 (1999).

[43] M. Berciu, "Green's function of a dressed particle", Phys. Rev. Lett. **97**, 036402 (2006).

[44] G. L. Goodvin, A. S. Mishchenko, and M. Berciu, "Optical conductivity of the holstein polaron", Phys. Rev. Lett. **107**, 076403 (2011).

[45] D. Balzer, T. J. A. M. Smolders, D. Blyth, S. N. Hood, and I. Kassal, "Delocalised kinetic monte carlo for simulating delocalisation-enhanced charge and exciton transport in disordered materials", Chem. Sci. **12**, 2276–2285 (2021).

[46] C. Zhang, E. Jeckelmann, and S. R. White, "Dynamical properties of the one-dimensional holstein model", Phys. Rev. B **60**, 14092–14104 (1999).

[47] E. Jeckelmann and S. R. White, "Density-matrix renormalization-group study of the polaron problem in the Holstein model", Phys. Rev. B **57**, 6376–6385 (1998).

[48] W. Li, J. Ren, and Z. Shuai, "Finite-temperature TD-DMRG for the carrier mobility of organic semiconductors", J. Phys. Chem. Lett. **11**, 4930–4936 (2020).

[49] W. Li, J. Ren, and Z. Shuai, "A general charge transport picture for organic semiconductors with nonlocal electron-phonon couplings", Nature Comm. **12**, 4260 (2021).

[50] W. Li, J. Ren, and Z. Shuai, "Finite-temperature td-dmrg for the carrier mobility of organic semiconductors", J. Phys. Chem. Lett. **11**, 4930–4936 (2020).

[51] J. Ren, W. Li, T. Jiang, Y. Wang, and Z. Shuai, "Time-dependent density matrix renormalization group method for quantum dynamics in complex systems", WIREs Comput. Mol. Sci. **12**, e1614 (2022).

[52] J. Bonča, S. A. Trugman, and M. Berciu, "Spectral function of the Holstein polaron at finite temperature", Phys. Rev. B **100**, 094307 (2019).

[53] D. Jansen, J. Bonča, and F. Heidrich-Meisner, "Finite-temperature density-matrix renormalization group method for electron-phonon systems: thermodynamics and Holstein-polaron spectral functions", Phys. Rev. B **102**, 165155 (2020).

[54] V. Janković and N. Vukmirović, "Spectral and thermodynamic properties of the Holstein polaron: hierarchical equations of motion approach", Phys. Rev. B **105**, 054311 (2022).

[55] Y. Tanimura, "Numerically "exact" approach to open quantum dynamics: the hierarchical equations of motion (HEOM)", J. Chem. Phys. **153**, 020901 (2020).

[56] V. Janković, "Charge transport limited by nonlocal electron-phonon interaction. i. hierarchical equations of motion approach", Phys. Rev. B **112**, 035111 (2025).

[57] H. De Raedt and A. Lagendijk, "Numerical calculation of path integrals: the small-polaron model", Phys. Rev. B **27**, 6097–6109 (1983).

[58] H. De Raedt and A. Lagendijk, "Numerical study of Holstein's molecular-crystal model: Adiabatic limit and influence of phonon dispersion", Phys. Rev. B **30**, 1671–1678 (1984).

[59] P. E. Kornilovitch, "Continuous-time quantum Monte Carlo algorithm for the lattice polaron", Phys. Rev. Lett. **81**, 5382–5385 (1998).

[60] P. E. Spencer, J. H. Samson, P. E. Kornilovitch, and A. S. Alexandrov, "Effect of electron-phonon interaction range on lattice polaron dynamics: A continuous-time quantum Monte Carlo study", Phys. Rev. B **71**, 184310 (2005).

[61] A. S. Mishchenko, N. V. Prokof'ev, A. Sakamoto, and B. V. Svistunov, "Diagrammatic quantum monte carlo study of the fröhlich polaron", Phys. Rev. B **62**, 6317–6336 (2000).

[62] N. V. Prokof'ev and B. V. Svistunov, "Polaron problem by diagrammatic quantum monte carlo", Phys. Rev. Lett. **81**, 2514–2517 (1998).

[63] J. Greitemann and L. Pollet, "Lecture notes on Diagrammatic Monte Carlo for the Fröhlich polaron", SciPost Phys. Lect. Notes, 2 (2018).

[64] R. P. Feynman, R. W. Hellwarth, C. K. Iddings, and P. M. Platzman, "Mobility of slow electrons in a polar crystal", Phys. Rev. **127**, 1004–1017 (1962).

[65] R. P. Feynman, "Slow electrons in a polar crystal", Phys. Rev. **97**, 660–665 (1955).

[66] A. S. Mishchenko, N. Nagaosa, G. De Filippis, A. de Candia, and V. Cataudella, "Mobility of Holstein polaron at finite temperature: an unbiased approach", Phys. Rev. Lett. **114**, 146401 (2015).

[67] D. Thirumalai and B. Berne, "Methods for simulating time correlation functions in quantum systems", Comp. Phys. Comm. **63**, 415–426 (1991).

[68] C. H. Mak and D. Chandler, "Solving the sign problem in quantum Monte Carlo dynamics", Phys. Rev. A **41**, 5709–5712 (1990).

[69] G. Cohen, E. Gull, D. R. Reichman, and A. J. Millis, "Taming the dynamical sign problem in real-time evolution of quantum many-body problems", Phys. Rev. Lett. **115**, 266802 (2015).

[70] R. Egger, L. Mühlbacher, and C. H. Mak, "Path-integral Monte Carlo simulations without the sign problem: multilevel blocking approach for effective actions", Phys. Rev. E **61**, 5961–5966 (2000).

[71] D. Kim, J. D. Doll, and D. L. Freeman, "Dynamic path integral methods: a maximum entropy approach based on the combined use of real and imaginary time quantum Monte Carlo data", J. Chem. Phys. **108**, 3871–3875 (1998).

[72] R. Levy, J. LeBlanc, and E. Gull, "Implementation of the maximum entropy method for analytic continuation", Comp. Phys. Comm. **215**, 149–155 (2017).

[73] O. Gunnarsson, M. W. Haverkort, and G. Sangiovanni, "Analytical continuation of imaginary axis data for optical conductivity", Phys. Rev. B **82**, 165125 (2010).

[74] E. Gallicchio, S. A. Egorov, and B. J. Berne, "On the application of numerical analytic continuation methods to the study of quantum mechanical vibrational relaxation processes", J. Chem. Phys. **109**, 7745–7755 (1998).

[75] M. Jarrell and J. Gubernatis, "Bayesian inference and the analytic continuation of imaginary-time quantum Monte Carlo data", Phys. Rep. **269**, 133–195 (1996).

[76] J. E. Gubernatis, M. Jarrell, R. N. Silver, and D. S. Sivia, "Quantum Monte Carlo simulations and maximum entropy: Dynamics from imaginary-time data", Phys. Rev. B **44**, 6011–6029 (1991).

[77] J. Schött, I. L. M. Locht, E. Lundin, O. Grånäs, O. Eriksson, and I. Di Marco, "Analytic continuation by averaging Padé approximants", Phys. Rev. B **93**, 075104 (2016).

[78] G. Mahan, *Many-particle physics* (Kluwer Academic, New York, 2000).

[79] A. Altland and B. Simons, *Condensed matter field theory* (Cambridge University Press, Cambridge, 2010).

[80] R. Kubo, "Statistical-mechanical theory of irreversible processes. i. general theory and simple applications to magnetic and conduction problems", Journal of the Physical Society of Japan **12**, 570–586 (1957).

[81] M. S. Green, "Markoff random processes and the statistical mechanics of time-dependent phenomena. ii. irreversible processes in fluids", Journal of Chemical Physics **22**, 398–413 (1954).

[82] J. W. Negele and H. Orland, *Quantum many-particle systems* (CRC Press, Boca Raton, FL, 1998).

[83] D. Emin, "Phonon-assisted transition rates i. optical-phonon-assisted hopping in solids", Adv. Phys. **24**, 305–348 (1975).

[84] S. Tomić and N. Vukmirović, "Quantum dots", in *Handbook of optoelectronic device modeling and simulation: fundamentals, materials, nanostructures, leds, and amplifiers - volume one, ed. j. piprek* (Taylor and Francis, 2017), pp. 419–448.

[85] I. G. Lang and Y. A. Firsov, "Kinetic theory of semiconductors with low mobility", Sov. Phys. JETP **16**, 1301–1312 (1963).

[86] J. Zinn-Justin, *Path integrals in quantum mechanics* (Oxford University Press, Oxford, 2005).

[87] H. Kleinert, *Path integrals in quantum mechanics, statistics, polymer physics, and financial markets* (World Scientific Publishing Co, Singapore, 2004).

[88] L. S. Schulman, *Techniques and applications of path integration* (Wiley, Hoboken, NJ, 1981).

[89] R. P. Feynman and A. R. Hibbs, *Quantum mechanics and path integrals* (McGraw-Hill, New York, 1965).

[90] R. P. Feynman, "Space-time approach to non-relativistic quantum mechanics", Reviews of Modern Physics **20**, 367–387 (1948).

[91] N. Wiener, "Differential-space", Journal of Mathematical Physics **2**, 131–174 (1923).

[92] M. Kac, "On distributions of certain wiener functionals", Transactions of the American Mathematical Society **65**, 1–13 (1949).

[93] P. A. M. Dirac, "The lagrangian in quantum mechanics", Physikalische Zeitschrift der Sowjetunion **3**, 64–72 (1933).

[94] C. Itzykson and J.-B. Zuber, *Quantum field theory* (McGraw-Hill, New York, 1980).

[95] J. Zinn-Justin, *Quantum field theory and critical phenomena* (Oxford University Press, Oxford, 1989).

[96] R. Kubo, *Statistical mechanics* (North-Holland, Amsterdam, 1965).

[97] P. A. M. Dirac, *The principles of quantum mechanics* (Oxford University Press, Oxford, 1948).

[98] G. C. Wick, "The evaluation of the collision matrix", Physical Review **80**, 268–272 (1950).

[99] M. H. Kalos and P. A. Whitlock, *Monte carlo methods* (Wiley-VCH, Weinheim, 2008).

[100] S. M. Wong, *Computational methods in physics and engineering* (Prentice Hall, World Scinetific Publishing Co, Singapore, 1997).

[101] N. Metropolis, A. W. Rosenbluth, M. N. Rosenbluth, A. H. Teller, and E. Teller, "Equation of state calculations by fast computing machines", J. Chem. Phys. **21**, 1087–1092 (1953).

[102] N. Metropolis and S. Ulam, "The monte carlo method", J. Amer. Stat. Assoc. **44**, 335–341 (1949).

[103] I. Georgescu, "The early days of monte carlo methods", Nature Reviews Physics **5**, 372 (2023).

[104] D. E. Knuth, *The art of computer programming, volume 2: seminumerical algorithms*, 3rd ed. (Addison-Wesley, Reading, MA, 1998).

[105] M. Betancourt, "A conceptual introduction to hamiltonian monte carlo", arXiv:1701.02434 (2018).

[106] D. Thirumalai and B. J. Berne, "On the calculation of time correlation functions in quantum systems", J. Chem. Phys. **79**, 5029–5033 (1983).

[107] J. Cao, L. W. Ungar, and G. A. Voth, "A novel method for simulating quantum dissipative systems", J. Chem. Phys. **104**, 4189–4197 (1996).

[108] P. E. Kornilovitch and E. R. Pike, "Polaron effective mass from Monte Carlo simulations", Phys. Rev. B **55**, R8634 (1997).

[109] R. Egger and C. H. Mak, "Low-temperature dynamical simulation of spin-boson systems", Phys. Rev. B **50**, 15210–15225 (1994).

[110] L. Song and Q. Shi, "A new approach to calculate charge carrier transport mobility in organic molecular crystals from imaginary time path integral simulations", J. Chem. Phys. **142**, 174103 (2015).

[111] B. A. Mason and K. Hess, "Quantum Monte Carlo calculations of electron dynamics in dissipative solid-state systems using real-time path integrals", Phys. Rev. B **39**, 5051–5059 (1989).

[112] M. Troyer and U.-J. Wiese, "Computational complexity and fundamental limitations to fermionic quantum monte carlo simulations", Phys. Rev. Lett. **94**, 170201 (2005).

[113] D. E. Makarov and N. Makri, "Path integrals for dissipative systems by tensor multiplication: condensed phase quantum dynamics for arbitrarily long time", Chem. Phys. Lett. **221**, 482–491 (1994).

[114] N. Makri, "Feynman path integration in quantum dynamics", Comput. Phys. Commun. **63**, 389–414 (1991).

[115] R. C. Aster, B. Borchers, and C. H. Thurber, *Parameter estimation and inverse problems* (Elsevier Academic Press, Amsterdam, 2013).

[116] H. J. Vidberg and J. W. Serene, "Solving the Eliashberg equations by means of N-point Padé approximants", J. Low Temp. Phys. **29**, 179–192 (1977).

[117] A. N. Tikhonov and V. Y. Arsenin, *Solutions of ill-posed problems* (Winston & Sons, Washington, D.C., 1977).

[118] G. Krilov, E. Sim, and B. J. Berne, "Quantum time correlation functions from complex time Monte Carlo simulations: A maximum entropy approach", J. Chem. Phys. **114**, 1075–1088 (2001).

[119] G. Krilov and B. J. Berne, "Real time quantum correlation functions. II. maximum entropy numerical analytic continuation of path integral Monte Carlo and centroid molecular dynamics data", J. Chem. Phys. **111**, 9147–9156 (1999).

[120] R. N. Silver, D. S. Sivia, and J. E. Gubernatis, "Maximum-entropy method for analytic continuation of quantum Monte Carlo data", Phys. Rev. B **41**, 2380–2389 (1990).

[121] K. S. D. Beach, R. J. Gooding, and F. Marsiglio, "Reliable padé analytical continuation method based on a high-accuracy symbolic computation algorithm", Phys. Rev. B **61**, 5147–5157 (2000).

[122] A. W. Sandvik, "Stochastic method for analytic continuation of quantum monte carlo data", Phys. Rev. B **57**, 10287–10290 (1998).

[123] A. W. Sandvik, "Constrained sampling method for analytic continuation", Phys. Rev. E **94**, 063308 (2016).

[124] C. E. Creffield, E. G. Klepfish, E. R. Pike, and S. Sarkar, "Spectral weight function for the half-filled Hubbard model: a singular value decomposition approach", Phys. Rev. Lett. **75**, 517–520 (1995).

[125] G. Baym and N. D. Mermin, "Determination of thermodynamic Green's functions", J. Math. Phys. **2**, 232–234 (1961).

[126] M. Rumetshofer, D. Bauernfeind, and W. von der Linden, "Bayesian parametric analytic continuation of Green's functions", Phys. Rev. B **100**, 075137 (2019).

[127] J. Otsuki, M. Ohzeki, H. Shinaoka, and K. Yoshimi, "Sparse modeling approach to analytical continuation of imaginary-time quantum monte carlo data", Phys. Rev. E **95**, 061302 (2017).

[128] K.-W. Sun and F. Wang, "Neural network analytic continuation for monte carlo: improvement by statistical errors", Chin. Phys. B **32**, 070705 (2023).

[129] M. Kliczkowski, L. Keyes, S. Roy, T. Paiva, M. Randeria, N. Trivedi, and M. M. Maśka, "Autoencoder-based analytic continuation method for strongly correlated quantum systems", Phys. Rev. B **110**, 115119 (2024).

[130] T. Dornheim, Z. A. Moldabekov, and P. Tolias, "Analytical representation of the local field correction of the uniform electron gas within the effective static approximation", Phys. Rev. B **103**, 165102 (2021).

[131] H. F. Trotter, "On the product of semi-groups of operators", Proc. Amer. Math. Soc. **10**, 545–551 (1959).

[132] S. Miladić and N. Vukmirović, "Method for obtaining polaron mobility using real and imaginary time path-integral Quantum Monte Carlo", Phys. Rev. B **107**, 184315 (2023).

[133] N. Prodanović and N. Vukmirović, "Charge carrier mobility in systems with local electron-phonon interaction", Phys. Rev. B **99**, 104304 (2019).

[134] S. H. Lin, C. H. Chang, K. K. Liang, R. Chang, Y. J. Shiu, J. M. Zhang, T.-S. Yang, M. Hayashi, and F. C. Hsu, "Ultrafast dynamics and spectroscopy of bacterial photosynthetic reaction centers", in *Advances in chemical physics* (John Wiley and Sons, Inc., 2002), pp. 1–88.

[135] G. Nan, X. Yang, L. Wang, Z. Shuai, and Y. Zhao, "Nuclear tunneling effects of charge transport in rubrene, tetracene, and pentacene", Phys. Rev. B **79**, 115203, 115203 (2009).

[136] V. Janković, P. Mitrić, D. Tanasković, and N. Vukmirović, "Vertex corrections to conductivity in the holstein model: a numerical-analytical study", Phys. Rev. B **109**, 214312 (2024).

[137] X. Yang, L. Wang, C. Wang, W. Long, and Z. Shuai, "Influences of crystal structures and molecular sizes on the charge mobility of organic semiconductors: oligothiophenes", Chem. Mater. **20**, 3205–3211 (2008).

[138] A. N. Sokolov, S. Atahan-Evrenk, R. Mondal, H. B. Akkerman, R. S. Sánchez-Carrera, S. Granados-Focil, J. Schrier, S. C. B. Mannsfeld, A. P. Zoombelt, Z. Bao, and A. Aspuru-Guzik, "From computational discovery to experimental characterization of a high hole mobility organic crystal", Nature Comm. **2**, 437 (2011).

[139] S.-H. Wen, A. Li, J. Song, W.-Q. Deng, K.-L. Han, and W. A. Goddard, "First-principles investigation of anistropic hole mobilities in organic semiconductors", J. Phys. Chem. B **113**, 8813–8819 (2009).

[140] B. Baumeier, J. Kirkpatrick, and D. Andrienko, "Density-functional based determination of intermolecular charge transfer properties for large-scale morphologies", Phys. Chem. Chem. Phys. **12**, 11103–11113 (2010).

[141] V. Coropceanu, J. Cornil, D. A. da Silva Filho, Y. Olivier, R. Silbey, and J.-L. Bredas, "Charge transport in organic semiconductors", Chem. Rev. **107**, 926 (2007).

[142] P. Mitrić, V. Janković, N. Vukmirović, and D. Tanasković, "Spectral functions of the Holstein polaron: exact and approximate solutions", Phys. Rev. Lett. **129**, 096401 (2022).

[143] K. Vafayi and O. Gunnarsson, "Analytical continuation of spectral data from imaginary time axis to real frequency axis using statistical sampling", Phys. Rev. B **76**, 035115 (2007).

[144] M. Panhans, S. Hutsch, and F. Ortmann, "Insight on charge-transfer regimes in electron-phonon coupled molecular systems via numerically exact simulations", Commun. Phys. **6**, 125 (2023).

Appendix A

Path-integral construction details

A.1 Action of exponential operators

In this appendix, the details of the evaluation of matrix elements of the exponential operators appearing in Sec. X are presented. For notational simplicity, explicit site indices are suppressed when no ambiguity arises, and the notation X^j is used to denote the set of phonon coordinates $\{X_n^j\}_{n=0}^{N-1}$ corresponding to all lattice sites at a given time slice j.

Evaluation of electronic matrix elements

Since the hopping Hamiltonian H_2 acts only on the electronic degrees of freedom, its action is determined entirely by the choice of electron basis. In the momentum representation, H_2 is diagonal and can be written as

$$H_2 = \sum_k \varepsilon(k) c_k^\dagger c_k, \qquad \varepsilon(k) = -2J\cos(k)\ . \tag{A.1}$$

Its action on a momentum basis state is therefore immediate,

$$\mathrm{e}^{-zH_2}|q;X\rangle = \mathrm{e}^{-z\varepsilon(q)}|q;X\rangle\ . \tag{A.2}$$

In the position representation, the operator e^{-zH_2} is no longer diagonal. Its matrix elements are obtained by inserting a resolution of identity in the momentum basis,

$$\langle r_j|\mathrm{e}^{-zH_2}|r_{j+1}\rangle = \sum_k \langle r_j|k\rangle \mathrm{e}^{-z\varepsilon(k)}\langle k|r_{j+1}\rangle\ . \tag{A.3}$$

Using the Fourier-transform convention

$$\langle k|r\rangle = \frac{1}{\sqrt{N}}\mathrm{e}^{\mathrm{i}kr}, \qquad \langle r|k\rangle = \frac{1}{\sqrt{N}}\mathrm{e}^{-\mathrm{i}kr}\ , \tag{A.4}$$

one obtains

$$\langle r_j|\mathrm{e}^{-zH_2}|r_{j+1}\rangle = \frac{1}{N}\sum_k \mathrm{e}^{\mathrm{i}k(r_{j+1}-r_j)}\mathrm{e}^{2Jz\cos(k)}\ . \tag{A.5}$$

The sum is invariant under $k \to -k$, because both $\cos(k)$ and $\cos(k(r_{j+1}-r_j))$ are even functions. The sine part therefore cancels in the sum, and the matrix element can be written in the form

$$I(z;r_{j+1}-r_j) = \frac{1}{N}\sum_k \cos\left(k(r_{j+1}-r_j)\right)\mathrm{e}^{2Jz\cos(k)}\ . \tag{A.6}$$

Since the momentum takes values

$$k = \frac{2\pi n}{N}, \qquad n = 0,1,\ldots,N-1\ , \tag{A.7}$$

one obtains exactly the expression in Sec.ref to the section

$$I(z; r_{j+1} - r_j) = \frac{1}{N} \sum_{n=0}^{N-1} \cos\left(\frac{2\pi n}{N} (r_{j+1} - r_j) \mathrm{e}^{2Jz\cos\left(\frac{2\pi n}{N}\right)} \right) . \tag{A.8}$$

The operator H_1 contains both the phonon potential term and the electron–phonon interaction term. For fixed phonon coordinates, the potential contribution acts as a scalar factor, while the electron–phonon interaction is diagonal in the electron site representation. It is therefore convenient to first evaluate the action of the electron-dependent part on the electronic basis states.

Using the relation

$$c_n^\dagger c_n |r\rangle = \delta_{n,r} |r\rangle , \tag{A.9}$$

one obtains

$$\exp\left(z \sum_n \sqrt{2M\omega_n} G X_n c_n^\dagger c_n \right) |r; X\rangle = \exp\left(z \sum_n \sqrt{2M\omega_n} G X_n \delta_{n,r} \right) |r; X\rangle . \tag{A.10}$$

Transforming this result to the momentum basis using

$$|q\rangle = \frac{1}{\sqrt{N}} \sum_r \mathrm{e}^{\mathrm{i}qr} |r\rangle , \tag{A.11}$$

gives

$$\exp\left(z \sum_n \sqrt{2M\omega_n} G X_n c_n^\dagger c_n \right) |q; X\rangle = \frac{1}{N} \sum_{q'} \sum_r \mathrm{e}^{-\mathrm{i}r(q-q')} \exp\left(z\sqrt{2M\omega_r} G X_r \right) |q'; X\rangle . \tag{A.12}$$

Including the phonon potential term then yields

$$\mathrm{e}^{zH_1} |q; X\rangle = \exp\left[z \sum_n \frac{1}{2} M\omega_n^2 X_n^2 \right] \frac{1}{N} \sum_{q'} \sum_r \mathrm{e}^{-\mathrm{i}r(q-q')} \exp\left(z\sqrt{2M\omega_r} G X_r \right) |q'; X\rangle . \tag{A.13}$$

Collecting the contributions arising from the action of e^{zH_2} and from the electronic part of e^{zH_1} on the electron momentum states, the electronic matrix elements can be written in terms of function $f_{q_i,q_j}(z; X)$, defined as

$$f_{q_i,q_j}(z; X) = \mathrm{e}^{z\varepsilon(q_i)} \frac{1}{N} \sum_r \mathrm{e}^{-\mathrm{i}r(q_i - q_j)} \mathrm{e}^{z\sqrt{2M\omega_r} G X_r} \tag{A.14}$$

Evaluation of phonon matrix elements

To evaluate the phonon contribution to the matrix elements, we consider expressions of the form

$$\langle X^j; q_j | \mathrm{e}^{zH_0} \mathrm{e}^{zH_1} | q_{j+1}; X^{j+1} \rangle . \tag{A.15}$$

Since the operator H_0 acts only on phonon momenta, we insert a resolution of identity in the phonon momentum basis,

$$1 = \int \left(\prod_{n=0}^{N-1} \mathrm{d}P_n \right) |\{P_n\}\rangle\langle\{P_n\}|. \tag{A.16}$$

Using the fact that

$$H_0 = \sum_{n=0}^{N-1} \frac{P_n^2}{2M}, \tag{A.17}$$

its action in the momentum basis is diagonal,

$$e^{zH_0}|\{P_n\}\rangle = \exp\left(z\sum_{n=0}^{N-1}\frac{P_n^2}{2M}\right)|\{P_n\}\rangle. \tag{A.18}$$

The coordinate-momentum overlaps are taken in the form

$$\langle X|P\rangle = \frac{1}{(2\pi)^{N/2}}\exp\left(\mathrm{i}\sum_{n=0}^{N-1}P_nX_n\right), \qquad \langle P|X\rangle = \frac{1}{(2\pi)^{N/2}}\exp\left(-\mathrm{i}\sum_{n=0}^{N-1}P_nX_n\right). \tag{A.19}$$

Using the previously derived action of e^{zH_2} and of the electronic part of e^{zH_1}, the matrix element factorizes into an electronic contribution encoded in the function $f_{q_{j+1},q_j}(z;X^{j+1})$, and a phonon-dependent contribution. The latter can be written as

$$\begin{aligned}\langle X^j;q_j|e^{zH_0}e^{zH_1}|q_{j+1};X^{j+1}\rangle = {}& \exp\left[z\sum_{n=0}^{N-1}\frac{M}{2}\omega_n^2(X_n^{j+1})^2\right]f_{q_{j+1},q_j}(z;X^{j+1})\\ &\times\frac{1}{(2\pi)^N}\int\left(\prod_{n=0}^{N-1}\mathrm{d}P_n\right)\exp\left[z\sum_{n=0}^{N-1}\frac{P_n^2}{2M}+\mathrm{i}\sum_{n=0}^{N-1}P_n(X_n^j-X_n^{j+1})\right].\end{aligned} \tag{A.20}$$

Since the exponent is a sum over independent phonon modes, the integral factorizes,

$$\frac{1}{(2\pi)^N}\prod_{n=0}^{N-1}\int\mathrm{d}P_n\,\exp\left[z\frac{P_n^2}{2M}+\mathrm{i}P_n(X_n^j-X_n^{j+1})\right]. \tag{A.21}$$

Each integral is evaluated by completing the square. For a fixed mode n,

$$z\frac{P_n^2}{2M}+\mathrm{i}P_n(X_n^j-X_n^{j+1}) = \frac{z}{2M}\left(P_n+\frac{M\mathrm{i}}{z}(X_n^j-X_n^{j+1})\right)^2+\frac{M}{2z}(X_n^j-X_n^{j+1})^2. \tag{A.22}$$

Thus,

$$\begin{aligned}\int\mathrm{d}P_n\,\exp\left[z\frac{P_n^2}{2M}+\mathrm{i}P_n(X_n^j-X_n^{j+1})\right] = {}& \exp\left[\frac{M}{2z}(X_n^j-X_n^{j+1})^2\right]\\ &\times\int\mathrm{d}P_n\,\exp\left[\frac{z}{2M}\left(P_n+\frac{M\mathrm{i}}{z}(X_n^j-X_n^{j+1})\right)^2\right].\end{aligned} \tag{A.23}$$

The remaining integral is Gaussian and can be evaluated analytically. For each mode n, one has

$$\int\mathrm{d}P_n\,\exp\left[z\frac{P_n^2}{2M}+\mathrm{i}P_n(X_n^j-X_n^{j+1})\right] = C_n(z)\,\exp\left[\frac{M}{2z}(X_n^j-X_n^{j+1})^2\right], \tag{A.24}$$

where $C_n(z)$ is the Gaussian normalization factor arising from the integration over P_n. Since the exponent is separable in the phonon modes, the full integral factorizes into a product of one-dimensional Gaussian integrals, yielding

$$\prod_{n=0}^{N-1}\int\mathrm{d}P_n\,\exp\left[z\frac{P_n^2}{2M}+\mathrm{i}P_n(X_n^j-X_n^{j+1})\right] = \left(\prod_{n=0}^{N-1}C_n(z)\right)\exp\left[\sum_{n=0}^{N-1}\frac{M}{2z}(X_n^j-X_n^{j+1})^2\right]. \tag{A.25}$$

Introducing the shorthand

$$C(z) = \prod_{n=0}^{N-1}C_n(z), \tag{A.26}$$

one obtains

$$\prod_{n=0}^{N-1} \int \mathrm{d}P_n \, \exp\left[z\frac{P_n^2}{2M} + \mathrm{i}P_n(X_n^j - X_n^{j+1}) \right] = C(z) \, \exp\left[\sum_{n=0}^{N-1} \frac{M}{2z}(X_n^j - X_n^{j+1})^2 \right]. \tag{A.27}$$

The factor $C(z)$ depends only on the time step and not on the phonon coordinates, and is therefore absorbed into the overall constants C_1, C_2, and C_3 used for the different contour segments. The explicit normalization factor is not needed in the final estimator, since such constants cancel in the normalized Monte Carlo averages.

Substituting this result back, the matrix element takes the form

$$\begin{aligned} \langle X^j; q_j | \mathrm{e}^{zH_0} \mathrm{e}^{zH_1} | q_{j+1}; X^{j+1} \rangle &= C(z) \, f_{q_{j+1},q_j}(z; X^{j+1}) \\ &\quad \times \exp\left[z \sum_{n=0}^{N-1} \frac{M}{2} \omega_n^2 (X_n^{j+1})^2 + \sum_{n=0}^{N-1} \frac{M}{2z}(X_n^j - X_n^{j+1})^2 \right]. \end{aligned} \tag{A.28}$$

The different contour segments are obtained by substituting the appropriate values of z. For example, for $z = -\tau$ one obtains

$$\begin{aligned} \langle X^j; q_j | \rho(-\tau) | q_{j+1}; X^{j+1} \rangle &= C_1 \, f_{q_{j+1},q_j}(-\tau; X^{j+1}) \\ &\quad \times \exp\left[-\tau \sum_{n=0}^{N-1} \left(\frac{M}{2} \omega_n^2 (X_n^{j+1})^2 + \frac{M}{2} \frac{(X_n^{j+1} - X_n^j)^2}{\tau^2} \right) \right], \end{aligned} \tag{A.29}$$

which coincides with the expression used in the main text.

A.2 Structure of the phonon action matrix $\mathcal{D}$ and the vector d

The action in the Eq. (ref to the equation) is given as

$$S[\mathbf{Y}] = \frac{1}{2} \mathbf{Y}^T \mathcal{D} \mathbf{Y} + \mathbf{Y}^T \cdot \mathbf{d} \, , \tag{A.30}$$

where $\mathcal{D}$ is square matrix of dimension $(m + 2Q)N$, and $\mathbf{d}$ is vector of the same dimension.

The structure of vector $\mathbf{d}$ is defined as

$$\mathbf{d} = \Delta(\{r\}) \cdot \mathbf{L} \, , \tag{A.31}$$

where vector $\mathbf{L}$ corresponds to the electron-phonon interaction strength and is given as

$$\mathbf{L} = \sqrt{2M} G \, \left(\mathbf{1}_{m+2Q} \otimes (\omega_0, \omega_1, \ldots, \omega_{N-1})^T \right) \, . \tag{A.32}$$

Here the $\mathbf{1}_{m+2Q}$ represents the column vector of dimension $m + 2Q$ whose all components equal to one, $\mathbf{1}_{m+2Q} = (1, 1, 1, \ldots, 1)^T$.

Matrix $\Delta(\{r\})$ is diagonal and its form depends on the configuration of electronic positions $\{r_0, r_1, \ldots, r_{m+2Q}\}$. The matrix $\Delta(\{r\})$ can be composed as

$$\Delta(\{r\}) = (T \otimes I_{N \times N}) \cdot G \, , \tag{A.33}$$

where $I_{N \times N}$ is unit matrix of dimension N, T diagonal square matrix of dimension $m + 2Q$, and G is a block-diagonal matrix of dimension $m + 2Q$. This construction ensures that the electron–phonon

interaction couples only to the phonon coordinate corresponding to the electron position at each time slice. The matrix G is given as

$$G = \begin{pmatrix} g(r_0) & 0 & 0 & & \dots & & 0 \\ 0 & g(r_1) & 0 & & \dots & & 0 \\ & & \ddots & & & & \\ & & & g(r_{m+Q-1}) & & & \\ & & & & g(r_{m+Q+1}) & & \\ & & & & & \ddots & \\ & & & & & & g(r_{m+2Q}) \end{pmatrix},$$

where each block $g(r_j)$ selects the phonon coordinate at the electron position r_j. The matrix $g(r_j)$ is diagonal of dimension $N \times N$ and its elements are Kronecker delta functions

$$g(r_j) = \begin{pmatrix} \delta_{0,r_j} & & & \\ & \delta_{1,r_j} & & \\ & & \ddots & \\ & & & \delta_{N-1,r_j} \end{pmatrix}.$$

The matrix T encodes the time discretization along the contour and is given as

$$T = \begin{pmatrix} \tau & & & & & & & & \\ & \ddots & & & & & & & \\ & & \tau & & & & & & \\ & & & -\mathrm{i}\Delta t & & & & & \\ & & & & \ddots & & & & \\ & & & & & -\mathrm{i}\Delta t & & & \\ & & & & & & \mathrm{i}\Delta t & & \\ & & & & & & & \ddots & \\ & & & & & & & & \mathrm{i}\Delta t \end{pmatrix}.$$

Concisely, its components can be written as

$$(T)_{i,j} = \begin{cases} 0 & , i \neq j \\ \tau & , i = j \quad \wedge \quad 0 \leq i \leq m-1 \\ -\mathrm{i}\Delta t & , i = j \quad \wedge \quad m \leq i \leq m+Q-1 \\ \mathrm{i}\Delta t & , i = j \quad \wedge \quad m+Q \leq i \leq m+2Q-1 \end{cases}$$

With this, the vector $\mathbf{d}$ is fully defined. The construction of the matrix $\mathcal{D}$ is presented next.

The matrix $\mathcal{D}$ appears in the same form in both electron basis representations. The matrix $\mathcal{D}$ is constructed as a sum of contributions arising from different terms in the phonon action. The first part of action to consider is the one where the phonon frequency ω_n appears, and the second part contains the phonon coordinate differences.

Specifically, the first part of phonon action reads

$$\tau \sum_{j=0}^{m-1} \sum_n \frac{M}{2} {\omega_n}^2 \left(X_n^{j+1}\right)^2 + (-\mathrm{i}\Delta t) \sum_{p=0}^{Q-1} \sum_n \frac{M}{2} {\omega_n}^2 \left(X_n^{m+p+1}\right)^2 + \mathrm{i}\Delta t \sum_{l=0}^{Q-1} \sum_n \frac{M}{2} {\omega_n}^2 \left(X_n^{m+Q+2+l}\right)^2 = \frac{M}{2} \mathbf{Y}^T \cdot A \cdot \mathbf{Y}$$

Matrix A is the diagonal matrix given as

$$A = T \otimes \Omega^2 ,$$

where $\Omega^2 = \mathrm{diag}\left(\omega_0^2, \omega_1^2, \ldots, \omega_{N-1}^2\right)$ and matrix T encoding the time variables was defined above in the construction of the vector $\mathbf{d}$.

Second part of the phonon action reads

$$\sum_{j=0}^{m-1}\sum_n \frac{M}{2}\frac{\left(X_n^{j+1}-X_n^j\right)^2}{\tau} + \sum_{p=0}^{Q-1}\sum_n \frac{M}{2}\frac{\left(X_n^{m+p+1}-X_n^{m+p}\right)^2}{(-\mathrm{i}\Delta t)} + \sum_{l=0}^{Q-1}\sum_n \frac{M}{2}\frac{\left(X_n^{m+Q+2+l}-X_n^{m+Q+1+l}\right)^2}{(\mathrm{i}\Delta t)} .$$

This part is split into three terms by expanding the squares of coordinate differences. These three terms are

$$(1) = \sum_{j=0}^{m-1}\sum_n \frac{M}{2}\frac{-2}{\tau}X_n^{j+1}X_n^j + \sum_{p=0}^{Q-1}\sum_n \frac{M}{2}\frac{-2}{(-\mathrm{i}\Delta t)}X_n^{m+p+1}X_n^{m+p} + \sum_{l=0}^{Q-1}\sum_n \frac{M}{2}\frac{-2}{(\mathrm{i}\Delta t)}X_n^{m+Q+2+l}X_n^{m+Q+1+l}$$

$$= \frac{1}{2}\mathbf{Y}^T(-2M\ C)(B\mathbf{Y}) = \frac{1}{2}\mathbf{Y}^T(-2M\ C\cdot B)\mathbf{Y}$$

$$(2) = \sum_{j=0}^{m-1}\sum_n \frac{M}{2}\frac{1}{\tau}\left(X_n^{j+1}\right)^2 + \sum_{p=0}^{Q-1}\sum_n \frac{M}{2}\frac{1}{(-\mathrm{i}\Delta t)}\left(X_n^{m+p+1}\right)^2 + \sum_{l=0}^{Q-1}\sum_n \frac{M}{2}\frac{1}{(\mathrm{i}\Delta t)}\left(X_n^{m+Q+2+l}\right)^2$$

$$= \frac{1}{2}\mathbf{Y}^T(M\ C)\mathbf{Y}$$

$$(3) = \sum_{j=0}^{m-1}\sum_n \frac{M}{2}\frac{1}{\tau}\left(X_n^{j}\right)^2 + \sum_{p=0}^{Q-1}\sum_n \frac{M}{2}\frac{1}{(-\mathrm{i}\Delta t)}\left(X_n^{m+p}\right)^2 + \sum_{l=0}^{Q-1}\sum_n \frac{M}{2}\frac{1}{(\mathrm{i}\Delta t)}\left(X_n^{m+Q+1+l}\right)^2$$

$$= \frac{1}{2}(B\mathbf{Y})^T(M\ C)(B\mathbf{Y}) = \frac{1}{2}\mathbf{Y}^T\left(B^T\cdot(M\ C)\cdot B\right)\mathbf{Y}$$

The matrix B is introduced to represent the cyclic shift of the phonon coordinates along the discretized contour,

$$B\cdot\mathbf{Y} = \left(Y^{m+2Q-1}, Y^0, \ldots, Y^{m+2Q-2}\right)^T = \left(X^0, X^1, \ldots, X^{m+Q-1}, X^{m+Q+1}, \ldots, X^{m+2Q}\right)^T .$$

It is given by

$$B = B'\otimes I_{N\times N},$$

where

$$B' = \begin{pmatrix} 0 & 0 & 0 & \ldots & 1 \\ 1 & 0 & 0 & \ldots & 0 \\ 0 & 1 & 0 & \ldots & 0 \\ & & \ddots & & \vdots \\ & & & 1 & 0 \end{pmatrix}.$$

The components of matrix B' are

$$(B')_{k,j} = \begin{cases} 1 & ,k=0 \ \wedge\ j=m+2Q-1, \\ 0 & ,k=0 \ \wedge\ j\neq m+2Q-1, \\ 0 & ,k=1,\ldots,m+2Q-1 \ \wedge\ j\neq k-1, \\ 1 & ,k=1,\ldots,m+2Q-1 \ \wedge\ j=k-1. \end{cases}$$

The matrix C can be written as

$$C = C'\otimes I_{N\times N}$$

where C' is the inverse of the diagonal matrix T. its components are therefore

$$(C')_{i,j} = \begin{cases} 0 & ,i\neq j \\ \\ (T_{i,j})^{-1} & ,i=j \end{cases}$$

Combining the phonon-frequency contribution with the three terms above, the matrix $\mathcal{D}$ is obtained in the form

$$\mathcal{D}' = A - 2C \cdot B + C + B^T \cdot C \cdot B \ ,$$

and

$$\mathcal{D} = M \ \mathcal{D}' \ .$$

The matrix $\mathcal{D}$ is therefore complex symmetric and has a positive-definite real part.

In case of calculations in imaginary time where the substitution $-\mathrm{i}\Delta t \rightarrow \Delta t$ is made, the elements of matrix T are real and consequently the matrix $\mathcal{D}$ is real symmetric.

Appendix B

Singluar value decomposition method for analytic continuation

In this appendix, the derivation of the expressions used in the singular value decomposition (SVD) method for obtaining the mobility from time-dependent current–current correlation functions is presented. In addition, selected details regarding the numerical implementation are briefly discussed.

The real part of the optical conductivity is related to the imaginary part of the retarded current–current correlation function in the frequency domain as [78]

$$\mathrm{Re}\ \sigma(\omega) = -\frac{\mathrm{Im}\ C^R(\omega)}{\omega}\ . \tag{B.1}$$

The retarded correlation function in the frequency domain is defined as

$$C^R(\omega) = \int_{-\infty}^{\infty} \mathrm{d}t\ C^R(t)\mathrm{e}^{\mathrm{i}\omega t}\ , \tag{B.2}$$

where the real-time retarded correlation function is given by

$$C^R(t) = -\frac{\mathrm{i}}{V}\theta(t)\langle[j(t), j(0)]\rangle\ , \tag{B.3}$$

with V denoting the system volume and $\theta(t)$ the Heaviside step function.

In the present approach, quantum Monte Carlo simulations provide the current–current correlation function in complex time,

$$C(z) = -\frac{1}{V}\langle j(z)j(0)\rangle\ , \tag{B.4}$$

where the complex time variable is defined as $z = t_{\mathrm{re}} - \mathrm{i}t_{\mathrm{im}}$, with $-\beta \leq t_{im} \leq 0$ and $t_{re} \geq 0$.

To establish the relation between this correlation function and the frequency-dependent conductivity, it is convenient to introduce additional correlation functions. The advanced correlation function is defined as [79]

$$C^A(t) = -\frac{\mathrm{i}}{V}\theta(-t)\langle[j(t), j(0)]\rangle\ , \tag{B.5}$$

while the greater ($C^>(t)$) and lesser ($C^<(t)$) correlation functions are given by

$$C^>(t) = -\frac{\mathrm{i}}{V}\langle j(t)j(0)\rangle\ , \tag{B.6}$$

$$C^<(t) = -\frac{\mathrm{i}}{V}\langle j(0)j(t)\rangle\ . \tag{B.7}$$

The retarded and advanced functions can be expressed in terms of these as

$$C^R(t) = \theta(t)\left(C^>(t) - C^<(t)\right)\ , \tag{B.8}$$

$$C^A(t) = -\theta(-t)\left(C^>(t) - C^<(t)\right)\ , \tag{B.9}$$

while the time-ordered correlation function satisfies

$$C(t) = \frac{1}{\mathrm{i}} C^{>}(t) \ . \tag{B.10}$$

In the frequency domain, these functions obey the relations

$$C^{>}(\omega) = \mathrm{e}^{\beta\omega} C^{<}(\omega) \ , \tag{B.11}$$

$$C^{R}(\omega) = C^{A}(\omega)^{*} \ , \tag{B.12}$$

$$C^{R}(\omega) - C^{A}(\omega) = C^{>}(\omega) - C^{<}(\omega) \ . \tag{B.13}$$

From these relations, one obtains

$$\mathrm{Im}\, C^{R}(\omega) = -\frac{1}{2\mathrm{i}} (1 - \mathrm{e}^{-\beta\omega}) C^{>}(\omega) \ , \tag{B.14}$$

and equivalently

$$C^{>}(\omega) = \frac{2\mathrm{i}\mathrm{Im}\, C^{R}(\omega)}{1 - \mathrm{e}^{-\beta\omega}} = \frac{-2\mathrm{i}\omega \mathrm{Re}\, \sigma(\omega)}{1 - \mathrm{e}^{-\beta\omega}} \ . \tag{B.15}$$

Using the spectral representation of the complex-time correlation function,

$$C(z) = -\mathrm{i} C^{>}(z) = \frac{-\mathrm{i}}{2\pi} \int_{-\infty}^{\infty} \mathrm{d}\omega \ C^{>}(\omega) \mathrm{e}^{-\mathrm{i}\omega z} \ , \tag{B.16}$$

one obtains the relation between the complex-time correlation function and the conductivity,

$$C(z) = \int_{-\infty}^{\infty} \mathrm{d}\omega \ \frac{-1}{\pi} \frac{\omega \mathrm{e}^{-\mathrm{i}\omega z}}{1 - \mathrm{e}^{-\beta\omega}} \mathrm{Re}\, \sigma(\omega) \ . \tag{B.17}$$

For the case of a single charge carrier, the conductivity can be expressed in terms of the mobility, yielding the final relation

$$\langle j(z) j(0) \rangle = \int_{-\infty}^{\infty} \mathrm{d}\omega \ \frac{1}{\pi} \frac{\omega \mathrm{e}^{-\mathrm{i}\omega z}}{1 - \mathrm{e}^{-\beta\omega}} \mathrm{Re}\mu(\omega) \ . \tag{B.18}$$

This expression defines the integral transform that relates the mobility in frequency space to the current–current correlation function in complex time. It serves as the basis for generating artificial correlation data from a known reference mobility, which is subsequently used to benchmark the analytic continuation procedure, as discussed in the main text.

Building on the previously introduced integral transform, the kernel is given by

$$K(z, \omega) = \frac{1}{\pi} \frac{\omega \mathrm{e}^{-\mathrm{i}\omega z}}{1 - \mathrm{e}^{-\beta\omega}} \ , \tag{B.19}$$

and the analytic continuation problem corresponds to the inversion of this integral relation.

In practice, the inverse problem of reconstructing the frequency-dependent mobility from the current–current correlation function evaluated at a discrete set of complex times is ill-posed and requires a careful numerical treatment. In the following, the singular value decomposition (SVD) approach to this problem is outlined.

The first step is to discretize Eq. (B.18) so that it corresponds to a finite set of complex time values. Let the vector $\mathbf{j}$ contain the values of the current–current correlation function, and let the vector $\mathbf{m}$ represent the mobility evaluated on a discrete frequency grid. The discretized version of Eq. (B.18) can then be written in the form

$$\mathbf{j} = \mathbf{K} \cdot \mathbf{m} \ , \tag{B.20}$$

where $\mathbf{K}$ is a known kernel matrix obtained from the discretization of the integral transform. The problem can be formulated in terms of real-valued quantities by treating real and imaginary parts separately.

The difficulty in solving this inverse problem arises from the fact that the matrix $\mathbf{K}$ is ill-conditioned, with singular values spanning many orders of magnitude and approaching zero.

Any real matrix can be decomposed using singular value decomposition in the form

$$\mathbf{K} = \mathbf{U}\mathbf{S}\mathbf{V}^T \ , \tag{B.21}$$

where $\mathbf{U}$ and $\mathbf{V}$ are orthogonal matrices, and $\mathbf{S}$ is a diagonal matrix whose entries s_i are the singular values. These are conventionally ordered as

$$s_1 \geq s_2 \geq \cdots \geq s_p \geq 0 \ . \tag{B.22}$$

By retaining only the p non-zero (or numerically significant) singular values, the matrix $\mathbf{G}$ can be written in reduced form as

$$\mathbf{K} = \mathbf{U}_p\mathbf{S}_p\mathbf{V}_p^T \ , \tag{B.23}$$

where $\mathbf{U}_p$, $\mathbf{V}_p$ and $\mathbf{S}_p$ denote the truncated matrices.

The corresponding pseudoinverse of $\mathbf{K}$ is given by

$$\mathbf{K}^i = \mathbf{V}_p\mathbf{S}_p^{-1}\mathbf{U}_p^T \ , \tag{B.24}$$

and the reconstructed mobility is obtained as

$$\mathbf{m}^i = \mathbf{K}^i\mathbf{j} \ . \tag{B.25}$$

This expression can be written explicitly as

$$\mathbf{m}^i = \sum_{k=1}^{p} \frac{\mathbf{U}_{.,i}^T \cdot \mathbf{j}}{s_i}\mathbf{V}_{.,i} \ , \tag{B.26}$$

where $\mathbf{U}_{.,i}$ and $\mathbf{V}_{.,i}$ denote the i-th columns of the matrices $\mathbf{U}$ and V, respectively. A detailed discussion of the interpretation of the pseudoinverse solution can be found in Ref. [115].

In practice, the direct use of this expression is limited by the presence of very small singular values. Even a small amount of noise in the input data $\mathbf{j}$ can be strongly amplified by division by s_i, leading to unstable and noisy reconstructions. To address this issue, the sum is truncated by introducing a cutoff for singular values, such that only terms with sufficiently large s_i are retained.

The choice of cutoff is guided by the noise level in the data. Denoting the estimated relative noise level by α, a common criterion is to retain only singular values satisfying $s_i \gtrsim \alpha s_1$. Consequently, higher-quality data (i.e., lower noise) allow more singular values to be included, leading to improved reconstruction accuracy. Furthermore, increasing the number of informative input data enhances the stability of the solution. In particular, the inclusion of real-time data in addition to imaginary-time data significantly improves the quality of the analytic continuation, as demonstrated in the main text.

The numerical implementation of the procedure requires the specification of a discrete frequency grid. The choice of frequency range and resolution influences the reconstructed mobility. An example illustrating the dependence of the results on the selected frequency interval is shown in Fig. B.1.

Additional input parameters required for the implementation include the set of complex time points, the corresponding current–current correlation function values, the inverse temperature β, and the cutoff criterion for singular values (or equivalently, the number of retained singular values). The dependence of the results on the singular value truncation is discussed in the main text.

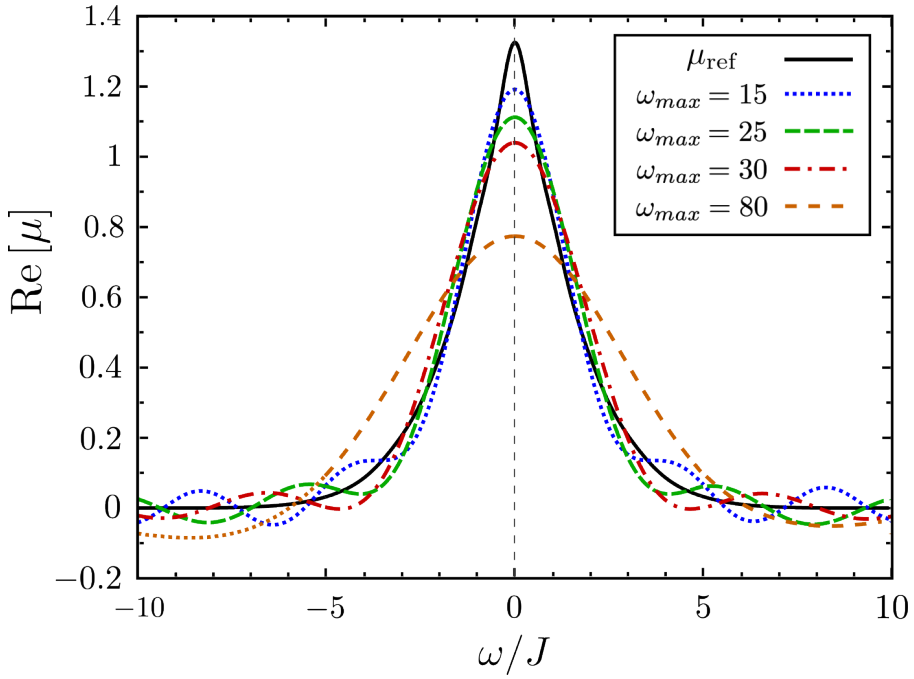

Figure B.1: Effect of frequency range on reconstructed mobility. The reference mobility (μ_{ref}) is shown together with reconstructions obtained using different intervals $[-\omega_{\text{max}}, \omega_{\text{max}}]$. The results are presented for model parameters $\omega_0/J = 1$, $G/J = 1$, and $T/J = 1$.

Appendix C

Monte Carlo simulation details

Technical aspects of the numerical calculations performed in this thesis are summarized in this appendix.

Data collection, analysis, and graphical representation were carried out using self-developed scripts written in C++, Python, Bash, and Gnuplot.

Quantum Monte Carlo (QMC) calculations of current–current correlation functions were performed on the PARADOX-IV supercomputing cluster at the Scientific Computing Laboratory, National Centre of Excellence for the Study of Complex Systems, Institute of Physics Belgrade.

The main QMC code used for the calculation of current–current correlation functions was implemented in C++. External libraries employed in the implementation include the GNU Scientific Library (GSL) and LAPACK, accessed through a C interface, for matrix diagonalization in the momentum-basis formulation.

Parallelization of the QMC simulations was achieved using the Message Passing Interface (MPI). All calculations were performed using 100 CPU cores in parallel. On each processor, the same QMC algorithm was executed with an independent random number generator seed determined by the processor index. The results obtained from individual processors were collected and aggregated on a master process, where mean values and corresponding statistical errors were evaluated. Statistical uncertainties were estimated using standard error analysis based on independent Monte Carlo samples. Typical simulation times ranged from few minutes to few hours depending on system size and parameter choice.

QMC algorithm in position representation

In this section, the numerical procedure used for the evaluation of current–current correlation functions in the position representation is described in detail.

Model parameters and discretization

The simulation is defined by the following parameters:

- system size N,
- number of phonon modes N_b,
- electron transfer integral J,
- electron–phonon coupling λ,
- phonon frequency ω,
- oscillator mass M,

- inverse temperature β,
- number of imaginary-time slices m,
- number of real-time slices Q.

The discretized time steps are defined as

$$\tau = \beta/m, \qquad \Delta t = t/Q.$$

Phonon frequencies and coupling constants are stored as vectors

$$\omega(n, b), \qquad \lambda(n, b),$$

where $0 \leq n < N$ labels lattice sites and $0 \leq b < N_b$ phonon modes.

Propagators

The imaginary-time propagator is defined as

$$I_0(l, \tau) = \frac{1}{N} \sum_{k=0}^{N-1} \cos\left(\frac{2\pi kl}{N}\right) \exp\left(2J\tau \cos\left(\frac{2\pi k}{N}\right)\right).$$

The real-time propagator is

$$I_1(l, \Delta t) = \frac{1}{N} \sum_{k=0}^{N-1} \cos\left(\frac{2\pi kl}{N}\right) \exp\left(-2iJ\Delta t \cos\left(\frac{2\pi k}{N}\right)\right).$$

For numerical implementation, the propagators are evaluated for all discrete lattice distances $l = 0, \ldots, N-1$ and stored as vectors.

The imaginary-time propagator $I_0(l, \tau)$ is real-valued and is stored directly as $I_0[l]$.

The real-time propagator $I_1(l, \Delta t)$ is complex-valued and is decomposed into magnitude and phase separately for the forward and backward real-time branches. The corresponding vectors are defined as

$$I_1[l] = |I_1(l, -\Delta t)|, \qquad I_2[l] = |I_1(l, \Delta t)|,$$

with phases

$$\phi_1(l) = \arg(I_1(l, -\Delta t)), \qquad \phi_2(l) = \arg(I_1(l, \Delta t)).$$

Although the magnitudes of the two propagators are equal, separate vectors are introduced in order to distinguish explicitly between the forward and backward real-time branches.

The corresponding minimum and maximum values,

$$I_0^{\min} = \min_l I_0[l], \qquad I_0^{\max} = \max_l I_0[l],$$

are determined from these arrays. Analogous definitions apply to the real-time propagators.

During the Monte Carlo sampling, $I_0[x]$ denotes the value of the propagator corresponding to the sampled lattice displacement x, i.e. the x-th entry of the precomputed array.

Phonon contribution

After integrating out the phonon degrees of freedom, the remaining contribution is expressed as a Gaussian form

$$d^T D^{-1} d,$$

where D is a complex symmetric matrix constructed from component matrices A, B, and C:

$$D = A - 2CB + C + B^T CB.$$

The inverse matrix D^{-1} is computed numerically.
The vector d is defined as

$$d = T \cdot G \cdot L,$$

where:

- L encodes the electron–phonon coupling along the discretized contour,
- G is the matrix arising from the discretized path integral and depends on the configuration of electron positions on the time contour,
- T is a diagonal matrix encoding the contour time structure, with diagonal entries given by

$$T_{jj} = \begin{cases} \tau & \text{for imaginary-time slices} \\ -i\Delta t & \text{for forward real-time slices} \\ i\Delta t & \text{for backward real-time slices} \end{cases}$$

Phase factor

The total phase factor originating from real-time propagation is given by

$$\text{phase} = \exp\left(i\Phi_1 + i\Phi_2\right),$$

where

$$\Phi_1 = \sum_{j=m+1}^{m+Q} \phi_1(l_j), \qquad \Phi_2 = \sum_{j=m+Q+1}^{m+2Q} \phi_2(l_j).$$

Here, l_j denotes the lattice displacement between consecutive electron positions along the sampled configuration at time slice j, computed with periodic boundary conditions.

Monte Carlo sampling

Monte Carlo Sampling of Electron Position Configurations

for each Monte Carlo sample $s = 1, \ldots, N_s$ **do**

- **Initial time-slice:**
  - Sample:

$$z[0] \leftarrow \text{Uniform}(0, N)$$

- **Imaginary-time propagation:**
  - **for** $j = 1, \ldots, m$ **do**
    - Sample trial position $x \leftarrow \text{Uniform}(0, N)$
    - Sample $r \leftarrow \text{Uniform}(0, 1)$

* **if**

$$I_0^{\min} + (I_0^{\max} - I_0^{\min})r \le I_0[x]$$

then accept: $z[j] = x$

- **Forward real-time propagation:**
  - **for** $j = m+1, \ldots, m+Q$ **do**
    * Sample trial position $x \leftarrow \text{Uniform}(0, N)$
    * Sample $r \leftarrow \text{Uniform}(0, 1)$
    * **if**

$$I_1^{\min} + (I_1^{\max} - I_1^{\min})r \le I_1[x]$$

then accept: $z[j] = x$

- **Backward real-time propagation:**
  - **for** $j = m+Q+1, \ldots, m+2Q$ **do**
    * Sample trial position $x \leftarrow \text{Uniform}(0, N)$
    * Sample $r \leftarrow \text{Uniform}(0, 1)$
    * **if**

$$I_2^{\min} + (I_2^{\max} - I_2^{\min})r \le I_2[x]$$

then accept: $z[j] = x$

- **Trajectory construction:**
  - $y[0] = z[0]$
  - **for** $j = 1, \ldots, m+2Q$ **do**

$$y[j] = (y[j-1] + z[j]) \bmod N$$

- **Estimator evaluation:**
  - Compute $C_{11}^{(s)}$
  - Compute $C_{jj}^{(s)}$

Output:

$$C_{11} = \frac{1}{N_s}\sum_{s=1}^{N_s} C_{11}^{(s)}, \qquad C_{jj} = \frac{1}{N_s}\sum_{s=1}^{N_s} C_{jj}^{(s)}$$

Estimator:

$$\frac{C_{jj}}{C_{11}}$$

Averaging and statistics

The full calculation is repeated multiple times with independent random seeds. Final results are obtained as averages over these runs, with statistical uncertainties estimated from the standard deviation.

Since configurations are sampled directly from the weight distribution, no equilibration phase is required, which significantly improves computational efficiency.

QMC algorithm in momentum representation

In the momentum representation, the sampling procedure is simplified, as the phonon coordinates are sampled directly.

As in the position representation, all constants, vectors, and the matrix D are first constructed. The eigendecomposition of the matrix D is performed using the LAPACK library (accessed through a C interface), yielding eigenvalues `eval[]` and eigenvectors `evec[]`, which are used in the sampling procedure.

This procedure corresponds to sampling from the Gaussian distribution defined by the quadratic form associated with the matrix D.

Monte Carlo Sampling of Phonon Coordinates

for each Monte Carlo sample $s = 1, \ldots, N_s$ **do**

- **Sampling in eigenmode space:**
  - **for** $k = 0, \ldots, (m + 2Q)NN_b - 1$ **do**
    - Sample $Z[k]$ from a normal distribution
    - Rescale:

$$Z[k] \leftarrow \frac{Z[k]}{\sqrt{\texttt{eval}[k]}}$$

- **Transformation to phonon coordinates:**
  - **for** $k = 0, \ldots, (m + 2Q)NN_b - 1$ **do**

$$Y[k] = \sum_{j=0}^{(m+2Q)NN_b-1} \texttt{evec}[j(m + 2Q)NN_b + k] \cdot Z[j]$$

- **Compute:**
  - $F(\mathbf{Y})$
  - $C_{11}^{(s)}, C_{jj}^{(s)}$
- **Estimator evaluation:**
  - $C_{11} = \frac{1}{N_s} \sum_{s=1}^{N_S} C_{11}^{(s)}, \qquad C_{jj} = \frac{1}{N_s} \sum_{s=1}^{N_S} C_{jj}^{(s)}$
  - $\frac{C_{jj}}{C_{11}}$

C.1 Details of Monte Carlo Calculations

In the following tables, detailed information on the Monte Carlo calculations of the current-current correlation functions performed in this thesis is provided.

For each calculation, the relevant simulation parameters are listed, including the number of Monte Carlo samples, system size, discretization of imaginary and real time, choice of representation, and the maximum accessible time range.

The results are grouped according to the calculations presented in Chapters 3 and 4.

For the calculations presented in Chapter 3, the tables include representative parameter sets corresponding to selected temperatures, together with additional details of the analytic continuation

procedure. Additional calculations were performed at intermediate temperature values, ensuring dense coverage of the parameter space, but are not included explicitly for brevity.

Table C.1: Details of Monte Carlo calculations of real- and imaginary-time current-current correlation functions, and of the analytic continuation procedure, used in Chapter 3.

G/J	T/J	real-time calculations (QMC)					imaginary-time calculations (QMC)					analytic continuation	
		$t_{\max}$	time step	N_s	basis	N_d	$t_{\max}$	time step	N_s	basis	N_d	$\omega_{\max}$	svs
0.141	10	30	0.1	10^4	momentum	15	0.06	0.002	10^5	position	10	5	23
	5	30	0.1	10^4	momentum	25	0.12	0.004	10^5	position	10	5	40
	2	30	0.1	10^4	momentum	55	0.3	0.01	10^5	position	10	5	40
	1	30	0.1	10^4	momentum	55	0.6	0.02	10^5	position	10	5	43
	0.5	30	0.1	10^4	momentum	55	1.2	0.04	10^5	position	10	/	/
0.5	10	4	0.1	10^4	momentum	10	0.06	0.002	10^5	position	10	10	13
	5	5	0.1	10^4	momentum	10	0.12	0.004	10^5	position	10	10	17
	2	5	0.1	10^4	momentum	10	0.3	0.01	10^5	position	10	10	20
	1	5	0.1	10^4	momentum	10	0.6	0.02	10^5	position	10	10	20
	0.5	1	0.1	10^4	momentum	10	1.2	0.04	10^5	position	10	/	/
1	10	1.6	0.02	10^6	position	10	0.06	0.002	10^5	position	10	20	11
	5	1.6	0.02	10^6	position	10	0.12	0.004	10^5	position	10	20	10
	2	1.6	0.05	10^6	position	10	0.3	0.01	10^5	position	10	20	11
	1	1	0.1	10^6	position	10	0.6	0.02	10^5	position	10	20	10
	0.5	1	0.1	10^6	position	10	1.2	0.04	10^5	position	10	20	10
2	10	1	0.01	10^6	position	10	0.06	0.002	10^5	position	10	80	25
	5	1.2	0.01	10^6	position	10	0.12	0.004	10^5	position	10	150	48
	2	1.3	0.025	10^6	position	10	0.3	0.01	10^5	position	10	200	55
	1	1.3	0.025	10^6	position	10	0.6	0.02	10^5	position	10	200	54
	0.5	1.4	0.05	10^6	position	10	1.2	0.04	10^5	position	10	200	40
2.83	10	1	0.01	10^6	position	10	0.06	0.002	10^5	position	10	200	24
	5	1	0.01	10^6	position	10	0.12	0.004	10^5	position	10	300	34
	2	1	0.02	10^6	position	10	0.3	0.01	10^5	position	10	360	51
	1	1	0.025	10^6	position	10	0.6	0.02	10^5	position	10	300	45
	0.5	1	0.025	10^6	position	10	1.2	0.04	10^5	position	10	280	44

N_s denotes the number of Monte Carlo samples and N_d the system size.
For real-time calculations, data are calculated at time points that are multiples of the time step and lie in the interval $(0, t_{\max})$.
For $G/J = 0.141$, the column N_d gives the number of sites required to calculate the data at $t_{\max}$.
The analytic continuation procedure is performed on a frequency grid of $100\,\omega_{\max}$ points in the interval $(-\omega_{\max}, \omega_{\max})$.

Table C.2: Details of Monte Carlo calculations of imaginary-time current-current correlation functions used in Chapter 4.

λ	T/J	$\omega_0 = J/3$				$\omega_0 = J$				$\omega_0 = 3J$			
		$J\Delta t$	N_s	N_d	basis	$J\Delta t$	N_s	N_d	basis	$J\Delta t$	N_s	N_d	basis
0.010	0.1	0.1	10^6	15	m	0.1	10^6	20	m	0.1	10^5	30	m
	0.2	0.1	10^5	15	m	0.1	10^5	15	m	0.1	10^5	25	m
	0.5	0.08	10^5	10	m	0.08	10^5	15	m	0.08	10^5	20	m
	1.0	0.05	10^2	80	m	0.05	10^3	60	m	0.04	10^5	15	m
	2.0	0.025	10^2	80	m	0.025	10^3	60	m	0.025	10^5	15	m
	5.0	0.01	10^2	80	m	0.01	10^3	60	m	0.01	10^5	15	m
	10.0	0.005	10^2	80	m	0.005	10^3	60	m	0.005	10^5	15	m
0.125	0.1	0.1	10^6	15	m	0.1	10^6	20	m	0.1	10^5	20	m
	0.2	0.1	10^5	15	m	0.1	10^5	15	m	0.1	10^5	15	m
	0.5	0.08	10^5	10	m	0.08	10^5	15	m	0.08	10^5	15	m
	1.0	0.05	10^3	10	m	0.05	10^3	20	m	0.04	10^5	15	m
	2.0	0.025	10^3	10	m	0.025	10^3	20	m	0.025	10^3	10	m
	5.0	0.01	10^3	10	m	0.01	10^3	20	m	0.01	10^3	10	m
	10.0	0.005	10^3	10	m	0.005	10^3	20	m	0.005	10^3	10	m
0.500	0.1	0.1	10^6	15	m	0.1	10^6	20	m	0.1	10^5	20	m
	0.2	0.1	10^5	15	m	0.1	10^5	15	m	0.1	10^5	15	m
	0.5	0.08	10^5	10	m	0.08	10^5	15	m	0.08	10^5	15	m
	1.0	0.05	10^4	7	m	0.05	10^4	10	m	0.05	10^5	15	m
	2.0	0.025	10^4	7	m	0.025	10^4	10	m	0.025	10^3	10	m
	5.0	0.01	10^4	7	m	0.01	10^4	10	m	0.01	10^3	10	m
	10.0	0.005	10^4	7	m	0.005	10^4	10	m	0.005	10^3	10	m
1.000	0.1	0.1	10^6	15	m	0.1	10^6	20	m	0.1	10^6	25	m
	0.2	0.1	10^5	15	m	0.1	10^5	15	m	0.1	10^6	20	m
	0.5	0.08	10^5	10	m	0.08	10^5	15	m	0.08	10^5	15	m
	1.0	0.02	10^5	7	p	0.02	10^5	7	m	0.02	10^5	15	m
	2.0	0.01	10^5	7	p	0.01	10^5	7	m	0.01	10^5	7	p
	5.0	0.004	10^5	7	p	0.004	10^5	7	m	0.004	10^5	7	p
	10.0	0.002	10^5	7	p	0.002	10^5	7	m	0.002	10^5	7	p
2.000	0.1	0.1	10^6	15	m	–	–	–	–	–	–	–	–
	0.2	0.1	10^5	15	m	0.1	10^6	20	m	–	–	–	–
	0.5	0.08	10^5	10	m	0.08	10^5	15	m	0.08	10^5	15	m
	1.0	0.02	10^5	7	p	0.02	10^5	10	p	0.02	10^5	7	p
	2.0	0.01	10^5	7	p	0.01	10^5	10	p	0.01	10^5	7	p
	5.0	0.004	10^5	7	p	0.004	10^5	10	p	0.004	10^5	7	p
	10.0	0.002	10^5	7	p	0.002	10^5	10	p	0.002	10^5	7	p

$J\Delta t$ denotes the time discretization step, N_s the number of Monte Carlo samples, and N_d the system size.
Basis labels: *m* denotes the electron momentum representation and *p* the electron position representation.

Appendix D

Self-Energy Expressions for Band and Polaron Band Transport

D.1 Self-energy in the band transport regime

In this section, the expressions for the self-energy in the band transport regime are summarized, together with the main steps of their evaluation. The detailed calculation of the momentum summation is based on standard contour integration techniques and is not reproduced here in full.

Within the Migdal approximation, where only processes involving a single phonon line are retained, the self-energy is given by

$$\Sigma_k(\omega) = \frac{G^2}{N} \sum_q \left[(n_{\mathrm{ph}} + 1) G^{(0)}_{k-q}(\omega - \omega_0) + n_{\mathrm{ph}} G^{(0)}_{k-q}(\omega + \omega_0) \right] , \tag{D.1}$$

where $G^{(0)}_k(\omega) = (\omega - \varepsilon_k + \mathrm{i}0^+)^{-1}$ denotes the Green's function of a free particle.

The evaluation of the self-energy requires the summation over momentum of the free Green's function. This summation can be written as

$$S(\omega) = \frac{1}{N} \sum_k G^{(0)}_k(\omega), \tag{D.2}$$

which, in the thermodynamic limit, is replaced by an integral over the Brillouin zone,

$$S(\omega) = \frac{1}{2\pi} \int_{-\pi}^{\pi} \frac{\mathrm{d}k}{\omega + 2J\cos k + \mathrm{i}\delta}, \qquad \delta \to 0^+. \tag{D.3}$$

The integral can be evaluated using contour integration in the complex plane by introducing the standard substitution $z = \mathrm{e}^{\mathrm{i}k}$, which maps the integration over k onto the unit circle $|z| = 1$. The integral then takes the form

$$S(\omega) = \frac{1}{2\pi} \oint_C \frac{\mathrm{d}z}{\mathrm{i}z \left[\omega + J\left(z + \frac{1}{z} \right) + \mathrm{i}\delta \right]}, \tag{D.4}$$

where C denotes the unit circle.

The integrand has two poles determined by the condition

$$\omega + J\left(z + \frac{1}{z} \right) + \mathrm{i}\delta = 0, \tag{D.5}$$

and the evaluation of the integral reduces to determining which of these poles lies inside the unit circle.

Two distinct cases arise depending on the relation $\omega/2J$.

For $|\omega/(2J)| > 1$, the poles lie on the real axis and the infinitesimal δ can be neglected in determining their position. In this case, only one of the poles lies inside the unit circle, and evaluation of the corresponding residue yields

$$S(\omega) = \frac{\mathrm{sgn}(\omega)}{\sqrt{\omega^2 - 4J^2}}. \tag{D.6}$$

For $|\omega/(2J)| < 1$, the infinitesimal δ plays a crucial role in determining the position of the poles. A careful expansion of the pole positions to linear order in δ shows that one of the poles lies inside the unit circle and the corresponding residue evaluates to

$$S(\omega) = -\frac{\mathrm{i}}{\sqrt{4J^2 - \omega^2}}. \tag{D.7}$$

The momentum summation in Eq. (D.1) thus yields the following expression for the sum

$$S(\omega) = \begin{cases} \dfrac{\mathrm{sgn}(\omega)}{\sqrt{\omega^2 - 4J^2}}\,, & \text{if } \left|\dfrac{\omega}{2J}\right| > 1 \\ \dfrac{-\mathrm{i}}{\sqrt{4J^2 - \omega^2}}\,, & \text{if } \left|\dfrac{\omega}{2J}\right| < 1 \end{cases} . \tag{D.8}$$

Substituting this result into Eq. (D.1), the self-energy takes the form

$$\Sigma(\omega) = G^2(n_{\mathrm{ph}} + 1)S(\omega - \omega_0) + G^2 n_{\mathrm{ph}} S(\omega + \omega_0)\ . \tag{D.9}$$

The imaginary part of the self-energy defines the quasiparticle lifetime, which enters the expression for the mobility through the scattering time.

The retarded Green's function is then obtained from the Dyson equation,

$$G_k^R(\omega) = \frac{1}{\omega - \varepsilon_k - \Sigma_k(\omega)}\ , \tag{D.10}$$

from which the spectral function follows as

$$A_k(\omega) = -\frac{1}{\pi}\mathrm{Im}\, G_k^R(\omega)\ . \tag{D.11}$$

Analysis of the resulting spectral function shows that $A_k(\omega)$ vanishes outside a finite frequency range determined by the electronic bandwidth and phonon energy, $|\omega| \gtrsim 2J + \omega_0$. In practical calculations, the frequency integration can therefore be restricted to a finite interval $|\omega| \le \omega_{\max}$, with $\omega_{\max}$ chosen slightly larger than $2J + \omega_0$.

The expectation values entering the current–current correlation function are expressed in terms of the spectral function as

$$\langle a_k^\dagger(t) a_k \rangle = \int_{-\infty}^{\infty} \mathrm{d}\omega\, \mathrm{e}^{\mathrm{i}\omega t} A_k(\omega) \mathrm{e}^{-\beta\omega}\ , \tag{D.12}$$

$$\langle a_k(t) a_k^\dagger \rangle = \int_{-\infty}^{\infty} \mathrm{d}\omega\, \mathrm{e}^{-\mathrm{i}\omega t} A_k(\omega)\ . \tag{D.13}$$

Substituting these expressions into the definition of the current–current correlation function yields

$$\langle j(t) j \rangle = \frac{J^2}{\pi}\frac{1}{N_c}\sum_k \sin^2(k) f_k(t) g_k(t)\ , \tag{D.14}$$

where

$$f_k(t) = \int_{-\infty}^{\infty} \mathrm{d}\omega\, \mathrm{e}^{\mathrm{i}\omega' t} A_k(\omega') \mathrm{e}^{-\beta\omega'}\ , \tag{D.15}$$

$$g_k(t) = \int_{-\infty}^{\infty} \mathrm{d}\omega \, \mathrm{e}^{-\mathrm{i}\omega' t} A_k(\omega') \,, \tag{D.16}$$

and

$$N_c = \frac{1}{2\pi} \sum_k \int_{-\infty}^{\infty} \mathrm{d}\omega \; A_k(\omega') \mathrm{e}^{-\beta\omega'} \,. \tag{D.17}$$

In the regime when $\frac{\omega_0}{2J} > 1$, single-phonon processes are suppressed for part of the spectrum, and the inclusion of higher-order contributions becomes necessary to obtain a finite scattering rate. The dominant correction arises from diagrams involving two phonon lines.

Within this approximation, the imaginary part of the self-energy can be written as

$$\mathrm{Im}\Sigma(k,\omega) = \frac{G^4}{N^2} n_{\mathrm{ph}}(n_{\mathrm{ph}}+1) \sum_{k_1} \mathrm{Im}\left[\frac{1}{\omega - \varepsilon_{k_1} + \mathrm{i}0^+}\right] \sum_{k_2} \left[\frac{1}{(\varepsilon_{k_2} + \omega_0 - \omega)^2} + \frac{1}{(\varepsilon_{k_2} - \omega_0 - \omega)^2}\right] \tag{D.18}$$

Carrying out the momentum summations leads to the compact expression

$$\mathrm{Im}\Sigma(\omega) = G^4 n_{\mathrm{ph}}(n_{\mathrm{ph}}+1) S_1 \left[S_2(\omega - \omega_0) + S_2(\omega + \omega_0)\right] \tag{D.19}$$

where

$$S_1 = \frac{1}{N} \sum_k \mathrm{Im}\left[\frac{1}{\omega - \varepsilon_k + \mathrm{i}0^+}\right], \tag{D.20}$$

$$S_2(x) = \frac{1}{N} \sum_k \frac{1}{(\varepsilon_k - x)^2}. \tag{D.21}$$

These sums can again be evaluated analytically. The function $S_1(\omega)$ is nonzero only within the electronic band and is given by

$$S_1(\omega) = \begin{cases} \dfrac{-1}{\sqrt{4J^2 - \omega^2}} \,, & \text{if } |\dfrac{\omega}{2J}| < 1 \,, \\ 0 \,, & \text{otherwise} \,, \end{cases} \tag{D.22}$$

while $S_2(x)$ takes the form

$$S_2(x) = \begin{cases} -\dfrac{z_1 + z_2}{J^2(z_1 - z_2)^3} \,, & \text{if } \dfrac{x}{2J} > 1 \\ \dfrac{z_1 + z_2}{J^2(z_1 - z_2)^3} \,, & \text{if } \dfrac{x}{2J} < -1 \end{cases} \tag{D.23}$$

with

$$z_{1,2} = \frac{1}{2}\left(-\frac{x}{J} \pm \sqrt{\frac{x^2}{J^2} - 4}\right). \tag{D.24}$$

These contributions restore a finite imaginary part of the self-energy in the regime where single-phonon processes are suppressed.

D.2 Self-energy in polaron band transport regime

In this section, the self-energy in the polaron band transport regime is summarized in a form consistent with Ref. [133], specialized to the case where the Lang–Firsov transformation is employed.

The first nonvanishing contribution to the retarded self-energy arising from the transformed interaction $\tilde{V}$ is given by

$$\Sigma_k(\omega) = \frac{\mathrm{i}}{2\pi} \frac{1}{N^2} \sum_q \int \mathrm{d}\omega_1 \; G^{\mathrm{R}}_{k-q}(\omega - \omega_1) D^{>}_{k-q,k,q}(\omega_1) \tag{D.25}$$

where

$$D^{>}_{k-q,k,q}(\omega) = -\mathrm{i}\sum_{R_1S_1R_2S_2} b_{R_1S_1R_2S_2kq}\int \mathrm{d}t\ \mathrm{e}^{\mathrm{i}\omega t}\left\{\mathrm{e}^{a_{R_1R_2S_1S_2}[(n_{\mathrm{ph}}+1)e^{-\mathrm{i}\omega_0 t}+n_{\mathrm{ph}}e^{\mathrm{i}\omega_0 t}]}-1\right\}, \tag{D.26}$$

and

$$b_{R_1S_1R_2S_2kq} = J^2\delta_{R_1,S_1\pm1}\delta_{R_2,S_2\pm1}\mathrm{e}^{\mathrm{i}[kR_1-(k-q)S_1]}\mathrm{e}^{\mathrm{i}[(k-q)R_2-kS_2]}. \tag{D.27}$$

To evaluate this expression, the exponential containing phonon operators is expanded using the identity

$$\mathrm{e}^{a\cos\theta} = \sum_{l=-\infty}^{\infty} I_l(a)e^{\mathrm{i}l\theta} \tag{D.28}$$

together with the relation

$$(n_{\mathrm{ph}}+1)\mathrm{e}^{-\mathrm{i}\omega_0 t} + n_{\mathrm{ph}}\mathrm{e}^{\mathrm{i}\omega_0 t} = 2\sqrt{n_{\mathrm{ph}}(n_{\mathrm{ph}}+1)}\cos\left[\omega_0\left(t+\mathrm{i}\frac{\beta}{2}\right)\right]. \tag{D.29}$$

This allows the self-energy to be expressed as a sum over multiphonon processes, leading to

$$\begin{aligned}\Sigma_k(\omega) = \frac{1}{N^2}\sum_q\sum_{R_1S_1R_2S_2} & b_{R_1S_1R_2S_2kq}\\ &\left\{[I_0(a_{R_1R_2S_1S_2}\cdot 2\sqrt{n_{\mathrm{ph}}(n_{\mathrm{ph}}+1)})-1]G^{\mathrm{R}}_{k-q}(\omega)+\right.\\ &\left.\sum_{l\neq0} I_l(a_{R_1R_2S_1S_2}\cdot 2\sqrt{n_{\mathrm{ph}}(n_{\mathrm{ph}}+1)})e^{-\frac{1}{2}l\omega_0\beta}G^{\mathrm{R}}_{k-q}(\omega+l\omega_0)\right\}.\end{aligned} \tag{D.30}$$

In the polaron band transport regime, the relevant energies are concentrated around the renormalized dispersion $\tilde{\varepsilon}_k$, which is relatively narrow. As a result, the dominant contribution to the self-energy at these energies arises from the term with $l = 0$, while terms with $l \neq 0$ are shifted by multiples of ω_0 and contribute at higher energies.

Retaining only the $l = 0$ contribution, and introducing the definition

$$S_0(R,\omega,J) = \frac{1}{N}\sum_k \frac{e^{\mathrm{i}kR}}{\omega+2J\cos k+\mathrm{i}0^+} \tag{D.31}$$

the self-energy reduces to

$$\begin{aligned}\Sigma_k(\omega) = \sum_{R_1=0,S_1,R_2,S_2} & J^2\delta_{R_1,S_1\pm1}\delta_{R_2,S_2\pm1}\mathrm{e}^{-2(\frac{g}{\omega_0})^2(2n_{\mathrm{ph}}+1)}\mathrm{e}^{\mathrm{i}k(R_1-S_2)}\\ & S_0\left(R_2-S_1,\omega,\tilde{J}\right)\left[I_0(2a_{R_1R_2S_1S_2}\sqrt{n_{\mathrm{ph}}(n_{\mathrm{ph}}+1)})-1\right].\end{aligned} \tag{D.32}$$

The function $S_0(R,\omega,J)$ can be evaluated analytically using the same contour integration techniques as in the band transport case. Introducing the notation $\tau = \frac{\omega}{2J}$, and the corresponding roots $z_1 = -\tau+\sqrt{\tau^2-1}$, $z_2 = -\tau-\sqrt{\tau^2-1}$, the result can be written as

$$S_0(R,\omega,J) = \begin{cases}\frac{z_1^R}{J(z_1-z_2)} & \tau>-1 \text{ and } R\geq 0\\ \frac{z_2^R}{J(z_2-z_1)} & \tau<-1 \text{ and } R\geq 0\\ \frac{z_1^R}{J(z_1-z_2)}+\frac{1}{Jz_1z_2} & \tau>-1 \text{ and } R=-1\\ \frac{z_2^R}{J(z_2-z_1)}+\frac{1}{Jz_1z_2} & \tau<-1 \text{ and } R=-1\\ \frac{z_1^R}{J(z_1-z_2)}+\frac{1}{Jz_1z_2}(\frac{1}{z_1}+\frac{1}{z_2}) & \tau>-1 \text{ and } R=-2\\ \frac{z_2^R}{J(z_2-z_1)}+\frac{1}{Jz_1z_2}(\frac{1}{z_1}+\frac{1}{z_2}) & \tau<-1 \text{ and } R=-2\end{cases} \tag{D.33}$$

This form of the self-energy reflects the dominant role of coherent processes in the polaron band transport regime.

Appendix E

Transport regime crossovers

In this appendix, a detailed analysis of the transport regime crossovers shown in Fig. 4.9 is presented for the phonon frequencies $\omega_0/J = 1/3$ and $\omega_0/J = 3$.

E.1 Transport regime crossovers in Fig. 4.9 for $\omega_0 = J/3$.

In this section, the transport regime crossovers shown in Fig. 4.9 are analyzed in more detail for $\omega_0 = J/3$.

For the weakest interaction strength, $\lambda = 0.010$, the results in Fig. 4.5 indicate that both band and hopping transport may, in principle, be relevant at higher temperatures. A more detailed examination of Fig. E.1 shows that the numerically exact data closely follow the band transport mobility, while the hopping mobility remains below the band mobility curve (see also Fig. 4.4). This confirms that the transport is governed by the band transport regime across the entire temperature range.

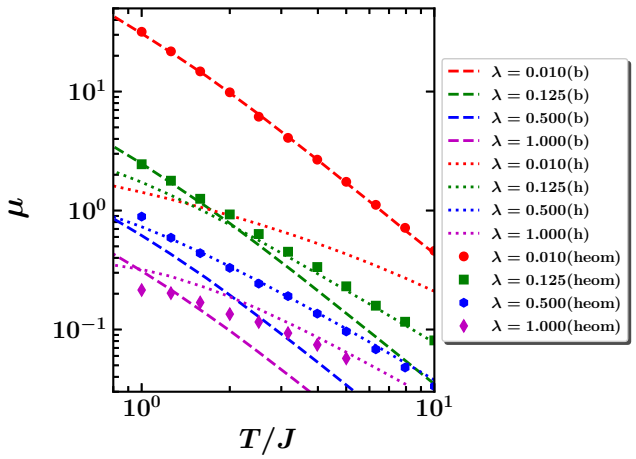

Figure E.1: Temperature dependence of the mobility for band and hopping transport at $\omega_0 = J/3$. Results for band transport (labeled "b") and hopping transport (labeled "h") are compared with numerically exact HEOM data (points).

At an interaction strength of $\lambda = 0.125$ and temperatures below $T/J = 1.0$, Fig. 4.5 indicates that band transport is the relevant regime. However, for temperatures $T/J = 2.0$ and 5.0, the identification of the transport regime becomes ambiguous.

The mobility data shown in Fig. E.1 indicate that, within the temperature interval $1.0 \leq T/J \leq 10.0$, a clear distinction between band and hopping transport cannot be made. A similar conclusion is reached from the real-time correlation functions in Fig. E.2, where the QMC results remain close to both the band and hopping transport expressions.

This region is therefore classified as an intermediate regime between band and hopping transport. At the highest temperatures, the transport behavior is assigned to the hopping regime, based on the results from Fig. 4.5.

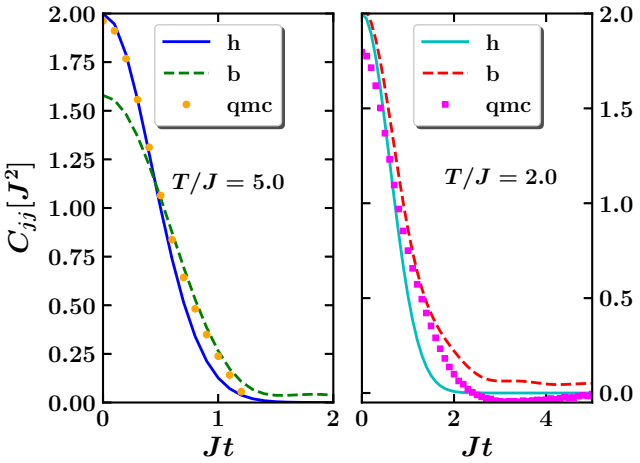

Figure E.2: Real time current-current correlation functions for $\omega_0 = J/3$, $\lambda = 0.125$, and the temperatures $T/J = 2.000$ and $T/J = 5.000$. Lines labeled with "h" correspond to functions obtained for hopping transport, lines labeled "b" correspond to functions obtained with expression for band transport and QMC results are represented with points.

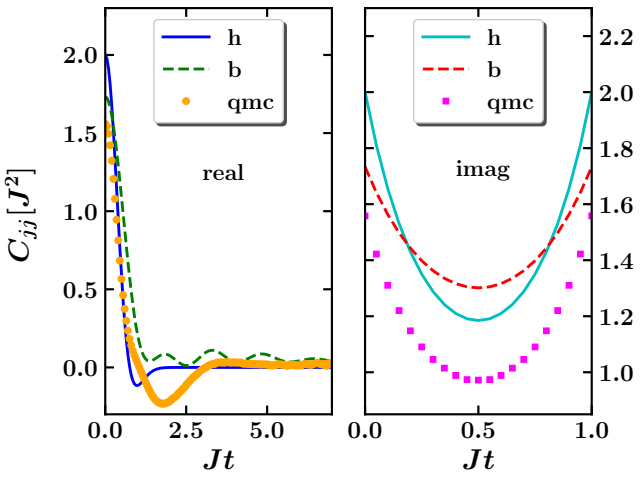

Figure E.3: Real and imaginary time current-current correlation functions for $\omega_0 = J/3$, $\lambda = 0.500$, and $T/J = 1.000$. Lines labeled with "h" correspond to functions obtained for hopping transport, lines labeled "b" correspond to functions obtained with expression for band transport and QMC results are represented with points.

At an interaction strength $\lambda = 0.500$, Fig. 4.5 indicates that hopping transport becomes the dominant mechanism for temperatures $T/J > 1.0$. The mobility data shown in Fig. E.1 confirm this behavior, as the numerically exact results closely follow the hopping transport curve over the temperature range $1.0 \leq T/J \leq 10.0$.

However, the analysis of the real-time correlation functions (Fig. E.3) shows that the identification of the transport mechanism at $T/J = 1.0$ remains ambiguous, as the QMC results are consistent with both band and hopping transport. At lower temperatures, $T/J < 1.0$, the results from Fig. 4.5 indicate that none of the three transport regimes provides a consistent description. This region is therefore represented as a white region in Fig. 4.9.

For an interaction strength $\lambda = 1.000$, Figs. 4.5 and E.1 indicate that hopping transport is the dominant mechanism over the temperature interval $1.0 \leq T/J \leq 10.0$. The analysis of the imaginary-

time correlation functions further supports this conclusion, showing that the numerical results are most consistent with the hopping transport expressions down to temperatures of the order $T/J \sim 1.0$.

At lower temperatures, Fig. 4.3 indicates that the polaron band transport regime is realized only for $T/J \lesssim 0.1$. Consequently, within the temperature range $0.1 \leq T/J \leq 10.0$, transport is assigned to the hopping regime for this set of parameters.

The same conclusion applies to the case $\lambda = 2.000$.

E.2 Transport regime crossovers in Fig. 4.9 for $\omega_0 = 3J$.

In this section, the transport regime crossovers shown in Fig. 4.9 are analyzed for $\omega_0 = 3J$.

For $\lambda = 0.010$, Fig. 4.5 indicates that both band and hopping transport satisfy the numerical criterion within the temperature range $1.0 \leq T/J \leq 10.0$. The distinction between the two mechanisms is made based on the analysis of real-time current–current correlation functions (Fig. E.4), which show that the numerical results are most consistent with conventional band transport for temperatures $0.5 \leq T/J \leq 10.0$.

This conclusion can be extended to lower temperatures based on the physical argument that, for weak interaction strength, a reduction in temperature suppresses electron–phonon scattering, thereby preserving the band transport mechanism.

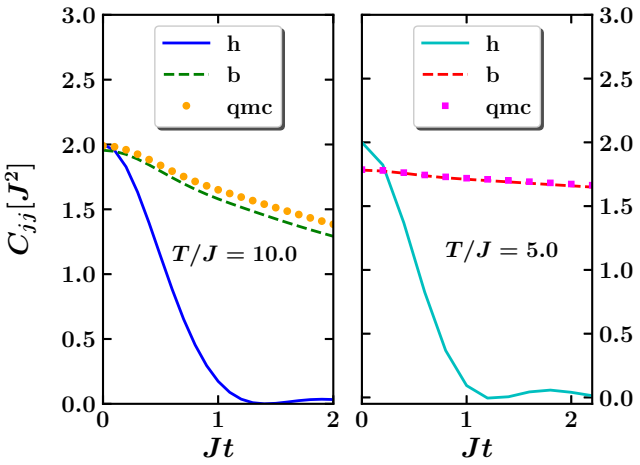

Figure E.4: Real time current-current correlation functions for $\omega_0 = 3J$, $\lambda = 0.010$, and the temperatures $T/J = 2.000$ and $T/J = 10.000$. Lines labeled with "h" correspond to functions obtained for hopping transport, lines labeled "b" correspond to functions obtained with expression for band transport and QMC results are represented with points.

For the next interaction strength, $\lambda = 0.125$, Fig. 4.5 shows that the imaginary-time criterion is satisfied for band transport in the temperature range $0.2 \leq T/J \leq 5$, and for hopping transport in the range $1 \leq T/J \leq 10$. The available mobility data (Fig. E.5) indicate that, for temperatures below $T/J = 5$, the transport behavior is best described by the band transport regime.

This conclusion is further supported by the real-time correlation functions shown in Fig. E.6 for $T/J = 2$, where the QMC results more closely follow the band transport curve. A more detailed analysis of the real-time current–current correlation functions (Fig. E.7) shows that, at $T/J = 5$, the system lies in an intermediate regime between band and hopping transport. At higher temperature, $T/J = 10.0$, both Fig. E.7 and Fig. 4.5 indicate that hopping transport becomes the relevant regime.

For the interaction strength $\lambda = 0.500$, the system can be considered to lie in the moderately strong coupling regime, where polaron band transport may be expected to occur. As shown in Fig. 4.5, the conditions for polaron band transport are satisfied in the temperature range $0.1 \leq T/J \leq 2$. In addition, the numerical criterion suggests possible agreement with band transport in the interval $0.5 \leq T/J \leq 2$, and with hopping transport for $1 \leq T/J \leq 10$.

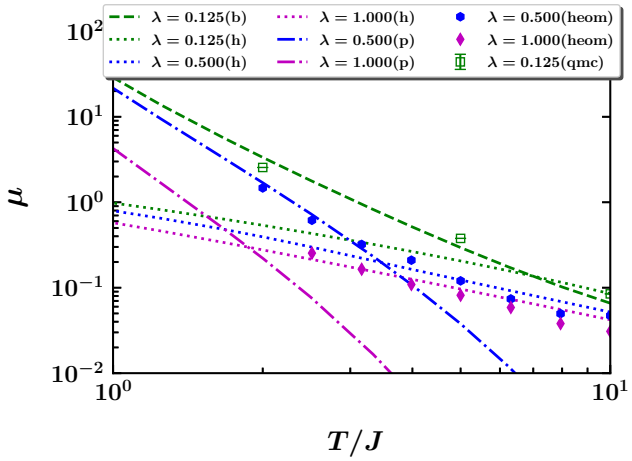

Figure E.5: Temperature dependence of the mobility for band, hopping, and polaron band transport at $\omega_0 = 3J$. Results labeled “b”, “h”, and “p” are compared with numerically exact HEOM data [33] (points).

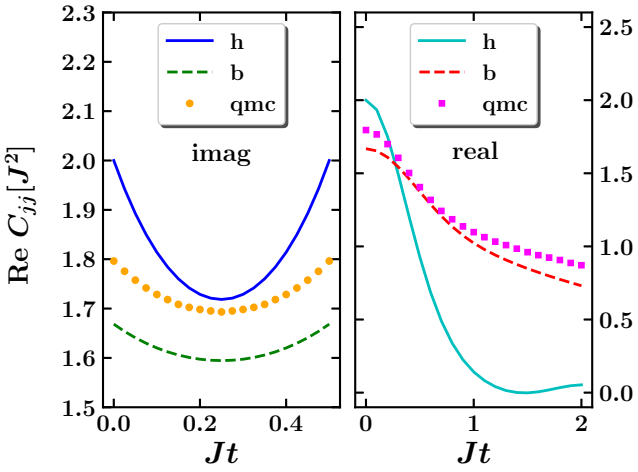

Figure E.6: Imaginary- and real-time current-current correlation functions shown for specified parameters $\omega_0 = 3J$, $\lambda = 0.125$, $T/J = 2.000$. Lines labeled with "h" correspond to functions obtained with Eq. 4.6 for hopping transport, lines labeled "b" correspond to functions obtained with expression for band transport and QMC results are represented with points.

The possibility of conventional band transport is ruled out based on the analysis of real-time current–current correlation functions. As illustrated in Fig. E.8, the QMC results deviate significantly from both the band and hopping transport expressions, indicating that neither description provides an adequate representation in this region.

Additional insight is provided by the available numerically exact HEOM data (Fig. E.5), which clearly demonstrate a crossover from polaron band to hopping transport. This transition occurs in the vicinity of the intersection between the corresponding mobility curves.

For the two strongest interaction strengths, $\lambda = 1.000$ and $\lambda = 2.000$, numerically exact data are not available at the lowest temperatures. The identification of transport regime transitions is therefore based on the conclusions established in the previous analysis.

For $\lambda = 1.000$, Fig. 4.5 indicates that the criterion for polaron band transport is satisfied in the temperature range $0.1 \leq T/J \leq 1.0$, while possible agreement with hopping transport is found for $0.5 \leq T/J \leq 10$. The possibility of conventional band transport is excluded for the same reasons as in the case of $\lambda = 0.500$. As shown in Figs. 4.3 and E.5, the mobility curves for polaron band and hopping transport intersect at approximately $T/J \approx 2$. This intersection is used to identify the crossover between the two regimes, with transport assigned to the polaron band regime for $T/J \lesssim 2$, and to the hopping regime for $T/J \gtrsim 2$.

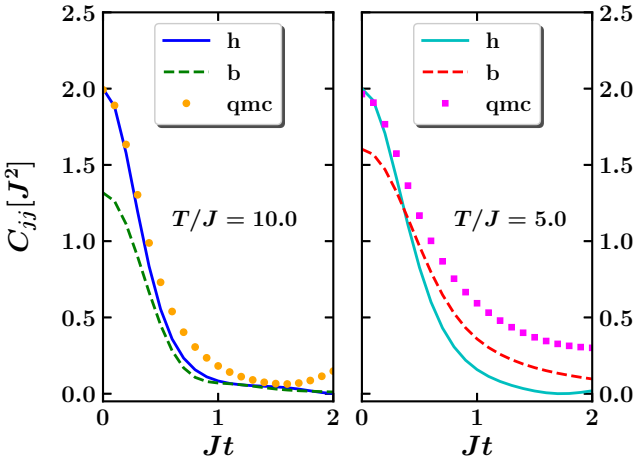

Figure E.7: Real-time current-current correlation functions for $\omega_0 = 3J$, $\lambda = 0.125$, and the temperatures $T/J = 5.000$ and $T/J = 10.000$. Lines labeled with "h" correspond to functions obtained for hopping transport, lines labeled "b" correspond to functions obtained with expression for band transport and QMC results are represented with points.

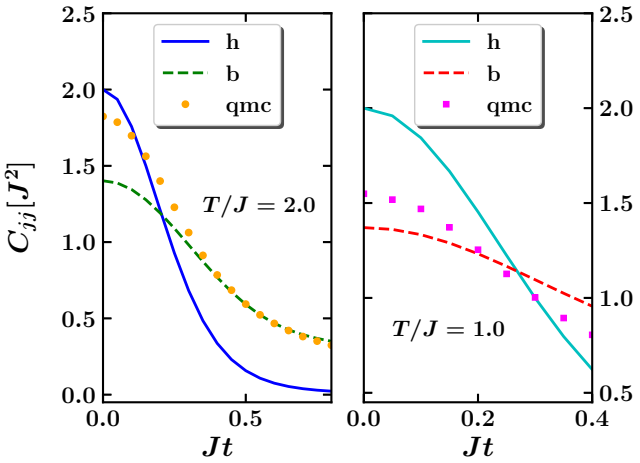

Figure E.8: Real-time current-current correlation functions for $\omega_0 = 3J$, $\lambda = 0.500$, and the temperatures $T/J = 1.000$ and $T/J = 2.000$. Lines labeled with "h" correspond to functions obtained for hopping transport, lines labeled "b" correspond to functions obtained with expression for band transport and QMC results are represented with points.

A similar analysis applies to $\lambda = 2.000$, where the intersection of the corresponding mobility curves occurs at approximately $T/J \approx 1.0$. Accordingly, transport is assigned to the polaron band regime for $T/J \lesssim 1.0$, and to the hopping regime for higher temperatures.

Biography

Suzana Miladić was born on January 3, 1995, in Novi Sad. She completed her elementary education in Bačka Palanka in 2010, after which she continued her schooling in Novi Sad, graduating from medical high school in 2014 as a physical therapist. She then enrolled at the Faculty of Sciences in Novi Sad, where she obtained her BSc degree in physics in 2018. She continued her studies at the Faculty of Physics in Belgrade, where she completed her MSc in September 2019 with a thesis titled "Spin resonance and relaxation in InSb nanowire quantum dots" under the supervision of Dr. Edib Dobardžić, for which she received the Faculty of Physics award “Prof. Dr. Ljubomir Ćirković”.

In late 2019, she enrolled in PhD studies at the Faculty of Physics in Belgrade in the field of condensed matter physics. Since December 2019, she has been employed at the Institute of Physics Belgrade, in the Scientific Computing Laboratory, where she conducts research on polaron transport under the supervision of Dr. Nenad Vukmirović. During her PhD, she participated in several conferences and workshops and received two awards for poster presentations. She also proposed and completed a smaller research project on polaron transport, supported by the SAIGE SEED grant for young researchers. Her PhD research was primarily conducted within the PolMoReMa project, led by Dr. Nenad Vukmirović.

Her PhD work resulted in two publications:

1. S. Miladić and N. Vukmirović, *Method for obtaining polaron mobility using real and imaginary time path-integral quantum Monte Carlo*, Phys. Rev. B **107**, 184315 (2023)
2. S. Miladić and N. Vukmirović, *Identification of the transport regimes of the one-dimensional Holstein model*, Phys. Rev. B **112**, 054314 (2025)

Изјава о ауторству

Име и презиме аутора Сузана Миладић

Број индекса 8010/2019

Изјављујем

да је докторска дисертација под насловом

Quantum Monte Carlo Study of Polaron Mobility

(Проучавање покретљивости поларона користећи квантне Монте Карло методе)

- резултат сопственог истраживачког рада;
- да дисертација у целини ни у деловима није била предложена за стицање друге дипломе према студијским програмима других високошколских установа;
- да су резултати коректно наведени и
- да нисам кршио/ла ауторска права и користио/ла интелектуалну својину других лица.

Потпис аутора

У Београду, _____

_____

Изјава о истоветности штампане и електронске верзије докторског рада

Име и презиме аутора Сузана Миладић

Број индекса 8010/2019

Студијски програм Физика конеднзоване материје и статистичка физика

Наслов рада Quantum Monte Carlo Study of Polaron Mobility
(Проучавање покретљивости поларона користећи квантне Монте Карло методе)

Ментор др Ненад Вукмировић

Изјављујем да је штампана верзија мог докторског рада истоветна електронској верзији коју сам предао/ла ради похрањивања у **Дигиталном репозиторијуму Универзитета у Београду.**

Дозвољавам да се објаве моји лични подаци везани за добијање академског назива доктора наука, као што су име и презиме, година и место рођења и датум одбране рада.

Ови лични подаци могу се објавити на мрежним страницама дигиталне библиотеке, у електронском каталогу и у публикацијама Универзитета у Београду.

Потпис аутора

У Београду, _____

_____

Изјава о коришћењу

Овлашћујем Универзитетску библиотеку „Светозар Марковић“ да у Дигитални репозиторијум Универзитета у Београду унесе моју докторску дисертацију под насловом:

Quantum Monte Carlo Study of Polaron Mobility

(Проучавање покретљивости поларона користећи квантне Монте Карло методе)

која је моје ауторско дело.

Дисертацију са свим прилозима предао/ла сам у електронском формату погодном за трајно архивирање.

Моју докторску дисертацију похрањену у Дигиталном репозиторијуму Универзитета у Београду и доступну у отвореном приступу могу да користе сви који поштују одредбе садржане у одабраном типу лиценце Креативне заједнице (Creative Commons) за коју сам се одлучио/ла.

1. Ауторство (CC BY)

2. Ауторство – некомерцијално (CC BY-NC)

3. Ауторство – некомерцијално – без прерада (CC BY-NC-ND)

4. Ауторство – некомерцијално – делити под истим условима (CC BY-NC-SA)

5. Ауторство – без прерада (CC BY-ND)

6. Ауторство – делити под истим условима (CC BY-SA)

(Молимо да заокружите само једну од шест понуђених лиценци.
Кратак опис лиценци је саставни део ове изјаве).

Потпис аутора

У Београду, _____

_____

1. **Ауторство.** Дозвољавате умножавање, дистрибуцију и јавно саопштавање дела, и прераде, ако се наведе име аутора на начин одређен од стране аутора или даваоца лиценце, чак и у комерцијалне сврхе. Ово је најслободнија од свих лиценци.

2. **Ауторство – некомерцијално.** Дозвољавате умножавање, дистрибуцију и јавно саопштавање дела, и прераде, ако се наведе име аутора на начин одређен од стране аутора или даваоца лиценце. Ова лиценца не дозвољава комерцијалну употребу дела.

3. **Ауторство – некомерцијално – без прерада.** Дозвољавате умножавање, дистрибуцију и јавно саопштавање дела, без промена, преобликовања или употребе дела у свом делу, ако се наведе име аутора на начин одређен од стране аутора или даваоца лиценце. Ова лиценца не дозвољава комерцијалну употребу дела. У односу на све остале лиценце, овом лиценцом се ограничава највећи обим права коришћења дела.

4. **Ауторство – некомерцијално – делити под истим условима.** Дозвољавате умножавање, дистрибуцију и јавно саопштавање дела, и прераде, ако се наведе име аутора на начин одређен од стране аутора или даваоца лиценце и ако се прерада дистрибуира под истом или сличном лиценцом. Ова лиценца не дозвољава комерцијалну употребу дела и прерада.

5. **Ауторство – без прерада.** Дозвољавате умножавање, дистрибуцију и јавно саопштавање дела, без промена, преобликовања или употребе дела у свом делу, ако се наведе име аутора на начин одређен од стране аутора или даваоца лиценце. Ова лиценца дозвољава комерцијалну употребу дела.

6. **Ауторство – делити под истим условима.** Дозвољавате умножавање, дистрибуцију и јавно саопштавање дела, и прераде, ако се наведе име аутора на начин одређен од стране аутора или даваоца лиценце и ако се прерада дистрибуира под истом или сличном лиценцом. Ова лиценца дозвољава комерцијалну употребу дела и прерада. Слична је софтверским лиценцама, односно лиценцама отвореног кода.